UNIVERSITY OF AMSTERDAM

UvA-DARE (Digital Academic Repository)

Reflecting on Higgs: Spin and parity measurement in the H → WW → eνμνμ channel

Oussoren, K.P.

Link to publication

Citation for published version (APA):
Oussoren, K. P. (2016). *Reflecting on Higgs: Spin and parity measurement in the H → WW → $ev_e\mu v_\mu$ channel*.

General rights
It is not permitted to download or to forward/distribute the text or part of it without the consent of the author(s) and/or copyright holder(s), other than for strictly personal, individual use, unless the work is under an open content license (like Creative Commons).

Disclaimer/Complaints regulations
If you believe that digital publication of certain material infringes any of your rights or (privacy) interests, please let the Library know, stating your reasons. In case of a legitimate complaint, the Library will make the material inaccessible and/or remove it from the website. Please Ask the Library: https://uba.uva.nl/en/contact, or a letter to: Library of the University of Amsterdam, Secretariat, Singel 425, 1012 WP Amsterdam, The Netherlands. You will be contacted as soon as possible.

UvA-DARE is a service provided by the library of the University of Amsterdam (http://dare.uva.nl)

Download date: 03 Nov 2020

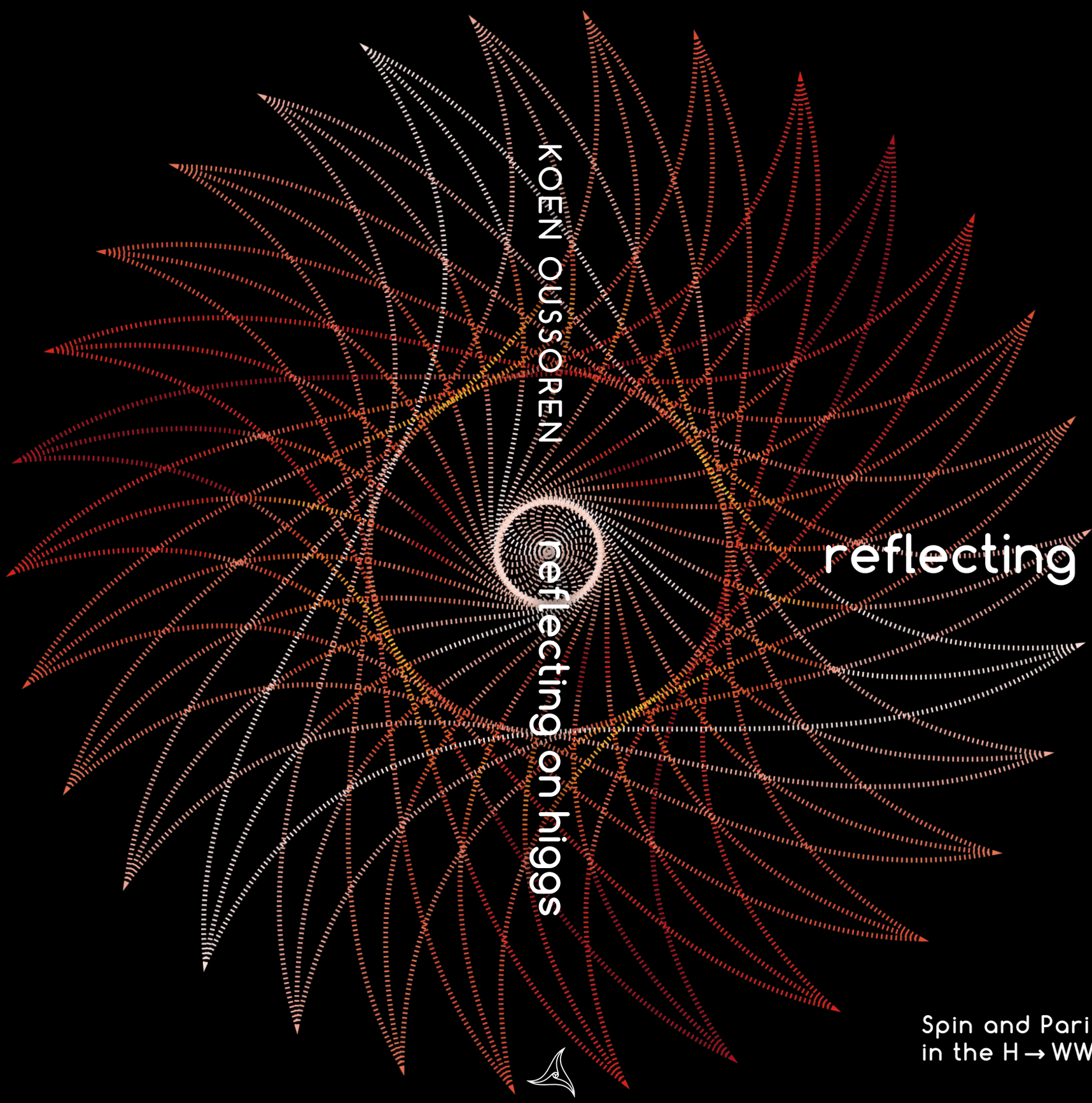

reflecting on higgs

KOEN OUSSOREN

Spin and Parity Measurement
in the H → WW → eνμν Channel

Reflecting on Higgs

Spin and Parity Measurement in the $H \to WW \to e\nu_e \mu\nu_\mu$ Channel

Koen Oussoren

Reflecting on Higgs

Spin and Parity Measurement in the $H \to WW \to e\nu_e \mu\nu_\mu$ Channel

ACADEMISCH PROEFSCHRIFT

ter verkrijging van de graad van doctor
aan de Universiteit van Amsterdam
op gezag van de Rector Magnificus
Prof. dr. ir. K.I.J. Maex
ten overstaan van een door het college van promoties
ingestelde commissie,
in het openbaar te verdedigen in de Agnietenkapel
op dinsdag 27 september 2016, te 10:00 uur

door

Koen Pieter Oussoren

geboren te Monnickendam

Promotiecommissie:

Promotor:	prof. dr.	S.C.M. Bentvelsen	Universiteit van Amsterdam
Copromotor:	dr. ir.	P.M. Kluit	Nikhef
Overige leden:	dr.	V. Dao	Universität Freiburg
	prof. dr.	E.L.M.P. Laenen	Universiteit van Amsterdam
	prof. dr.	H.G. Raven	Vrije Universiteit
	prof. dr.	P.M. Kooijman	Universiteit van Amsterdam
	prof. dr.	A.N.J.J. Schellekens	Radboud Universiteit Nijmegen
	prof. dr. ir.	P.J. de Jong	Universiteit van Amsterdam

Faculteit der Natuurwetenschappen, Wiskunde en Informatica

Copyright 2016 by Koen Oussoren ©
Reflecting on Higgs
Typeset in XCharter by using LaTeX
Cover Title: "Multiple Eddies"
Cover Design by Buro Brouns
Printed by Gildeprint

ISBN: 978-94-6233-347-5

This work is part of the research program of the *Stichting voor Fundamenteel onderzoek der Materie (FOM)*, which is part of the *Nederlandse organisatie voor Wetenschappelijk Onderzoek (NWO)*. It was carried out at the *Nationaal Instituut voor Subatomaire Fysica (Nikhef)* in Amsterdam, the Netherlands.

Voor Opa & Oma

“A circle? What could it mean?” He let his thoughts flow. A perfectly round line, no beginning, no end, no deviation. If expanded infinitely, it would become the universe. If contracted, it would become co-equal with the infinitesimal dot in which his soul resided. His soul was round. The universe was round. Not two. One. One entity - himself and the universe.

“Musashi” by Eiji Yoshikawa

Contents

Introduction

Why do we study the properties of elementary particles? Because we understand that the Universe we live in and all interactions that take place can be attributed to the existence and properties of elementary particles and how they interact with one another. A great deal of knowledge about these particles is collected by observing processes in our Universe and studying its evolution, as well as by doing experiments like colliding particles head-on at high energies to see if we can create new particles. A large part of this knowledge is incorporated in what we call the Standard Model (SM) of elementary particle physics, which was formulated as a fundamental theory in the '70s of the last century. Besides, describing the known particles at the current time, it also predicted the existence of particles like the W and Z boson, which were discovered in the '80s. The Higgs particle is the last missing piece of the SM and the bosonic particle discovered in 2012 with CERN's ATLAS and CMS detectors is a plausible Higgs candidate.

This thesis is about measuring the spin and parity quantum properties of the Higgs boson. According to the SM, the Higgs is a scalar boson, meaning that it is spin-less and stays invariant under parity or mirror operations. The spin and parity measurement can reveal if the discovered Higgs-like particle in 2012 fulfils all criteria of a SM Higgs and thereby completes the SM. However, if the measurement would confirm a different spin or parity than the SM prediction, it would mean we are dealing with so-called beyond SM physics (BSM) and opens up the possibility of new, non-SM, elementary particles and new types of interactions. And even if the spin and parity measurement is in line with a SM Higgs boson, small deviations from the SM expectations can hint to the existence of new BSM particles.

For the measurement of the Higgs spin and parity, we will focus the analysis on the $H \to WW \to e\,\nu_e\,\mu\,\nu_\mu$ channel, which is one of the possible decay options for a SM Higgs boson. Unfortunately, we can not measure Higgs bosons directly due to their instant decay into other particles. However, spin and parity are conserved quantities and passed on to the W bosons and subsequently to the charged leptons and neutrinos. The spin and parity is conveyed in correlations found in the angular and momentum distributions of these final state leptons and neutrinos. This thesis explains how to exploit these correlations in order to measure the Higgs spin and parity.

The thesis layout is as follows:

- **Chapter 1** Gives a theoretical overview of the Standard Model of elementary particles, the processes involving the Higgs boson and conceptual problems with the SM. It also introduces the Effective Field Theory (EFT) approach to describe unknown physics beyond the Standard Model.
- **Chapter 2** Describes physics at the LHC and the performance of the ATLAS detector.
- **Chapter 3** Presents simulation studies performed via the EFT approach. Personally, I contributed to the comparison of LO and NLO ggF production processes. In addition I studied whether the NLO processes could influence the spin/CP studies performed in ATLAS.
- **Chapter 4** Describes an algorithm that allows to boost to the Higgs rest-frame. The algorithm can be used in the decay of the Higgs to two W bosons, which decay each to a charged lepton and a neutrino. The algorithm relies on solving a quadratic equation to find the longitudinal momentum component of the dineutrino system and thereby solves the Higgs boost vector. Further, variables of interest are introduced to study the spin and parity of a SM Higgs and other BSM bosonic particles.
- **Chapter 5** Gives an overview of the event selection that will be used as input to the spin and parity analysis. The SM Higgs prediction will be combined with the irreducible background to give a precise estimate of the total expected events. Special attention is paid to the reconstruction of the transverse momentum of the Higgs boson. It was found that combining several independent methods into one combined method yields a more precise reconstruction of the Higgs transverse momentum.
- **Chapter 6** Introduces the actual spin and parity analysis of this thesis. I introduce the several alternative spin and parity models and construct a statistical model in order to compare the alternative models with the SM hypothesis.
- **Chapter 7** Shows the results obtained from various spin-2 models and the compatibility of the data with the SM prediction is discussed.
- **Chapter 8** Shows the results obtained for several discrete spin-0 models. In the second part the results are presented about a study on mixing the SM Higgs with BSM parity-even or parity-odd Higgs particles.
- **Conclusion** Summarises the analysis and results of this thesis and presents an outlook for future analysis at the LHC.
- **Appendices** Auxiliary material supporting the analysis and results chapters can be found here.
- **Popular Summary** At the end, a summary intended for a broad audience and written in both English and Dutch.

Theoretical Overview

1

In this first chapter we introduce the Standard Model of elementary particle physics[1–4]. The Standard Model (SM) is a fundamental theory that withstands the rigorous tests that have been conducted the last couple of decades. It is remarkable how precise the SM predictions agree with experiments for the electromagnetic, weak and strong interactions. Nevertheless, the SM has conceptual problems when describing the constituents of our Universe, as we will point out. New theories are proposed by theorists to describe physics beyond the SM, also commonly referred to as Beyond Standard Model (BSM) physics and some of these predict the existence of new fields and particles.

We will first describe the elementary particles of the SM and how they interact with one another through the mediation of force carriers. The theoretical description is based on introductory texts on particle physics such as Ref. [5–7]. After, the focus will be on processes involving interactions with the Higgs boson, as this thesis is about the properties of the Higgs boson. Next, we will introduce the various problems that arise when using the SM to describe our Universe and the need for BSM. There are various types of BSM physics, but for the purpose of this thesis the processes that affect the spin/CP properties of the Higgs are discussed in detail. We end this chapter by introducing the Effective Field Theory (EFT) to describe BSM physics and how this can be used as a way to probe New Physics in the Higgs sector.

1.1 The Standard Model of Particle Physics

The Standard Model is a collection of fermions, with spin-1/2, and bosons, with spin-1. The only exception is the Higgs boson, which is a scalar particle, having spin-0. The fermions are the building blocks of all the matter in the Universe. The bosons are the force carriers of three out of four fundamental forces in nature: the electromagnetic force, the weak (nuclear) force and the strong (nuclear) force. These forces are responsible for interactions between charged particles, radioactive decay and the stability of protons and neutrons. The fourth force, gravity, is not incorporated in the SM. In the following subsections we will describe the categories of fermions and the different types of spin-1

bosons. All the elementary SM particles and their properties are summarised in Table 1.1 and 1.2. The Higgs boson will be described in the next section.

1.1.1 Quarks and Leptons

The SM fermions can be divided in two classes called the quarks and leptons. The main difference between these types is that the quarks have a property called colour, while leptons are colourless particles. Both the quarks and leptons can be subdivided in three generations, increasing in mass. Within each generation their are two quark flavours and two lepton flavours. A charged left-handed[1] lepton forms a pair with a left-handed neutrino of the same type in a doublet. The other doublet is formed by combining a left-handed up-type and a left-handed down-type quark. The right-handed lepton and quark flavours are not combined, but remain singlets. The formation of doublets will become clear when talking about the charged weak interactions. Table 1.1 lists all the SM fermions and their properties. For each fermion there is a corresponding antiparticle with opposite quantum numbers.

(Anti)Quarks can have one of the three (anti)colour charges: (anti)red, (anti)green or (anti)blue. The quarks will form objects out of two or three quarks, called mesons and baryons respectively. These are colour neutral and are obtained by combining quarks from the three (anti)colours or combining a colour with its corresponding anticolour. There are no free quarks in nature, but only combinations of quarks that are colour neutral. The up and down-quarks from the first generation will form protons and neutrons and together with the electrons they form the atoms and all the elements occurring in our Universe. The quarks and charged leptons in the second and third generation will subsequently decay to lower generation particles.

1.1.2 Fundamental Forces

In order for the fermions to interact with one another a bosonic particle is exchanged to mediate the force. The type of force is defined by the type of boson being exchanged. In general, forces act on the properties of particles. The electromagnetic force only acts on particles with an electric charge and the exchange boson of this type is the photon γ. The strong force acts on fermions with a colour charge, which are the quarks. The boson being exchanged is the gluon g and it ensures the stability of the proton and the neutron by keeping its constituent quarks together. Due to the a special property related to symmetry, gluons carry a colour charge as well and thereby interact with themselves. There are eight

[1] A fermion is right-handed/left-handed if its wave function is an eigenstate of the $\frac{1}{2}(1\pm\gamma^5)$ projection operator. All fermion wave functions can be decomposed in left-handed and right-handed components.

Generation	leptons			Quarks		
	Flavour	Charge (e)	Mass (GeV)	Flavour	Charge (e)	Mass (GeV)
1st	ν_e	0	$< 3 \cdot 10^{-9}$	u(up)	2/3	$2.3 \cdot 10^{-3}$
	e	-1	$511 \cdot 10^{-6}$	d(down)	-1/3	$4.8 \cdot 10^{-3}$
2nd	ν_μ	0	$< 0.19 \cdot 10^{-3}$	c(charm)	2/3	1.275
	μ	-1	$113.4 \cdot 10^{-3}$	s(strange)	-1/3	0.095
3rd	ν_τ	0	< 0.018	t(top)	2/3	173.21
	τ	-1	1.777	b(bottom)	-1/3	4.6

Table 1.1: The properties of the elementary fermions of the SM. The masses are taken from Ref. [9].

Boson	Charge (e)	Mass (GeV)	Interaction
γ	0	0	Electromagnetic
$W^\pm$	± 1	80.385 ± 0.015	Weak
Z	0	91.188 ± 0.002	Weak
g	0	0	Strong

Table 1.2: The properties of the elementary bosons of the SM, except the Higgs, and which interactions they mediate. The masses are taken from Ref. [9].

types of gluons that can be exchanged. Photons do not carry an electric charge with them, so there does not exist a self-interaction between photons.

The strong and electromagnetic forces do not change the flavour of a fermion. The weak force on the other hand can change a fermion's flavour. The charged weak interaction works on left-handed doublets by letting an up-type quark or neutrino change in a down-type quark or charged lepton, or the other way around. However, the quark flavour eigenstates involved in the weak interactions are not the same as the quark mass eigenstates measured in experiments. The flavour eigenstate is a mixed combination of mass eigenstates. Effectively it means that the weak interaction can change the quark flavour between different generations. The bosons being exchanged are the $W^\pm$ bosons and because of their electric charge, they also change the charge of the fermions. There is also a neutral weak gauge boson called the Z boson, but it does not let particles change flavour. It acts on both left-handed and right-handed fermions.

The electromagnetic and weak forces can be combined in one electroweak force, which takes care of the interaction of all charged particles and types of flavour. The strong force can be described by the theory of quantum chromo dynamics, QCD, but will not be discussed in this thesis. For more information on QCD we refer to Ref. [8].

1.1.3 Lagrangian Formalism

In order to predict the likelihood of particles interacting with each other, amplitudes of certain process have to be calculated. A consistent way of constructing amplitudes is the use of a Lagrangian formalism. A Lagrangian is the difference between the kinetic and potential energy of a dynamical system, and is normally defined as density per volume: $L = \int \mathscr{L} dx dy dz$. In order to find the interactions, the action has to be minimised: $S = \int \mathscr{L} d^4x$, or equivalently, by solving the Euler-Lagrange equation:

$$\partial_\mu \left[\frac{\partial \mathscr{L}}{\partial(\partial_\mu \phi_i)} \right] = \frac{\partial \mathscr{L}}{\partial \phi_i} \tag{1.1}$$

The action S has to be dimensionless, so the terms making up $\mathscr{L}$ are not allowed to have any other dimensions than four. From the terms in the Lagrangian $\mathscr{L}$ we can couple particles with each other by using the Feynman-rules and construct Feynman-diagrams. The diagrams are then used to calculate amplitudes and enable us to predict cross-sections for scattering processes and decay widths of unstable particles.

1.2 The Higgs Boson

Due to interactions with the Higgs boson, particles get their masses and the strength of the coupling is proportional to the mass of the particle itself. The mechanism behind this is electroweak symmetry breaking (EWSB)[10–15]. Below, only a simplified version is given of EWSB, but a good introduction to this topic can be found in Ref. [7]. We will explain which processes are involved in creating the Higgs boson and its subsequent decay to SM particles, with a focus on decay to W bosons. We end this section by discussing the spin and charge-parity properties in the $H \to WW \to l\nu l\nu$ channel.

1.2.1 Scalar Interactions

The Higgs mechanism starts with a complex scalar doublet:

$$\Phi = \frac{1}{\sqrt{2}} \begin{pmatrix} \phi_1 + i\phi_2 \\ \phi_3 + i\phi_4 \end{pmatrix} \tag{1.2}$$

The Lagrangian that describes these complex scalar fields is given by:

$$\mathscr{L}_\Phi = (D^\mu \Phi)^\dagger (D_\mu \Phi) - V(\Phi) \tag{1.3}$$

In this formula the covariant derivative is defined as:

$$D_\mu = \partial_\mu - ig\frac{1}{2}\sigma_a W_\mu^a(x) - ig'\frac{1}{2}YB_\mu(x) \tag{1.4}$$

with $a = 1,2,3$. There are three gauges fields W_μ^a with coupling strength g and one gauge field B_μ with coupling strength g'. They belong to the SU(2) and U(1) symmetry groups respectively and combined this covariant derivative is used for a SU(2) × U(1) symmetry group. The σ_a are the Pauli-matrices describing the weak isospin and Y represents the hypercharge. The complex scalar doublet in Eq. 1.2 is chosen such that its weak isospin is 1/2 and it has a hypercharge of +1. The potential V in Eq. 1.3 is given by:

$$V(\Phi) = \mu^2(\Phi^\dagger\Phi) + \lambda(\Phi^\dagger\Phi)^2 \tag{1.5}$$

with $\lambda > 0$ and $\mu^2 < 0$ as to get the desired potential (Mexican hat). The gauge fields W_μ^a and B_μ are combined and rotated to obtain the $W_\mu^\pm$, Z_μ and A_μ fields:

$$\begin{aligned} W_\mu^\pm &= \frac{1}{\sqrt{2}}(W_\mu^1 \mp iW_\mu^2) \\ Z_\mu &= \cos(\theta_W)W_\mu^3 - \sin(\theta_W)B_\mu \\ A_\mu &= \sin(\theta_W)W_\mu^3 + \cos(\theta_W)B_\mu \end{aligned} \tag{1.6}$$

where θ_W is the weak mixing angle, also known as the Weinberg angle.

The electro-weak vacuum is then broken by requiring the following:

$$\frac{1}{\sqrt{2}}\begin{pmatrix}\phi_1 + i\phi_2 \\ \phi_3 + i\phi_4\end{pmatrix} \xrightarrow{EWSB} \frac{1}{\sqrt{2}}\begin{pmatrix}0 \\ v + H + i\rho\end{pmatrix} \tag{1.7}$$

The EWSB breaks the SU(2) × U(1) symmetry to a U(1) symmetry with electric charge as the conserved quantity. The complex scalar doublet describes now a expectation for the electroweak vacuum v and a field belonging to a scalar boson H. The complex field ρ can be removed by letting it be absorbed as the longitudinal components of the weak gauge bosons W and Z. The Lagrangian involving the Higgs after EWSB is written out as the following:

$$\mathscr{L}_H = \frac{1}{2}(\partial_\mu H)(\partial^\mu H) + (v+H)^2\left[\frac{g^2}{4}W_\mu^\dagger W^\mu + \frac{1}{8}(g^2+g'^2)Z_\mu^\dagger Z^\mu\right] - \lambda v^2 H^2 - \lambda v H^3 - \frac{1}{4}H^4 \tag{1.8}$$

Writing out the terms involving $W_\mu^\dagger W^\mu$ and $Z_\mu^\dagger Z^\mu$ gives us the W and Z boson masses: $M_W = \frac{1}{2}vg$ and $M_Z = \frac{1}{2}v\sqrt{g^2+g'^2}$. The terms involving $HW_\mu^\dagger W_\mu$ and $HZ_\mu^\dagger Z^\mu$ represent the HWW and HZZ vertices. The mass of the Higgs boson is parametrised as $M_H = \sqrt{2\lambda v^2}$ and the last two terms of Eq. 1.8 represent trilinear and quartic Higgs self-interactions.

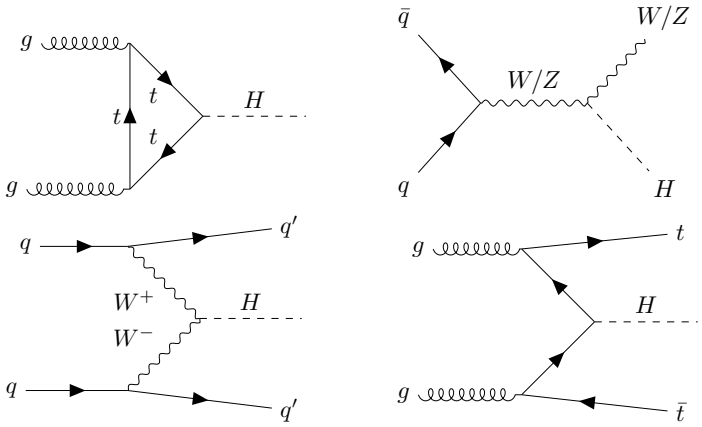

Figure 1.1: Feynman-diagrams for Higgs production. Clockwise from top left: gluon-gluon fusion Higgs (ggF), associated Higgs (VH), $t\bar{t}$ associated Higgs (ttH) and vector boson fusion Higgs (VBF).

The only field that remains massless and does not appear in Eq. 1.8 is A_μ describing the photon.

The complete SM Lagrangian is given by:

$$\mathscr{L}_{SM} = \mathscr{L}_{EW} + \mathscr{L}_H + \mathscr{L}_{Yukawa} + \mathscr{L}_{QCD} \tag{1.9}$$

where only $\mathscr{L}_H$ is written out in Eq. 1.8. The other terms are not discussed in this thesis, but a comprehensive overview is given in chapter one of Ref. [16].

1.2.2 Higgs Production and Decay at Hadron Colliders

There are four main production processes to create a Higgs boson: in decreasing cross-section, the gluon-gluon fusion (ggF) [17], the vector boson fusion (VBF) [18], the associated (VH) [19] and $t\bar{t}$ associated Higgs (ttH) [20] production modes. The corresponding Feynman diagrams are depicted in Fig. 1.1. In the ggF production modes the gluons fuse together with the help of a top quark triangle, which then merges to a scalar particle. The gluons can not couple directly to the Higgs, because they are massless. The other processes involve either a heavy quark like the top or a heavy gauge boson as the W and Z bosons. Fig. 1.2 shows the production cross-sections in pp collisions of all the four different modes as a function of the Higgs mass at a centre-of-mass energy of 8 TeV. It is clear that over the whole mass range, the ggF production mode is several orders larger than the other three modes.

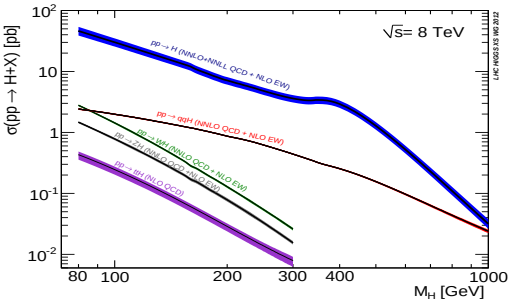

Figure 1.2: Higgs production cross-sections as function of the Higgs mass for the production processes shown in Fig. 1.1 at $\sqrt{s} = 8$ TeV. Figure taken from Ref. [21].

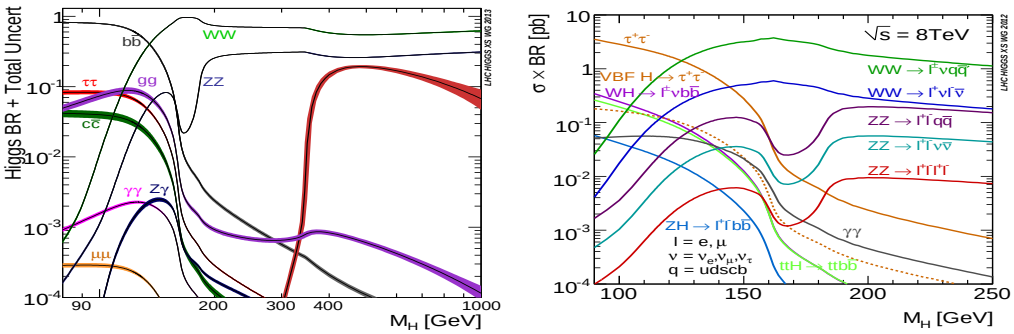

Figure 1.3: Left, the branching ratio for Higgs decay to SM particles as function of the Higgs mass. On the right plot is the corresponding cross-section for Higgs production times the branching ratio for a certain final state of decay products also as function of the Higgs mass. Figure taken from Ref. [21].

After the production, the Higgs boson will subsequently decay to fermions or bosons, depending on the mass of the Higgs. Fig. 1.3 shows the branching ratio of the Higgs boson to the other SM particles as function of its mass. The Higgs couples strongest to top quarks, but because the top mass is large, the threshold for decay to top quarks is quite high. For Higgs masses below 300 GeV the dominant decay modes are through W and Z bosons and for masses below 140 GeV the decay to b quarks becomes kinematically favoured.

1.2.3 Discovery of a Higgs-like Boson

In 2012 both the ATLAS and CMS collaborations announced the discovery of a bosonic particle with mass around 125 GeV[22, 23]. An excess was observed in the the ZZ, WW and $\gamma\gamma$ channels, significant enough to be not a part of other SM processes. The significance was in the order of 5.1 standard deviations and thereby enough to claim a discovery.

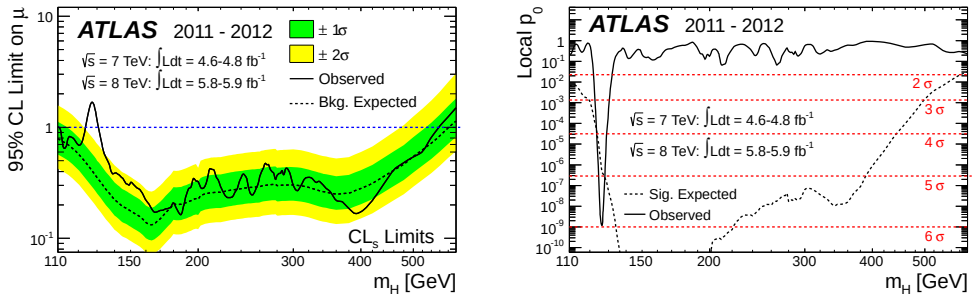

Figure 1.4: Plots that have been used for the discovery in July 2012. The plot on the left shows the expected and observed upper limits on $\mu = \sigma/\sigma_{SM}$ of a SM without a Higgs boson as function of various Higgs masses. The observed excess of data is indicated by the peak at 125 GeV. The plot on the right shows the local significance of any excess over the whole Higgs mass range. Figures taken from Ref. [22].

Fig. 1.4 shows the expected and measured 95% confidence limits on the Higgs production cross-section as function of M_H for the ATLAS data set of 2011 and the beginning of 2012. The cross-section σ is normalised to the SM expectation: $\mu = \sigma/\sigma_{SM}$. The excess at 125 GeV is clearly visible and the right plot in Fig. 1.4 shows the probability for the SM without a Higgs boson to fluctuate towards the measurement in data.

After the discovery in 2012, the properties of the new bosonic particle were studied in order to confirm it to be a Higgs boson from the SM. Fig. 1.5 shows the result of the Higgs coupling strength to fermions and bosons as function of the particle mass. The complete ATLAS data set of 2011 and 2012 has been used and the observations are in good agreement with the SM prediction. This confirms the generation of the particle masses through EWSB, but the SM also predicts the resonance of the Higgs field to be a scalar boson. In order to put that prediction to the test, the spin and CP of the resonance has to be measured.

1.2.4 Spin and CP in the $H \to WW \to l\nu l\nu$ Decay Channel

The SM predicts the spin of the Higgs to be zero and to be CP-even. CP stands for the combination of the charge (C) and parity (P) operations. The C operator changes the sign of a particle's charge and thereby creating the corresponding antiparticle. The P operator mirrors the spatial coordinates ($\vec{x}$ becomes $-\vec{x}$). The charge and parity operations have the property that $C^2 = 1$ and $P^2 = 1$ and therefore eigenstates of C and P have eigenvalues $+1$ and -1. This also applies to the eigenstates of the combined CP operation. A particle is said to be CP-even if the combined charge and parity operation leaves the wave-function of the particle untouched, indicating an identity operation. CP-odd particles get a negative

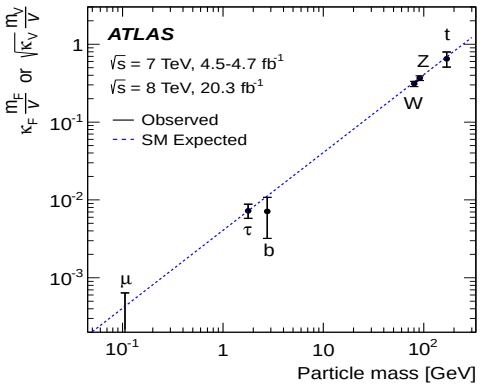

FIGURE 1.5: The coupling strength of the Higgs boson to fermions and gauge bosons as function of particle mass. The complete ATLAS data set of 2011 and 2012 is used and the observations are in good agreement with the SM expectation. Figure taken from Ref. [24].

sign in front of their wave-function after the CP operation:

$$\text{CP-even: } |S\rangle \xrightarrow{CP} +|S\rangle \tag{1.10}$$

$$\text{CP-odd: } |S\rangle \xrightarrow{CP} -|S\rangle \tag{1.11}$$

The CP operation can also be applied on interaction terms from a Lagrangian as in Eq. 1.8. CP-odd terms would receive a minus sign after CP.

Fig. 1.6 shows graphically what happens when performing a CP operation on an electron and a Higgs boson. Because the Higgs has zero electric charge and no other conserved quantum numbers, it is its own antiparticle. Combine this with the fact that a SM Higgs has spin-0 and the CP operation will yield the same state, hence the Higgs is CP-even. Even though only the parity operation P is relevant for the Higgs, we will refer in the remainder of this thesis to the term CP.

We will explicitly investigate the consequences of the spin-0 nature of the Higgs boson in the $H \to WW \to l\nu l\nu$ channel. The W bosons are spin-1 particles and because the total spin is conserved, the spins of the two W bosons have to align in such a way to add up to zero. We measure spin by choosing an axis and measure the projection of the total spin on this particular axis, also referred to as helicity. In the following we take the axis parallel to the W boson momentum in the Higgs rest-frame. In this frame the W bosons are back-to-back in order to conserve momentum. There are three possible directions the spin of a W boson can have with respect to this axis: $+1$, -1 and 0, that is either parallel/antiparallel to the W boson momentum or perpendicular tot it. These helicity states are referred to

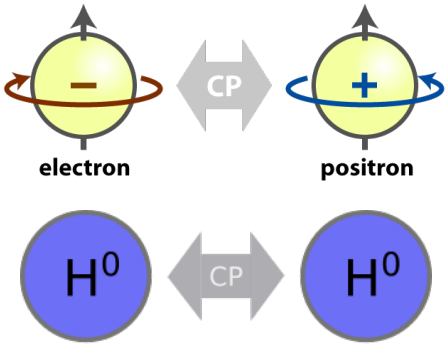

Figure 1.6: The CP operation changes a right-handed electron to a left-handed positron. The coloured arrows indicate the spin-orientation. A CP operation on the Higgs boson yields the same particle. Figure is an adaptation from Ref. [25].

as transversely(+1/-1) and longitudinal(0) polarised W respectively. Fig. 1.7 shows the three allowed W helicity configurations in order to ensure a spin-0 Higgs boson.

As long as the W bosons are in one of the three allowed helicity configurations, the decay of the Higgs to W bosons has no preferred direction. The decay products are distributed isotropically, and if it is not, it would indicate that the decaying particle was not a scalar boson. So in principle, the absence of any angular correlation between the W momentum axis and any other fixed orientation axis, is what we would expect from a spin-0 resonance. However, in its decay a W boson couples only to left-handed fermions and right-handed antifermions, a typical feature of the charged weak interactions. In the decay of the W, its decay products can be assumed to be relativistic and the handedness of a fermion is identical to its helicity, the projection of its spin along its momentum axis. The right-handed fermions have helicity $+\frac{1}{2}$ and the left-handed fermions have helicity $-\frac{1}{2}$. The decay products of the W therefore have a preferred direction with respect to the helicity state of the W. Fig. 1.7 indicates the direction of the spin of the W bosons and its decay products by thick blue arrows. In two of the configurations the charged leptons are aligned, just as the neutrinos are. The nett effect is that for these two configuration we expect small opening angles between the charged leptons. Only the third configuration with longitudinally polarised W bosons yields an isotropic decay for the charged leptons. Note that all the configurations stay the same after applying a CP operation and therefore ensure the CP-even nature of the Higgs. We will show chapters 3 and 4 how to exploit this feature of the charged leptons when testing particular hypotheses with a different spin or CP for the Higgs.

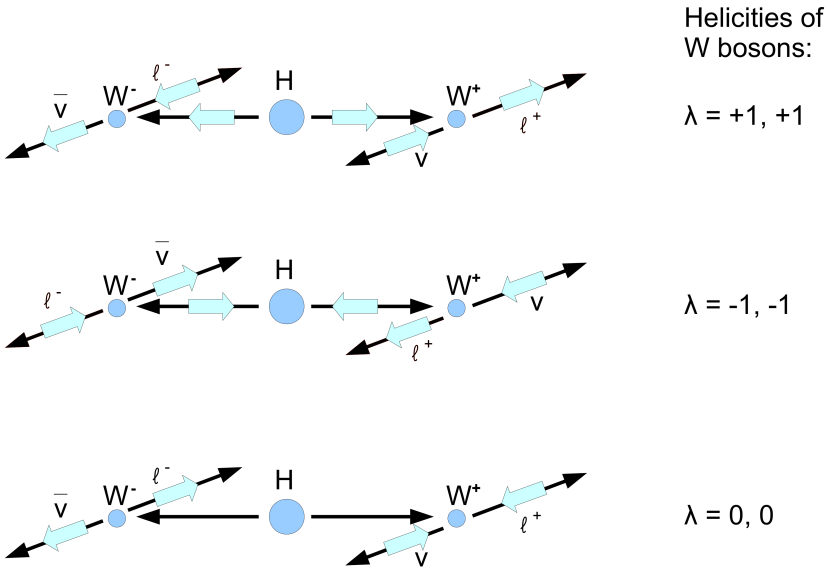

Figure 1.7: All possible helicity states of the W bosons to ensure the spin-0 nature of the Higgs boson. The thin black arrows indicate the momentum of the particles, while the thick blue arrows represent the direction of the spin. Figure adapted from Ref. [16].

1.3 Higgs Physics beyond the Standard Model

The SM gives an elegant description of the electro-weak and strong forces and by including the Higgs boson, it has a mechanism of how particles obtain mass. However, there are some serious issues which can not be answered by the SM and it is, so to say, not the ultimate theory of particle physics in our Universe. This section will state some of the general issues that arise and to which the SM only yields poor results. We steer the focus to how physics related to the Higgs, and especially the spin/CP nature of the Higgs, can give answers.

1.3.1 Problems with the SM

In the following we will list some open questions to which we have no satisfactory answer yet:

- Can the gravitational force be included in the SM?
- Why is there a hierarchy in the fermion masses?
- What type of particles are dark matter?

- What is dark energy?
- Is there more than one Higgs boson?
- Why is there almost no antimatter in the Universe?
- Can the strong and the electroweak forces be combined into one unified force?

The list is can be made longer, but we pick out the ones that influence the Higgs sector. The question if there exist more Higgs bosons is obviously related to the topic of this thesis. The other questions are related to gravity and the matter-antimatter asymmetry in the Universe.

More Higgs bosons can be introduced in the theory of the SM by including a second complex scalar doublet in Eq. 1.2 and thereby generating extra scalar particles. There are several possibilities for the W and Z bosons to couple to extra Higgs bosons. There is a wide variety of models that can achieve this by incorporating extra complex scalar doublets, as discussed in the next section.

In the case that the Higgs boson is a spin-2 tensor, this will leave a clear signature in the angular distribution of the charged leptons. As discussed before, a spin-0 Higgs would result in small opening angles between the charged leptons in the $H \to WW \to l\nu l\nu$ decay channel. For a spin-2 tensor the W bosons have to align their spins to add up to two, leading to different helicity configurations than shown in Fig. 1.7. Large opening angles between the charged leptons are now expected. If the observed particle has spin-2 it can not be part of the SM, but would be an indication of BSM physics.

The matter-antimatter imbalance in the Universe and the possible relation to the Higgs boson is a subtle issue. During the creation of the Universe, the same amount particles as antiparticles were created. When particles interact with one another through the strong and electromagnetic force, the total amount of particles and antiparticles is conserved. However, there are processes involving the weak interactions where this balance between particles and antiparticles is broken. It is related in how the weak interactions let particles change from one generation to another[26, 27]. The main point is that for these particular processes after applying a CP operation, the CP conjugate process yields different results. This difference is known as CP violation and causes a preference of matter over antimatter for the weak interactions. This CP violation is incorporated in the SM, but turns out to be too weak to justify the abundance of matter in the Universe. CP violation in the Higgs sector could resolve this problem by allowing new types of interactions where there is a difference between the interaction and its CP conjugate counter part.

1.3.2 2HDM

A model where more than one Higgs particle is introduced is the two-Higgs-doublets-model (2HDM)[28, 29]. We shortly point out what the general structure of a 2HDM Lagrangian is and focus on the coupling to W bosons.

All 2HDMs start with the introduction of another complex scalar doublet analogous to Eq. 1.2:

$$\Phi_a = \frac{1}{\sqrt{2}} \begin{pmatrix} \phi_1 + i\phi_2 \\ \phi_3 + i\phi_4 \end{pmatrix}_a, a = 1, 2 \tag{1.12}$$

One of the most general gauge invariant scalar potentials that can be made with these two doublets is the following:

$$\begin{aligned} V(\Phi_1, \Phi_2) = {} & m_{11}^2 \Phi_1^\dagger \Phi_1 + m_{22}^2 \Phi_2^\dagger \Phi_2 - [m_{12}^2 \Phi_1^\dagger \Phi_2 + \text{h.c.}] \\ & + \frac{1}{2}\lambda_1 (\Phi_1^\dagger \Phi_1)^2 + \frac{1}{2}\lambda_2 (\Phi_2^\dagger \Phi_2)^2 + \lambda_3 (\Phi_1^\dagger \Phi_1)(\Phi_2^\dagger \Phi_2) + \lambda_4 (\Phi_1^\dagger \Phi_2)(\Phi_2^\dagger \Phi_1) \\ & + \left\{ \frac{1}{2}\lambda_5 (\Phi_1^\dagger \Phi_2)^2 + \left[\lambda_6 (\Phi_1^\dagger \Phi_1) + \lambda_7 (\Phi_2^\dagger \Phi_2) \right] \Phi_1^\dagger \Phi_2 + \text{h.c.} \right\} \end{aligned} \tag{1.13}$$

The variables m_{12}^2, λ_5, λ_6 and λ_7 can be complex, but a lot of models remove the λ_6 and λ_7 terms by imposing a $\Phi_1 \to -\Phi_1$ symmetry. In order for this potential to be CP conserving all coefficients have to be real, but this is not a necessity. Choosing for both doublets a non-zero vacuum expectation value (vev)[28]:

$$\Phi_a = \begin{pmatrix} \phi_a^+ \\ (v_a + \eta_a + i\rho_a)/\sqrt{2} \end{pmatrix}, a = 1, 2 \tag{1.14}$$

analogous to Eq. 1.7. Three out of the eight degrees of freedom from the two scalar doublets in Eq. 1.12 are absorbed in the longitudinal components of the W and Z bosons. The remaining five degrees of freedom represent five Higgs bosons: two CP-even scalars h and H, one CP-odd pseudoscalar A and two charged scalars $H^\pm$. The masses of the charged and pseudoscalar bosons can be obtained by diagonalising the mass matrices with the ratio of the two vev, also referred to as:

$$\tan\beta = \frac{v_1}{v_2} \tag{1.15}$$

where $v^2 = v_1^2 + v_2^2 = (246\ \text{GeV})^2$. The mass matrices of the CP-even Higgs bosons can be diagonalised by the angle α, which mixes the h and H states with each other. One of the CP-even Higgses with the lowest mass is identified as the observed boson at 125 GeV.

With the addition of four extra Higgs bosons, there is a new set of couplings to SM particles that can be constructed. For this thesis it suffices to focus only on couplings involving W bosons. Using the doublet configuration of Eq. 1.14 and filling it in Eq. 1.13, yields

terms that correspond to hWW and HWW coupling terms with strength proportional to $\sin(\beta-\alpha)$ and $\cos(\beta-\alpha)$ respectively. The AWW term vanishes and tree level couplings to a charged scalar boson are not allowed by conservation of charge. If the W bosons are not completely decoupled from the h boson or the H boson, we expect that processes involving hWW and HWW vertices interfere with each other. This interference might change the kinematics of the final state particles.

There are 2HDMs that depart from the general potential in Eq. 1.13 and/or assume a different vev scheme for the two doublets. This would then open a window to allow CP violating terms and interactions. For example, observing a clear sign of processes involving a non-zero AWW coupling, would indicate to explore additional terms than are expressed in Eq.1.13.

We discussed the various problems that arise when imposing the validity of the Standard Model and introduced Beyond Standard Model physics to cope with some of these problems. The main focus in this thesis is on BSM where we expect changes in interactions with the Higgs boson, involving spin and CP. In the next section we will introduce a theoretical tool to incorporate the effects of BSM physics in the Higgs sector in a general way.

1.4 Effective Field Theory

Going to physics beyond the SM introduces in general a lot of new free parameters. It can be very difficult to determine the validity of any new model, because the parameters can be tuned in such a way to fit with the current observations. Due to the great succes of the SM it is a priori not clear where to look for hints for New Physics. The Effective Field Theory (EFT) approach can be a helping hand. The main assumption is that New Physics (NP) expected above a certain energy scale has effect on SM processes defined far below this scale. This can be achieved by adding extra terms to the SM Lagrangian and suppressing the relative strength of these new terms by dividing them with a cutoff scale Λ. The larger the cutoff scale, the weaker the contribution to processes taking place below this scale. The effects of NP manifest themselves by modifications of the cross-sections or kinematics of SM processes.

In this section we will introduce an EFT related to couplings of the Higgs boson to the other SM particles, but here we focus on the effects it has on the HWW coupling.

1.4.1 Higgs Characterisation Model

One convenient EFT to model BSM contributions into the SM Higgs interactions is the Higgs characterisation Model described in Ref. [30]. For the spin/CP studies the Higgs

characterisation model is a versatile tool for generating processes with new particles with different spin and CP properties within the MadGraph5_aMC@NLO framework[31]. The effective Lagrangian describes the part of all SM particles except the Higgs boson and a part for the kinematics and interactions of a boson resonance X_J with integer spin J:

$$\mathscr{L}_{HC} = \mathscr{L}_{\text{SM}-H} + \mathscr{L}_{X_J}, \text{ with } J = 0,1,2 \tag{1.16}$$

The original SM Lagrangian is recovered when $\mathscr{L}_{X_J}$ is chosen to be a CP-even scalar with the same coupling strength to the fermions and bosons as is predicted in the SM. The complete definition of the Lagrangian $\mathscr{L}_{X_J}$ can be found in Ref. [30].

In the next subsections we will describe the Lagrangian $\mathscr{L}_{X_J}$ for a spin-0 and spin-2 resonance coupling to W bosons. The $J = 1$ hypothesis has been studied extensively and resulted in the exclusion of spin-1 Higgs boson at more than 99% confidence limits when combining the ATLAS $H \to WW^*$ and $H \to ZZ^*$ analyses (see chapter 6 in Ref. [32]). The spin-1 hypothesis has not been included in the analysis described in this thesis, and therefore, will not be discussed further.

1.4.2 spin-0

The coupling of a general spin-0 resonance, X_0, to W bosons is described by the following Lagrangian:

$$\begin{aligned}\mathscr{L}_0^W = \Big\{ & c_\alpha \kappa_{SM}\, g_{HWW}\, W_\mu^+ W^{-\mu} \\ & - \frac{1}{2}\frac{1}{\Lambda}\Big[c_\alpha \kappa_{HWW}\, W^+_{\mu\nu} W^{-\mu\nu} + s_\alpha \kappa_{AWW}\, W^+_{\mu\nu} \tilde{W}^{-\mu\nu} \Big] \\ & - \frac{1}{\Lambda} c_\alpha \kappa_{H\partial W} \left(W_\nu^+ \partial_\mu W^{-\mu\nu} + h.c. \right) \Big\} X_0 \end{aligned} \tag{1.17}$$

The various κ are used to set the strength of the corresponding coupling terms and the $c_\alpha = \cos\alpha$ and $s_\alpha = \sin\alpha$ define the contributions from the CP-even and CP-odd parts respectively with a mixing angle[2] α. The g_{HWW} is the SM coupling of Higgs to W bosons and Λ a cutoff scale at which the NP is expected to arise.

$$W_{\mu\nu} = \partial_\mu W_\nu - \partial_\nu W_\mu \tag{1.18}$$

is the field strength tensor and the dual tensor is defined as:

$$\tilde{W}_{\mu\nu} = \frac{1}{2}\epsilon_{\mu\nu\rho\sigma} W^{\rho\sigma} \tag{1.19}$$

[2]Not to be confused with the mixing angle α for mixing CP-even Higgs bosons h and H used in the 2HDMs!

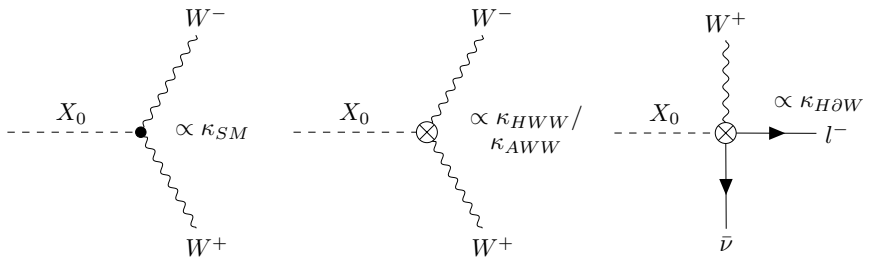

Figure 1.8: Possible XWW couplings based on the spin-0 Lagrangian in Eq. 1.17. The blobs indicate effective couplings and the corresponding κ terms from the Lagrangian are indicated as well.

Model	κ_{SM}	κ_{HWW}	κ_{AWW}	$\kappa_{H\partial W}$	$\cos(\alpha)$
SM	1	0	0	0	1
BSM 0^+	0	1	0	0	1
BSM 0^-	0	0	1	0	0
Mix	1	$\neq 0$	$\neq 0$	$\neq 0$	$\neq 0$

Table 1.3: Settings for the κ and $\cos(\alpha)$ to get various model scenarios. In principle a mixed sample has an non-zero combination of the four κ terms and $\cos(\alpha)$.

Setting $\kappa_{SM} = 1$, $\cos\alpha = 1$ and all other κ to zero, yields the SM Higgs coupling to W bosons. The κ_{HWW} and κ_{AWW} couplings are related to dimension-6 operators[33], while the $\kappa_{H\partial W}$ coupling is a derivative operator related to a contact interaction. By giving these last three couplings non-zero values, BSM effects can be studied. Table 1.3 shows which κ and α settings have to be chosen to get back the SM prediction, BSM scenarios or a mixture of SM with BSM. Fig. 1.8 shows which types of vertices can be constructed when using the coupling terms expressed in Eq. 1.17. The blobs in the diagrams indicate that the coupling is an effective one. If multiple κ terms are in use, multiple diagrams interfere which each other and affect the cross-section and kinematic distributions of X_0 decay to W bosons. We will show in chapters 3 and 4 how the kinematics of the final state leptons are related to the underlying XWW coupling.

1.4.3 spin-2

The Lagrangian for a spin-2 minimal coupling is defined as:

$$\mathscr{L}_2^p = \sum_{p=V,f} -\frac{1}{\Lambda}\kappa_p T^p_{\mu\nu} X_2^{\mu\nu} \tag{1.20}$$

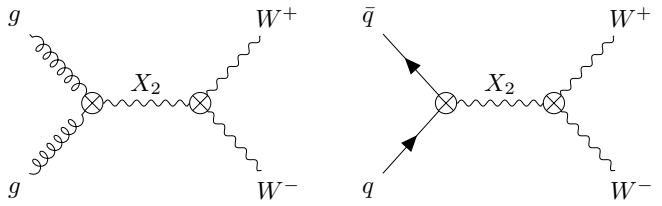

Figure 1.9: The ggF (left) and $q\bar{q}$ (right) spin-2 production modes and subsequent decays to W bosons.

ggF	:	$q\bar{q}$	HC settings
0.96	:	0.04	$\kappa_g = 1, \kappa_q = 1$
1.0	:	0.0	$\kappa_g = 1, \kappa_q = 0$
0.0	:	1.0	$\kappa_g = 0, \kappa_q = 1$

Table 1.4: κ values for the gluon and quark coupling to a spin-2 resonance, corresponding to different fractions of gluon-gluon fusion and $q\bar{q}$ annihilation at LO.

where $T^p_{\mu\nu}$ is the energy-momentum tensor and V and f denote vector bosons and fermions. Λ is again the cutoff scale. The Lagrangian is inspired by a Randall-Sundrum graviton scenario[34]. There are two possible production modes for the spin-2 resonance: the $q\bar{q}$ and the ggF production modes. Fig.1.9 shows the diagrams for the two production modes and subsequent coupling to W bosons. The spin-configuration of the initial gluons or quarks is transferred to the resonance boson and passed on to the helicity configuration of the W bosons. This is contrary to the spin-0 resonances, where the initial and final state helicity configurations can be combined as a scalar product and in principle can be considered decoupled. For the spin-2 processes the couplings are described by a product of matrices that only allow certain combinations of initial and final state helicity configurations. It is needless to say, that the production mode affects the possible final state configurations. Therefore, the spin-2 resonance is tested by producing it only through ggF or $q\bar{q}$ and by choosing a mixture between the two production modes. Table 1.4 shows which κ values from Eq. 1.20 correspond to what fraction of the ggF compared to $q\bar{q}$ production modes when producing a spin-2 resonance.

The setting for which $\kappa_g = \kappa_q = 1$ we define as the universal coupling (UC) scenario. The Feynman-diagrams in Fig. 1.9 are at leading order (LO) and in order to improve the accuracy when calculating the process, next-to-leading order (NLO) QCD diagrams are included. The NLO QCD variants of the diagrams in Fig.1.9 would include extra possibilities for the production as is indicated in Fig. 1.10, where the spin-2 boson is accompanied by an extra gluon or quark in the outgoing states.

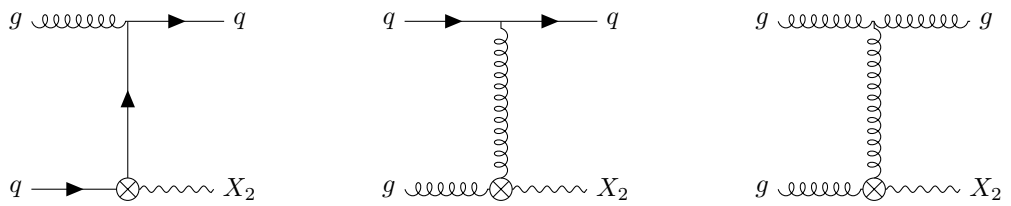

Figure 1.10: The three NLO QCD spin-2 production diagrams, where the spin-2 resonance is produced together with an additional quark or gluon in the outgoing state.

When $\kappa_g \neq \kappa_q$ we are dealing with a non-universal coupling (NUC) scenario. For LO effects the $q\bar{q}$ and ggF production processes are completely independent. However, the NLO processes for NUC contain an extra gluon or quark and have diagrams that will interfere which each other, because the initial and final states are indistinguishable from each other. For example, this is the case with the first two diagrams in Fig. 1.10. The matrix elements for such processes contain a term proportional to $(\kappa_q - \kappa_g)^2$, which grows with $s^3/m^4\Lambda^2$ and leads to unphysical phenomena at high energies, also referred to as unitarity violation. The onset of unitarity violation has large consequences for the shape of the Higgs transverse momentum and some spin-sensitive observables when NUC scenarios are chosen. In chapter 3 we will show what the differences are in kinematic distributions for spin-2 UC and NUC models. For a more detailed discussion about the unitarity violation aspect of spin-2 see section 4.1 of Ref. [30].

1.5 Summary

In this chapter we introduced the Standard Model of elementary particles and the interactions these particles can have with each other. We described the coupling of the Higgs boson to W bosons and how the spin properties are transferred to the final state leptons during the W decay. The SM predicts the Higgs boson to be a CP-even scalar.

The SM predictions are very accurate, but nevertheless it can not be the ultimate theory of particle physics. We introduced some of these problems and argued that BSM physics can help to answers these. New Physics phenomena might manifest themselves in the Higgs sector. 2HDMs would enlarge the Higgs sector by including four additional scalar bosons and opening up the possibility for new couplings to W bosons. The kinematics of the final state leptons would tell us more about the underlying coupling.

Lastly, we introduced the EFT approach to incorporate New Physics with dimension-6 operators in a model independent way in the SM. The Higgs characterisation model allows for modifications of the Higgs coupling to the other SM fermions and bosons by replacing

the SM Higgs Lagrangian by an effective Lagrangian describing a bosonic resonance X_J with spin $J = 0, 1, 2$. The focus in this thesis is on new spin-0 and spin-2 couplings to W bosons.

In chapters 3 and 4 we will discuss the kinematics of the $H \to WW \to l\nu l\nu$ process and how the spin-0 and spin-2 variants affect the kinematics of the final state leptons. In the next chapter we will describe the LHC complex and the ATLAS detector.

The ATLAS Experiment

2

The study of elementary particles required the construction of ever larger machines during the last couple of decades. To test the Standard Model under extreme circumstances and to discover possible deviations, the Large Hadron Collider, LHC, has been constructed at CERN. Protons are accelerated to very high energies and collided head-on inside detectors such as the ATLAS detector. This chapter will firstly discuss the LHC complex and its machine parameters. Secondly, we will introduce the ATLAS detector and its components. Finally, we will discuss the reconstruction of events and identify physics objects. We will highlight the performance of the ATLAS detector.

2.1 The Large Hadron Collider

The Large Hadron Collider, LHC[35–38], is a 27 km circular accelerator situated at CERN near Geneva. It is designed to accelerate and collide protons at a centre-of-mass energy of 14 TeV. Fig.2.1 shows the complex of machines that the LHC is part of. Protons begin their journey at LINAC2, where they are accelerated to an energy of 50 MeV. Through a chain of pre-accelerators as the Booster, PS and SPS, the protons are finally injected into the LHC ring at an energy of 450 GeV. In the LHC the proton beams are tuned and accelerated to the desired energy before collision. The collision energies that are reached are 3.5 TeV (2010 & 2011), 4.0 TeV (2012) and 6.5 TeV (2015) and correspond to centre-of-mass energies of 7 TeV, 8 TeV and 13 TeV respectively.

The protons are injected in bunches in both clockwise and anticlockwise directions. In 2012 the ring was filled with 1400 bunches during a collision run. Each bunch contains approximately 10^{11} protons and the time interval between two bunches is 50 ns. In 2015 this was further reduced to 25 ns. 1200 superconductive dipole magnets require the bending power to keep the protons, which have approximately the speed of light, in their circular orbit. The magnets produce a field of 8.3 Tesla in order to do that. The beams cross at four interactions points and at these points the four main detectors are situated. ATLAS[40–42] and CMS[43] are general purpose detectors that study a wide variety fundamental questions. The LHCb experiment[44] focuses on the physics of B mesons and CP violation

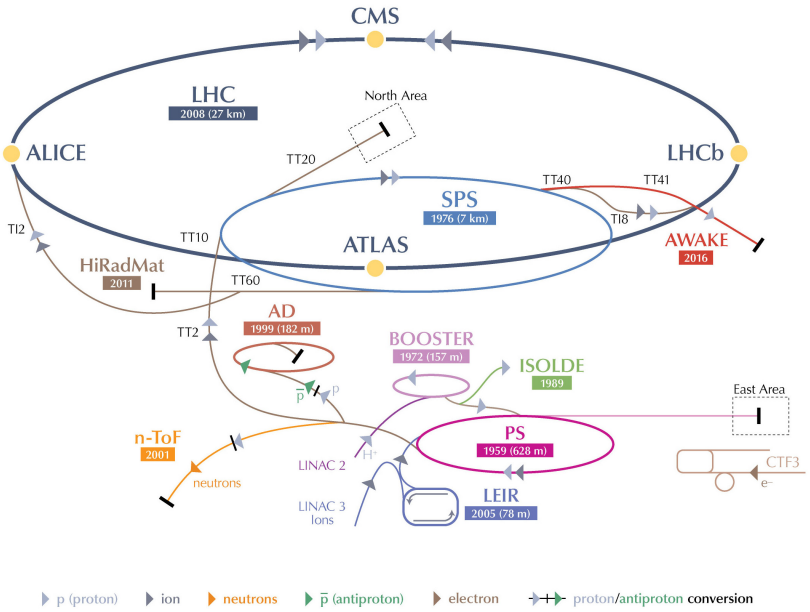

Figure 2.1: Graphical representation of the LHC ring, its pre-accelerators and others systems[39].

involving b quarks. The ALICE experiment[45] studies the formation and properties of the quark-gluon plasma right after the Big Bang.

Besides the high collision energy, the second objective of the LHC is to have a high rate of physics processes with small cross-sections and high mass. This rate dN/dt depends on two crucial factors:

$$\frac{dN}{dt} = L\sigma \tag{2.1}$$

where L is the instantaneous luminosity and σ the cross-section that depends on the centre-of-mass energy $\sqrt{s}$ and the specific process as well. Increasing the luminosity or the cross-section will increase the rate of the physics process. The LHC is designed to optimise both the centre-of-mass energy and the instantaneous luminosity. The latter can be expressed in terms of beam parameters as:

$$L = \frac{f_{rev}\, N_b\, n_p^2}{4\pi\, \sigma_T^2} \tag{2.2}$$

where f_{rev} is the revolution frequency, N_b the number of bunches, n_p the number of protons per bunch and σ_T the transverse beam size at the collision point. During a run the LHC

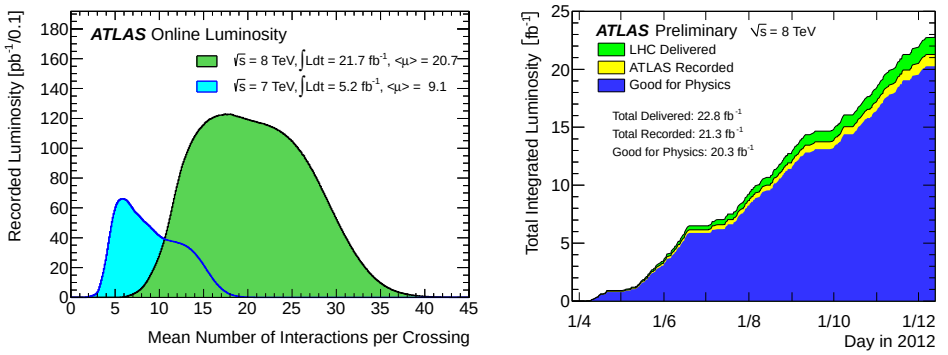

Figure 2.2: Left, the average number of interactions per bunch crossing weighted with the recorded luminosity for the 2011 and 2012 data sets. Right, the total amount of integrated luminosity delivered by the LHC and recorded by the ATLAS detector over the year 2012. Figure taken from Ref. [46].

tunes these parameters to optimise the luminosity. In 2012 an instantaneous luminosity of $7.73 \times 10^{33}\text{cm}^{-2}\text{s}^{-1}$ was reached. The amount of total collected data is expressed as the integral of the instantaneous luminosity over time. The ATLAS detector has accumulated $\int Ldt = 21.3\,\text{fb}^{-1}$ during the 2012 run and from that, $20.3\,\text{fb}^{-1}$ was good for physics analysis. Fig. 2.2 shows this collection of data with the ATLAS detector during 2012 in the right figure. On the left, there is the average amount of interactions for every bunch crossing, also known as pile-up, in ATLAS for the years of 2011 and 2012.

2.2 The ATLAS Components

The ATLAS detector[40–42] is a cylindrical multi-purpose detector with an almost hermetic coverage around the proton-proton interaction point to prevent particles escaping detection as much as possible. Its design is symmetric in the forward, backward and transverse directions. It consists of three magnet system and four main subdetectors, which will be discussed below. Fig. 2.3 gives a cutaway view from the ATLAS detector with the components indicated.

The coordinate system is defined as follows: the x axis pointing to the centre of the LHC, the y axis pointing upwards and the z axis pointing along the beam pipe. Due to its cylindrical design it is convenient to work with polar coordinates. The angle ϕ is defined in the $x-y$ plane with $\phi = 0$ starting at the x axis and going clockwise. The angle θ is

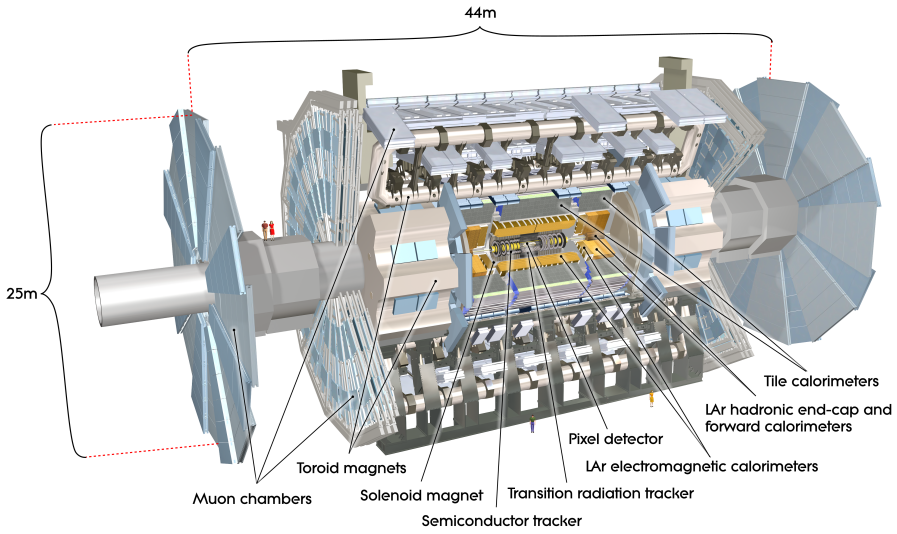

Figure 2.3: Cutaway view of the ATLAS detector showing the various subdetectors and the toroid magnets system[42].

with respect to the beam pipe, but normally the pseudorapidity is used instead:

$$\eta = -\ln\left(\tan\frac{\theta}{2}\right) \tag{2.3}$$

The advantage is that the difference in pseudorapidity between two object remains Lorentz-invariant under boosts along the z axis. The total angular distance between to objects is defined as:

$$\Delta R = \sqrt{(\Delta\phi)^2 + (\Delta\eta)^2} \tag{2.4}$$

2.2.1 The Inner Detector

The inner detector (ID) is the first subdetector that particles encounter after being produced at the interaction point. The main objective is to track particles without too much disturbing the direction and minimising the energy loss due to multiple scattering with the inner detector components. It is composed of three components:

- The pixel detector
- The semi conductor tracker, SCT
- The transition radiation tracker, TRT

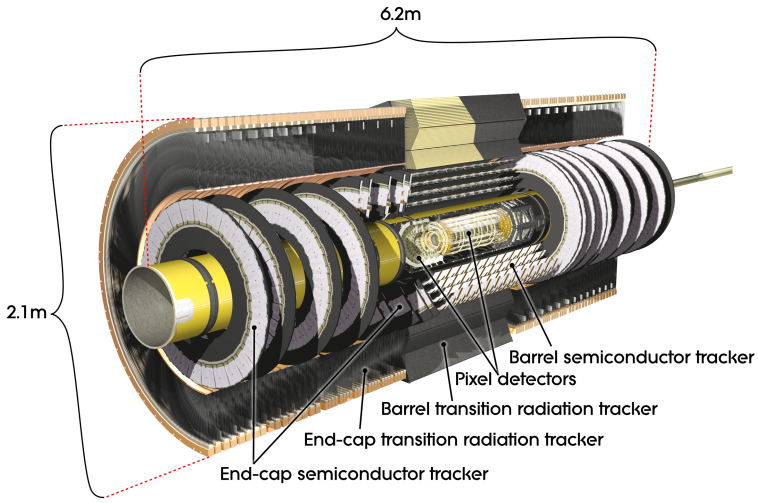

Figure 2.4: Cutaway view from the inner detector, showing the pixel detector, the SCTs and the TRTs[42].

All three subcomponents are embedded in a 2 Tesla magnetic field pointing along the z axis, generated by the solenoid magnet that surrounds the whole inner detector. The field ensures the curvature of charged particles and thereby enables the determination of the momentum of the tracks. Fig.2.4 gives a cutaway view of the inner detector with its pixel, SCT and TRT subdetectors. In October 2012 operational fraction of the pixel, SCT and TRT channels was 95.0%, 99.3% and 97.5% respectively[47].

Pixel Detector

The innermost component and thereby closest to the beam pipe and interaction point is the pixel detector. It consists of three concentric cylindrical layers in the barrel region ($|\eta| < 1.7$) and three discs on each end-cap side ($1.7 < |\eta| < 2.5$). The closest layer is 5 cm from the centre, while the furthest is 12 cm. The pixels are made out of silicon sensors and by applying a bias voltage, traversing charged particles induce an electrical current which can be read out. Because the pixel sensors are bombarded by a huge amount of particles during each bunch crossing, they have to be radiation hard and be able to handle high particle multiplicities. In order to reconstruct vertices all the pixels have a spatial resolution of 10 μm in the $r-\phi$ plane and 115 μm in z. As of 2015, the pixel detector was extended with a fourth layer in the barrel region, called the Insertable B-Layer (IBL). With a radius of 3.2 cm it is the closest layer to the collision point.

SCT

The next component surrounding the pixel detector is the SCT. It uses strips of silicon and has a similar operation as the silicon pixel sensors. It has four cylindrical layers in the barrel region and it has nine discs at each end-cap region. Each strip sensor is 6.4 cm long and provides a two-dimensional measurement. Another strip sensor placed slightly on top is rotated with respect to the lower sensor by 40 mrad and a three-dimensional measurement can be obtained. The spatial resolution is 17 μm in the $r-\phi$ plane and 580 μm in z.

TRT

The outermost layer is occupied by the TRT ranging from a radius of 55 to 108 cm. It consists of many straw tubes with a diameter of 4 mm. The straws are aligned with the beam pipe in the barrel region, while being perpendicular to the beam pipe in the end-cap regions. Each straw contains a tungsten wire under high voltage in the centre and is filled with a mixture of xenon, carbon-dioxide and oxygen. When a charged particle traverses the straw tube, the gas is ionised. The freed electrons drift towards the wire in the centre and the drift-time is directly proportional to the distance of the track. This distance can be calculated with a 130 μm accuracy. On average 36 straws are hit by a charged particle from the interaction point.

2.2.2 The Calorimeter

Contrary to the inner detector, the calorimeter tries to maximise the amount of interactions for traversing particles. The lost energy during these interactions is used to either ionise electrons or excite special materials that emit photons, which are guided by waveguides to photomultiplier tubes. The more ionised electrons or photons are produced, the more energetic was the particle. The inner part of the calorimeter, the electromagnetic calorimeter (ECAL), is where the electrons and photons mainly deposit their energy, while hadrons do that mainly in the outer hadronic calorimeter (HCAL). Both calorimeters are based on an alternating sampling of an active and a passive material. Energetic particles interact with the passive material and release their energy in the form of a cascade of new particles. When the cascade reaches the active material, its energy ionises electrons or excites materials that emit photons and are guided to the readout channels. Fig. 2.5 shows the different components of the ECAL, HCAL and the forward calorimeters (FCAL). The total coverage is $|\eta| < 4.9$, but hadrons can leak in the gap region of $1.3 < |\eta| < 1.6$, which is used for service materials and cables. In October 2012 the operational fraction of the ECAL, HCAL and FCAL channels was 99.9%, 98.3% and 99.8% respectively[47].

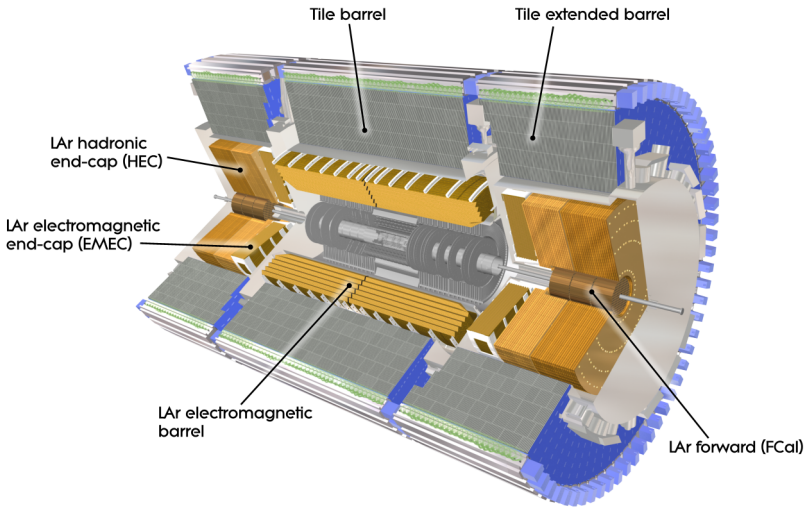

Figure 2.5: Cutaway view of the ECAL, HCAL and FCAL components of the calorimeter[42].

Electromagnetic Calorimeter

The ECAL uses lead for the passive and liquid argon as the active material in the barrel and end-cap region. Energetic particles ionise the argon gas and the freed electrons are collected by applying a high voltage. The design of the lead layers has an accordion structure in order to prevent any dead spots in the detector. The argon has to be cooled down to 87 K for its optimal use. In the barrel region its coverage is $|\eta| < 1.475$, while in the end-cap regions it goes up to $1.375 < |\eta| < 3.2$.

Energetic photons convert to e^+e^- pairs and electrons and positrons emit photons through bremsstrahlung when interacting with the lead in the ECAL. A cascade of electrons, positrons and photons is the result, referred to as a shower. The length of these showers is described by radiation lengths X_0, which is the distance an electron has to travel through a material to loose $1/e$ of its energy. The ECAL is designed to optimise the energy absorption, which comes down to a thickness of $22X_0$ in the barrel region and $24X_0$ in the end-caps. The overall granularity is $\Delta\phi \times \Delta\theta = 0.025 \times 0.025$ and provides information of the shower depth and shape.

Hadronic Calorimeter

Hadronic particles typically start to deposit energy at the end of the ECAL and loose most of their energy in the much denser HCAL surrounding the ECAL. It uses iron as a passive material and plastic scintillators as active material. The scintillators are excited when energetic particles pass through it and subsequently emit photons. In the tile barrel and tile extended barrel the iron and the plastic material are structured as tiles in an alternating sandwich. The size is chosen to be about 10λ, where the interaction length λ is the distance for a hadron to travel in order to loose $1/e$ of its energy. This corresponds to a outer radius of about 4.2 m in the barrel region and to a length of 6.1 m extending along the beam axis on both sides. This size is small enough to accurately measure the energy of hadronic particles and minimises the punch-through of hadrons into the muon system.

Due to high radiation the HCAL in the end-cap and the FCAL use copper and tungsten as passive material and liquid argon as the active material. The tile barrel and tile extended barrels covers a region of $|\eta| < 1.7$, the LAr hadronic end-cap covers a region of $1.5 < |\eta| < 3.2$ and the FCAL goes up to $3.1 < |\eta| < 4.9$. The overlap prevents dead regions.

2.2.3 The Muon Spectrometer

The outermost and largest part of the ATLAS detector is the muon system (MS) together with the toroid magnets. It gives ATLAS its impressive size of 44 m in length and a diameter of 25 m. Its purpose is to bend muons in the magnetic field created by the toroid magnets and measure the direction, momentum and charge of the muons in the muon spectrometer. Muons in the range of 0.1 to 10 GeV are minimum ionising particles and therefore leave little energy inside the underlying calorimeter. A muon needs at least 3 GeV to reach the muon system. Fig.2.6 gives a cutaway view of the several components of the muon system and the magnets. Below we describe the three main components: the toroid magnets, the precision chambers, and the trigger chambers.

Toroid Magnets

Charged particles follow circular trajectories inside magnetic fields and the more energetic they are, the larger the radii of these tracks wil be. The toroid magnets are therefore crucial in the determination of the momentum of the muons. In the barrel region there are eight toroids with a length of 25.3 m, which corresponds to a range of $|\eta| < 1.4$, and generate a field of approximately 0.5 T. In each end-cap region there are eight smaller toroids that fit inside the barrel toroids and cover a range of $1.6 < |\eta| < 2.7$. The magnetic field there is approximately 1 T. Together, the barrel and end-cap toroid generate a cylindrical magnetic

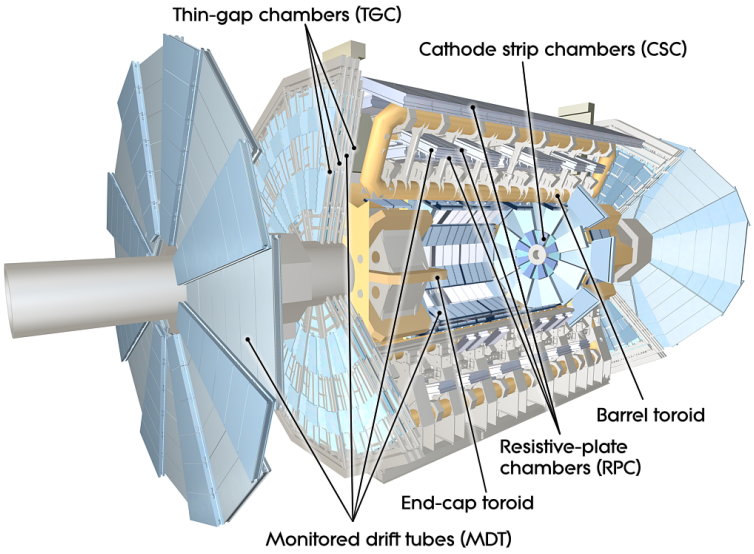

Figure 2.6: Cutaway view of the Muon System showing the toroid magnets, the MDT and CSC precision chambers and the RPC and TGC trigger chambers[42].

field with the beam pipe as its central axis. This orientation is perpendicular to most muon trajectories and ensures maximum bending power.

Precision Chambers

The majority of the muon system consists of stations with monitored drift tubes (MDT) with the purpose of detecting traversing muons and provide hits as input to muon tracking algorithms. Both in the barrel and end-cap regions the MDT stations are grouped in three layers: inner, middle and outer. The orientation of the tubes in the stations is orthogonal to most muon trajectories. Only in the inner layer of the end-caps closest to the beam pipe the MDTs have been replaced by cathode strip chambers (CSC), because these can operate at a very high data rate.

A MDT is an aluminium tube with a diameter of 30 mm and filled with a mixture of argon and carbon-dioxide. In its centre there is a tungsten wire acting as anode when the tube is put on high voltage. A traversing muon ionises the gas and freed electrons drift towards the centre. The time it takes to drift to the centre is directly proportional to the drift radius and each tube has a resolution of about 80 μm to locate the traversing muon. The position of the muon along the length of the tube can not be determined. Each MDT station has two groups of multi-layers of three to four layers of MDTs, which means that track segments in the station have a resolution of 35 μm.

The CSCs are a collection of multiple anode wires and two cathode strips with a gas mixture in between the two planes. They are multi-wire proportional chambers and are able to deal with a data rate of 1000 Hz/cm^{-1}. Traversing muons ionise the gas and the freed electrons induce charges on the anode wires. Due to a rotation of 90 degrees of the cathode strips with respect to each other a three-dimensional measurement is possible. A CSC has a spatial resolution of 40μm × 5mm. The operational fraction was 99.7% for the MDT stations and 96.0% for the CSC stations in 2012[47].

Trigger Chambers

The trigger chambers are used for fast muon identification in the trigger system, explained in section 2.2.4. They have good time resolution, which is essential for triggering, and also provide spatial information that can be used for track reconstruction. There are two types of technologies used for triggering: resistive plate chambers (RPC) used in the barrel region and thin gap chambers (TGC) for in the end-cap regions.

The RPCs consists of two plates separated by a 2 mm gap filled with a gas mixture. Traversing muons ionise the gas and freed electrons drift towards the anode strips on the plates. In each RPC station there are two RPCs that provide information of the ϕ and η angles of the track respectively. It has a spatial resolution of about 10 mm and a time resolution of approximately 1.5 ns.

The TGCs are multi-wire proportional chambers like the CSC and are installed in the end-cap regions. The gap is so small that a 4 ns time resolution is achieved. The spatial resolution is about 2-7 mm. The operational fraction of RPCs and TGCs was 97.1% and 98.2% respectively in 2012[47].

2.2.4 Trigger and Data Acquisition

With a bunch crossing every 50 ns, about 20.7 interactions per bunch crossing in 2012 and having on average 1.5 MB data per event, the ATLAS detector produces about 25 to 30 TB of data every second. This is rate is too large for processing and therefore a selection procedure has to be implemented to reduce this amount by means of a trigger system. The majority of the proton-proton interactions result in low energetic particles and interesting processes such as Higgs production have very low rates. The ATLAS trigger system is designed to make a fast selection of interesting collisions. It has some degree of redundancy so in case an event is missed by one trigger it is selected by another and it is efficient enough to select rare interesting processes. A schematic overview of the trigger system and data acquisition is given in Fig.2.7. The system is made up out of three systems: the L1 Trigger, the L2 Trigger and Event Filter (EF).

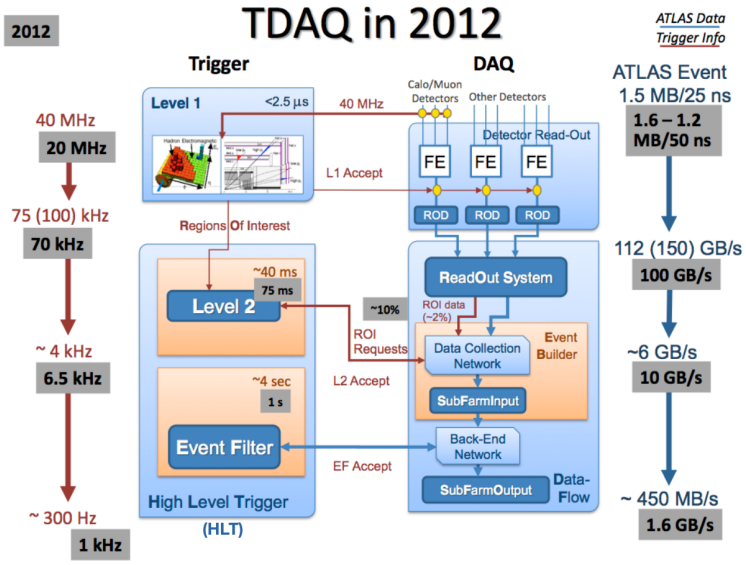

Figure 2.7: Schematic overview of the ATLAS trigger system together with the data acquisition. The numbers in the grey boxes are the 2012 performances[48].

L1 Trigger

The L1 trigger is the first level for data selection and needs to make very fast decisions. It is hardware based and has 2.5 μs to reduce the data rate from 20 MHz to 70 kHz. It uses information from the triggers in the Muon spectrometer and in both calorimeters using a reduced granularity. Simple algorithms look for areas with signatures of high-p_T photons, electrons, muons, jets or high missing E_T, the so called regions of interest (ROI). With the help of lookup tables the L1 checks if a ROI passes a certain momentum or energy threshold and isolation criteria and during its decision the events are stored in pipeline memories. After passing the required criteria, L1 sends the event together with the ROIs to the readout buffers (ROB) in order to be processed by the L2 trigger.

L2 Trigger

The next step in the trigger system is software based and reduces the rate further to about 6.5 kHz in about 40 ms. The full detector granularity is used for each ROI and L2 applies stricter criteria than L1. When an event passes the L2 criteria an event is send from the ROB to the event builder, which reads out the complete detector information of an event. This is then used as input for the EF. The L2 trigger forms together with the EF the High Level Trigger (HLT) and as of 2015 these are completely integrated into one HLT system.

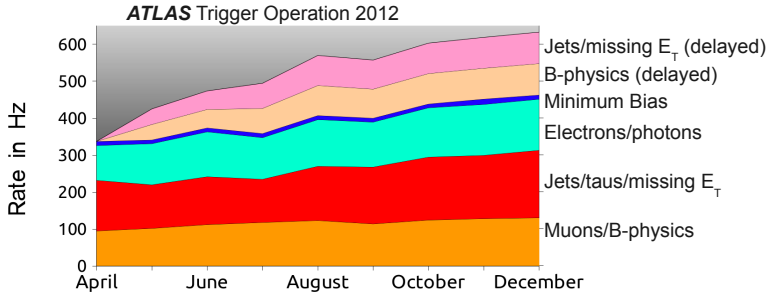

Figure 2.8: The EF output rates of various physics streams during the 2012 data run[49]. The total output rate increased from approximately 330 Hz in April to more than 600 Hz in December due to increased available computing power for the EF.

EF Trigger

Using the full detector information and granularity, the EF takes about 4 s for each event from the event builder to make a final decision. The output rate of interesting events is in the order of 1 kHz and the data is passed on to mass storage devices. Depending on the triggers they pass at the L1, L2 and EF stages, events are assigned to different streams related to the objects that have been identified in each event. Fig.2.8 shows the EF output rate of several streams during the 2012 run. An event can be assigned to multiple streams if it was selected by multiple triggers.

2.3 Simulating Physics in ATLAS

In order to compare a theoretical prediction with experimental data, the prediction needs to contain a modelling of the interactions during the pp collision as well as a way to simulate the detector response when particles, originating from the interaction point, traverse it. In high energy physics this relies on computer simulations, using a lot of CPU power. The complete simulation can be split up into four consecutive steps:

- **Event Generation**: the processes that take place during the pp collision are modelled with event generators that make use of Monte Carlo (MC) techniques for random generation.
- **Detector Simulation**: particles that leave the interaction point traverse several components of the detector and thereby different materials. Energy loss and scattering influence the particles trajectory and have to be properly modelled.

- **Digitisation**: the detector components that have been hit or contain energy deposits should convert this information into an electronic signal. This process is called digitisation and quantifies the response of the detector to traversing particles. From this point onwards the real and simulated data are treated identically.
- **Event Reconstruction**: at this point, there is technically no difference between simulated and real data. Both undergo the ATLAS trigger software selections and are fed to the reconstruction algorithms to reconstruct events and define physics objects.

After these steps, data and simulation can be compared with each other. Besides comparing the theoretical prediction, MC simulations can also help to test the performance of the ATLAS detector components and improve the overall understanding of the detector as a whole. In section 2.4 we present the performance of the ATLAS detector and the physics objects.

Event generation will be discussed in detail in chapter 3. The event reconstruction with a particular focus the on the $H \to WW \to e\nu_e \mu\nu_\mu$ events and relevant for the Higgs spin and CP analysis presented in this thesis, can be found in chapter 5. The remainder of this section focusses on the other three simulation steps involving detector modelling.

2.3.1 Detector Modelling

The modelling of the ATLAS detector is done by the GEANT4[50] software, which simulates the detector geometry and the propagation of particles through the various materials. The output of GEANT4 is then passed on to the digitisation software to model the detector's readout response.

The full simulation is very precise, especially the modelling of the calorimeter, and thereby consumes a large amount of CPU time. Due to the large amount of events to be generated and time constraints, a speed-up of the simulation is developed. For this purpose the AtlFast-II[51] package has been made and implements a simplified description of the calorimeter. Instead of simulating the full calorimeter response, the particle showers are parametrised. It has been compared to the full simulation and leads to similar results. A full simulation of an event containing jets can take up to 45 CPU minutes, while AtlFast-II reduces it to approximately 90 seconds[52]. The amount of simulation time is reduced by factor of 10 to 20 without loss of accuracy.

2.4 Reconstruction and Performance

During an event, particles inside the protons interact, new particles are created and interact with the components of the ATLAS detector while leaving the collision point. These interaction points are recorded electronically as hits and energy deposits. For event reconstruction and object identification it is necessary to reconstruct tracks from the hits in the ID and segments in the MS and create clusters from energy deposits in the calorimeters. The information is then used to identify physics objects such as photons, electrons, muons, taus and jets. Neutrinos can not be detected directly, but carry transverse momentum and thereby cause an imbalance in the transverse momentum. This section will discuss how the different components of an interesting physics event can be reconstructed and how the ATLAS detector performs. The reconstruction of τ leptons and photons are not relevant for the spin and CP studies presented in chapter 6 and will therefore be omitted. Information on tau and photon reconstruction can be found in Ref. [53] and Ref. [54] respectively.

2.4.1 Track and Vertex Reconstruction

Charged particles leave hits in the ID and due to the high multiplicity of traversing charged particles, tracking and vertex algorithms have to be robust against pile-up conditions. A high luminosity is good for the increase in rate of interesting physics, but it gives also more pile-up. It makes pattern recognition more difficult, leads to more ambiguity when assigning hits to tracks and leads to longer computing times. The track algorithm, called NEWT[55], has been designed for this purpose.

Tracking

Track reconstruction starts with converting hits from the pixel detector, SCT and TRT to space-points, which are used as input to two algorithms: inside-out and outside-in. The inside-out combines 3 space-points from the pixel detector and first layer of the SCT into a track seed. By using a Kalman-Filter[57] the seed is extrapolated to space-points further outwards. The outside-in algorithm starts with hits from the TRT and extends inward to the interaction point by adding silicon hits. It is used to reconstruct secondary particles that originate from the decay of primary particles. Space-points that do not lie on the track and reduce the fit quality are called outliers. Points where the track traverses and a space-point is expected, but there is no hit, are called holes.

If a space-point is assigned to more than one track there is an ambiguity, which is resolved by assigning the hit to the track with the best fit. The other track(s) is then refitted without the overlapping hit. This procedure is repeated until all overlap is removed. The track

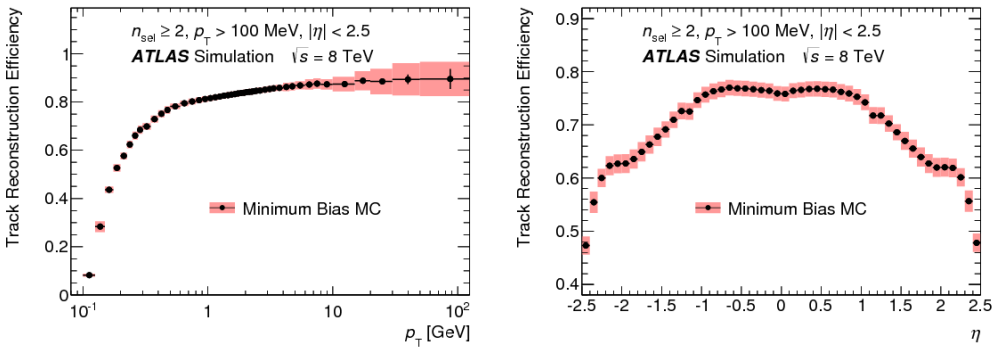

Figure 2.9: Track reconstruction efficiency as function of the transverse momentum, p_T (left), and as function of the pseudorapidity, η (right). The efficiency is determined from the ratio of matched Truth-level to reconstructed tracks[56].

candidates are than extended to the TRT and a refit is done. Finally quality cuts based on the number of good hits, holes and outliers are applied to the candidate tracks. Only tracks with at least nine hits in the silicon-based detectors, no holes in the pixel detector and having a $p_T > 400$ MeV are considered robust. This requirement significantly reduces the amount of fake tracks, which are track candidates from wrong hits.

To determine the efficiency of the ID tracking, MC simulations are used and the results are shown in Fig. 2.9 for minimum bias simulation at $\sqrt{s} = 8$ TeV. The fraction of truth particles with $p_T > 100$ MeV and $|\eta| < 2.5$ that can be matched with the reconstructed tracks determines the efficiency. Only the tracks that are robust have been used.

Vertexing

The reconstructed tracks are used as input to the vertex finding algorithm[58]. The type of vertices can be primary vertices, indicating the point of the hard scatter, and secondary vertices, which are signs of decay of heavy short-lived particles. The tracks form a vertex when they match a certain criteria in the interaction region. Other tracks are added in several iterations. If a track is more than 7σ incompatible with a vertex, it is removed and used as a seed for another vertex. This process is repeated until the algorithm can not make more vertices with at least two tracks. If there are multiple vertices in an event, the one with the highest squared transverse momentum sum of its tracks, $\sum p_T^2$, is called the primary vertex.

Fig. 2.10 shows in the left plot the efficiency of the tracking reconstruction as a function of the selected tracks. The efficiency is higher than 99% for vertices with at least four tracks. The plot on the right shows the efficiency to reconstruct the hard-scatter interactions as a

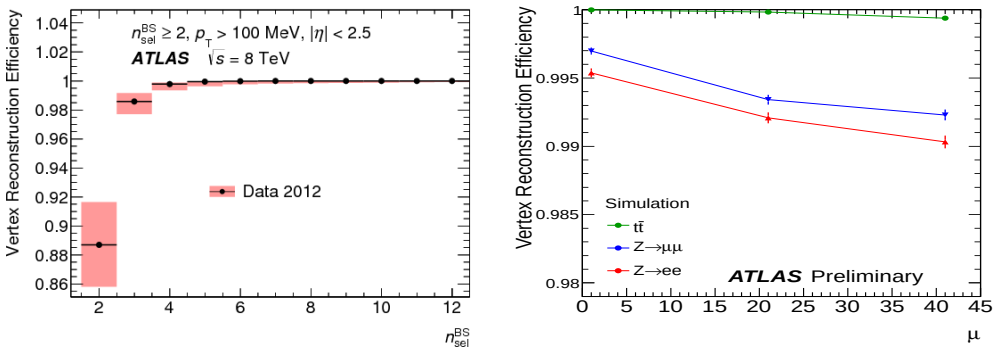

Figure 2.10: On the left, vertex reconstruction efficiency as function of the amount of selected tracks[56] and on the right, the Efficiency to reconstruct the hard process as a function of pile-up for the $t\bar{t}$, $Z \to \mu\mu$ and $Z \to ee$ processes[59].

function of the average amount of interactions per bunch crossing, μ. The three simulated processes are $t\bar{t}$, $Z \to \mu\mu$ and $Z \to ee$. The vertex finding is very robust, because for all pile-up conditions the efficiency of finding the right vertex stays above the 99%.

2.4.2 Electron Reconstruction

Electrons follow a curved trajectory in the ID and deposit their energy in the ECAL. Therefore, a track from the ID has to be matched with an energy cluster in the ECAL. The electron reconstruction starts by dividing the ECAL into a grid of towers, which have a 0.025×0.025 size in $\phi - \eta$ space. The estimated energy of a tower is the total energy sum of all calorimeter cell within the tower. A candidate seed is a group towers with 3×5 units in $\phi - \eta$ space and fulfilling the requirement of $E_T > 2.5$ GeV. The creation of seeds is done by a sliding window algorithm[60].

Next is the matching of the seed cluster with an ID track with $p_T > 0.5$ GeV that is extrapolated to the middle of the ECAL. Due to bremsstrahlung electrons can loose a significant amount of energy through photon emission and this has consequences for the electron trajectory. Since 2012 a Gaussian Sum Filter (GSF) algorithm[61] has been included in order to refit the ID track taking bremsstrahlung into account. There is a match with ID track and seed cluster when the distances between the two are $|\phi| < 0.1$ and $|\eta| < 0.05$. For this candidate electron the four-momentum is calculated. The η and ϕ information is taken from the ID track, unless there are less than four silicon hits, the η is taken from the ECAL cluster. For the electron energy determination, the cluster is enlarged to 3×7 units. The total energy is an estimation of how much energy is deposited in front, within, outside and beyond the cluster.

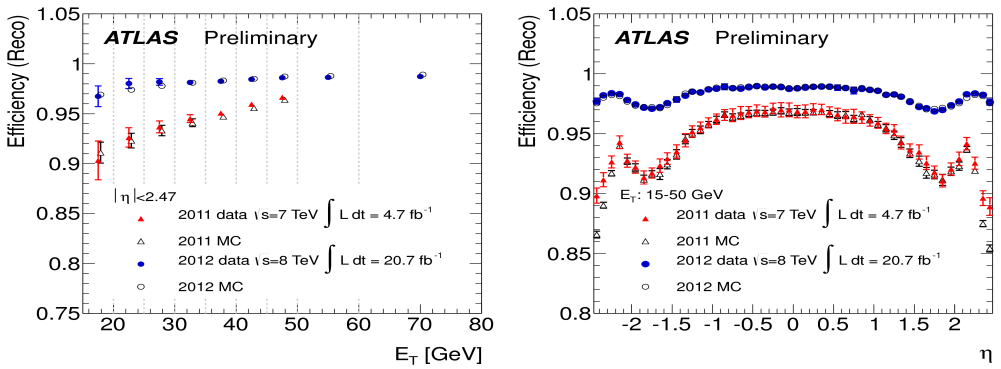

Figure 2.11: Electron reconstruction efficiencies as function of E_T (left) and η (right) by using tag-and-probe electrons from $Z \rightarrow ee$ decays. The 2011 data set is indicated in red and blue is for the 2012 data set. The dashed grey lines indicate the size of the used E_T bins[62].

With these criteria there are still various other objects that can be confused with an electron, such as converted photons or jets. In order to resolve this issue reconstructed electron objects are classified into three main types with increasing background rejection: *loose*, *medium* and *tight*[62]. The quality cuts are optimised into bins of E_T and η as to take into account the performance of the different zones in the detector. For the analysis presented in this thesis, we used electrons of the type *medium++* and *tight++*, which have extra quality cuts optimised for high pile-up conditions. For example, the number of hits and holes of the tracks in the ID is important and the full set of requirements can be found in Ref. [60].

In order to determine the efficiency of the electron reconstruction, the tag-and-probe method[60, 63] is applied. The method uses the leptons from $Z \rightarrow ee$ decay. One of the electrons has to fulfil all criteria for electron reconstruction and forms the tag. The other electron is associated with an object based on an EM cluster and forms the probe. The efficiency is the ratio of probe electrons that also pass the criteria for electron reconstruction to the total amount of probe electrons. Both leptons are required to have opposite charge and their invariant mass should be corresponding to M_Z. Fig. 2.11 shows the efficiency as function of E_T and η for the full 2011 and 2012 data sets. In 2011 no GSF algorithm was used, but it was implemented in 2012. The use of the algorithm lead to a significant improvement of the reconstruction efficiency in 2012.

Fig. 2.12 shows the reconstruction efficiency of the three types of electron classifiers, using either a cut-based or a Likelihood-based method. The *tight* electrons have the lowest efficiency due to harder quality cuts, but have the highest purity. The efficiency as function of number of primary vertices changes very little, indicating the robustness of the classifiers against pile-up.

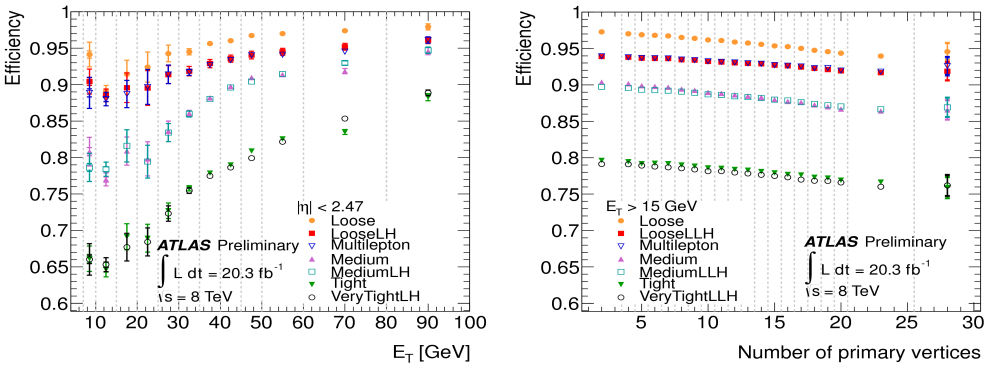

Figure 2.12: The efficiencies for the electron classifiers, *loose*, *medium* and *tight* as function of E_T (left) and number of primary vertices (right) for the 2012 data set. The dashed grey lines indicate the sizes of the used bins[62].

2.4.3 Muon Reconstruction

Muons are identified by using the information of the ID and MS separately or combined. The information of the calorimeter is mainly used for efficiency studies. The muon reconstruction algorithms have a good momentum resolution for muons ranging from the GeV to the TeV scale. Reconstructed muons are of four different types[64]:

- **Stand-Alone (SA)**: Only information from the MS is used and it requires hits in at least two layers of the muon stations in order to fit a curved trajectory. The track is extrapolated inward to the ID to determine the closest approach to the beam pipe. Energy loss in the calorimeters is taken into account. It is mainly used for the forward region, $2.5 < |\eta| < 2.7$, where the ID has no coverage.
- **Combined (CB)**: Uses tracking information from both the ID and the MS and yields the best momentum resolution of the four methods. It is also used for most physics analysis. The coverage is limited to $|\eta| < 2.5$, the ID acceptance.
- **Segment-tagged (ST)**: Track from the ID is matched to one segment in the MS, either a MDT or CSC station. It is good for reconstructing low-p_T muons and regions with less muon chambers ($1.1 < |\eta| < 1.3$).
- **Calorimeter-tagged**: Track from the ID is matched to a calorimeter cluster, which fulfils the criteria of a minimum ionising particle. It has a low efficiency, but helps to recover CB muons in the region of $|\eta| < 0.1$, where there are less chambers due to service cables.

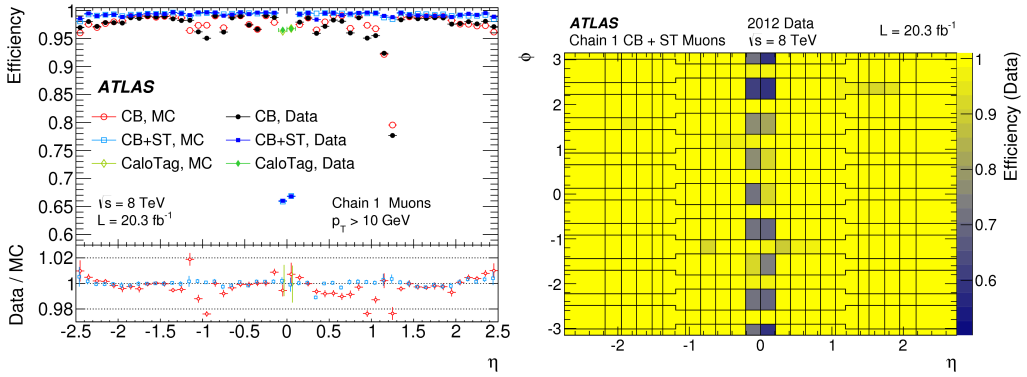

Figure 2.13: Muon reconstruction efficiencies for data and MC simulations as function of η (left). Various muon reconstruction types are tested[65]. On the right, the data efficiency as a function of η and ϕ.

The reconstruction is using three types of algorithms, also called Chains. Chain-I, or STACO[66], statistically combines the track information from the ID and MS by using covariance matrices. Chain-II, or MUID[67], uses the hits from the ID and MS and does a global refit of the track. Chain-III, or the third Chain[65], combines the best practices of STACO and MUID and will be the only method in Run-II. For the analysis presented in this thesis only CB muons reconstructed with Chain-I have been used.

The reconstruction efficiency has been determined by using the tag-and-probe method in $Z \rightarrow \mu\mu$ decays and in $J/\Psi \rightarrow \mu\mu$ decays for low-p_T muons. The tag muon has to be reconstructed as combined and triggered the event, while the probe muon is required to be identified in the calorimeter. Furthermore, the muons should be oppositely charged, be isolated from other objects in the detector and have an invariant mass close to M_Z or $M_{J/\Psi}$. The probe is then checked if it can be reconstructed as ST or CB. The efficiency is then given by the following product:

$$\epsilon(\text{type}) = \epsilon(\text{type}|\text{ID}) \cdot \epsilon(\text{ID}) \tag{2.5}$$

where ϵ(ID) is the ID efficiency and ϵ(type|ID) the matching efficiency for the muon type (ST or CB).

In the following we will use the notion of a scale factor defined as:

$$SF = \epsilon^{data}/\epsilon^{MC} \tag{2.6}$$

For physics analyses it is important that the MC simulation can be compared very precisely with the actual data. Any differences in efficiency when comparing simulation and data

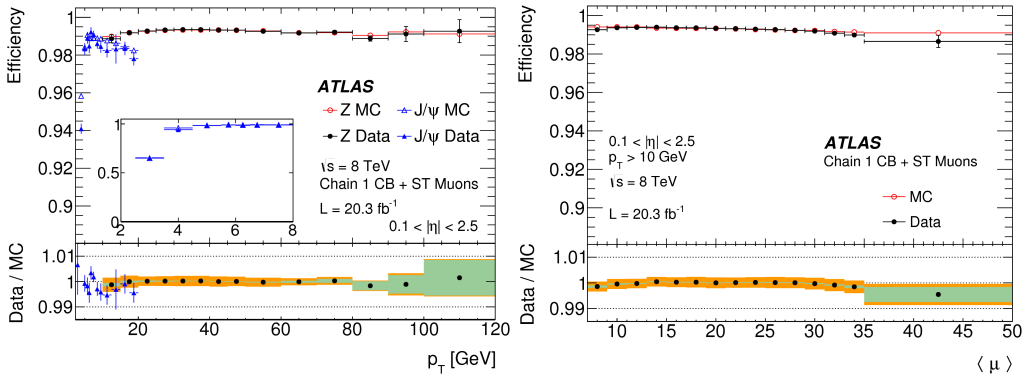

Figure 2.14: Muon reconstruction efficiency as function of p_T (left) and number of interactions per bunch crossing (right). The inset plot shows muons from $J/\Psi \to \mu\mu$ decay. The green and orange bands are the statistical and systematic uncertainties respectively[65].

are therefore corrected with the help of scale factors. By scaling the MC sample with the efficiency scale factor discrepancies between data and simulation are reduced.

Fig.2.13 shows the muon reconstruction efficiency of various muon types for MC simulation and data as function of η and the data efficiency as function of η and ϕ. The gap for CB muons around $\eta = 0$ is almost completely recovered by CaloTag muons. The data and MC agreement is within the 0.5% level over most of the η coverage.

Fig. 2.14 shows the efficiencies as function of muon p_T and pile-up. The efficiency stays for the most part above the 99% level, but reduces at the per mille level for higher pile-up conditions. Scale factors such as in Eq. 2.6 are used to correct the SM simulation to the data for the precise comparisons in various physics analysis. The data/MC agreement is on the per mille level for the muon efficiencies.

2.4.4 Jets

Quarks and gluons are partons that can not occur as single partons in nature and combine into color neutral hadrons. During the pp collision, any involved parton that is a quark or gluon will radiate off other gluons or quarks and thereby loose energy. Eventually all the newly created particles combine into hadrons, which can propagate freely until they decay. This shower of particles, that originated from one parton, is referred to as a jet. These jets are complicated objects and the total energy of all its constituent particles is related to the energy of the original parton. Jets leave large and wide deposits of energy in the calorimeter, mainly in the hadronic part. For the analysis in this thesis we also study the $H \to WW \to l\nu l\nu$ channel with one jet in the final state. We will discuss its phenomenology in more detail in chapter 3.

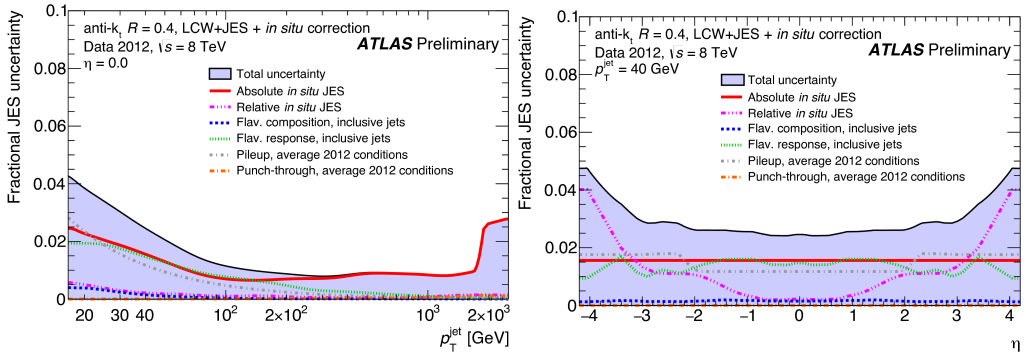

FIGURE 2.15: The systematic uncertainty of the JES as function of the jet p_T (left) and η (right). The data set contains the average pile-up conditions of 2012[68].

Reconstruction of jets starts with a topological clustering algorithm[69]. Cells in the HCAL have to exceed a certain signal/noise threshold and will be used as seed clusters. The neighbouring cells around the seed are added to the cluster if they also pass the signal/noise threshold. Finally, a ring of outer cells is added with a signal/noise ratio above 0. If there is more than one local maximum, the cluster is split. The cluster(s) is then fed to the FASTJET jet reconstruction pacakage[70].

For the analysis in this thesis, FASTJET's anti-k_T algorithm is used[71]. It is infrared and collinear safe, meaning that emission of soft or collinear gluons do not affect the jet reconstruction. It combines the distance and momentum of object i and j and the distance between an object and the beam B:

$$d_{ij} = min(p_{Ti}^{-2}, p_{Tj}^{-2}) \frac{\Delta R_{ij}^2}{R} \tag{2.7}$$

$$d_{iB} = p_{Ti}^{-2} \tag{2.8}$$

Here $\Delta R_{ij}^2 = \Delta\phi_{ij}^2 + \Delta\eta_{ij}^2$, R is the jet size parameter, which is chosen to be 0.4, and the p_T the transverse momentum of the object. If $d_{ij} < d_{iB}$ object i and j are merged into a new object k. This procedure is repeated for all $j \neq k$ objects, until no more objects can be combined. The final object is a called a jet, and the procedure starts over with another set of clusters. This reconstruction algorithm ensures that the distance between two jet centres is at least $2R$.

Due to the sampling of active and passive materials, the limited the calorimeter acceptance, pile-up and other effects, some of the jet energy escapes detection. In order to restore the true jet energy from the measured jet energy, a jet calibration scheme is applied[72]. The ECAL and HCAL components have been calibrated based on electromagnetic and hadronic

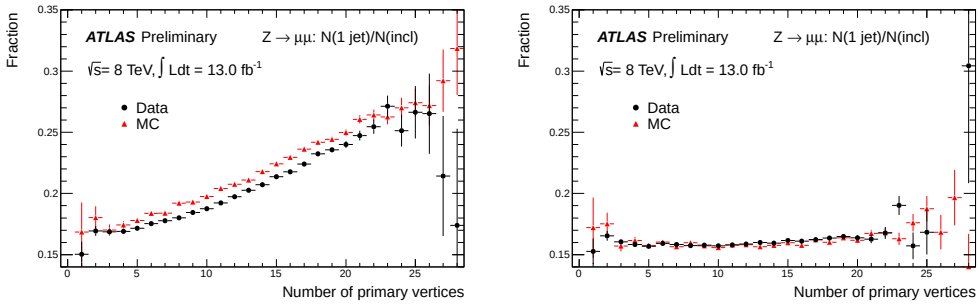

FIGURE 2.16: The ratio of $Z \rightarrow \mu\mu$ events plus one additional jet compared to the inclusive $Z \rightarrow \mu\mu$ events as a function of primary vertices. The plot on the left has no cut on JVF, while the plot on the right a cut of JVF > 0.5 has been applied[73].

showers respectively. These are supplemented with corrections from MC simulation studies. The calibration and MC correction are referred to as the jet energy scale (JES). Fig. 2.15 shows the systematic uncertainty of the JES as a function of jet p_T and η. The uncertainty is less than one percent of a 1 TeV central jet and on average below the 4% level for a 40 GeV jet.

Pile-up negatively affects the reconstruction of jets, so a method has been devised to make it more robust for high pile-up conditions. Tracks inside the jet not originating from the primary vertex are likely to be from other processes, such as pile-up. A variable known as the jet vertex fraction (JVF)[72] is defined as the ratio of the scalar momentum sum $\sum p_T$ of all the tracks within $\Delta R < 0.4$ of the jet axis and associated with the primary vertex compared to the total track momentum sum in the jet:

$$\text{JVF} = \sum_{\text{tracks}}^{\text{PV}} p_T \Big/ \sum_{\text{tracks}}^{\text{all}} p_T \tag{2.9}$$

A JVF of 0 would mean a jet is purely made up out of pile-up tracks. Jets with no associated tracks get a JVF = -1 assigned to them. Fig.2.16 shows the fraction of $Z \rightarrow \mu\mu$ events with an additional jet compared to the inclusive $Z \rightarrow \mu\mu$ events as a function of number of primary vertices. In the left figure, no cut on JVF is applied and the fraction steadily rises. On the right, a JVF > 0.5 has been applied and the fraction stays constant, indicating a robustness against pile-up conditions. The analysis in this thesis also applies JVF > 0.5 for reconstructed jets.

An important background to the $H \rightarrow WW \rightarrow l\nu l\nu$ channel plus one additional jet is the $t\bar{t}$ channel, where both the top quarks decay to a bottom quark. Vetoing events which have b-jets are therefore a useful criteria to get rid of $t\bar{t}$ background. Due to its relatively long life time of 1.5 ps, a B meson is capable to travel several millimetres before decaying. The b

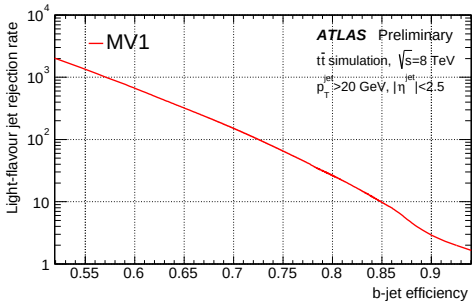

FIGURE 2.17: The light-flavour rejection rate as a function of the b-jet efficiency of the MV1 b-tagging algorithm[74].

decay products will therefore point back to a secondary vertex. There are several b-tagging algorithms[75] that make use of the presence of secondary vertices. For our analysis we used the MV1 algorithm[76], which is a neural network that weights the output of other b-jet tagging algorithms. The MV1 output is a probability that a jet originated from a light-flavour or a b quark. For an analysis a certain b-tag efficiency, also known as working point, can be chosen. Fig. 2.17 shows the light-flavour jet rejection as a function of the b-tag efficiency. High light-flavour rejection power leads to a lower efficiency, but to a higher purity of the b-tagged jets. The analysis in this thesis uses a MV1 working point at which there is an 85% efficiency for b-jets in inclusive $t\bar{t}$ events. At this point the light-flavour jet rejection rate is a factor 10.

2.4.5 Missing Energy

In pp collisions at the LHC, the longitudinal momentum of the proton constituents is not known, but the transverse to the beam there is no net momentum [1], so after the interaction the momentum of the particles leaving the primary vertex have to be balanced in the transverse plane. An imbalance in p_T, also referred to as missing transverse energy (MET), could therefore indicate the presence of neutrinos or even stable BSM particles that do not interact sufficiently with matter to be detected. In the $H \rightarrow WW \rightarrow l\nu l\nu$ analysis neutrinos are present and thereby a large amount of p_T imbalance is expected.

The calculation of the MET is relatively straightforward[77]:

$$E_T^{miss} = -\left(\sum_{objects} E_T + \sum_{soft} E_T \right) \tag{2.10}$$

[1] The proton constituents do in fact carry a little bit of transverse momentum, but this is negligible compared to the longitudinal component.

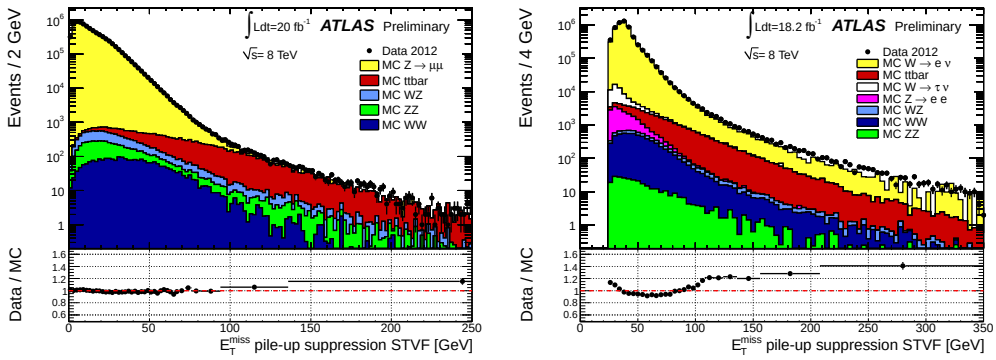

Figure 2.18: Comparisson between data and MC simulation as a function of E_T^{miss} for $Z \to \mu\mu$ events (left) and $W \to e\nu$ events (right)[78].

where the first sum is over all the hard objects that fulfil the minimum requirement for object identification, such as photons, electrons, muons, taus and jets, while the second is for all the soft objects that fail to fulfil any identification criteria. There are in fact two independent ways to determine the soft object: through energy deposition in the calorimeter or by using track information from the ID. The MET from the former is commonly referred to as E_T^{miss}, while the later is known as p_T^{miss}. In section 5.3 we will give a proper definition of the two, but for now it suffices to state that the missing transverse energy is just the negative vector sum of all hard and soft objects in an event.

The performance of E_T^{miss} has been studied with $Z \to \mu\mu$ and $W \to e\nu$ events. In the first process no p_T imbalance is expected, so it is a good probe to test the amount of fake E_T^{miss} in an event. In later process we expect real E_T^{miss} because of the presence of a neutrino. Fig. 2.18 shows the comparison between data and MC simulation for both processes. All the events have undergone a special pile-up suppression cut known as STVF[78]. The fake E_{miss}^T is well modelled as can be seen in the $Z \to \mu\mu$ sample. The modelling in the $W \to e\nu$ is even after the STVF cut slightly off. A possible reason for the discrepancy is that QCD background is not included in the simulation.

Fig. 2.19 shows what the resolution of E_{miss}^T and p_T^{miss} as a function of increasing pile-up for events with zero jets on the left and one jet on the right. The $p_T^{miss(trk)}$ variable is a simplified version of p_T^{miss}. It is clear that the p_T^{miss} is very pile-up robust in the 0-jet events compared to E_T^{miss}. For the 1-jet events the p_T^{miss} resolution steadily worsens with increasing pile-up, due to the fact that the neutral components of jets do not leave behind any tracks in the ID and make estimating the missing transverse energy harder.

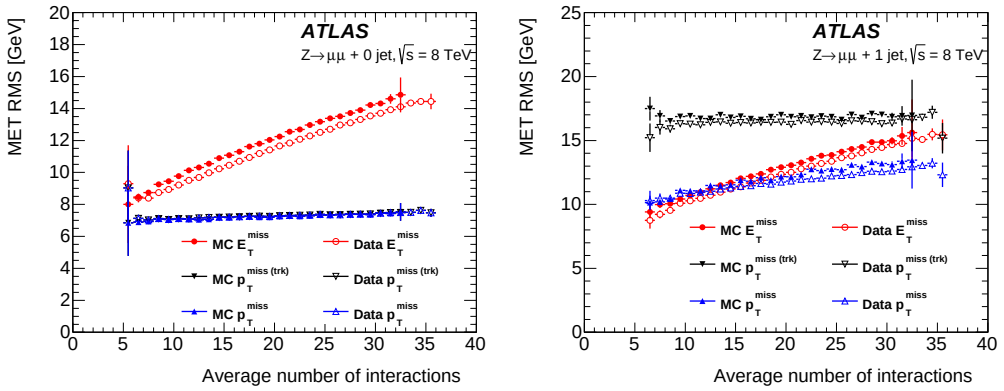

Figure 2.19: In red E_T^{miss} and blue p_T^{miss} as a function of pile-up for the $Z \to \mu\mu$ channel without any jets (left) and with one jet (right). $p_T^{miss(trk)}$ is a simplified version of p_T^{miss} [79].

2.4.6 Trigger Performance

Due to the high data rate and the rare occurrence of producing a Higgs boson, the trigger system has the task to reject background without removing too many signal events. The selection of the events for the $H \to WW \to e\nu_e\mu\nu_\mu$ channel relies on a trigger requiring either a single lepton or two leptons. Table 2.1 shows the minimum p_T requirements for the Level-1 trigger and the High-level trigger. Their efficiency is measured by using the tag-and-probe method with a data set containing $Z/\gamma* \to ee, \mu\mu$ candidates. For example, Fig. 2.20 shows the Level-1 and High-Level efficiency for the single muon trigger in the barrel ($\eta < 1.05$) and end-cap regions ($\eta > 1.05$), with respect to offline reconstructed muons in the same regions. The trigger requirements correspond with that of the single lepton trigger for the muon in Table 2.1. The triggers reach a plateau right after the p_T threshold. The end-cap region reaches about 85%, which is higher than the 70% in the barrel region[80]. The drop in efficiency has to do with the reduced efficiency to measure muons in the central region $\eta = 0$ in the muon spectrometer.

For the electrons, the single lepton trigger has an average efficiency of approximately 90%. The advantage of the dilepton triggers is that it increases the acceptance of low-p_T leptons. Imposing a more stringent threshold on the lepton p_T is then applied offline.

For the spin/CP analysis only the single and the dilepton trigger for e, μ will be relevant, as will be pointed out in chapter 5, where we discuss the selection criteria used for the $H \to WW \to e\nu_e\mu\nu_\mu$ channel.

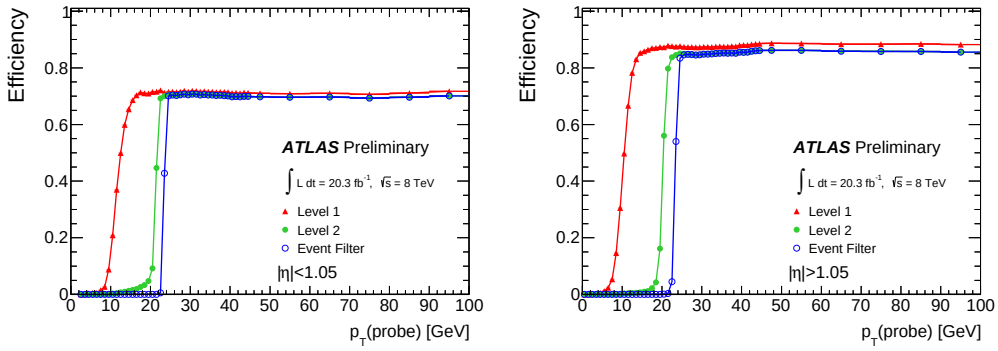

Figure 2.20: The efficiencies for the Level-1 and High-level single muon trigger as a function of the muon p_T and with respect to offline reconstructed muons using the tag-and-probe method. The left plot shows the efficiency in the barrel region, which is lowered compared to the end-cap region due to the drop in muon reconstruction efficiency in the central region ($\eta = 0$). The right plot shows the efficiency for the end-cap region. The trigger requirements are from Table 2.1. Figure taken from Ref. [80].

Name	Level-1 Trigger	High-Level trigger
Single lepton		
e	18 or 30	24i or 60
μ	15	24i or 36
Dilepton		
e, e	10 and 10	12 and 12
μ, μ	15	18 and 8
e, μ	10 and 6	12 and 8

Table 2.1: The minimum p_T requirements (in GeV) for the single and dilepton triggers for the Level-1 and High-Level trigger for the data taking in 2012. The Level-1 μ,μ dilepton trigger requires only a single muon. The "i" stands for an extra isolation criteria on the ID tracks. The "or" and "and" are logical. Table taken from Ref. [79].

2.5 Summary

In this chapter we described the main components of the ATLAS detector and discussed their performance to reconstruct events and identify physics objects. The performance is adequate to measure the final state particles of the $H \to WW \to e\nu_e\,\mu\nu_\mu$ channel with high precision. This information will be crucial in order to determine the Higgs spin and CP by looking at kinematic variables based on the charged leptons, the missing transverse energy and additional jets. The next chapter will introduce some kinematic variables sensitive to spin and CP defined in the laboratory frame.

Higgs Monte Carlo Simulations

3

In the previous chapter we have pointed out how the ATLAS detector measures the particles that come from the pp interaction. This chapter will start with describing what actually happens during the pp collision. The complex phenomenology requires several steps and the use of dedicated generator programs. In the second part we focus which types of generators can be used for the pp interaction. In the last section we present a MC study for leading-order (LO) versus next-to-leading-order (NLO) QCD Higgs production. We have generated events for the $H \to WW \to e\nu_e \mu\nu_\mu$ channel by interfacing the HC model from chapter 1 with the MadGraph5 and aMC@NLO generators. We generated Higgs samples for several spin and parity hypotheses and compared kinematic variables that are sensitive to the Higgs spin and parity. With the aMC@NLO generator we can generate the 0-jet events at NLO QCD and compare the differences events at LO 0-jet events generated with MadGraph5.

3.1 Proton-proton Phenomenology

Protons are composite objects consisting of three valence quarks, gluons and sea quarks formed through quark-antiquark creation. All these partons carry a fraction of the total momentum of the proton. This leads to complicated processes during a pp collision as is indicated in Fig.3.1. The main process can be subdivided into several steps:

- **Hard Scatter (HS)**: Two partons with a relatively large fraction of the total momentum of each proton interact with one another and cause a large momentum transfer. The energy is large enough to create heavy particles and therefore the HS is the most important interaction for the creation of new heavy particles.
- **ISR/FSR**: Coloured particles radiate off gluons and, if electrically charged, photons. Partons involved in the HS can radiate off particles before the main interaction, a process which is referred to as initial state radiation (ISR). After the HS, the partons can radiate off energetic particles as well, a process called final state radiation (FSR). In principle the ISR/FSR is handled by the parton shower, but if the energy of the radiated particle is high compared to the energies involved in the HS, it should be included in the description of the HS as well.

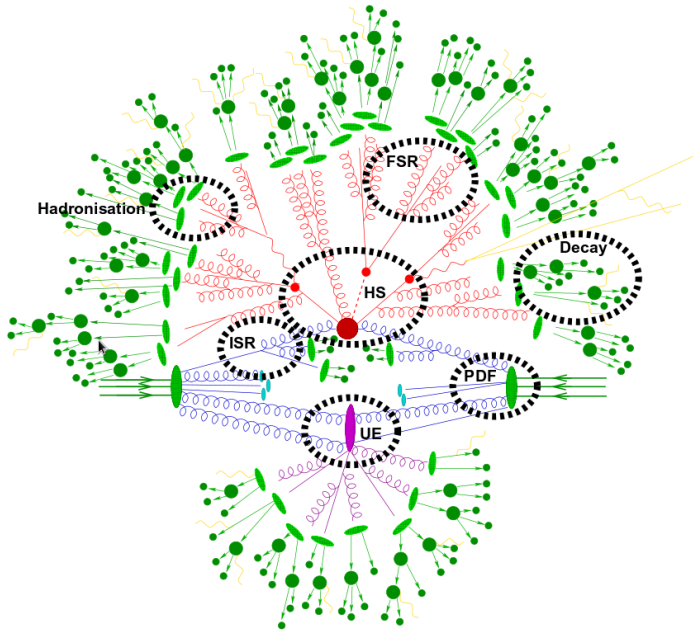

Figure 3.1: Schematic representation of a proton-proton collision at the LHC. The hard scattering process (HS) takes up the most energy. The other processes are explained in the text. Picture taken from Ref. [81] and the original version can be found in Ref. [82].

- **Parton Shower (PS)**: All the coloured particles have to combine into colourless objects due to confinement. Quarks radiate off gluons and energetic gluons can split up in quark-antiquark pairs and loose energy. This process is called showering and happens not only to the partons from the HS, ISR and FSR, but also to the other partons in the protons that were not involved in any interaction.
- **Hadronisation and Decay**: The parton shower will result in colourless hadrons and photons, which form cone-shaped jets of particles. Hadrons with heavy quarks subsequently decay to lighter and more stable hadrons.
- **Underlying Event (UE)**: All the interactions that can not be traced back to the HS are called the underlying event.
- **PDF**: A parton distribution function (PDF) describes the probability of a parton carrying momentum fraction x of the total proton momentum. It is used to calculate the cross-section $\sigma_{pp\to X}$, as is explained in the next section.

3.1.1 The Partonic Cross-section and PDFs

The flavour and momentum fraction that a parton carries inside the proton varies from collision to collision. The momentum of all the partons have to add up to the total proton momentum. In order to calculate the cross-section for the creation of a heavy particle X from a pp collision, the cross-section for the HS has to be convoluted with the probability of the partons carrying a certain momentum fraction. The cross-section can be written as the sum over all partons and an integral of probabilities:

$$\sigma_{pp\to X} = \sum_{a,b} \int \hat{\sigma}_{ab\to X} f_a(x_1, Q^2) f_b(x_2, Q^2) dx_1 dx_2 \tag{3.1}$$

The sum is over the partons a and b that are involved in the hard interaction creating the heavy particle X, the cross-section for the HS is indicated by $\hat{\sigma}_{ab\to X}$ and the last part are two functions $f(x, Q^2)$ describing the probability of a parton having momentum fraction x, also known as Bjorken-x[83], at a momentum transfer Q^2. These two functions are the parton probability distributions PDFs and describe parts of the pp interaction that can not be calculated peturbatively. The HS, however, can be calculated peturbatively and splitting the hard part from the soft part in Eq. 3.1 is known as factorisation. It allows to calculate for example the ggF Higgs production during a pp interaction by using the ggF Feynman-diagram in Fig. 1.1 convoluted with the corresponding gluon PDFs.

Due to their non-perturbative nature, PDFs have to be determined from experiments. Deep inelastic scatterings between electrons and protons, for example, are used for this purpose. This process is well understood and by performing precision measurements the PDFs can be extracted from the results. HERA's H1 and ZEUS experiments for example did do such measurements[84]. Dedicated groups such as MRST[85] and CTEQ[86] publish the PDFs. Fig. 3.2 shows the PDFs for quarks and gluons for momentum transfer scales $Q^2 = 10$ GeV^2 and $Q^2 = 10^4$ GeV^2 and parametrised by MSTW2008. The density of low momentum fraction particles increases with increasing Q^2. Sea quarks and gluons therefore become more visible inside the proton at higher energies.

The cross-section $\hat{\sigma}_{ab\to X}$, also known as the partonic cross-section, can be described by a expansion series in α_s, the strong coupling constant. The first order in α_s is referred to as the leading order (LO). It is defined at the lowest order in the coupling in which the desired final state can be made. Often this consists of tree level diagrams, but not always: Higgs production in gluon fusion happens at LO through a top quark loop. Higher orders in α_s, such as NLO and next-to-NLO (NNLO), include diagrams with more vertices (at NLO this means for example one-loop diagrams as well as one-parton ISR/FSR diagrams) and make the calculation of the cross-section more precise. However, the computations become more extensive and complex, and also α_s is becoming increasingly small at high energies. Therefore, the contributions of higher order diagrams are becoming less important to the

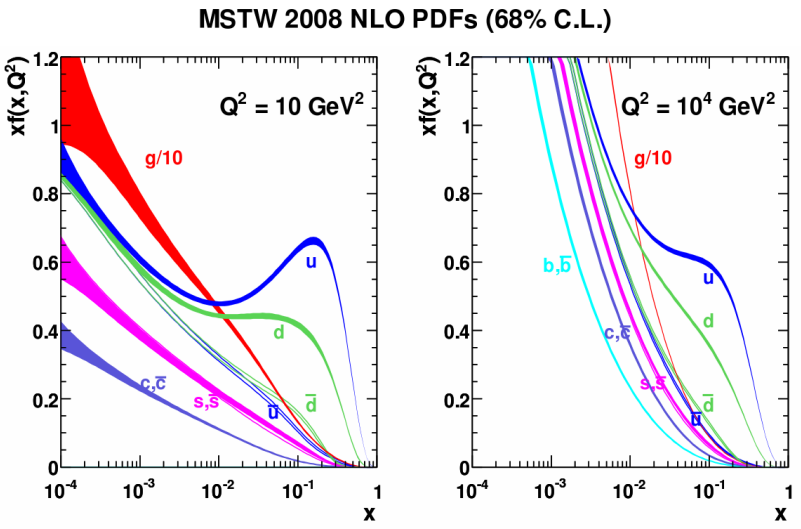

Figure 3.2: PDFs for quarks and gluons inside the proton as a function of the momentum fraction x. On the left, the momentum transfer scale is at $Q^2 = 10$ GeV^2 and on the right, it is at $Q^2 = 10^4$ GeV^2. The PDFs have been parametrised by MSTW2008 and the error bars indicate the 68% confidence level[85].

calculation of the cross-section. For some processes the NLO calculations are so large that instead, as a somewhat crude approximation, the LO processes are used and scaled with so-called k factors, which is the ratio of the NLO/LO cross-sections. This is exact for the total cross-section, by definition, but is at best a good approximation when applied to differential distributions.

3.2 Event Generators

The processes involved in the proton-proton phenomenology have to be properly modelled to make sensible predictions. Various types of event generators have been developed to describe the different steps mentioned in section 3.1. The HS involves the calculation of the matrix element (ME) and the outgoing partons have to undergo the showering, hadronisation and decay steps. Almost all generators that model SM processes are also capable to model BSM phenomenology. We describe below some of the generators that have been used to generate MC events for the analysis. The full list is mentioned in chapter 5.

General purpose generators can do all the steps involved in generating events. Libraries are used to extract precalculated ME for several SM and BSM processes. The HS involves

processes of the type $2 \to 2$ or $2 \to 1$. The two most common general purpose generators are PYTHIA[87, 88] and HERWIG[89], which are very similar but vary slightly in colour flow and parton showering scheme. The UE is characterised by low momentum transfers and is mainly based on phenomenological models, which are implemented by generators such as JIMMY[90]. Pile-up is included by adding separately generated events.

To include processes of the type $2 \to n$, with $n > 2$, other generators have to be used such as MADGRAPH5[31] or ALPGEN[91]. These generators only calculate the ME and are also referred to as ME calculators. In principle the processes of the type $2 \to 3$ and higher are only at LO and to fully include all the NLO effects, diagrams with loops and external partons have to be included as well. Special ME calculators which take the NLO virtual contributions into account are aMC@NLO[92] and POWHEG[93]. In section 3.3 we show how aMC@NLO addresses this issue. All the ME calculators have to be interfaced with PYTHIA or HERWIG for the PS and hadronisation to obtain physical results.

During the PS, partons can radiate off other particles by means of ISR and FSR. One problem that can arise is that radiation of an extra particle during the PS has been taken into account already by the HS. This is double counting and in order to prevent it, a scale is chosen which defines the hardness of the process. If the particle's energy (or transverse momentum) is above the scale, the process is handled by the ME calculator and when it is below the scale, it is passed on to the PS. The choice of the scale is done by the MLM scheme[94] and it enables to merge processes with different final state multiplicities into one inclusive sample.

3.3 MC Studies for Higgs Models

In this section we present a MC simulation study performed with the MADGRAPH5 and aMC@NLO generators. The goal was to generate $H \to WW \to l\nu l\nu$ events at LO and NLO QCD level and study the differences in the kinematic distributions that are sensitive to the Higgs spin and CP. The HC model introduced in section 1.4.1 was used to select a scalar boson X with quantum numbers $J^P = 0^+$, 0^-, 1^+, 1^- and 2^+ and coupling to W bosons. As mentioned before, we will omit the results on the 1^+ and 1^+ hypothesis, but shortly comment on the outcome at the end of this chapter. As of 2014 the MADGRAPH5 and aMC@NLO generators have been merged into one framework called MADGRAPH5_aMC@NLO and is documented in detail in Ref. [95].

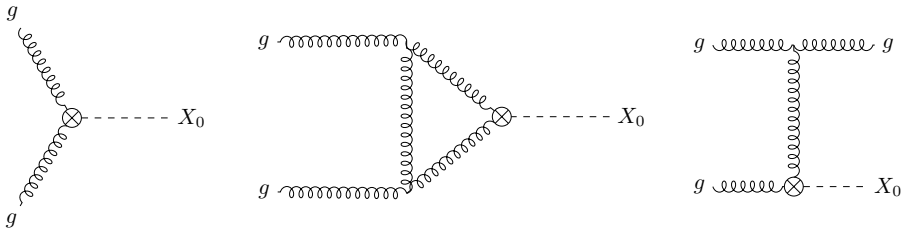

FIGURE 3.3: Feynman diagrams for the production of a scalar resonance X_0, corresponding to the HC model. The crossed blob indicates an effective coupling. The first diagram is at LO, the middle a virtual NLO diagram and the last a real NLO diagram. It is the virtual NLO diagram that aMC@NLO takes into account into its subtraction scheme to achieve NLO accuracy for the 0-jet events.

3.3.1 NLO QCD Diagrams

Fig. 3.3 shows the generation of a scalar particle X_0 through the ggF process. Instead of using a top-loop like in the ggF Higgs production diagram in Fig. 1.1, the loop has been replaced by an effective coupling from the HC model. The diagram on the left is at tree level, while the other two are a virtual and a real NLO QCD diagram. The MadGraph5 generator produces processes of the type $2 \to n$, with $n = 1, 2, 3$, etc., meaning X_0 + n-1 external partons. The extra partons can be from the HS process in the ME calculation or branch off from another parton during the PS. In order to make an inclusive sample, the events with different parton multiplicities are merged. The MLM scheme is used to prevent double counting. The calculations, however, are still at LO and did not include the virtual NLO diagram in the ME calculation from Fig. 3.3.

The aMC@NLO generator does include the virtual gluon diagram by using the MC@NLO formalism[92]. In principle it gives a handle for the PS simulator to treat the hard emissions from the initial state particles, by treating it as a NLO computation. The soft and collinear emissions are still treated by the PS MC, so it allows for a smooth transition between the hard and soft emission regions. The tree level, or Born process, virtual and real NLO diagrams are supplemented with negative terms related to these diagrams. With this subtraction method the MC@NLO formalism can create infrared-safe observables to a NLO accuracy. The full NLO result for all observables is obtained by expanding the MC@NLO results in the strong coupling constant α_s. The subtraction method leads to events with negative weights, but this happens to only a small fraction of events and the number can be reduced even further by proper tuning of the generator. It achieves NLO accuracy for the phase space involving the HS, which is a difficult region for a LO PS. And it achieves the accuracy of a LO PS in the soft emission region, where the NLO computation has to resum large logarithms.

The subtraction method has to know which type of PS MC is used (PYTHIA or HERWIG), because it influences the backward evolution of the showering from the initial state particles, the dead zones for hard emission and the matching of local counter terms in the soft region[92]. As soon as the PS MC is properly matched, events can be created with NLO accuracy. We are now able to check if Higgs spin and parity sensitive variables change when including NLO accuracy for the hard regions of phase space.

3.3.2 Generator Settings

For the Higgs MC studies samples of 200k events were generated for a scalar resonance X with different spin and parity, coupling to W bosons with subsequent decay to leptons and neutrinos. The MADGRAPH5 generator calculated the ME for the following process:

$$pp \to X_{J^{CP}} \to W^+W^- \to e^+\,\nu_e\,\mu^-\,\bar{\nu}_\mu + N_{ext} \tag{3.2}$$

where, $N_{ext} = 0, 1, 2$ the number of external QCD partons from ISR and for $J^{CP} = 0^+$, 0^-, 1^+, 1^- and 2^+ hypotheses were chosen. In Table 3.1 the corresponding HC settings for the used hypotheses are displayed. The 2^+mix model is a spin-2 UC model while, the other spin-2 models belong to the NUC category (see 1.4.3) and are discussed in section 3.3.4. The aMC@NLO generator calculates the ME at NLO for the same $X_{J^{CP}}$ production and decay process for $N_{ext} = 0$. Higher parton multiplicities are due to the PS MC and therefore at LO. The simulated pp collision are generated at a centre-of-mass energy of $\sqrt{s} = 8$ TeV and the mass of the resonance is set at $M_X = 125$ GeV.

The PDF set used by MADGRAPH5 was CTEQ6L1 and the merging scale was set at $Q^{ME}_{min} = 40$ GeV. aMC@NLO used the MSTW2008 NLO PDF set with the factorisation and normalisation scales $\mu_F = \mu_R = M_X$. The samples were showered with PYTHIA 6.4 p_T-ordered using the CTEQ5L set as PDF. After the PS, hadronisation and decay steps, the final state particles have been clustered into jets with FASTJET's anti-k_T algorithm with $\Delta R = 0.4$. Reconstructed jets were also required to have $p_T > 25$ GeV.

For the MC studies no kinematic cuts have been applied. The simulation is setup to fully hadronise the partons with the PS and includes the decay of heavy quarks. No detector acceptance cuts have been applied.

3.3.3 Kinematic Distributions

In this part we present the results of the MC studies by showing some spin and CP sensitive variables from the events generated with the aMC@NLO generator and split up in a 0-jet and 1-jet category. At the bottom of each distribution we show the MADGRAPH5 over

Model	Spin-0					Spin-2	
	κ_{SM}	κ_{HWW}	$\kappa_{H\partial W}$	κ_{AWW}	$\cos(\alpha)$	κ_g	κ_q
0^+ (SM)	1	0	0	0	1	-	-
0^-	0	0	0	1	0	-	-
2^+mix	-	-	-	-	-	1	1
$2^+q\bar{q}$	-	-	-	-	-	0	1
2^+ggF	-	-	-	-	-	1	0

Table 3.1: HC model settings for the hypotheses used in the MC studies. The cutoff scale Λ is set to 1 TeV for all models, but in the end all the models are normalised to unity in order to compare the changes in shape of some kinematic distributions.

aMC@NLO ratio (MG/aMC) in order to compare the two generators. For the 0-jet events this means we can check the LO process versus the NLO process. For the 1-jet events it is the LO process for both generators, so we expect similar results. For all the plots we only show the results for the $J^{CP} = 0^+$, 0^- and 2^+mix hypotheses and discuss the differences. We will discuss the following kinematic variables:

- $\Delta\phi_{ll}$: The opening angle in the transverse plane between the charged leptons. As discussed in section 1.2.4, we expect small opening angles for a spin-0 Higgs, while a spin-2 boson will have large opening angles.
- p_T^{ll}: The transverse momentum of the dilepton system. For the spin-0 hypothesis the leptons tend to be more collinear and therefore the momentum of the dilepton system is high. For the spin-2 hypothesis the leptons tend to be more antiparallel and results in lower momentum for the dilepton system.
- M_{ll}: The invariant mass of the dilepton system. The more collinear the leptons are the lower the invariant mass for the dilepton system and vice versa. Therefore, the spin-2 hypothesis tends to have larger M_{ll} values compared to spin-0.
- M_T: The transverse mass[96] of the charged leptons and the missing transverse energy vector $\vec{E}_T^{miss}$:
$$M_T = \sqrt{(E_T^{ll} + E_T^{miss})^2 - |\vec{p}_T^{ll} + \vec{E}_T^{miss}|^2} \tag{3.3}$$
where $(E_T^{ll})^2 = (p_T^{ll})^2 + M_{ll}^2$. This variable combines both lepton and neutrino kinematics and should in principle be sensitive to spin and CP. It has an endpoint at 125 GeV, because it is a projection of the mass of the resonance M_X, which is in our case the Higgs with a mass of 125 GeV.

These variables are all defined in the laboratory frame and are the most commonly used for spin and CP analysis in the $H \to WW \to l\nu l\nu$ channel.

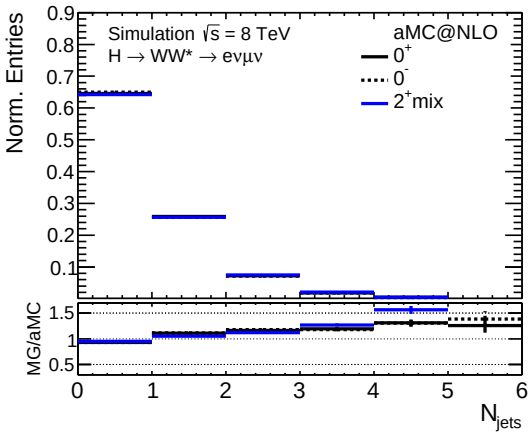

Figure 3.4: Amount of events as function of jet multiplicity N_{jets}. The events have been normalised to unity. Bottom plot shows the MadGraph5 over aMC@NLO ratio.

Fig.3.4 shows the amount of jets, N_{jets}, reconstructed per event. The 0-jet and 1-jet events take up more than 90% of the total amount of events, therefore we will omit the results for the 2-jet and higher events. The statistical error bars are so small that for most bins they are not visible. The spin-0 and spin-2 hypotheses lead to identical results so the number of jets is not influenced by spin or parity. The rise in ratio versus the jet multiplicity for MadGraph5 is due to merging of samples with higher parton multiplicities from the ME calculation. The PS produces softer jets than the ones produced with the ME.

0-jet Distributions

Fig. 3.5 shows the four kinematic variables for the 0-jet events. The difference between the spin-0 and spin-2 hypotheses we pointed out earlier are clearly visible and in line with predictions. $\Delta\phi_{ll}$ and M_{ll} are the strongest discriminating variables. To separate 0^+ and 0^- hypotheses the $\Delta\phi_{ll}$ variable performs the best. There is virtually no difference between the MadGraph5 and aMC@NLO generators. We can therefore conclude that the NLO corrections have no significant effect on the spin and parity sensitive variables in the 0-jet events.

1-jet Distributions

Fig.3.6 shows the four kinematic variables of the 1-jet events. A noticeable difference with Fig.3.5 is that the $\Delta\phi_{ll}$ and p_T^{ll} variables perform less on discriminating spin-0 from spin-2. The MadGraph5 versus aMC@NLO comparison shows that the generators only differ in

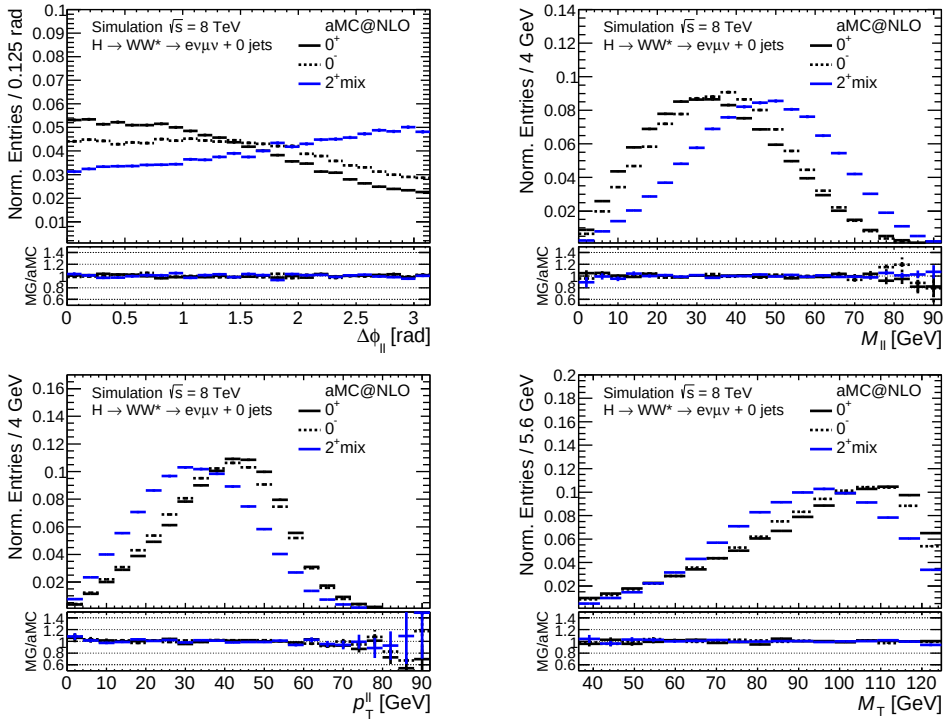

Figure 3.5: The four kinematic distributions for the 0-jet events. Events have been normalised to unity.

the tail of p_T^{ll} distribution. This can be attributed again to the fact that the merging of the events with higher jet multiplicities for MadGraph5 leads to a harder p_T spectrum.

These studies confirm that the virtual NLO corrections from aMC@NLO have little to no effect on the spin and CP sensitive variables for the 0-jet when compared to the LO events from MadGraph5. The 1-jet events are at LO for both generators and the spin and CP variables are very similar for both generators. We can therefore safely generate events for the $H \to WW \to l\nu l\nu$ process for different spin and CP with the MadGraph5 generator. This significantly reduces the amount of computation time (about a factor 10) needed to generate the events. What we also see from these studies is that some variables like $\Delta\phi_{ll}$ loose discriminating power in the 1-jet events. In Fig. 3.7 we can see that the Higgs p_T is significantly higher in the 1-jet events compared to the 0-jet. This can be attributed to the recoil from the hard-emission of a gluon (or quark) from the incoming partons. The higher the recoil and thereby the Higgs p_T, the more boosted are the final state leptons. This distorts the spin and CP sensitive variables and thereby reduces the discrimination power. It is therefore recommended to boost to the Higgs rest-frame so distortions due to boosts can be compensated for. In chapter 4 we introduce a method how to boost to the

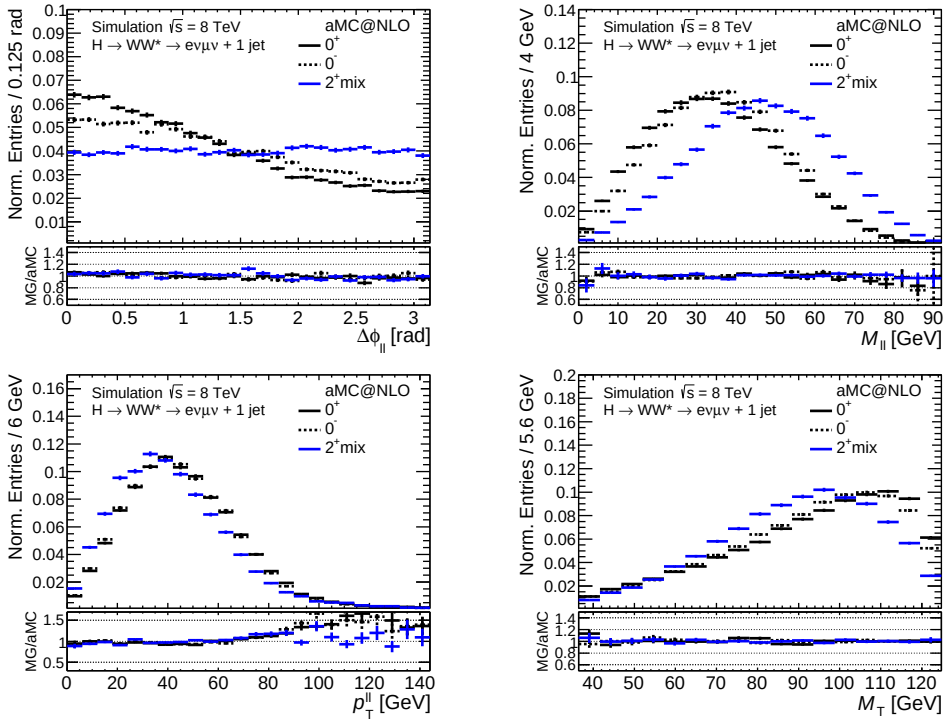

Figure 3.6: The four kinematic distributions for the 1-jet events. Events have been normalised to unity.

Higgs rest-frame for the $H \to WW \to l\nu l\nu$ channel and define new spin and CP sensitive variables.

The comparison of MadGraph5 and aMC@NLO for the 1^+ and 1^- hypotheses yielded the same results as for the spin-0 and spin-2 hypotheses. No significant difference was observed in the spin and CP sensitive variables comparing the LO to NLO processes.

3.3.4 Unitarity Violation in Spin-2 Samples

Finally, we have to address an important issue regarding the QCD NLO diagrams for creating a spin-2 Higgs boson. It is the onset of unitarity violation at high energies for the NUC spin-2 models as was introduced in section 1.4.3. In this section we compare the spin-2 models from Table 3.1 related to Table 1.4 by generating events with the MadGraph5 and aMC@NLO generators.

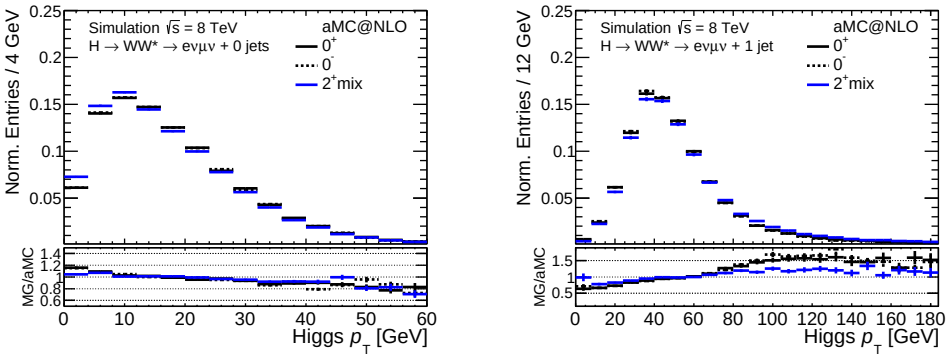

Figure 3.7: The Higgs transverse momentum distributions for the 0-jet and 1-jet events, normalised to unity. The MadGraph5/aMC@NLO difference can be attributed to the merging of samples with higher jet multiplicities for MadGraph5. This results in a softer p_T spectrum for the 0-jet, but a harder spectrum for the 1-jet events.

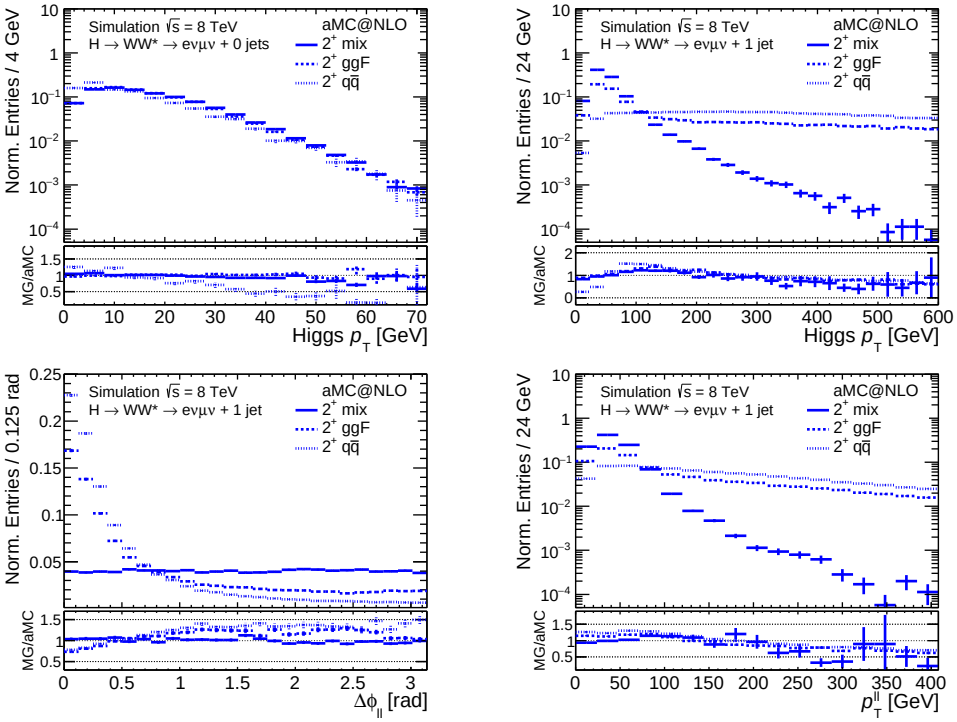

Figure 3.8: Onset of unitarity violation for the spin-2 NUC models in the 1-jet events. On the top left, the 0-jet distribution for p_T^H shows that both UC and NUC models behave properly. In the 1-jet distribution on the right, however, the NUC models show unitarity violating behaviour for high values of p_T^H. The bottom two plots show what effect the onset of unitarity violation has on the $\Delta\phi_{ll}$ and p_T^{ll} variables.

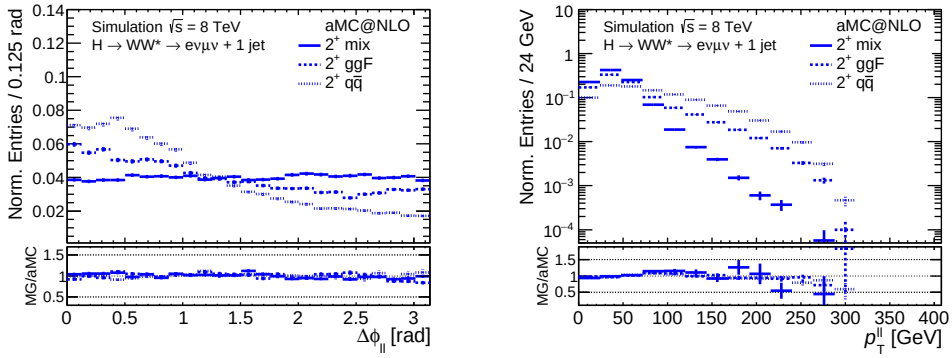

Figure 3.9: $\Delta\phi_{ll}$ and p_T^{ll} variables for the spin-2 UC and NUC models for the 1-jet category after imposing a $p_T^H < 300$ GeV cut.

Fig. 3.8 shows on top the Higgs p_T distributions for 0-jet and 1-jet events. The 0-jet distributions shows that the UC and NUC models show similar behaviour. This is expected, because the problems lies with the NLO diagrams with one additional external parton as in Fig. 1.10. The ME for these diagrams contains a term proportional to $(\kappa_q - \kappa_g)^2$, which does not cancel and grows with $s^3/m^4\Lambda^2$. This can be seen by the large (almost) flat tails in the 1-jet p_T^H distribution for the NUC models. The dip in the 0-jet MadGraph5/aMC@NLO ratio for the $q\bar{q}$ NUC model is because the MadGraph5 events are more prone to migrate to the 1-jet and higher jet multiplicity samples during the merging into one inclusive sample. The 1-jet distribution shows a regular exponential reduction of events with higher p_T^H for the UC spin-2 model. However, the NUC models have a nearly flat p_T^H distribution over the whole range. This is the onset of unitarity violation for high Higgs p_T values and results in unphysical phenomena. The unitarity violating effect is also clearly visible in the 1-jet $\Delta\phi_{ll}$ and p_T^{ll} distributions at the bottom of Fig. 3.8.

The 1-jet events have a significant amount of events compared to the other jet multiplicities (about 25%) so it is preferable to include the 1-jet events for testing spin-2 UC and NUC models. In order to prevent the onset of unitarity violation a cut on the Higgs p_T is set to cut away the part that causes the problem. Deciding where the cut has to be placed depends on the cutoff scale Λ used for the EFT. For the spin-2 UC and NUC studies it was set at $\Lambda = 1$ TeV, so at this scale the EFT breaks down. Setting the p_T cut at one third of the cutoff scale is well below the onset of unitarity violation. For the MC studies we have chosen to set the cut at $p_T^H < 300$ GeV. As can be seen from Fig. 3.8, the cut has no influence on the 0-jet events and cuts away a minimal part of the spin-2 UC events for the 1-jet distribution. Fig. 3.9 shows that the p_T^H cut brings the NUC models closer to the UC model.

3.4 Summary

In this chapter we discussed the complex phenomenology involved in pp collisions and the several types of MC generators that are used to model these processes. We also presented the results of MC studies related to Higgs production and subsequent decay to W bosons and leptons. Events generated with the MadGraph5 and aMC@NLO generators showed that kinematic variables, which are sensitive to the Higgs spin and CP, were not affected by the virtual NLO correction when compared to LO 0-jet events and the generators gave similar results for the LO 1-jet events. However, we noticed that due to the Higgs transverse momentum p_T^H, the distributions of the variables get distorted. It is therefore preferable to perform spin and CP studies with variables defined in the Higgs rest-frame and that will be the topic of the next chapter.

Higgs Rest-Frame Reconstruction

4

In order to test if the boson discovered in 2012 is in fact a SM Higgs boson, its spin and CP properties are preferably measured in the rest-frame. Spin and momentum conservation dictate the decay products to follow certain momentum and angular distributions characteristic for the spin/CP nature of the Higgs. In a boosted frame these distributions are distorted and, in general, loose discrimination power due to finite detector resolutions. Also the orientation of the rest-frame itself is important to measure properties and there are various well-known rest-frames used throughout history[97–99]. This chapter discusses one of these rest-frame orientations, known as the Collins-Soper(CS) frame[99]. Firstly, we will explain how it is defined and how to boost to it from the lab-frame. Secondly, we introduce an algorithm necessary to reconstruct the z component of the dineutrino system in the $H \to WW \to l\nu l\nu$ channel. Without this component, we do not have enough information to boost to a proper Higgs rest-frame. Lastly, we show the characteristic angular and momentum distributions of the charged leptons in the CS-frame. These distributions will form the cornerstones of the analysis described in later chapters.

4.1 Collins-Soper Frame

In 1977 John C. Collins and Davison E. Soper proposed a method to incorporate the transverse momentum of partons in the Drell-Yan production of muon pairs[99]. In the Drell-Yan model a virtual photon is created through the annihilation of a quark from one hadron with an antiquark from another hadron[100]. The photon decays into two muons subsequently. At high enough energies the quarks are assumed to be collinear with the incident hadrons and therefore the angular distribution of the muons is $1 + \cos^2\theta$, where θ is the angle between the beam axis in the lab-frame and the muon momentum in the dimuon centre-of-mass frame. However, for large transverse momentum of the dimuon system, the quarks are no longer collinear in the dimuon rest-frame and the muon angular distribution does not only depend on the polar angle θ, but also on the azimuthal angle ϕ.

Collins and Soper redefined the axes to which the angles θ and ϕ are to be measured in the dimuon rest-frame. When the momentum of the incident partons are expressed as $\vec{p}_A$ and $\vec{p}_B$ in the dimuon rest-frame, the redefined z axis is the bisection of $\vec{p}_A$ and $-\vec{p}_B$. Then

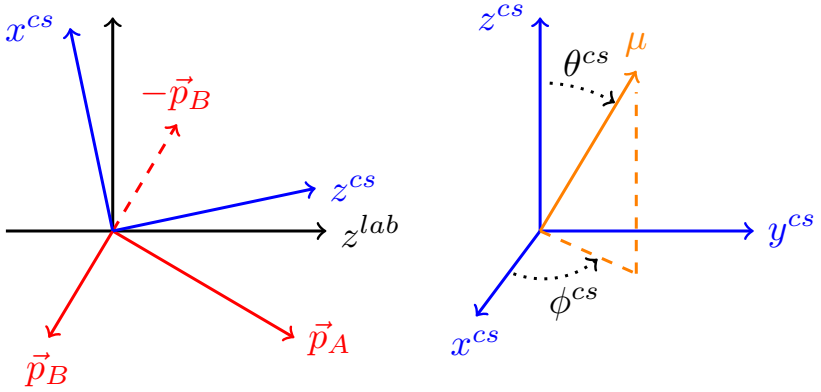

Figure 4.1: Left, definition of the Colins-Soper frame based on the parton momenta $\vec{p}_A$ and $\vec{p}_B$. Right, the definition of the CS-angles for any particle.

θ^{cs} is the angle with respect to this new z axis. The azimuthal angle ϕ^{cs} is measured with respect to a new x axis, which lies in the plane formed by $\vec{p}_A$ and $\vec{p}_B$ and pointing away from the sum vector $\vec{p}_A+\vec{p}_B$. Fig. 4.1 shows the definition of the axes in the CS-frame and how the angles θ^{cs} and ϕ^{cs} are defined for any particle in the CS-frame. Including the azimuthal angle the Drell-Yan angular distribution is modified to:

$$\frac{dN}{d\Omega} \propto 1+\cos^2\theta+(\frac{1}{2}-\frac{2}{3}\cos^2\theta)\mathrm{A}_0 + 2\cos\theta\sin\theta\cos\phi\,\mathrm{A}_1+\frac{1}{2}\sin^2\theta\cos 2\phi\,\mathrm{A}_2 \tag{4.1}$$

The coefficients A_n depend on the momentum transfer and pseudorapidity and in the limit of $Q^2 \to \infty$ the Drell-Yan model predicts $\mathrm{A}_n \to 0$ and thereby recovering the $1+\cos^2\theta$ relation.

To use the CS-frame for the $H \to WW \to l\nu l\nu$ channel the Drell-Yan photon in the description above should be replaced by the Higgs boson, which will be at rest in the CS-frame. The partons p_A and p_B as in Fig. 4.1 are the incoming gluons that fuse into a Higgs (or the quark-antiquark pair for the $q\bar{q}$ production mode of a spin-2 tensor). We will then define the angles θ^{cs} and ϕ^{cs} for the charged leptons coming from the W decay. If there is enough statistics, it is possible to make angular distributions of the charged leptons parametrised as in Eq. 4.1 and with their own coefficients A_n^{ll}. These coefficients (for the $H \to WW \to l\nu l\nu$ channel) can be fitted and can be checked for dependance on the Higgs (transverse) momentum. The coefficients can also describe a non-SM Higgs with different spin and parity.

We conducted a small study with a SM Higgs sample and confirmed that the coefficients A_n^{ll} indeed have a dependance on the boost of the Higgs. However, the amount of statistics for the SM Higgs signal is too low for the 2012 data set and the pp collisions at the LHC do not give a clean enough environment to measure precisely these coefficients A_n^{ll}. Future accelerators like an e^+e^- collider reaching energies of 1 TeV would be able to ensure a clean environment and an abundance of Higgs production, making it possible to fit these coefficients A_n^{ll}. However, for the analysis presented in this thesis, boosting to CS-frame gives us an advantage compared to the lab-frame for studying different spin and CP hypotheses as explained in the next section.

To summarise, the reasons for using the CS-frame as the orientation for the Higgs spin and CP analysis used throughout this thesis are the following:

- The frame is easy to reconstruct as soon as the Higgs energy-momentum vector is reconstructed and has a fixed orientation with respect to the transverse component of the Higgs.
- The frame has a fixed x and y axis.
- The frame is covariant under rotation about the z axis
- It is straightforward to change to different reference frames, like the Gottfried-Jackson frame[98], by just rotating the z axis.

4.2 Boosting to the CS-frame

To boost the Higgs boson from the laboratory frame to the CS-frame, we make use of a boost matrix originally defined in Ref. [101]:

$$\begin{pmatrix} E \\ p_x \\ p_y \\ p_z \end{pmatrix}_{CS} = \begin{pmatrix} \frac{Q_E}{\sqrt{Q^2}} & -\frac{p_T}{\sqrt{Q^2}} & 0 & -\frac{Q_z}{\sqrt{Q^2}} \\ -\frac{p_T Q_E}{\sqrt{Q^2} X_T} & \frac{X_T}{\sqrt{Q^2}} & 0 & \frac{p_T Q_z}{\sqrt{Q^2} X_T} \\ 0 & 0 & 1 & 0 \\ -\frac{Q_z}{X_T} & 0 & 0 & \frac{Q_E}{X_T} \end{pmatrix} \begin{pmatrix} E \\ p_x \\ p_y \\ p_z \end{pmatrix}_{lab} \tag{4.2}$$

where Q is the momentum of the Higgs boson, p_T the transverse momentum of the Higgs boson and $X_T = \sqrt{Q^2 + p_T^2}$. We generated about 200k events for the $H \to WW \to l\nu l\nu$ channel with the aMC@NLO generator at parton level and showered subsequently the events with Pythia6. External partons have been clustered into jets by using FastJet. No acceptance cuts or smearing effect have been applied. At this point we have still full access to the kinematics of the final state leptons and neutrinos, allowing us to fully reconstruct

the four-vector of the Higgs. We will therefore use the term "Truth Level" to indicate the access to all the kinematical quantities in an event in the following figures.

Fig.4.2 shows the angular and momentum correlations between the charged leptons in the CS-frame and the laboratory frame. There are clear correlations visible in the CS-frame, but in the lab-frame these features are largely washed out due to the boost of the Higgs system. This effect is especially strong for the θ angles and the momenta. The correlations in the 2D ϕ plane remain largely intact when going from the CS-frame to the boosted lab-frame. The opening angle between the charged leptons, $\Delta\phi_{ll}$, exploits this feature and is mainly distorted by the Higgs transverse momentum. The events where the Higgs is produced with one or more jets, the Higgs transverse momentum is high and weakens the sensitivity of $\Delta\phi_{ll}$ even further[16].

Fig.4.3 shows the same 2D correlations in the CS-frame as in Fig.4.2, but for a spin-2 UC and a pseudoscalar spin-0 hypothesis, which were generated from the EFT Lagrangians Eq.1.17 and Eq.1.20. Compared to the SM Higgs, there are clear differences in the lepton angular and momenta correlations. The spin-2 hypothesis mainly populates regions which are depleted for the SM in the angular phase spaces. The 0^- model looks similar to the SM hypothesis, but the momenta correlations are different.

In order to exploit the differences in correlations in Fig.4.2 and 4.3 we project the events in the 2D correlation plots on the two diagonals. For 2D ϕ correlation plot, for example, the first projection is defined as $\Delta\phi_{ll}^{cs} = \phi_{l^+}^{cs} - \phi_{l^-}^{cs}$ and the second projection we define as $\Sigma\phi_{ll}^{cs} = \phi_{l^+}^{cs} + \phi_{l^-}^{cs}$. The six projections have been plotted in Fig. 4.4 for the SM Higgs together with the 0^- and spin-2 UC hypotheses.

The complete four-vector of the Higgs particle is lost if taking into account that the neutrinos can not be measured in any detector, but only information like missing transverse energy is available. Determining the z component of the Higgs is a challenging task which will be explained in the next section.

4.3 Reconstruction of the Dineutrino System

The true four-momentum of the Higgs is calculated by using the four-momenta of the final state leptons and neutrinos:

$$p_H^2 = M_H^2 = (E_{ll} + E_{\nu\nu})^2 - (\vec{p}_{ll} + \vec{p}_{\nu\nu})^2 \tag{4.3}$$

where $E_{ll/\nu\nu}$ and $\vec{p}_{ll/\nu\nu}$ is the energy and momentum of the dilepton/dineutrino system. The energy and momentum of the leptons in this equation are known, because the leptons are fully reconstructed. For the neutrinos only the transverse components can be measured

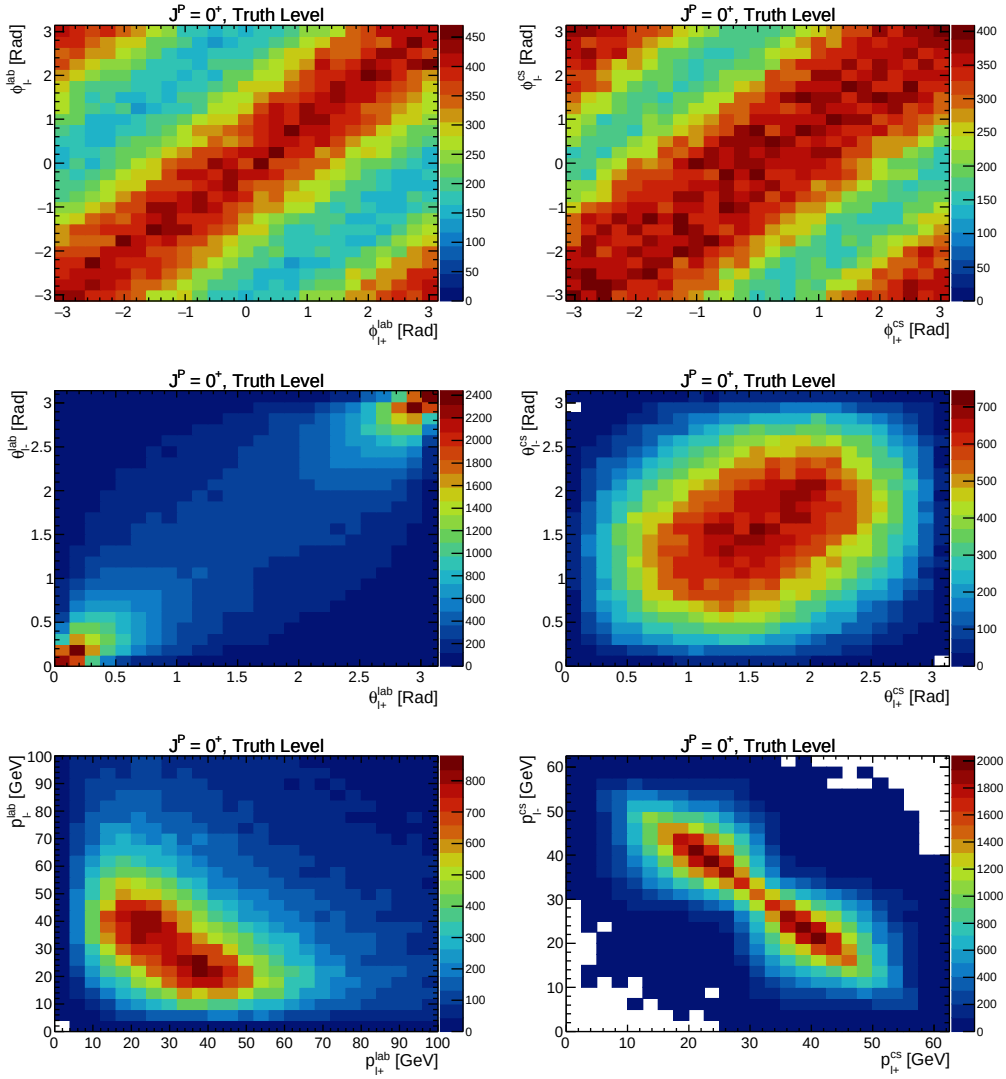

Figure 4.2: The 2D distributions of the charged lepton angular and momentum distributions defined in the lab-frame(left) and for the Collins-Soper frame(right). ϕ_{l^+} versus ϕ_{l^-} (top), θ_{l^+} versus θ_{l^-} (middle) and p_{l^+} versus p_{l^-} (bottom).

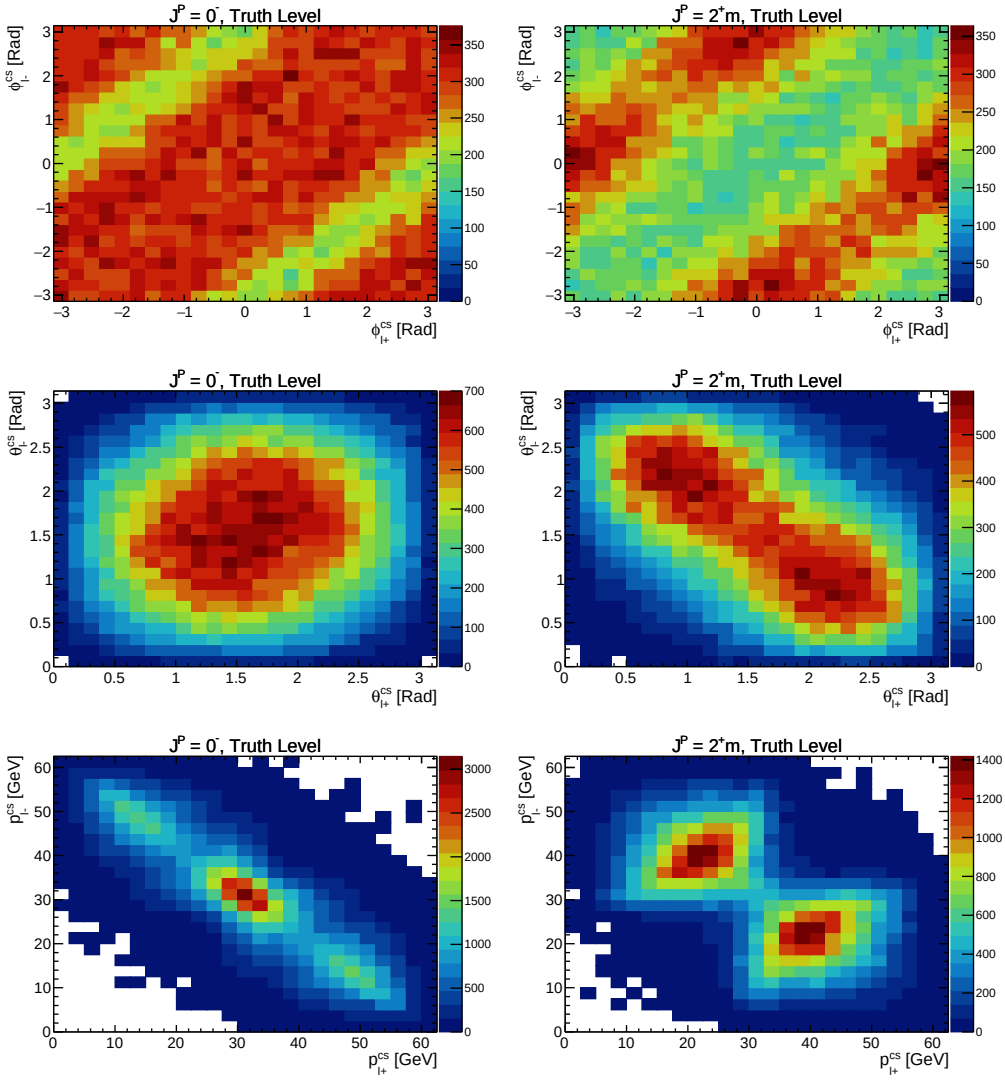

Figure 4.3: The 2D distributions of the charged lepton angular and momentum distributions for the 0^- hypothesis(left) and for the spin-2 UC hypothesis(right) defined in the Collins-Soper frame. ϕ_{l^+} versus ϕ_{l^-} (top), θ_{l^+} versus θ_{l^-} (middle) and p_{l^+} versus p_{l^-} (bottom).

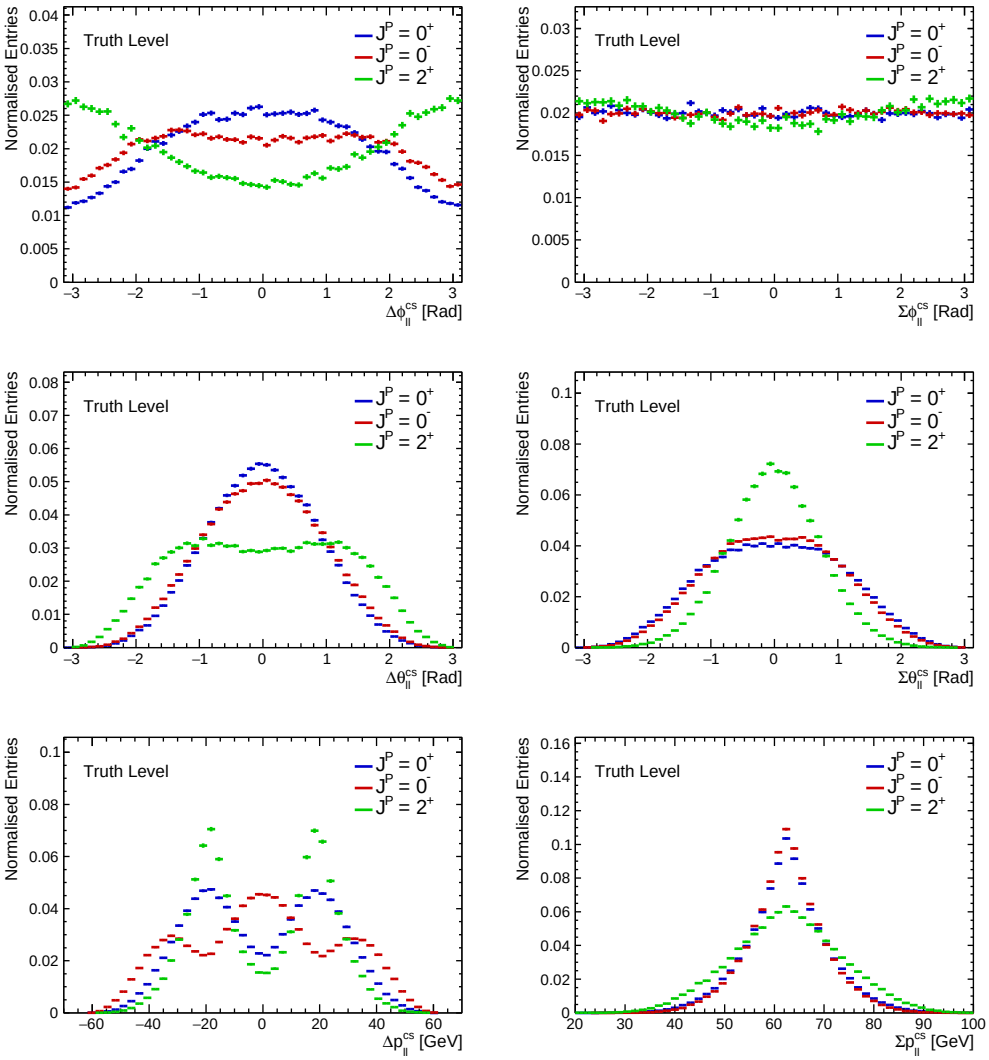

Figure 4.4: 1D projections on the diagonals of the 2D distributions of Fig. 4.2 and 4.3, but only for the variables in the CS-frame. The distributions on the left represent the projection of the difference and the distributions on the right represent the projection of the sum. The angular projections have been remapped to range from $-\pi$ to π.

as E_x^{miss} and E_y^{miss} and the total transverse energy as $E_T^{miss} = \sqrt{(E_x^{miss})^2 + (E_y^{miss})^2}$. The z component of the dineutrino system, $p_{\nu\nu,z}$, the total energy, $E_{\nu\nu}$ and therefore also the invariant mass, $M_{\nu\nu}$ are left as undetermined. With this information the $p_{H,x}$ and $p_{H,y}$ components are fixed, but in order to get the $p_{H,z}$ component, $p_{\nu\nu,z}$ has to be estimated. We do this by firstly rewriting equation 4.3:

$$M_H^2 = 2E_{ll}E_{\nu\nu} - 2\vec{p}_{ll} \cdot \vec{p}_{\nu\nu} + M_{ll}^2 + M_{\nu\nu}^2 \tag{4.4}$$

Replacing $E_{\nu\nu} = \sqrt{M_{\nu\nu}^2 + (E_T^{miss})^2 + (p_{\nu\nu,z})^2}$ and writing out the momenta in their components yields:

$$M_H^2 = 2E_{ll}\sqrt{M_{\nu\nu}^2 + (E_T^{miss})^2 + (p_{\nu\nu,z})^2} - 2p_{ll,x}E_x^{miss} - 2p_{ll,y}E_y^{miss} - 2p_{ll,z}p_{\nu\nu,z} + M_{ll}^2 + M_{\nu\nu}^2 \tag{4.5}$$

By imposing constraints on M_H and $M_{\nu\nu}$ the only unknown left in this equation is $p_{\nu\nu,z}$. M_H is fixed to 125 GeV, since the aim of this study to measure the properties of the discovered Higgs-like boson. The shape of the $M_{\nu\nu}$ can not be used, because an alternative spin hypothesis influences the $M_{\nu\nu}$ distribution in a different way than a spin-0 Higgs. Therefore $M_{\nu\nu}$ is fixed to the mean value of its distribution $M_{\nu\nu} = 30$ GeV, which is based on MC simulation studies[16]. Although this leads to a small bias in the reconstruction, it does not prefer a specific solution to equation 4.5.

The variables in Eq.4.5 that are known are combined into one expression, denoted as M_{fix}^2:

$$M_{fix}^2 = M_H^2 - M_{ll}^2 - M_{\nu\nu}^2 + 2p_{ll,x}E_x^{miss} + 2p_{ll,y}E_y^{miss} \tag{4.6}$$

Replacing the known variables in Eq.4.5 by M_{fix}^2, the equation can be rewritten as quadratic in $p_{\nu\nu,z}$:

$$0 = \overbrace{((p_{ll,z})^2 - E_{ll}^2)}^{\text{a}}(p_{\nu\nu,z})^2 + \overbrace{M_{fix}^2 p_{ll,z}}^{\text{b}} p_{\nu\nu,z} + \overbrace{\frac{1}{4}M_{fix}^4 - E_{ll}^2((E_T^{miss})^2 + M_{\nu\nu}^2)}^{\text{c}} \tag{4.7}$$

The two solutions to this formula are $(-b \pm \sqrt{\Delta})/(2a)$, where the determinant $\Delta = b^2 - 4ac$. The solutions can be either real, imaginary or coincide, corresponding to $\Delta > 0$, $\Delta < 0$ and $\Delta = 0$ respectively. For the cases where $\Delta = 0$ the solution for $p_{\nu\nu,z}$ is trivial and unique. For the other two cases the solutions for $p_{\nu\nu,z}$ are not trivial and special procedures are needed in order to get a unique solution.

Solutions for negative determinants

Imaginary solutions to Eq. 4.7 do not lead to valid values for $p_{\nu\nu,z}$. This happens when the values of the input parameters deviate from their true values, especially for the parameters $M_{\nu\nu}$ and M_H. $M_{\nu\nu}$ and M_H are fixed, so for events with negative determinant their values diverge too much from the true value. Based on MC simulation studies, events with negative determinant have always a $M_{\nu\nu} < 30$ GeV, so therefore Eq. 4.7 is solved again, but by setting $M_{\nu\nu}$ equal to zero. After this procedure the determinant becomes positive.

Solutions for positive determinants

A positive determinant leads to two distinct solutions for $p_{\nu\nu,z}$ and a specific method should decide which of the two solutions yields the best result, that is, closest to the true value of $p_{\nu\nu,z}$. In Ref. [16] this problem has been studied and it was shown that the solution that selects the smallest value of $|\cos\theta_{ll}^{cs,lab}|$ is preferable, where $\theta_{ll}^{cs,lab}$ is the angle of the dilepton system in the Higgs rest-frame with respect to the z^{lab} axis as in the left figure of Fig. 4.1.

4.3.1 Effect of Reconstruction

Having devised a method to construct the $p_{\nu\nu,z}$ component, the Higgs four-momentum can be determined for each event. Now we are able to use Eq. 4.2 to boost to the CS-frame and study the effects of the dineutrino $p_{\nu\nu,z}$ reconstruction on the angular and momentum distributions of the charged leptons. Variables that are constructed in the CS-frame having the dineutrino system reconstructed with the algorithm from the previous section, will be indicated with an asterisk sign, for example ${}^*\Delta\phi_{ll}^{cs}$.

Fig. 4.5 shows the effect of the dineutrino reconstruction algorithm on the θ^{cs} angles and p^{cs} momenta. Due to the constraints on the invariant mass of the neutrinos, $M_{\nu\nu}$, there are constraints on the allowed lepton momenta and θ angles. There is a depletion of events in the 2D θ^{cs} correlation plot which is visible as a large dip in the center of the ${}^*\Sigma\theta_{ll}^{cs}$ distribution. The constraint on the lepton momenta introduces a lower kinematic cutoff at ${}^*\Sigma p_{ll}^{cs} = 59$ GeV. These two projection variables are the most affected of all six projection variables. Nevertheless, the discrimination power to test several spin and CP hypotheses still remains.

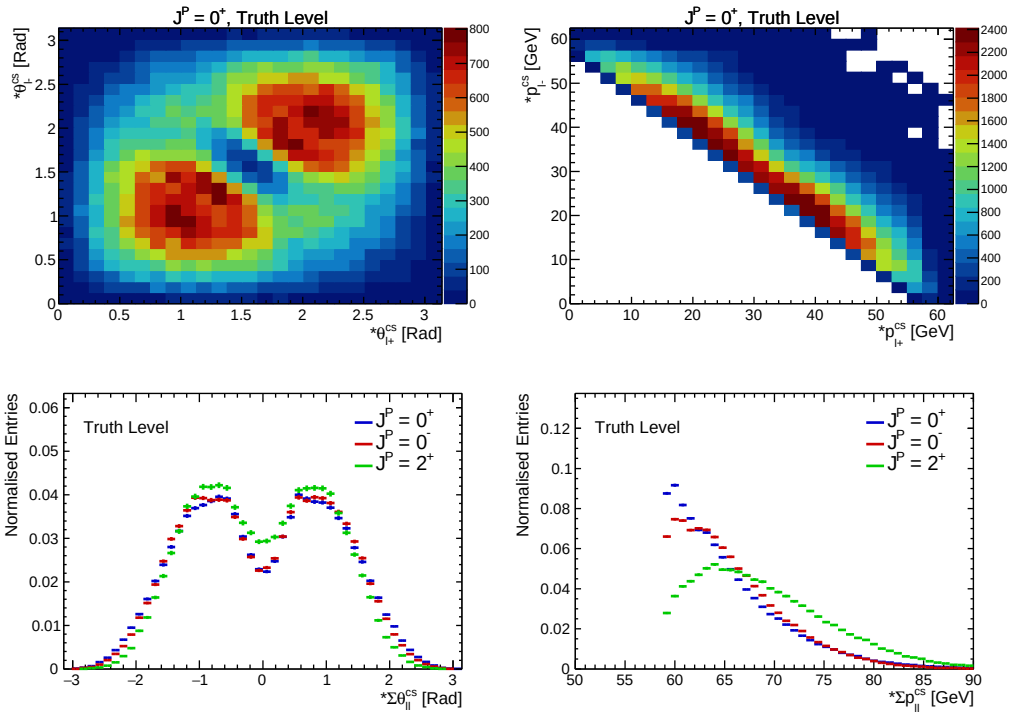

Figure 4.5: The dineutrino reconstruction algorithm puts constraints on the θ angle and the momenta of the charged leptons. The effects are clearly visible in the sum projections as a depletion around ${}^*\Sigma\theta^{cs}_{ll} = 0$ and a lower cutoff at ${}^*\Sigma p^{cs}_{ll} = 59$ GeV.

4.4 ATLAS Geometry and Acceptance

Up to this point, we have not taken into account the acceptance and the resolution effects of an experiment like the ATLAS detector. Therefore we will apply acceptance cuts in order to mimmic the ATLAS geometry and smear the missing transverse energy at Truth Level to include detector resolution effects. For the acceptance we reject events where the charged leptons have $|\eta| > 2.5$ and apply the preselection criteria from Table 5.3. The transverse momentum of the leptons is at least $p_T^{lep} > 15$ GeV and the invariant mass of the dilepton system $M_{ll} > 10$ GeV. The true value of E_T^{miss} is smeared to make it similar to the reconstructed E_T^{miss} distribution. We then require $E_T^{miss} > 20$ GeV for all events. We also reject events with two jets with $p_T^{jet} > 25$ GeV or more, so effectively creating a sample with events having zero or only one jet. We will refer to term "Reco Level" to indicate that acceptance cuts and E_T^{miss} smearing has been applied.

Due to the smearing of E_T^{miss}, about 10% of the events have a negative determinant when solving Eq. 4.7, even when setting $M_{\nu\nu}$ to zero. In order to obtain still real values for $p_{\nu\nu,z}$ the algorithm is slightly changed[16]. The $M_H = 125$ GeV constrained is dropped and instead the value for $p_{\nu\nu,z}$ is calculated that minimises the derivative of the Eq. 4.5 with respect to $p_{\nu\nu,z}$: $\partial M_H^2 / \partial p_{\nu\nu,z} = 0$. The solution for $p_{\nu\nu,z}$ is:

$$p_{\nu\nu,z} = p_{ll,z} \frac{\sqrt{(E_T^{miss})^2 + M_{\nu\nu}^2}}{\sqrt{E_{ll}^2 - (p_{ll,z})^2}} \tag{4.8}$$

The $M_{\nu\nu}$ value is fixed to 0 in this formula and is only shown for completeness.

Fig. 4.6 shows the 6 projections of Fig. 4.4 using the dineutrino reconstruction algorithm, including E_T^{miss} smearing, the ATLAS acceptance and the preselection criteria from Table 5.3. The discriminating features can be clearly observed and the variables are good to use for studying spin and CP. The little bump at ${}^*\Sigma\theta_{ll}^{cs} = 0$ is due to the events where Eq. 4.7 had no real solutions and Eq. 4.8 is used instead. The two peaks visible in the ${}^*\Sigma p_{ll}^{cs}$ distribution for SM and 0^- models is when switching the $M_{\nu\nu}$ constraint from 30 GeV to 0 GeV to obtain real solutions for Eq. 4.7.

4.4.1 Resolutions

Fig. 4.7 shows the performance of the dineutrino reconstruction algorithm at Truth Level and Reco Level in terms of resolutions. The θ and momenta sum and difference variables have a good resolution even after the E_T^{miss} smearing. The sum projection ${}^*\Sigma\phi_{ll}^{cs}$ is spread over a large range.

4.5 Summary

In this chapter we expressed the needs for a proper defined rest-frame in order to optimally measure the Higgs spin and CP properties. The Colin-Soper frame fits these criteria and is used as reference frame. In order to boost to this frame, the z component of the dineutrino is reconstructed with a dedicated reconstruction algorithm described in the previous sections. When having applied the boost to the Higgs rest-frame, the kinematic distributions of the charged leptons are shown for the different spin/CP hypotheses. The effects of the reconstruction algorithm on these distributions were discussed in detail. An alternative spin/CP hypothesis induces changes in the (di)lepton kinematic distributions and are used to measure the spin and CP of the Higgs boson.

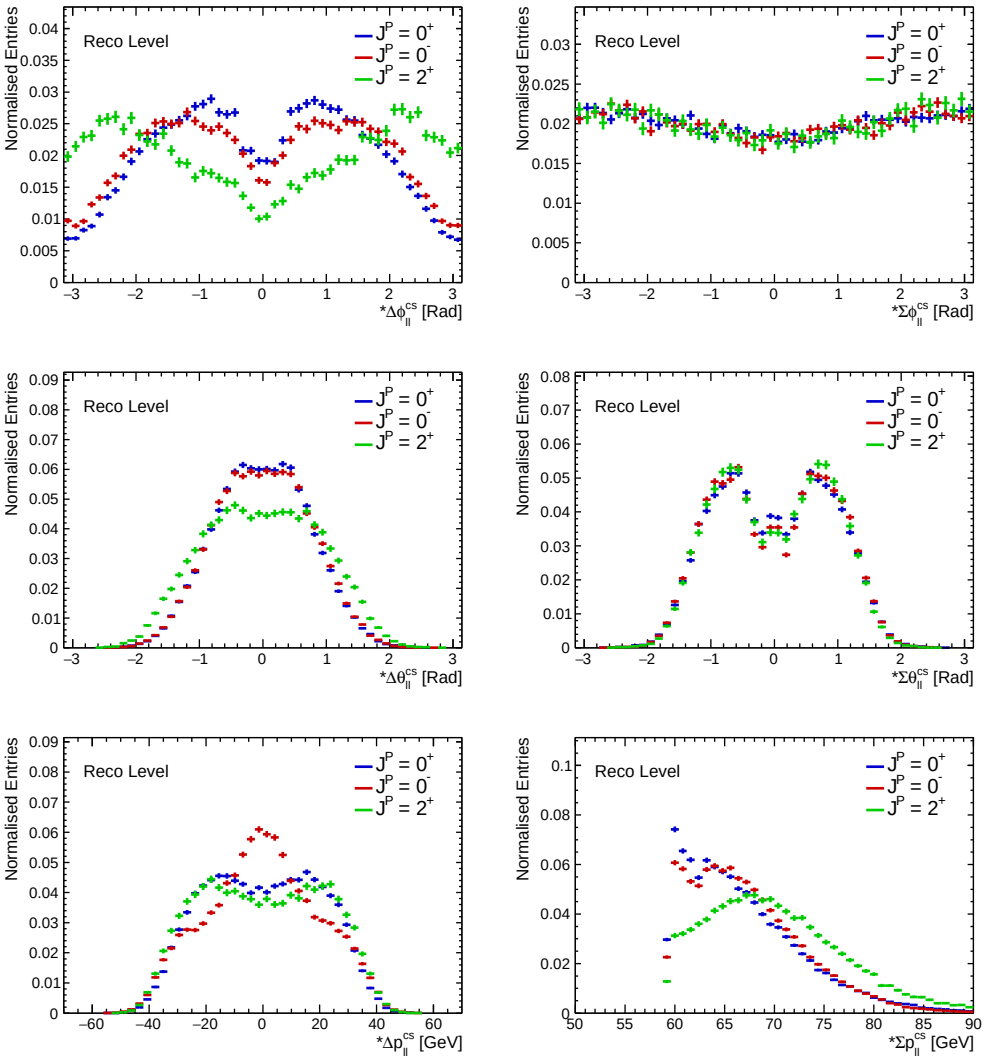

Figure 4.6: Variables with smeared missing energy, ATLAS geometry acceptance constraints and the preselection criteria from Table 5.3. See text for details.

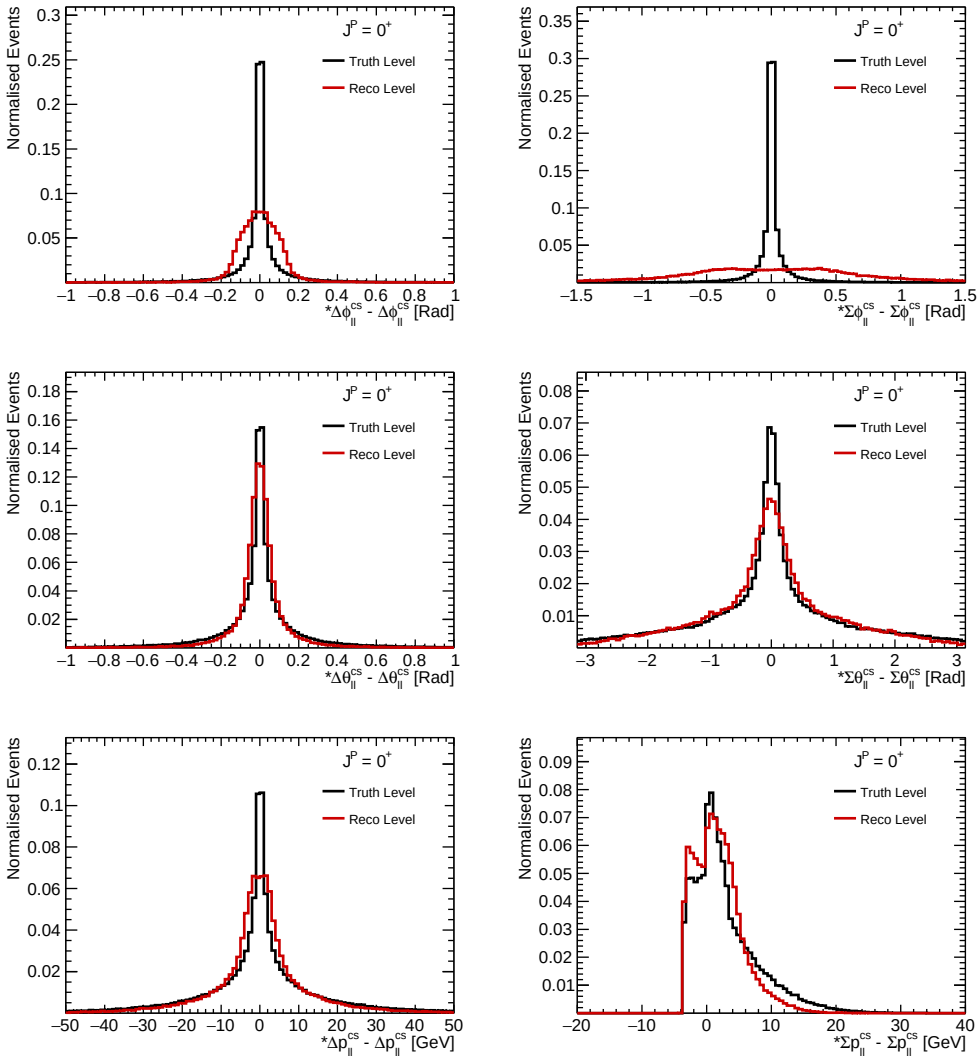

Figure 4.7: Resolution of the sum and difference kinematical variables for the Truth Level and Reco Level using the same events.

Event Selection

5

In chapter 4 we discussed the kinematic variables defined in the Higgs rest-frame that are sensitive to the spin and CP of the Higgs boson. These variables will be used as input for the spin/CP analysis, which is the topic of the next chapter. But before the analysis can start, we need to prepare the data sample in order to improve the signal sensitivity over the background. Only when the background is properly modelled, we get an accurate estimate of how the signal changes the yield and shape of the spin/CP sensitive variables. This will be the main part of this chapter.

Firstly, we discuss the processes that contribute to the background of the Higgs decay to W bosons and how to model them with MC simulations. Secondly, we introduce selection requirements, also known as cuts, to increase the spin and CP sensitivity of the signal compared to the background. Thirdly, a method is introduced to improve the resolution of the Higgs transverse momentum and thereby improves the dineutrino reconstruction algorithm from 4.3. After applying all the selection requirements (see chapter 6 in Ref. [16]), we create six kinematic variables in a signal enriched sample, known as signal region (SR). Lastly, we will show how to determine an accurate estimate of the yield of the dominant backgrounds inside the signal region by means of dedicated background control regions (CR).

5.1 Backgrounds

The final state of $H \to WW \to e\nu_e \mu\nu_\mu$ will lead to events in the ATLAS detector with an electron, a muon and missing transverse energy E_T^{miss}. The object definition and identification criteria has been discussed in chapter 2. The final state may also include in addition one or more jets, when an event passes the jet selection criteria. There are multiple SM processes that can mimic the signal final state, because they have the same final state particles or some of the particles are misidentified. The most dominant backgrounds with non-negligible contributions to the signal for the 0-jet and 1-jet categories are stated below:

- WW coming from SM processes other than Higgs decay forms an almost irreducible background to the signal, because it has an identical final state. Only differences in the invariant mass of the WW system and different shapes in the final state kinematics due to the W boson helicity configurations can help to distinguish this background from signal.

- $Z \rightarrow \tau\tau$ is the dominant Drell-Yan (DY) background process, where a Z boson or virtual photon γ^* decays to a pair of τ leptons. The subsequent decays of the τ leptons leads to E_T^{miss} and, possibly, an electron and a muon, so mimicking the signal final state. DY decays into a pair of electrons or muons, where one of the final state leptons is misidentified respectively as a muon or electron, form a smaller contribution to this background.

- **Top** background coming from top quark pair ($t\bar{t}$) or single top production. A top quark decays mainly into a W boson and a b quark, so $t\bar{t}$ production can lead to final states with two leptons, E_T^{miss} and two b-jets. Single top production has E_T^{miss}, two leptons and one b-jet (Wt channel) or a jet is misidentified as a lepton (single t channel). Due to the presence of jets in these final states, the top quark background is mainly present in the 1-jet category.

- **W+jets** background leads to a final state with a lepton and E_T^{miss}, when the W decays leptonically, and a particle inside the jet is identified as a muon or electron. Also the QCD multijet background, where more than one jet is misidentified as a lepton, is included in the W+jets sample.

- **Other VV** is the remaining category of non-WW decays: $W\gamma^*$, $Z\gamma^*$, WZ^*, and ZZ^*. For $W\gamma^*$ the virtual photon is converted to a lepton pair, but one conversion lepton is measured and oppositely flavoured to the lepton from the W decay. For the $Z\gamma^*$ process this is also the case, but one of the leptons from the Z decay escapes detection. This process is rare and forms a tiny contribution to the other VV background. Finally, there are contributions from WZ^* and ZZ^* processes, where at least one lepton escapes detection and causes E_T^{miss}.

The $e\nu\mu\nu$ channel is the most sensitive channel of the leptonic decays channels of the W bosons[79]. The same flavour channels $e\nu e\nu$ and $\mu\nu\mu\nu$ have large backgrounds that can not be removed without greatly reducing the sensitivity to the spin and CP models[102]. Also the 2-jet and higher jet multiplicities are excluded from this analysis, due to the increasing complexity to deal with the final state topology. In addition, the presence of VBF Higgs in the 2-jet final state has consequences for the use of the EFT Lagrangian in Eq. 1.17 as was pointed out in Ref. [103]. The contribution of VBF Higgs in the 1-jet category turned out to be negligible and we therefore attribute the signal in the 0-jet and 1-jet categories only to the ggF Higgs production process.

5.2 Data and MC Simulation Samples

The basis of an analysis is to start with a precise modelling of the signal and background. For that purpose dedicated MC generators were used to model the signal and backgrounds necessary for the spin/CP analysis in the $H \to WW \to e\nu_e \mu\nu_\mu$ channel. In chapter 3 we introduced the type of generators that are used and which part of the phenomenology of the pp collision they can describe. Here we only shortly motivate which generators were used for the signal and background samples mentioned in the previous section. A detailed study on signal and background modelling using dedicated MC generators can be found in Ref. [79].

5.2.1 Data at $\sqrt{s} = 8$ TeV

For the spin/CP analysis in the $H \to WW \to e\nu_e \mu\nu_\mu$ channel data from proton-proton collisions at $\sqrt{s} = 8$ TeV was collected during the 2012 LHC run with the ATLAS detector. The total data set corresponds to an integrated luminosity of 20.3 fb^{-1}. The events that were recorded relied on triggers which required either a single high-p_T lepton or two leptons (See section 2.4.6). The threshold for the single lepton trigger was set on $p_T > 24$ GeV, both for electrons and muons. The dilepton trigger was set on $p_T > 8$ GeV for the muon and $p_T > 12$ GeV for the electron. With these requirements the trigger efficiencies for the signal events are 95% for events with a leading electron and a subleading muon and 81% for events with a leading muon and a subleading electron[79]. The efficiencies are for events without jets, but the efficiencies are slightly larger for events with one additional jet. Also data quality requirements have been imposed on the events in order to reject events where the relevant components of the detector were not operating properly.

5.2.2 Background MC

Table 5.1 shows the backgrounds that have been modelled and the generator choice for that particular purpose. Also the cross-section time branching ratio $\sigma \cdot B$ is indicated for each process calculated at $\sqrt{s} = 8$ TeV. In the calculation the $t \to Wb$, $W \to l\nu$ and $Z \to ll$ were included. The l represents the e, μ and τ leptons and the γ^* indicates processes, where the photon is not on-shell. Most samples have one generator calculating the matrix element of the hard process, while the showering, hadronisation and underlying event are modelled with another generator. POWHEG[93] includes NLO corrections in α_s. ALPGEN[91] and SHERPA[82] can provide better description up till five extra partons when higher multiplicities become important. ACERMC[104] and GG2VV[105] are LO generators and only used for a few cases. PYTHIA6[87], PYTHIA8[88], HERWIG[89] or SHERPA[82] are used

to match the matrix-element with the parton shower model, to perform the hadronisation and simulate the underlying event. HERWIG is combined with JIMMY[90] to model the underlying event. The PDF sets used are taken from CT10[86] for the POWHEG, SHERPA and GG2VV samples and the CTEQ6L1[106] PDF sets were used for the ALPGEN, HERWIG, ACERMC, PYTHIA6 and PYTHIA8 samples. Only the $Z\gamma^*$ DY sample uses a different PDF set, namely MRST PDF set[107]. Pile-up was modelled with PYTHIA8 and the ATLAS detector response is simulated with GEANT4[50, 108].

A MC generator that models a process at LO, can not give the most accurate prediction of the cross-section when it is known at NLO level. There exist dedicated programs that can calculate the cross-sections beyond LO and the last column of Table 5.1 displays the normalisation to the required order and which specific generator is used for the calculation. MCFM[109] is used for WW and some non-WW diboson production processes, TOP++2.0[110] for the Top background and DYNNLO[111] for the Drell-Yan backgrounds.

The non-WW diboson processes are generated using filters, which selects a specific phase space that mimics final state of the $H \to WW \to e\nu_e\mu\nu_\mu$ channel. These filters are introduced to optimise the modelling in the different regions of phase space of the diboson processes and are indicated in the "Filter" column in Table 5.1. Some of the diboson processes are separately generated for different phase space regions and are merged together to one full sample later on. Overlapping regions are then removed from one of the subsamples so the full sample has no overlap.

The W+jets and the multijet background do not have dedicated MC generators, but instead use a data-driven method to get a better estimation. This will be discussed in section 5.6.5.

5.2.3 Signal MC

The signal samples mentioned in Table 5.1 are the SM Higgs, models where the Higgs is a spin-2 or a non-SM spin-0 particle and models where the SM Higgs interferes with a BSM spin-0 resonance. The SM Higgs is modelled with POWHEG and the parton showering/hadronisation is performed with PYTHIA8. The Higgs mass is set at $M_H = 125$ GeV and the used PDF set is CT10. The cross-section is calculated with NNLO accuracy and NNLL QCD corrections and NLO EW corrections have been applied. The cross-section times branching ratio $\sigma \cdot B = 0.435$ pb and the SM Higgs sample has been normalised to this value. Furthermore, the p_T^H distribution of the SM Higgs sample has been reweighted to the prediction given by the HRES2.1 program[113, 114]. It calculates at the NNLO+NNLL level and gives a more precise description of the p_T^H distribution than the one generated and modelled with POWHEG.

The other signal samples have been generated with the MADGRAPH5_AMC@NLO generator using the Higgs characterisation model and showered with PYTHIA6 using the CTEQ6L1

Category	MC Generator	Filter	$\sigma \cdot B$(pb)	Normalisation
Signal Samples				(POWHEG)
SM $H \to WW^*$	POWHEG+PYTHIA8		0.435	NNLO+NNLL
$J^P = 2^+$ UC	MADGRAPH5_aMC@NLO+PYTHIA6		-	(to SM sample)
$J^P = 0^-$	MADGRAPH5_aMC@NLO+PYTHIA6		-	(to SM sample)
Background Samples				
WW				
$q\bar{q} \to WW$ and $qg \to WW$	POWHEG+PYTHIA6		5.68	NLO (MCFM)
$gg \to WW$	GG2VV+HERWIG		0.196	LO (GG2VV)
Drell-Yan				
Z/γ^*	ALPGEN+HERWIG	$M_{ll} > 10$ GeV	16500	NNLO (DYNNLO)
Top				(TOP++2.0)
$t\bar{t}$	POWHEG+PYTHIA6		26.60	NNLO+NNLL
Wt	POWHEG+PYTHIA6		2.35	NNLL
$tq\bar{b}$	ACERMC+PYTHIA6		28.40	idem.
$t\bar{b}$	POWHEG+PYTHIA6		1.82	idem.
Other VV				
$W\gamma$	ALPGEN+HERWIG	$p_T^\gamma > 8$ GeV $\Delta R(\gamma, l) > 0.25$	369	NLO (MCFM)
$W\gamma^*$	SHERPA	$M_{ll} \leq 7$ GeV, $N_{lep} = 2$ $p_T^l > 5$ GeV, $\lvert\eta_l\rvert < 3$	12.2	NLO (MCFM) LO (SHERPA)
WZ	POWHEG+PYTHIA8	$M_{ll} > 7$ GeV	12.7	NLO (POWHEG)
$Z\gamma$	SHERPA	$p_T^\gamma > 8$ GeV, $\Delta R(\gamma, l) > 0.1$ $M_{ll} > 10$ GeV	163	NLO (MCFM)
$Z\gamma^*$	SHERPA	$M_{ll} \leq 4$ GeV $M_{ll} > 4$ GeV	7.31	NLO (MCFM)
ZZ	POWHEG+PYTHIA8	$M_{ll} \leq 4$ GeV	0.773	LO (SHERPA)
$ZZ \to ll\nu\nu$	POWHEG+PYTHIA8	$M_{ll} \leq 4$ GeV	0.504	idem.

TABLE 5.1: Summary of the MC samples used to model the signal and background processes. The $\sqrt{s} = 8$ TeV cross-sections times branching fraction, $\sigma \cdot B$ are also indicated. The decays of $t \to Wb$, $W \to l\nu$ and $Z \to ll$ are included in the calculation. For these decay processes l refers to e, μ or τ leptons. Table is reproduced from Ref. [112].

PDF set. The spin-2 UC and 0^- hypotheses have already been discussed in great detail chapters 3 and 4. The exact choice for the κ and Λ settings will be discussed in section 6.1 of the next chapter. We will also then introduce models with a BSM CP-even spin-0 Higgs boson and SM interference models, where the SM Higgs interferes with a BSM spin-0 particle.

5.3 Event Selection

The MC generators simulate the shape of the kinematic distributions of the signal and background processes. Based on the shape information we decide to apply selection criteria on data in order to remove background and improve the signal over background sensitivity. We first apply data quality cuts in order to remove events where relevant detector components were not operating properly. After that, another set of cuts, known as the preselection, will be applied to data sample. After the preselection, the sample will be split up into 0-jet and 1-jet categories and these will each have their own optimisation for the selection of the signal. These are the final selection criteria. All the selection requirements used for the preselection and final selection are presented in Table 5.3 and the motivation for each cut is discussed in the subsections below. We end this section with Table 5.4, known as cutflow table, where for each sample the amount of expected events is shown together with the observed events from data after applying each cut from the preselection and final selection for the signal region. Also the normalisation factors and event yields of the background CR are shown and will be discussed in section 5.6.

5.3.1 Object Selection and Quality Cuts

The definitions of the objects occurring in an event and their reconstruction performance are explained in detail in section 2.4. Here we will present and explain the requirements of the objects used as input for the analysis.

Primary Vertex

The primary vertex for each event should have at least three tracks with $p_T \geq 400$ MeV. The selected primary vertex (out of the many vertices in an event) is the one vertex with the highest $\sum p_T^2$ of its associated tracks.

Leptons

For the analysis electrons within 10 GeV $< E_T <$ 25 GeV must satisfy the *tight*++ requirement[62], which reduces the backgrounds from light flavour jets and photon conversion. The region $E_T >$ 25 GeV uses the medium++ selection criterium for the leptons, because misidentification of background becomes less important. The muon selection uses only the CB muons reconstructed with the Chain-I algorithm. Both the muon and electron are required to have a $p_T >$ 15 GeV and a pseudorapidity of $|\eta| < 2.5$. Electrons that end up in the transition region ($1.37 < |\eta| < 1.52$) are removed from the event.

Furthermore, the electrons and muons are required to originate from the primary vertex and should be isolated objects. The first requirement is obtained by cutting on the longitudinal and transverse impact parameters z_0 and d_0 respectively. The transverse impact parameter is the distance d_0 of the lepton track with respect to the primary vertex in the transverse plane. This distance is then divided by its estimated uncertainty σ_{d_0}. Both the electron and muon have to fulfil $|d_0/\sigma_{d_0}| < 3.0$. The longitudinal impact parameter z_0 is measured along the z axis and the cut applied on $|z_0 \sin(\theta)|$. More forward tracks have longer projections on the z axis, so hence the *sin* in the formula. Electrons have to fulfil $|z_0 \sin(\theta)| < 0.4$ mm and muons $|z_0 \sin(\theta)| < 1.0$ mm.

The second criterium, the isolation, is obtained by comparing the lepton energy and track momentum with respect to the total energy and track momentum in a cluster around the lepton. The track isolation takes the scalar sum of all momenta $\sum p_T$ in a cone of $\Delta R = 0.3$ in $\eta - \phi$ space around the lepton, but excluding the lepton p_T itself. The tracks used in this sum are all required to come from the primary vertex and have $p_T >$ 400 MeV for electrons and $p_T >$ 1 GeV for muons. The ratio $\sum p_T / p_T$ is then used to determine the track isolation. The calorimeter isolation uses a similar variable: sum all energies $\sum E_T$ deposited in the electromagnetic and hadronic calorimeter in a cone of $\Delta R = 0.3$ around the electron or muon cluster, after removal of the electron or muon. The cells that are 0.125×0.175 in $\eta \times \phi$ around the barycentre of the electron are removed from the calculation, while all the cells within $\Delta R < 0.05$ of the muon are removed. Table 5.2 shows all the track and calorimeter isolation criteria used for different ranges in p_T of the muon and electron. Especially electrons and muons originating from jets tend to have higher $\sum p_T / p_T$ and $\sum E_T / E_T$ values.

Jets

Jets are reconstructed from energy clusters in the calorimeters by using the anti-k_T algorithm with a radius parameter $R = 0.4$[71]. Reconstructed jets are required to have $p_T >$ 25 GeV and a pseudorapidity cut of $|\eta| < 4.5$. The cut on transverse momentum is increased to $p_T >$ 30 GeV when the jet is in the forward region $2.4 < |\eta| < 4.5$ to become

p_T (GeV)	Track isolation $\sum p_T/p_T$	Calo isolation $\sum E_T/E_T$
Electrons		
$15-20$	< 0.08	< 0.24
> 20	< 0.10	< 0.28
Muons		
$15-20$	< 0.08	< 0.12
$20-25$	< 0.12	< 0.18
> 25	< 0.12	< 0.30

TABLE 5.2: Track and calorimeter isolation criteria for different ranges in p_T of the muon and electron candidates.

less sensitive to pile-up conditions. To reduce the jets coming from pile-up even more, a requirement is imposed on the jet vertex fraction JVF, which is defined as the ratio of the scalar momentum sum $\sum p_T$ of all the tracks within $\Delta R = 0.4$ of the jet axis and associated with the primary vertex compared to the total track momentum sum in the jet. A jet is removed from the event when the fraction is below 50%, JVF < 0.50[115]. Because there is no tracking in the forward region, the JVF cut can only be applied to jets with $|\eta| < 2.5$.

For the reconstruction of b-jets, all jets with a $p_T > 20$ GeV and within $|\eta| < 2.5$ acceptance are selected. These jets are subsequently fed to the MV1 algorithm[74], which is set at an operating point of 85%. The misidentification of jets from light flavour quarks as b-jet is then 10%.

Overlap Removal

After imposing all the impact and isolation requirements on the leptons and jets, it is still possible for an object to be in close proximity of another object. These overlapping objects are likely to originate from one object and therefore one of the objects is removed to end up with only one. The overlap removal procedure follows a couple of steps in the following order:

1. If there is a muon and an electron with $\Delta R < 0.1$, the electron is removed.
2. If there are two electrons with $\Delta R < 0.1$, the electron with the lowest E_T is removed.
3. If there is an electron and a jet with $\Delta R < 0.3$, the jet is removed.
4. If there is a muon and a jet with $\Delta R < 0.3$, the muon is removed.

Missing Energy/Momentum

Due to neutrinos escaping detection, we expect to see a momentum imbalance in the transverse plane for the signal $H \to WW \to e\nu_e \mu\nu_\mu$ process. The missing transverse momentum[116] is calculated as the negative vector sum of all the objects that are reconstructed and identified as leptons, photons and jets, and the remaining soft objects that have typically low p_T:

$$E_{x/y}^{miss} = -p_{x/y}^{e} - p_{x/y}^{\mu} + \sum_{jets,\gamma} -p_{x/y}^{calo} + \sum_{soft} -p_{x/y}^{calo} \tag{5.1}$$

The calorimeter has a large coverage in pseudorapidity and can therefore be used to estimate the amount of missing momentum from neutral particles escaping detection. For the calculation in Eq. 5.1 we use leptons selected by the analysis, photons and jets with $E_T > 20$ GeV and define energy clusters in the calorimeter not being assigned to leptons, photons or jets as soft objects. The energy of the reconstructed objects are calibrated with their own specific object calibration and also the soft objects are calibrated to the deposited energy cluster. The resulting missing momentum is denoted as E_T^{miss} and more commonly referred to as missing transverse energy.

Instead of extracting the soft component of Eq. 5.1 from the calorimeter, another method uses tracks from the inner detector for estimating the soft component. It takes the negative sum of all the tracks from the inner detector with $p_T > 0.5$ GeV and which originate from the primary vertex. Tracks that are associated with leptons, but not from jets, are omitted from the calculation. The resulting quantity is referred to as p_T^{miss}:

$$p_{x/y}^{miss} = -p_{x/y}^{e} - p_{x/y}^{\mu} + \sum_{jets,\gamma} -p_{x/y}^{calo} + \sum_{soft,jets} -p_{x/y}^{track} \tag{5.2}$$

5.3.2 Preselection

The first requirement for a candidate $H \to WW \to e\nu_e \mu\nu_\mu$ event is the presence of an electron and muon with opposite charge. To optimise the cuts on the lepton transverse momentum, different energy thresholds are set for the most energetic lepton, known as the leading lepton, and the less energetic subleading lepton. The cut of 15 GeV on the subleading lepton reduces the amount of fake leptons at the cost of cutting in the characteristic shoulder structure of the Δp_{ll}^{cs} for the 0^- model as can be seen when comparing the Δp_{ll}^{cs} distribution from Fig. 4.4 with the ${}^*\Delta p_{ll}^{cs}$ distributions from Fig. 4.6. The lower limit on M_{ll} is good at rejecting low mass DY events. Due to neutrinos in the final state, we expect a significant amount of missing transverse energy and we can either decide to put a lower limit on E_T^{miss} or p_T^{miss}. DY and W+jets backgrounds tend to have lower p_T^{miss} values compared to the signal p_T^{miss}. The difference is larger than when looking at the

Preselection			
Variable			Requirement
Quality Cuts		=	Dectector working properly
N_{lep}		=	2, $e\mu$, opposite sign
p_T^{lep} (leading)		>	22 GeV
p_T^{lep} (subleading)		>	15 GeV
M_{ll}		>	10 GeV
p_T^{miss}		>	20 GeV

0-jet Selection			1-jet Selection		
Variable		Requirement	Variable		Requirement
N_{jets}	=	0	N_{jets}	=	1
p_T^{ll}	>	20 GeV	b-veto	=	No b-jets with $p_T > 20$ GeV
M_{ll}	<	80 GeV	max M_T^l	>	50 GeV
$\Delta\phi_{ll}$	<	2.8	$M_{\tau\tau}$	<	$\lvert M_Z - 25\text{ GeV}\rvert$
M_T	>	62.5 GeV	M_{ll}	<	80 GeV
M_T	≤	150 GeV	$\Delta\phi_{ll}$	<	2.8
$(P_T^H$	<	125 or 300 GeV)	M_T	≤	150 GeV
			$(P_T^H$	<	125 or 300 GeV)

Table 5.3: Pre and final selection cuts to optimise the signal sensitivity over background $S/\sqrt{B}$. The brackets around the cut on p_T^H indicate that it is only applied when testing one of the NUC spin-2 models and the cutoff on the p_T^H is required.

E_T^{miss} variables. Therefore we apply a cut of $p_T^{miss} > 20$ GeV in order to reduce the DY and W+jets background without affecting the signal too much. All preselection cuts are listed at the top in Table 5.3.

5.3.3 0-jet Selection

After applying the preselection we split up the sample in a 0-jet and 1-jet category. To get the 0-jet sample, we apply a jet-veto cut removing all events with at least one object identified as a jet. This sample is dominated by the WW and $Z \to \tau\tau$ backgrounds, contributing 53% and 23% respectively to the total expected events. However, imposing only the jet-veto results in a signal contribution of less than 2%, which is not sensitive enough for spin and CP studies. The additional (final) cuts for this jet category are mainly focused to remove the WW and $Z \to \tau\tau$ backgrounds, without affecting too much the signal. A cut on the transverse momentum of the dilepton system p_T^{ll} and a cut on the opening angle

$\Delta\phi_{ll}$ are very effective in cutting away the WW and $Z \to \tau\tau$ backgrounds. The muon and electron are expected to be more anticollinear on average for these backgrounds, resulting in lower p_T^{ll} and larger $\Delta\phi_{ll}$. The last cut is on transverse mass M_T defined as Eq. 3.3 in section 3.3.3 and mainly rejects on the WW and top quark background as can be seen in Table 5.4.

The signal over background significance $S/\sqrt{B}$ is 2.3 when just imposing the jet-veto and is increased to 3.5 when applying the final 0-jet selection criteria. All 0-jet cuts are listed on the left in Table 5.3.

5.3.4 1-jet Selection

A 1-jet event has exactly one object identified as a jet. Events with more than one object identified as jet are removed from the analysis sample. The 1-jet category is dominated by more than 50% by top quark backgrounds after the preselection. Due to the expectation of one or more b-jets in the event a b-veto is applied to reduce the Top backgrounds. DY decay of $Z \to \tau\tau$ in combination with jets, forms the second largest background to the 1-jet category. The invariant mass of the τ pair, $m_{\tau\tau}$, is expected to be close to the Z boson mass resonance. The $m_{\tau\tau}$ variable is calculated with the use of the collinear approximation[117], which relies on the assumption that the visible decay products of the τ are collinear with the τ flight direction and that all the E_T^{miss} is coming from the neutrinos of the τ decays. The $m_{\tau\tau} < (M_Z - 25$ GeV) cut largely reduces the $Z \to \tau\tau$ background.

The remaining cuts are applied on the variables M_T^l, M_{ll}, $\Delta\phi_{ll}$ and M_T. M_T^l is a variable related to the transverse mass of the lepton:

$$M_T^l = \sqrt{2p_T^l \cdot E_T^{miss} \cdot (1 - \cos\Delta\phi_{l,E_T^{miss}})} \tag{5.3}$$

where the $\Delta\phi_{l,E_T^{miss}}$ is the transverse opening angle between the lepton and the missing transverse momentum. The DY and W+jets backgrounds have smaller transverse lepton masses compared to the signal so a lower limit is set on the highest M_T^l. M_{ll} and $\Delta\phi_{ll}$ are, as in the 0-jet category, good variables to reject WW and $Z \to \tau\tau$ backgrounds. Setting an upper limit on M_T removes WW and top quark backgrounds.

The significance of signal over background $S/\sqrt{B}$ after applying the 1-jet final selection criteria is 1.9 and all 1-jet cuts are listed on the right in Table 5.3.

	ggF [125 GeV]	WW	$WZ/ZZ/W\gamma$	$t\bar{t}$	Single Top	$Z \to \ell\ell + \gamma$/jets	$Z \to \tau\tau + \gamma$/jets	W+jets	Total Bkg.	Observed
Quality cuts	650.0 ± 3.3	10033.6 ± 13.6	3782.2 ± 19.3	59515.1 ± 28.8	5683.8 ± 7.2	1145.8 ± 59.5	17787.4 ± 53.2	18714.0 ± 46.8	116661.7 ± 100.0	111442
$p_T^{(sub)leading} > (15)22$ GeV	513.7 ± 2.9	9368.1 ± 13.2	2769.2 ± 16.1	55849.4 ± 27.9	5320.6 ± 6.8	349.1 ± 23.6	11523.9 ± 42.6	7218.4 ± 27.7	92398.7 ± 66.3	94686
Opposite sign leptons	513.1 ± 2.9	9335.5 ± 13.2	1385.0 ± 11.5	58309.4 ± 29.2	5524.7 ± 6.8	226.8 ± 23.0	11479.2 ± 42.5	4288.6 ± 21.6	90549.3 ± 63.3	90893
$M_{ll} > 10$ GeV	513.1 ± 2.9	9335.5 ± 13.2	1385.0 ± 11.5	58309.4 ± 29.2	5524.7 ± 6.8	226.8 ± 23.0	11479.2 ± 42.5	4267.0 ± 21.5	90527.6 ± 63.3	90893
$p_T^{miss} > 20$ GeV	423.2 ± 2.7	8553.9 ± 12.6	1074.4 ± 10.1	35368.4 ± 22.7	4078.6 ± 5.9	146.5 ± 19.7	7682.8 ± 35.6	1937.8 ± 13.2	58842.3 ± 51.4	60037
0j: $N_{jets} = 0$	249.8 ± 2.0	6436.2 ± 11.9	518.0 ± 7.3	769.3 ± 3.4	379.9 ± 1.9	84.3 ± 14.4	2836.8 ± 22.2	937.9 ± 8.0	11962.2 ± 31.2	12133
0j: $p_T^{ll} > 20$ GeV	235.3 ± 2.0	6155.1 ± 11.6	492.7 ± 7.1	737.3 ± 3.3	366.8 ± 1.9	65.5 ± 10.8	1562.3 ± 16.4	802.4 ± 7.0	10182.1 ± 25.2	10338
0j: $M_{ll} < 80$ GeV	230.7 ± 2.0	2859.3 ± 7.9	323.8 ± 5.9	240.5 ± 1.9	137.3 ± 1.3	45.4 ± 7.8	1398.8 ± 15.5	437.0 ± 5.6	5442.1 ± 20.9	5781
0j: $\Delta\phi_{ll} < 2.8$	217.7 ± 1.9	2794.6 ± 7.8	311.4 ± 5.8	235.4 ± 1.9	134.9 ± 1.2	31.7 ± 4.8	513.5 ± 9.1	365.6 ± 4.9	4387.1 ± 15.1	4730
0j: 62.5 GeV $< m_T \leq 150$ GeV	216.0 ± 1.9	2323.2 ± 7.1	294.7 ± 5.7	142.2 ± 1.5	81.8 ± 1.0	30.9 ± 4.8	512.4 ± 9.0	355.6 ± 4.8	3740.7 ± 14.6	4052
0j: $Z \to \tau\tau$ control region	19.3 ± 0.6	86.2 ± 1.3	18.2 ± 1.3	8.9 ± 0.4	4.0 ± 0.3	15.7 ± 6.2	1916.4 ± 18.5	128.2 ± 4.1	2177.6 ± 20.0	2198
0j: WW control region	4.6 ± 0.3	2182.4 ± 7.0	116.5 ± 3.3	286.1 ± 2.1	143.1 ± 1.2	14.0 ± 5.9	140.2 ± 4.9	277.8 ± 3.7	3160.1 ± 11.8	3170
1j: $N_{jets} = 1$	131.1 ± 1.5	2645.4 ± 7.2	425.6 ± 6.1	7673.0 ± 10.5	2106.5 ± 4.2	59.1 ± 13.4	4195.7 ± 24.7	720.5 ± 8.4	17825.7 ± 32.8	17888
1j: b-veto	113.6 ± 1.4	2310.6 ± 6.7	360.6 ± 5.6	1473.5 ± 4.6	504.2 ± 2.2	49.6 ± 12.4	3654.6 ± 22.8	580.6 ± 7.3	8933.7 ± 28.8	8947
1j: max $M_T^l > 50$ GeV	94.6 ± 1.3	2183.5 ± 6.5	318.3 ± 5.3	1414.3 ± 4.5	484.7 ± 2.2	39.1 ± 11.1	1552.2 ± 15.2	393.4 ± 5.5	6385.4 ± 21.9	6467
1j: $M_{\tau\tau} < \lvert M_Z - 25\text{ GeV}\rvert$	78.4 ± 1.1	1597.4 ± 5.6	233.7 ± 4.6	1005.1 ± 3.8	353.8 ± 1.8	18.8 ± 5.3	547.0 ± 9.4	236.6 ± 4.1	3992.4 ± 14.3	4067
1j: $M_{ll} < 80$ GeV	77.4 ± 1.1	805.1 ± 4.0	152.2 ± 3.8	465.5 ± 2.6	175.0 ± 1.4	12.1 ± 3.6	524.5 ± 9.2	145.5 ± 3.5	2279.9 ± 12.2	2370
1j: $\Delta\phi_{ll} < 2.8$	72.6 ± 1.1	768.0 ± 3.9	145.0 ± 3.7	451.2 ± 2.5	169.3 ± 1.3	6.2 ± 1.1	227.4 ± 5.9	127.9 ± 3.2	1894.9 ± 9.1	2014
1j: $M_T \leq 150$ GeV	71.8 ± 1.1	554.8 ± 3.3	131.4 ± 3.6	267.2 ± 1.9	103.4 ± 1.1	5.8 ± 1.0	227.1 ± 5.9	122.9 ± 3.1	1412.6 ± 8.6	1569
1j: $Z \to \tau\tau$ control region	14.8 ± 0.5	85.4 ± 1.3	20.7 ± 1.3	47.6 ± 0.8	15.6 ± 0.5	5.4 ± 3.3	938.3 ± 11.5	54.1 ± 2.7	1167.2 ± 12.5	1184
1j: WW control region	1.9 ± 0.2	1170.5 ± 4.8	130.4 ± 3.2	808.3 ± 3.4	262.0 ± 1.5	16.6 ± 8.7	81.0 ± 3.5	171.9 ± 3.0	2640.7 ± 12.0	2647
1j: Top control region	13.3 ± 0.5	292.0 ± 2.5	54.0 ± 2.2	5452.1 ± 8.9	1399.5 ± 3.3	3.9 ± 1.9	150.0 ± 5.2	88.1 ± 3.3	7439.6 ± 11.9	7422

Table 5.4: Cutflow showing the expected event yields for all the MC simulation samples and the events observed in data for each cut of the preselection, final 0-jet and final 1-jet selection criteria for the signal region (SR) as in Table 5.3 and the various background control regions (CR) as defined in Table 5.5. The backgrounds have been normalised according to Eq.5.12, except for the W+jets estimate which is determined by a data-driven method. The quoted uncertainties are statistical only.

5.4 Determination of the Higgs Transverse Momentum

Before we discuss the distributions of the kinematic variables in the Higgs rest-frame after the final selection, we will focus in this section on the resolution of the Higgs transverse momentum. We introduce two methods to reconstruct the p_T^H: the Calo-based method uses E_T^{miss} as in Eq.5.1; the Track-based method uses p_T^{miss} as in Eq.5.2. Both methods combine then the dilepton system with E_T^{miss} or p_T^{miss} to reconstruct the Higgs transverse momentum. The dineutrino reconstruction algorithm described in section 4.3 would benefit from a precise reconstruction of p_T^H. This can be achieved by merging the Calo- and Track-based methods into one Combined method. We will show that the Combined method yields a better resolution for p_T^H than the Calo- and Track-based methods separately.

For this study a MC sample was generated with POWHEG and showered with PYTHIA8 describing the production of a SM Higgs with a mass of 125 GeV at $\sqrt{s} = 8$ TeV. The showered events have then undergone the GEANT4 simulation, digitisation and event reconstruction steps to simulate the ATLAS response. The information of the Higgs transverse momentum was stored right after the parton showering step and is used to test the performance of the different p_T^H reconstruction methods.

5.4.1 Calo- and Track-based Method

The total transverse momentum of the Higgs boson is the vectorial sum of the transverse dilepton and dineutrino components:

$$\begin{pmatrix} p_x^H \\ p_y^H \end{pmatrix}_{tot} = \begin{pmatrix} p_x^{ll} \\ p_y^{ll} \end{pmatrix} + \begin{pmatrix} p_x^{\nu\nu} \\ p_y^{\nu\nu} \end{pmatrix} \tag{5.4}$$

For the Calo-based method the dineutrino vector is replaced by the missing transverse energy E_T^{miss} from Eq.5.1 scaled with a correction factor α_{calo}:

$$\begin{pmatrix} p_x^H \\ p_y^H \end{pmatrix}_{calo} = \begin{pmatrix} p_x^{ll} \\ p_y^{ll} \end{pmatrix} + \begin{pmatrix} E_x^{miss'} \\ E_y^{miss'} \end{pmatrix} \tag{5.5}$$

with

$$E_{x/y}^{miss'} = -p_{x/y}^{e} - p_{x/y}^{\mu} \quad + \sum_{jets,\gamma} -p_{x/y}^{calo} \quad + \alpha_{calo} \cdot \sum_{soft} -p_{x/y}^{calo} \tag{5.6}$$

Because the information from the calorimeter is fully calibrated, the scale factor $\alpha_{calo} = 1$ gives the best results in estimating the total p_T^H.

The Track-based method uses a corrected version of the p_T^{miss} from Eq.5.2 to get the p_T^H for the 0-jet events:

$$\begin{pmatrix} p_x^H \\ p_y^H \end{pmatrix}_{track,0j} = \begin{pmatrix} p_x^{ll} \\ p_y^{ll} \end{pmatrix} + \begin{pmatrix} p_x^{miss'} \\ p_y^{miss'} \end{pmatrix}_{0j} \tag{5.7}$$

with

$$p_{x/y}^{miss',0j} = -p_{x/y}^{e} - p_{x/y}^{\mu} + \sum_{\gamma} -p_{x/y}^{calo} + \alpha_{track}^{0j} \cdot \sum_{soft} -p_{x/y}^{track} \tag{5.8}$$

where α_{track}^{0j} is the factor to scale the track component of p_T^{miss} to get the total missing transverse momentum and is determined from MC simulation studies. For this thesis we found the best results when $\alpha_{track}^{0j} = 2.5$ for all values of p_T^{miss}. There is a slight rise in this scale factor when $p_T^{miss} > 60$ GeV, but this region has a large statistical uncertainty and therefore the deviation from 2.5 can be neglected.

For the 1-jet events the Track-based method needs some slight modifications with respect to the 0-jet events. The jet component is subtracted in order to scale the soft component and thereafter, the jet is added back again. The corrected p_T^{miss} for the 1-jet events has the following form:

$$\begin{aligned} p_{x/y}^{miss',1j} = & -p_{x/y}^{e} - p_{x/y}^{\mu} + \sum_{jets,\gamma} -p_{x/y}^{calo} \\ & + \alpha_{track}^{1j} \left(\sum_{soft,jets} -p_{x/y}^{track} + p_{x,y}^{jet} \right) - p_{x,y}^{jet} \end{aligned} \tag{5.9}$$

α_{track}^{1j} is the factor to scale the track component of p_T^{miss} for the 1-jet events. The Higgs transverse momentum for the 1-jet events is defined then as follows:

$$\begin{pmatrix} p_x^H \\ p_y^H \end{pmatrix}_{track,1j} = \begin{pmatrix} p_x^{ll} \\ p_y^{ll} \end{pmatrix} + \begin{pmatrix} p_x^{miss'} \\ p_y^{miss'} \end{pmatrix}_{1j} \tag{5.10}$$

From MC simulation studies $\alpha_{track}^{1j} = 2.2$ gave the best results in terms of shape and resolution.

Fig. 5.1 shows the p_T^H distributions reconstructed via the Calo-based and the Track-based methods, together with the p_T^H created from truth information. The sample used to make the distributions is the SM Higgs simulation sample. All the preselection and final selection cuts from Table 5.3 have been applied, except for the cuts on M_T and p_T^H. The size of the MC sample is 228k events for the 0-jet category and 79k events for the 1-jet category.

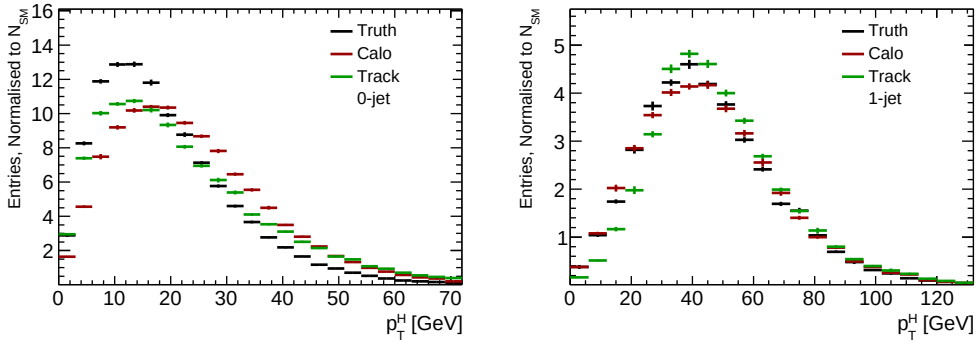

Figure 5.1: Higgs transverse momentum distributions from Truth level, from construction using the Calo-based method and from construction using the Track-based method. All the preselection and final selection cuts from Table 5.3 have been applied, except for the cuts on M_T and p_T^H.

5.4.2 Combined Method

The Calo-based and Track-based method can be merged to obtain a Combined method:

$$\begin{pmatrix} p_x^H \\ p_y^H \end{pmatrix}_{comb,0j/1j} = W \cdot \begin{pmatrix} p_x^H \\ p_y^H \end{pmatrix}_{calo} + (1-W) \cdot \begin{pmatrix} p_x^H \\ p_y^H \end{pmatrix}_{track,0j/1j} \tag{5.11}$$

Fig. 5.2 shows how the p_T^H distribution from the Combined method compares to the true p_T^H distribution when $W = 0.5$. Especially for the 0-jet category the Combined method resembles the truth better than the Calo-based and Track-based methods do in Fig. 5.1. In Fig. 5.3 the differences of the true p_T^H versus the reconstructed p_T^H per event for each method are plotted. It is clear that the Combined method leads to a smaller bias and an improved resolution for p_T^H for both the 0-jet and 1-jet categories. $W = 0.5$ gave the best results in terms of shape and resolution and will be used for the analysis.

The p_T^H from the Combined method will be only used as input for the dineutrino reconstruction algorithm. For the cut on p_T^H as stated in Table 5.3 the transverse momentum from the Track-based reconstructed Higgs in Eq. 5.7 is used. It turns out that for the NUC spin-2 models replacing the cut on the p_T^H from the Track-based Higgs by the same cuts on the p_T^H from the Combined method Higgs has a negligible effect on the event yields. Therefore, from here on, any reference to the cut on p_T^H for the NUC spin-2 models means the cut on the transverse momentum of the Track-based Higgs as in Eq. 5.7, unless stated otherwise.

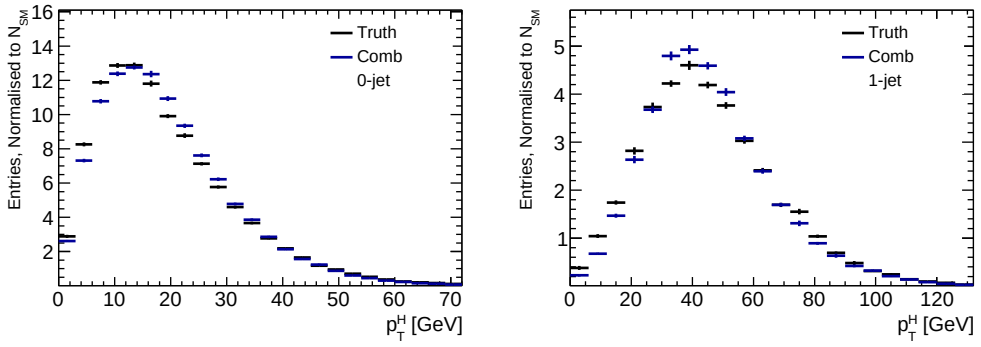

Figure 5.2: Higgs transverse momentum distributions comparing the p_T^H from the Combined method with the truth p_T^H.

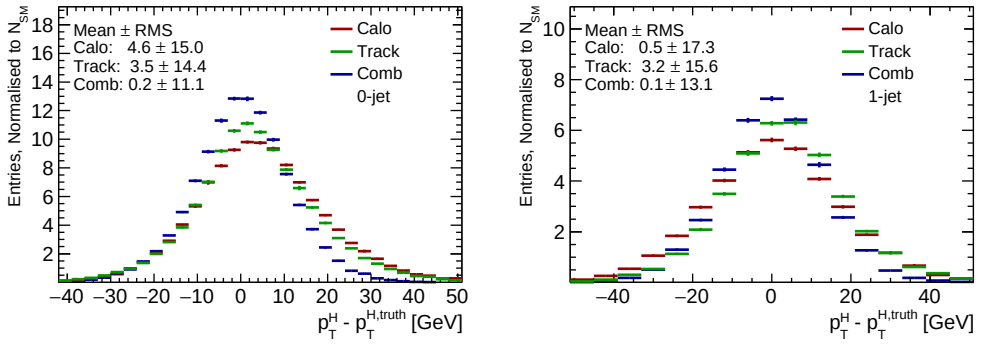

Figure 5.3: Resolution of the Higgs transverse momentum for the Calo-based, the Track-based and the Combined method.

5.5 Signal Region

In this section we will present the relevant distributions for the MC simulation and the data in the signal region. All the distributions are organised in the same way. The events from the simulated SM Higgs are indicated with red. Other colours represent the backgrounds, which were discussed in section 5.1. The background event yields have been normalised through dedicated CR, which will be discussed section 5.6. All the MC distributions are stacked to give a prediction for signal+background. The total statistical and systematic uncertainties are indicated by the shaded area. The observed data is represented by the black dots and black error bars. All the distributions are also accompanied by a ratio plot, where the observed data is divided by the total MC simulation. It serves as a diagnostic tool to check if the modelling of the signal+background expectation agrees with the data. The

yellow bands indicate the combined error of the statistical and systematic uncertainties, which will be discussed more in detail in section 6.4.

We will show the p_T^H distributions calculated with the methods described in section 5.4. The other variables used for the pre and final selection in Table 5.3 showed good agreement between MC simulation and the data and can be found in Ref. [112]. In the next section, for the signal and control regions we will show the distributions for the spin/CP sensitive variables (the projections as in Fig.4.4 and 4.6) for both the 0-jet and 1-jet categories.

5.5.1 p_T^H Distributions

Fig. 5.4 shows the p_T^H distributions for the 0-jet and 1-jet categories. It is immediately apparent that the WW background dominates both jet categories, followed by $Z \to \tau\tau$. The top quark background is mainly contributing to the 1-jet category as expected. The Calo-based method undershoots the data a bit around 10 GeV for the 0-jet category. The Combined method shows a good modelling of the 0-jet category, because the data and MC show good agreement over the whole p_T^H range. For the 1-jet category all the methods perform well and show good agreement in the more populated regions of the distribution. The tails have a lesser data/MC agreement, but there is a large statistical uncertainty in this area.

5.5.2 Spin and CP Sensitive Variables

Fig. 5.5 and Fig. 5.6 show the SR 0-jet and 1-jet category for the spin/CP sensitive variables in the Higgs rest-frame with the Collins-Soper orientation. There is an overall good agreement between data and MC simulation and no indication of mismodelling. These plots are good to use for the input for the actual spin/CP analysis which will be presented in chapter 6.

5.6 Background Estimation

Before finalising this chapter, we will discuss the method for estimating the background contribution to the SR by means of measurements in dedicated CRs. It has two main benefits: 1) By scaling to the SR from a measurement in the CR, the overall modelling of the background in the SR will be improved. 2) The uncertainty on the background yield in the SR can be reduced by using a CR with enough statistics. This second benefit improves the sensitivity of the spin/CP analysis.

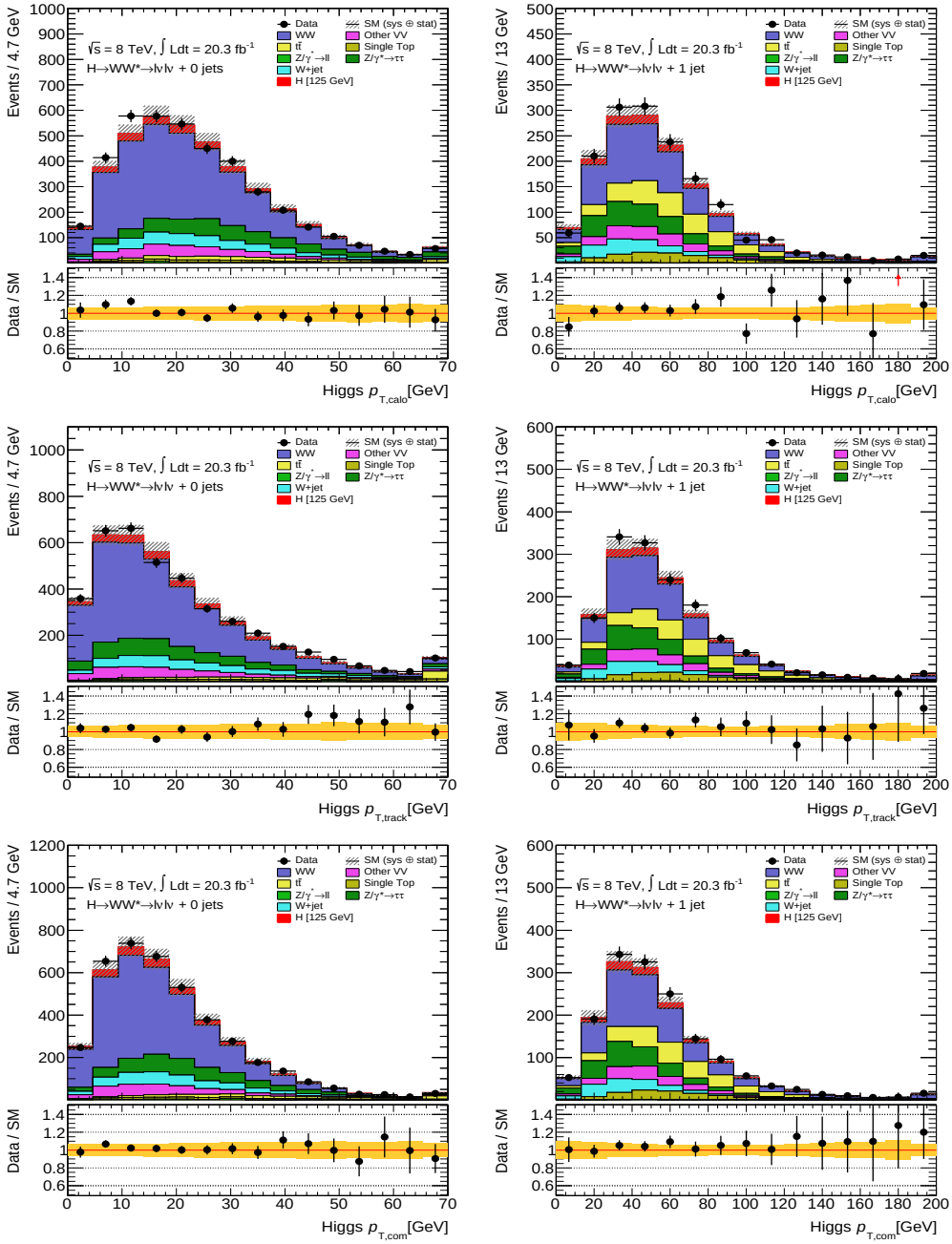

FIGURE 5.4: p_T^H distributions for the Calo-based method (top), the Track-based method (middle) and the Combined method (bottom) for the 0-jet (left) and 1-jet (right) categories in the SR.

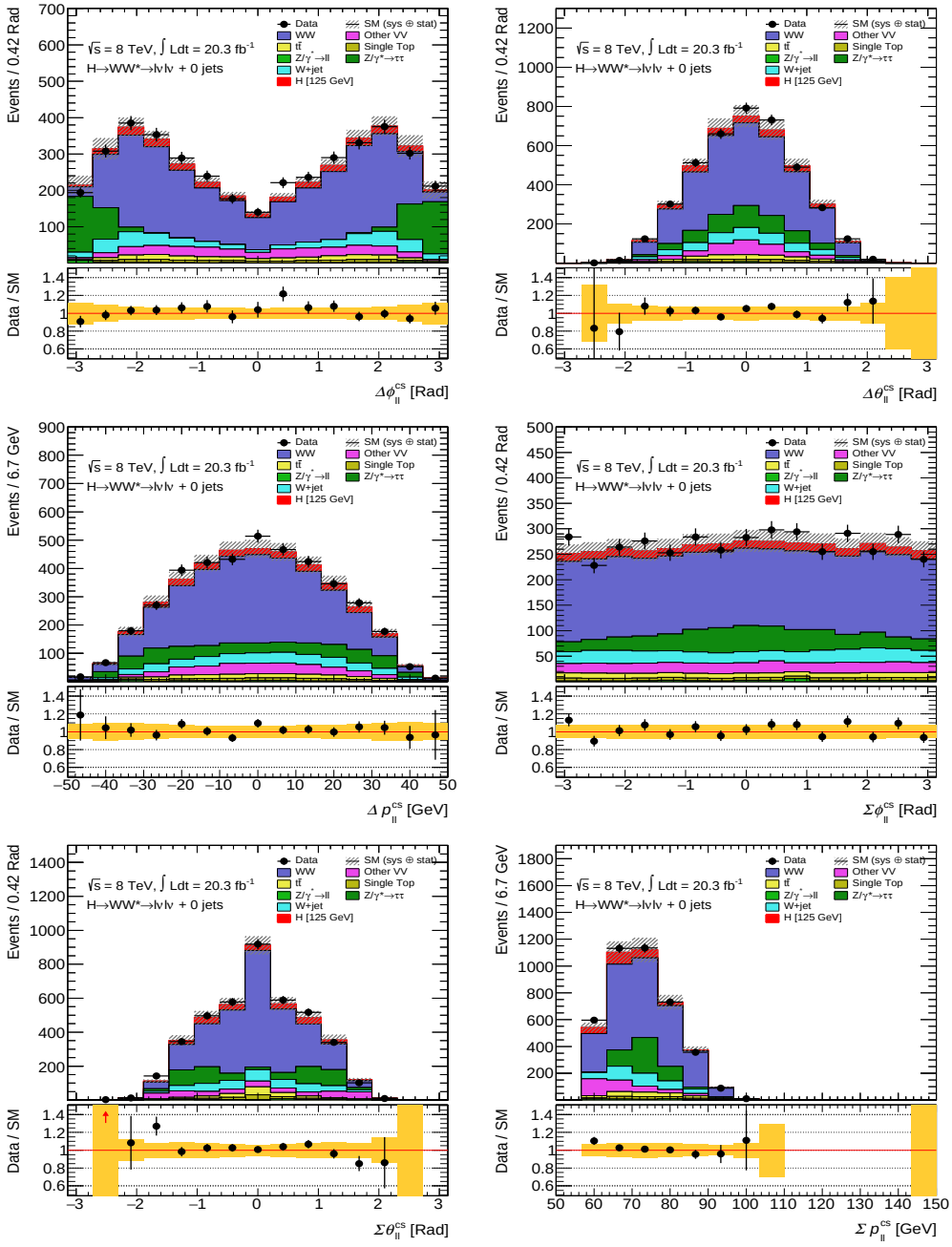

Figure 5.5: Spin/CP sensitive variables defined in Higgs rest-frame for the 0-jet SR. The superscript "CS" indicates that the Collins-Soper orientation is chosen for the rest-frame definition.

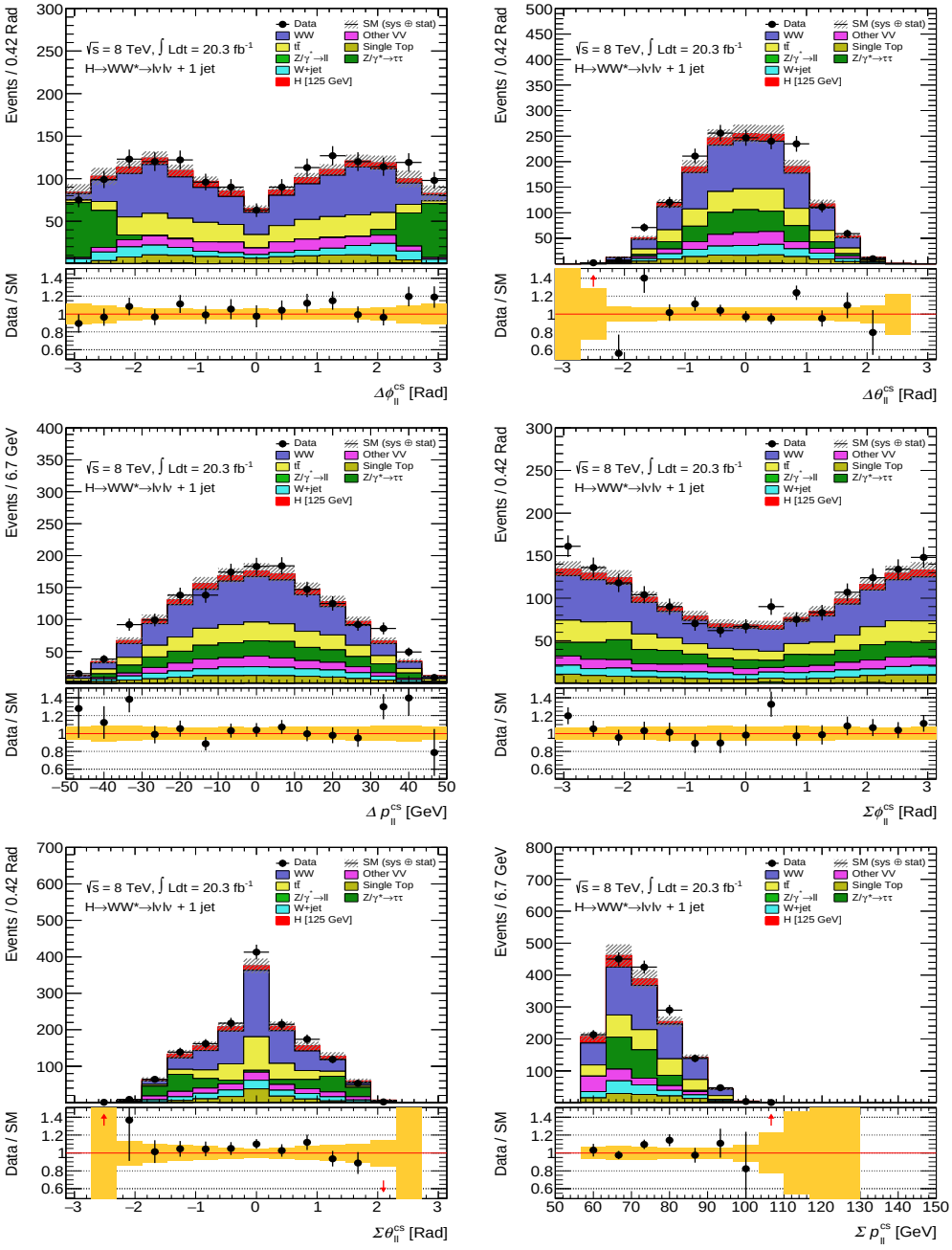

Figure 5.6: Spin/CP sensitive variables defined in Higgs rest-frame for the 1-jet SR. The superscript "CS" indicates that the Collins-Soper orientation is chosen for the rest-frame definition.

Control Region	Selection
WW CR 0-jet	Preselection, $p_T^{ll} > 20$ GeV and 80 GeV $< M_{ll} <$ 150 GeV
WW CR 1-jet	Preselection, b-veto, $M_{\tau\tau} < \lvert M_Z - 25\text{ GeV}\rvert$, $M_T^l > 50$ GeV and $M_{ll} > 80$ GeV
$Z \to \tau\tau$ CR 0-jet	Preselection, $M_{ll} < 80$ GeV and $\Delta\phi_{ll} > 2.8$
$Z \to \tau\tau$ CR 1-jet	Preselection, b-veto, $M_T^l > 50$ GeV, $M_{ll} < 80$ GeV and $M_{\tau\tau} < \lvert M_Z - 25\text{ GeV}\rvert$
Top CR 1-jet	Preselection, at least one b-jet and $M_{\tau\tau} < \lvert M_Z \rvert - 25$ GeV$\rvert$

Table 5.5: The various control regions and their specific selection criteria. The preselection is the same as in Table 5.3.

Each dedicated CR will have a specific set of selection criteria, which will make it orthogonal to the SR and optimal for a particular background. However, the criteria can not be too different from the SR selection in order to minimise the uncertainty on the extrapolation from the CR to the SR. This is achieved by maintaining the preselection criteria as in Table 5.3, but only inverting some of the cuts from the final selection. In Table 5.5 the specific selection criteria for each CR are shown and will be discussed in the following sections.

For each CR we will only show the $\Delta\phi_{ll}^{cs}$ and $\Delta\theta_{ll}^{cs}$ variables defined in the Higgs rest-frame to give a general overview. The other variables have similar performance in terms of modelling.

5.6.1 Extrapolation and Normalisation Factors

The expected background yield in the SR is estimated with the help of a CR:

$$B_{SR}^{cor} = B_{SR}^{ori} \cdot \underbrace{(N_{CR} - B_{CR}^{other})/B_{CR}}_{\text{normalisation } \beta} = (N_{CR} - B_{CR}^{other}) \cdot \underbrace{B_{SR}^{ori}/B_{CR}}_{\text{extrapolation } \alpha} \tag{5.12}$$

where B stands for the MC estimate of the events of a particular background and N_{CR} the observed events in the CR. B_{SR}^{ori} is the original expected event yield and B_{SR}^{cor} is the corrected event yield in the SR, while B_{CR}^{other} is the expected amount of other background processes in the CR and therefore needs to be subtracted from N_{CR}. The error on B_{SR}^{cor} is determined by the statistical error on N_{CR} and the theoretical error on α. With a large amount of statistics in the control region CR and and a large enough MC simulation sample, the errors on N_{CR} and α can be reduced and will then result in a significantly smaller error for B_{SR}^{cor} compared to B_{SR}^{ori}. In the tables that will follow from here on, we will only state the normalisation β.

5.6.2 WW Background

The WW 0-jet CR is obtained by applying all preselection cuts, the $p_T^{ll} > 20$ GeV cut and inverting the SR cut on M_{ll} to 80 GeV $< M_{ll} <$ 150 GeV. The WW background tends to have larger M_{ll} values compared to the Higgs signal. Fig. 5.7 shows the resulting distribution for the WW CR with a purity of 69% WW events. The normalisation β extracted for the 0-jet WW CR is 1.17 ± 0.03.

The WW 1-jet CR also uses all the preselection cuts and, additionally, the b-veto, $M_T^l > 50$ GeV and $M_{ll} > 80$ GeV from the final 1-jet selection criteria. The WW purity of the sample is 44.3% and the normalisation factor is 1.10 ± 0.05. From Fig.5.7 it is clearly visible that the $t\bar{t}$ events have the second largest contribution to WW CR and together with the single top background causes a 40% contamination. Therefore, a special extrapolation factor from the 1-jet Top CR to the WW CR is used in this analysis to accurately estimate the top quark contamination. Fig.5.7 also shows that the modelling of the WW MC sample has no significant problems for both the 0-jet and 1-jet categories. There were also extrapolation factors used from the $Z \to \tau\tau$ 0-jet and 1-jet CRs to the WW 0-jet and 1-jet CRs. However, the $Z \to \tau\tau$ contamination in the WW CR is for both jet categories below the 5% level and has little effect on the WW normalisation.

5.6.3 $Z \to \tau\tau$ Background

The $Z \to \tau\tau$ 0-jet CR uses all preselection cuts, the jet-veto and $M_{ll} < 80$ GeV criteria from the final 0-jet selection. Because the final leptons from the $Z \to \tau\tau$ decay have large opening angles, the related SR cut is inverted to $\Delta\phi > 2.8$. The 1-jet CR also uses all the preselection cuts, applies a b-veto, max $M_T^l > 50$ GeV and inverts the τ invariant mass cut to $|M_{\tau\tau} - M_Z| < 25$ GeV. The $Z \to \tau\tau$ purity is 88% and 80% in the 0-jet and 1-jet CRs respectively. The high purity of the CRs is clearly visible in Fig. 5.8. The $Z \to \tau\tau$ normalisation factors are 0.94 ± 0.05 and 1.08 ± 0.05 for the 0-jet and 1-jet categories. The bins with enough statistics indicate that there is a good modelling of the $Z \to \tau\tau$ sample.

5.6.4 Top Background

Top CR is only defined for the 1-jet events. All preselection cuts are used and there is the requirement of exactly one b-tagged jet. There are no second b-tagged jets with 20 GeV $< p_T <$ 25 GeV allowed in the event. From the 1-jet final selection criteria only the max $M_T^l > 50$ GeV and the $M_{\tau\tau} < |M_Z - 25\ \text{GeV}|$ cuts are applied. Fig. 5.9 shows the distributions for the 1-jet Top CR and it has a purity of 92%. The figure also indicates a

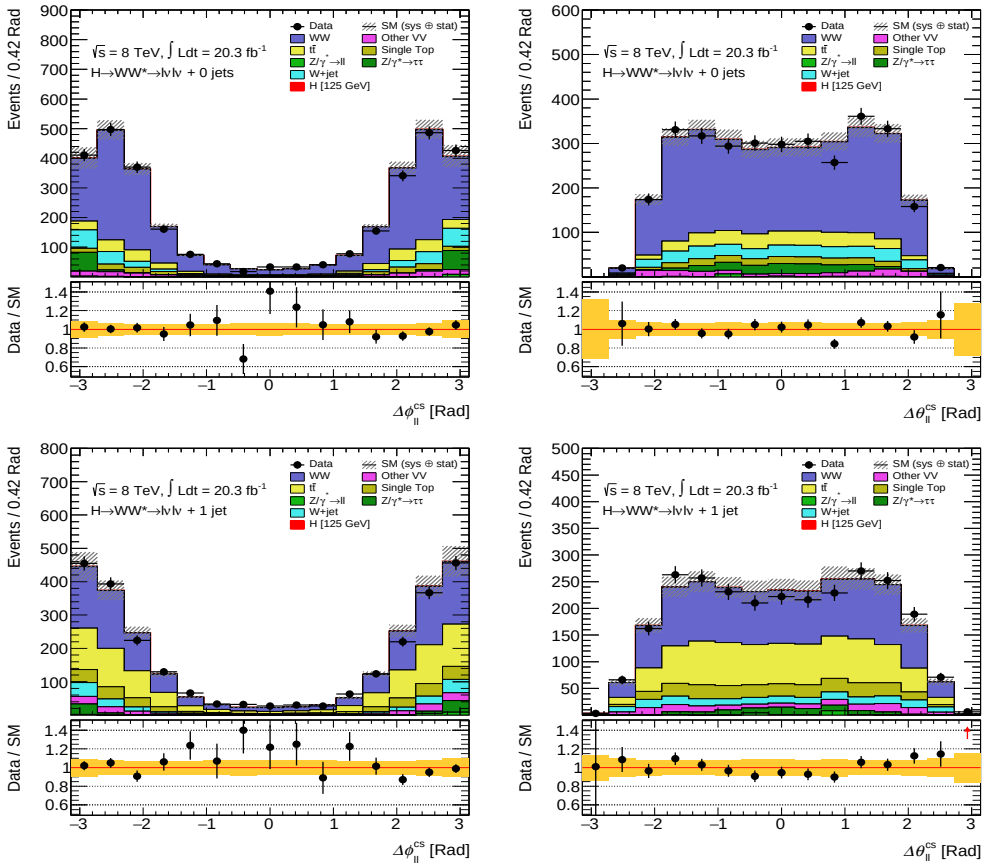

FIGURE 5.7: WW CR 0-jet (top) and 1-jet (bottom) categories.

good modelling of the top quark MC simulation compared to the observed data. The Top CR normalisation factor is 1.00 ± 0.04.

5.6.5 W+jets

The W+jets sample is the only background that uses a fully data-driven method to estimate its contribution, because it leads to better results than by normalising to the MC sample. The CR is obtained by requiring one of the leptons to satisfy all identification and isolation criteria as explained in section 5.3.1 and the other has to fail these criteria, but satisfies a looser selection criteria. These last leptons are marked as anti-identified and are for the W+jets background mostly originating from a jet that is misidentified as a lepton or contain a lepton coming from the decay of a heavy quark. The purity of the W+jets in the

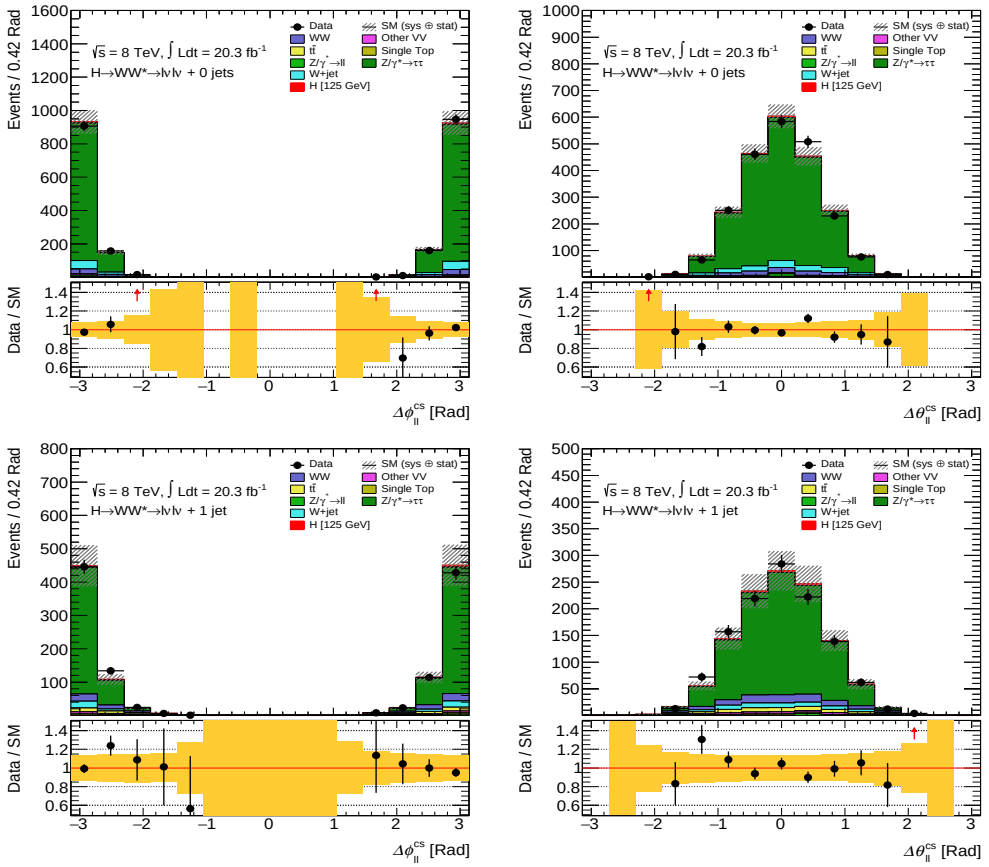

FIGURE 5.8: $Z \to \tau\tau$ CR 0-jet (top) and 1-jet (bottom) categories.

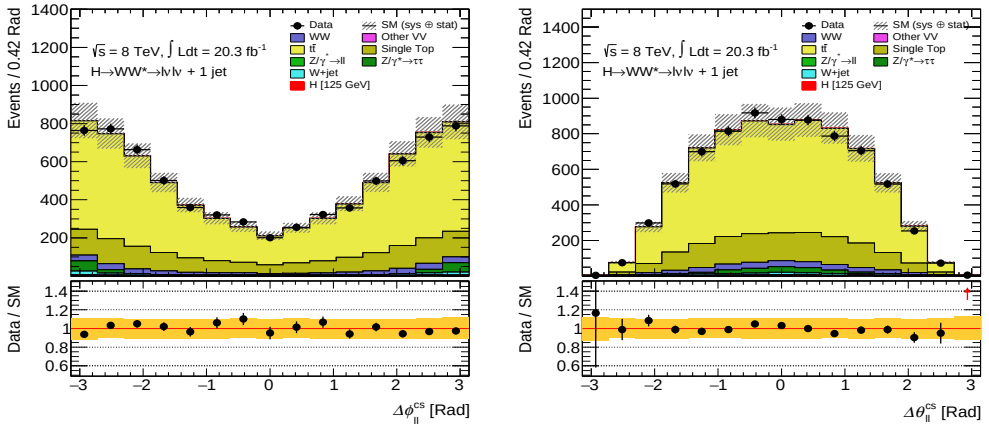

FIGURE 5.9: Top CR for the 1-jet category.

CR is higher than 85%. The QCD multijet background has been included in the W+jets sample as well. Its contribution is very small and due to large uncertainties on the W+jets samples the differences between the two types of backgrounds are negligibly small.

To get the extrapolation factor to calculate the number of W+jets in the SR, a data sample with Z+jets is used. The Z+jets sample has a high cross-section and a high selection efficiency. To get a sample which mimics the W+jets background, one identified lepton is removed and there has to be one anti-identified lepton in the event. We get then one sample where all the leptons pass all the selection criteria and one that contains anti-identified leptons. The extrapolation factors are then determined by looking at the ratio of the two samples for each p_T and η bin of the anti-identified lepton. Small corrections due to the difference in the light flavour and heavy flavour jet contributions to the Z+jets and W+jets samples have been applied based on MC simulation studies.

In Ref. [16] a validation study on the W+jets and non-WW diboson modelling has been performed by using a validation region, where the leptons have the same sign. The results from the validation region showed that both backgrounds were properly modelled and assuring the modelling inside the SR.

5.7 Summary

In this chapter we have discussed which SM processes form the dominant backgrounds to the $H \to WW \to e\nu_e\mu\nu_\mu$ channel. The backgrounds are modelled and the cross-section times branching ratio normalised with the help of dedicated MC generators. We then explained how cutting on several kinematic variables could improve the signal over background sensitivities for the 0-jet and 1-jet categories.

There are two methods to reconstruct the p_T^H: the Calo-based method uses mainly calorimeter information for the soft (low-p_T) objects and the Track-based method using information from the inner detector for the soft objects. The merging of the two methods into one Combined method resulted in a better modelling and a better resolution of the p_T^H compared to the Calo-based and Track-based methods separately. The p_T^H from the Combined method is used as input to the dineutrino reconstruction algorithm.

After applying all the selection criteria the modelling of the SM signal plus background were compared to the data. The spin/CP sensitive variables defined in the Higgs rest-frame showed good agreement between MC simulation and the data. The backgrounds have been normalised by using dedicated CRs and also the distributions of the CRs showed good modelling of the data.

We are now ready to discuss the actual spin/CP analysis. In the next chapter we will define the exact setting of the alternative signal models and how to set up a statistical model that will help us discriminate between the SM Higgs boson and an alternative BSM Higgs boson.

Analysis Method

6

In this chapter we present the main analysis method. First, we summarise the spin-2 and spin-0 scenarios that are tested with respect to the Standard Model hypothesis. We will show the settings of the MC generator used to generate particular models with corresponding κ, $\cos(\alpha)$ and Λ from the Higgs characterisation model, which is an effective field theory (EFT) introduced in chapter 1. Second, we define the "Constructed Variables" by using the kinematic variables in the CS-frame that will be used in a fit model to discriminate between the SM and the alternative models. Lastly, we explain the use of toy experiments to determine the probability of the fit result. Later, in the following two chapters we will apply the described analysis method and discuss the outcome of the results for the spin-2 and spin-0 models.

6.1 Selected Models

We generate a total of fourteen samples by choosing specific settings of the EFT Lagrangians for spin-2 and spin-0 from Eq.1.17 and 1.20: five spin-2 models, three spin-0 models and six models, where a BSM spin-0 coupling interferes with the SM Higgs coupling. All these models are going to be tested with respect to the SM prediction and the results are presented in chapters 7 and 8.

Table 6.1 shows the settings for the spin-2 models. The first model at the top has the universal couplings (UC) settings, whereas the other models have non-universal coupling (NUC) and require an additional cut on the Higgs transverse momentum p_T^H in order to cut off the unitarity violating behaviour as discussed in chapter 3.

Table 6.2 shows the settings for the selected BSM spin-0, which have $\kappa_{SM} = 0$ and $\kappa_{BSM} = 1$ (κ_{HWW}, κ_{AWW} or $\kappa_{H\partial W}$), and SM interference models, which have $\kappa_{SM} = 1$ and $\kappa_{BSM} = 1$. For the interference models the choice of the cutoff scale Λ is based on a study on the cross-section calculation with the MadGraph5_aMC@NLO generator, using the same settings as for the aMC@NLO generator mentioned in section 3.3. The main process was the following:

$$pp \rightarrow X_0 \rightarrow W^+W^- \rightarrow e^+ \nu_e \mu^- \bar{\nu}_\mu \tag{6.1}$$

2^+ Hypothesis	κ_g	κ_q	p_T^H cutoff (GeV)
UC	1	1	–
NUCg125	1	0	125
NUCg300	1	0	300
NUCq125	0.5	1	125
NUCq300	0.5	1	300

Table 6.1: κ_{BSM} settings and upper limits for the Higgs transverse momentum for the spin-2 models. The first model has the settings for universal coupling (UC). The other models are non-universal (NUC) and require a cut on p_T^H due to unitarity violating behaviour as is explained in chapter 3. The letters g and q indicate which type of κ_{BSM} is dominant in the production.

The X_0WW coupling is determined by the settings of κ_{BSM} and Λ of the spin-0 EFT Lagrangian. In order to test each κ_{BSM} term separately, we set κ_{HWW}, κ_{AWW} or $\kappa_{H\partial W}$ to 1 and all the others equal to zero, including κ_{SM}. In the case of testing the κ_{AWW} term also $\cos(\alpha)$ is set to zero. Λ is set at 1 TeV during these tests. The cross-section for each κ_{BSM} test is proportional to $(\kappa_{BSM}/\Lambda)^2$. Using these settings the following relation holds when choosing two different Λ values:

$$\frac{\sigma_a}{\sigma_b} = \left(\frac{1/\Lambda_a}{1/\Lambda_b}\right)^2 \tag{6.2}$$

Rewriting this equation the following the way:

$$\Lambda_a = \Lambda_b \cdot \sqrt{\sigma_b/\sigma_a} \tag{6.3}$$

and fill in for σ_a the total SM cross-section for the process in Eq. 6.1, $\Lambda_b = 1$ TeV and for σ_b the value calculated with the MadGraph5_aMC@NLO generator. The resulting value for Λ_a indicates that when setting the cutoff scale to this particular value and setting the corresponding κ_{BSM} term equal to 1, yields a cross-section equal to the SM cross-section for this particular process. Effectively the sample is hereby normalised to the SM.

Table 6.3 shows the results of calculating the cross-sections studies for different settings of the EFT. The Λ values in the last three rows were calculated with the help of Eq. 6.3. As expected the cross-sections for these rows are similar to the SM cross-section. For the interference models the ratio κ_{BSM}/Λ decides the overall strength of the BSM coupling compared to the SM coupling and indirectly the amount of interference between the two. The choice of setting $\kappa_{BSM} = 1$ and finding the corresponding Λ to yield a cross-section similar to the SM, is an arbitrary but convenient one. Fixing Λ to a particular value and looking for the right setting for each κ_{BSM} term works just as well. In the end, it is the ratio κ_{BSM}/Λ that drives the resulting cross-section.

Hypothesis	κ_{SM}	κ_{AWW}	κ_{HWW}	$\kappa_{H\partial W}$	$\cos(\alpha)$	Λ (GeV)
0^-	0	1	0	0	0	125.5
0^+h	0	0	1	0	1	125.5
$0^+\partial$	0	0	0	1	1	125.5
SM + 0^-	1	1	0	0	$\frac{1}{2}\sqrt{2}$	62
SM − 0^-	1	−1	0	0	$\frac{1}{2}\sqrt{2}$	62
SM + 0^+h	1	0	1	0	1	59
SM − 0^+h	1	0	−1	0	1	59
SM + $0^+\partial$	1	0	0	1	1	143
SM − $0^+\partial$	1	0	0	−1	1	143

Table 6.2: Settings for κ_{SM} and κ_{BSM} for the spin-0 models. At the top, the three models with only one BSM spin-0 coupling and at the bottom, the six models where a BSM spin-0 coupling interferes with the SM. The choice of the cutoff scale Λ is based on cross-section studies displayed in Table 6.3. At the chosen value of Λ, the calculated cross-section of the BSM process, mediated by only one BSM spin-0 coupling (κ_{HWW}, κ_{AWW} or $\kappa_{H\partial W}$), approaches the SM cross-section.

σ (fb)	κ_{SM}	Λ (GeV)	κ_{HWW}	$\kappa_{H\partial W}$	κ_{AWW}	$\cos(\alpha)$
33.92 ± 0.34	1	–	0	0	0	1
0.118 ± 0.002	0	1000	1	0	0	1
0.686 ± 0.007	0	1000	0	1	0	1
0.133 ± 0.002	0	1000	0	0	1	0
34.12 ± 0.38	0	59	1	0	0	1
33.96 ± 0.48	0	143	0	1	0	1
33.79 ± 0.42	0	62	0	0	1	0

Table 6.3: Settings used for κ_{SM} and κ_{BSM} of the EFT and the resulting cross-section and error for the process in Eq. 6.1 calculated with the MadGraph5_aMC@NLO generator. The Λ in the last three rows are calculated with the help of Eq.6.3. For the SM calculation the Λ is irrelevant, because all κ_{BSM} are set to zero.

Fig.6.1 shows the σ_{BSM}/σ_{SM} cross-section ratio for a scan of κ_{HWW} versus $\cos(\alpha)$, where the κ_{HWW} coupling interferes with the SM Higgs coupling and σ_{BSM} the corresponding cross-section. The κ_{SM} is fixed to 1, Λ is set 59 GeV, and the a fine grid of 100 by 100 is chosen for κ_{HWW} in the range of $[-1\,;1]$ and $\cos(\alpha)$ in the range of $[-1\,;1]$. The scan shows some interesting features: large constructive interference for positive κ_{HWW}, while for negative κ_{HWW} destructive interference reduces the σ_{BSM} to almost 50% of the σ_{SM}. Also for positive κ_{HWW} values, the ratio is almost proportional to $(\kappa_{SM} + \kappa_{HWW})^2$ as expected. Inspecting the change of the ratio with respect to $\cos(\alpha)$, we see that the cross-section vanishes for $\cos(\alpha)$ values around zero as was expected. Similar results have been obtained making scans of $\kappa_{H\partial W}$ versus $\cos(\alpha)$ and κ_{AWW} versus $\cos(\alpha)$ (see App.A).

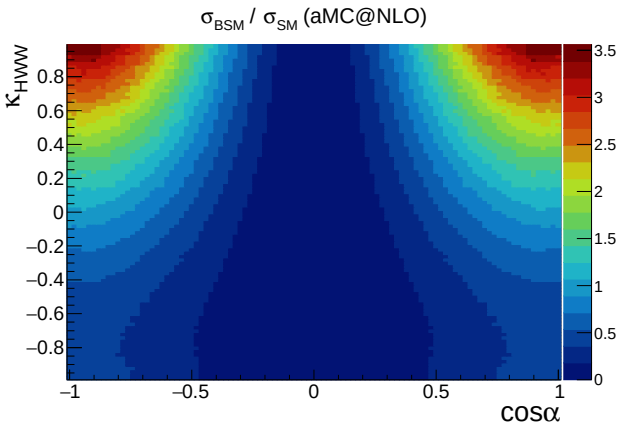

Figure 6.1: The σ_{BSM}/σ_{SM} ratio for a scan of κ_{HWW} versus cos(α). κ_{SM} is fixed to 1 and Λ is fixed at 59 GeV.

Fixing Λ to their specific values for each κ_{BSM} as in Table 6.2 and 6.3 lead to large interference effects in the range of κ_{BSM} between -1.0 and $+1.0$. It turns out that these settings also have large effects on the shape variables. This will be discussed in more detail in chapter 8.

6.1.1 Generation of the Models

The creation of the samples for the spin-2 models from Table 6.1 and the 0^- model is done by generating H + 0,1,2 partons at LO with the MadGraph5_aMC@NLO generator and subsequent showering with Pythia6 (see Table 5.1). The samples for the CP-even BSM spin-0 models and SM interference models from Table 6.2 are created from only one MC sample at LO by using a matrix element reweighting technique described in Ref. [112]. This sample had for its parameters the following HC settings: $\kappa_{SM} = 1$, $\kappa_{AWW} = 2$, $\kappa_{HWW} = 2$, $\kappa_{H\partial W} = 2$ and cos(α) = 0.3. It has been generated with the MadGraph5_aMC@NLO generator at parton level and showered with Pythia6. The reweighting technique has been validated and studied in detail in Ref. [32].

6.2 Constructed Variables

Having defined the models in the previous section, a final discriminating variable is constructed from of the kinematic distributions defined in the CS-frame.

6.2.1 The Discriminating Observables

The variables used for the analysis are the momenta, θ and ϕ angles of the charged leptons in the CS-frame. From these the sum and difference variables, as in Fig. 4.4 and Fig. 4.6, are constructed:

$$\begin{aligned}
\Delta\phi_{ll}^{cs} &= \phi_{l+}^{cs} - \phi_{l-}^{cs} \\
\Delta\theta_{ll}^{cs} &= \theta_{l+}^{cs} - \theta_{l-}^{cs} \\
\Delta p_{ll}^{cs} &= \frac{\left(p_{l+}^{CS} - p_{l-}^{cs}\right)\cdot\pi}{62.5\text{ GeV}} \\
\Sigma\phi_{ll}^{cs} &= \phi_{l+}^{cs} + \phi_{l-}^{cs} \\
\Sigma\theta_{ll}^{cs} &= \theta_{l+}^{cs} + \theta_{l-}^{cs} \\
\Sigma p_{ll}^{cs} &= \frac{\left(p_{l+}^{cs} + p_{l-}^{cs} - 59.3\text{ GeV}\right)\cdot\pi}{42\text{ GeV}}
\end{aligned} \tag{6.4}$$

All variables have been remapped to range between $-\pi$ to π. Only the Σp_{ll}^{cs} variable ranges from 0 to π, because the region below 0 is not populated due to the effect of the dineutrino reconstruction algorithm explained in chapter 4. These are the same variables as presented in Fig. 5.5 and 5.6, but without the remapping of $\Delta\theta_{ll}^{cs}$, $\Sigma\theta_{ll}^{cs}$, Δp_{ll}^{cs} and Σp_{ll}^{cs}. The corresponding remapped distributions can be found in App. B.

The next step is to bin the variables from Eq. 6.4 and construct a single histogram with all bins together. We call this histogram the "Constructed Variables" in which each event appears six times, one at a time for each of the six variables from Eq. 6.4. This Constructed Variable is going to be used to test the SM versus an alternative hypothesis. Table 6.4 shows over which bins the variables are being distributed. In principle, the total range of a certain variable is divided over the total amount of bins. However, some variables have low statistics in the first and last few bins and this causes problems later on when doing the fit to data. In order to cope with this problem, we constructed an underflow and overflow bin for some variables as indicated in Table 6.4. The central region of the range is described by a finer binning and hence more sensitive to shape modulations in the variable.

Fig. 6.2 shows the resulting histograms of the Constructed Variables for the 0-jet and 1-jet SM and spin-2 signal samples as an example. It is clearly visible that the ranges containing the $\Delta\phi_{ll}^{cs}$, $\Delta\theta_{ll}^{cs}$ and Σp_{ll}^{cs} distributions contain the most discrimination power between these particular models, as was expected from the simulations in chapter 4.

Variable				Range [Rad]			
	Starts at bin	Ends at bin	Bin total	Coverage	binwidth	Underflow	Overflow
$\Delta\phi_{ll}^{cs}$	1	15	15	$[-\pi\,;\pi]$	0.419	–	–
$\Delta\theta_{ll}^{cs}$	16	30	15	$[-2.2\,;2.2]$	0.293	$[-\pi\,;-2.2]$	$[2.2\,;\pi]$
Δp_{ll}^{cs}	31	45	15	$[-2.2\,;2.2]$	0.293	$[-\pi\,;-2.2]$	$[2.2\,;\pi]$
$\Sigma\phi_{ll}^{cs}$	46	60	15	$[-\pi\,;\pi]$	0.419	–	–
$\Sigma\theta_{ll}^{cs}$	61	75	15	$[-2.0\,;2.0]$	0.267	$[-\pi\,;-2.0]$	$[2.0\,;\pi]$
Σp_{ll}^{cs}	76	90	15	$[0\,;2.2]$	0.147	–	$[2.2\,;\pi]$

Table 6.4: The sum and difference variables from Eq. 6.4 are arranged into Constructed Variables with 90 bins in total. The numbers are indicated where the variable starts and ends in the Constructed Variables distribution. The ranges are defined such that each bin has enough statistics. The dash sign in the last two columns indicates that there is no need for overflow and underflow regions.

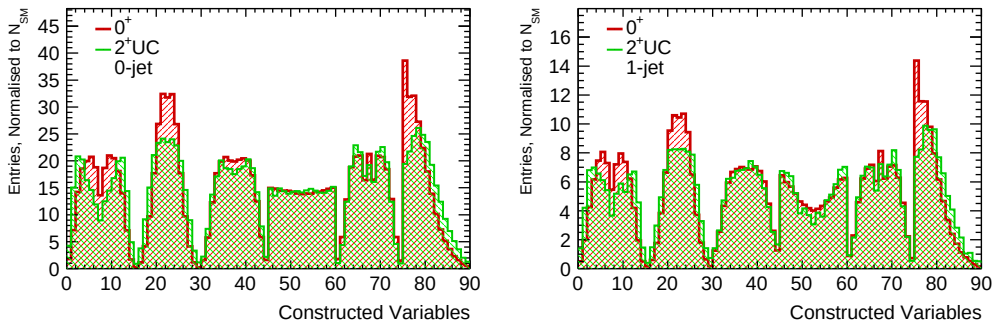

Figure 6.2: Distributions of the Constructed Variables used for the analysis. The SM and spin-2 UC signal hypothesis are compared with each other for the 0-jet(left) and 1-jet(right) categories. The errors are small compared to the expectation and are therefore not drawn. The shapes for the background processes can be found in Fig.5.5, 5.6, B.1 and B.2.

6.3 Likelihood Function

The statistical analysis is based on the use of likelihood functions[118]. For the test of the SM versus the fourteen alternative hypotheses, the likelihood function will be constructed from the Constructed Variables as shown in Fig. 6.2. Firstly, we explain the basics of likelihood construction with and without normalisation factors. We will then introduce a parameter to test different hypotheses. After that we will show how to include systematic uncertainties into the likelihood. Lastly, an example is shown for the SM hypothesis fit to data.

6.3.1 Statistical Model

The probability to observe N events during the data taking of an experiment, can be calculated by making use of a Poisson distribution:

$$P(N|\mu s + b) = \frac{e^{-\lambda}\lambda^N}{N!} \tag{6.5}$$

where $\lambda = \mu s + b$, the expected amount of events, and N the observed events in data. The distribution itself describes a probability density normalised to unity and integrating over a certain range will return the probability of the experimental outcome to be within that particular range. The expected amount of events consists of the background b and signal s times a the strength parameter μ. This parameter μ is needed when beforehand it is not entirely certain how big the signal contribution will be. This is relevant for the spin-2 and

spin-0 models that are going to be tested, because the cross-section is not straightforward to predict for these models. After observing N events, the value μ can be changed in order to get the highest probability, without having to change b and s. In this case the Likelihood function, $\mathscr{L} = P(N|\mu s + b)$, only depends on μ and for μ one maximises the likelihood.

The situation gets more complicated when also the expected background b has an uncertainty. An auxiliary measurement in a control region, where no or almost no signal is expected and mainly consists of background events, can be used to estimate the yield of the expected background in the signal region. The likelihood function will change in the following way:

$$\mathscr{L}(\mu, \mu_{CR}) = P(N|\mu s + \mu_{CR} b) P(N_{CR}|\mu_{CR} b_{CR}) \tag{6.6}$$

It is almost the same equation as Eq.6.5, but now an extra parameter μ_{CR} is introduced to indicate the yield of the background contribution in the signal region. The auxiliary measurement is also included in the likelihood, by adding the Poisson probability to measure N_{CR} events in the control region while expecting $\mu_{CR} b_{CR}$ background. The main assumption here is that the amount of expected background b in the signal region is directly proportional to the expected b_{CR} in the control region. This proportionality is indicated by the parameter μ_{CR} (in principle this is β from Eq.5.12). Maximising the likelihood will now also entail finding the best value for μ_{CR}, besides that of μ. The parameter μ_{CR} is known as a nuisance parameter and μ_{CR} belongs to the category of normalisation factors in this example.

The general way of including nuisance parameters in the likelihood function is the following:

$$\mathscr{L}(\mu, \vec{\mu}_{CR}, \vec{\theta}\,) = P(N|\mu s(\vec{\theta}) + b(\vec{\theta}, \vec{\mu}_{CR})) \times \prod_{j}^{N_{sys}} A(\tilde{\theta}_j|\theta_j) \times \prod_{l}^{N_{CR}} P(N_{CRs,l}\,|\,\mu_{CR,l}\; b_{CR,l}) \tag{6.7}$$

The likelihood depends now on multiple nuisance parameters written as a vector $\vec{\theta}$, all with their own probability function $A(\tilde{\theta}_j|\theta_j)$ based on auxiliary measurements, and normalisation factors written in the vector $\vec{\mu}_{CR}$ from N_{CR} control regions. The $\tilde{\theta}_j$ here means the measured θ_j and could be, for example, the measurement of the energy resolution of the calorimeter. Also the signal s and background b become functions of the nuisance parameters and maximising the likelihood involves finding the best values not only for μ, but for all θ_j and $\mu_{CR,l}$.

In order to test two different signal hypotheses s_1 and s_0 and include them into the likelihood we introduce the parameter of interest (POI) ϵ:

$$s = \epsilon s_1 + (1 - \epsilon)\, s_0 \tag{6.8}$$

Setting $\epsilon = 1$ will select the s_1 signal hypothesis, while setting $\epsilon = 0$ will select s_0. The likelihood will now depend on the parameter ϵ as well, and by either fixing it to 0 or 1 (conditional fit), one particular signal hypothesis can be tested. It is also possible to set ϵ as a free parameter (unconditional fit) and find the value that maximises the likelihood, $\hat{\epsilon}$. A fitted $\hat{\epsilon}$ between 0 and 1 indicates that contributions of both hypotheses are needed to get a good fit to data, while values above (below) 1 (0) would indicate that the data prefer stronger s_1 (s_0) features, which separate it from the s_0 (s_1) hypothesis.

We have now the ingredients to use the histogram of the Constructed Variables from the previous section to construct a likelihood function. Each bin is described by a Poisson distribution so the likelihood will become the product of the distribution belonging to each bin for each jet sample:

$$\begin{aligned}\mathscr{L}(\epsilon, \mu, \vec{\mu}_{CR}, \vec{\theta}\,) = \\ &\prod_{j}^{N_{jets}} \prod_{i}^{N_{bins}} P\big(N_{i,j} \,|\, \mu\,(\epsilon\, S_{SM,i,j}(\vec{\theta}) + (1-\epsilon)\, S_{alt,i,j}(\vec{\theta})) + B_{i,j}(\vec{\theta}, \vec{\mu}_{CR})\big) \\ &\times \prod_{k}^{N_{sys}} A(\tilde{\theta}_k|\theta_k) \times \prod_{l}^{N_{CR}} P(N_{CRs,l} \,|\, \mu_{CR,l}\; b_{CR,l})\end{aligned} \tag{6.9}$$

Setting $\epsilon = 1$ will select the SM signal hypothesis, while $\epsilon = 0$ will select the alternative signal. The total contributions from all the different backgrounds is indicated by B, all systematic uncertainties are included with $A(\tilde{\theta}|\theta)$ and all normalisation factors from the different control regions are included through $P(N_{CR}|\mu_{CR} b_{CR})$. Notice that here the parameter μ is treated as a nuisance parameter, while in the previous example it was the POI.

Eq.6.9 would be the likelihood of choice, if only the following assumption holds: the sum of entries in the Constructed Variables histogram has to reflect the amount of available data from the measurement. Unfortunately this is not the case, because the histogram is made out of six distributions, so each event appears six times. The statistical uncertainty is therefore reduced by a factor of $\sqrt{6}$. This would especially influence the uncertainty of the signal strength parameter μ. To circumvent this problem, another normalisation parameter is introduced, called μ_{norm}, together with a new control region which is the signal region. The μ_{norm} normalisation factor is only applied to the signal region for the Constructed Variables and absorbs the reduction factor $\sqrt{6}$ into its error. The rate parameter μ becomes a free parameter that will be constrained by the newly defined control region (SR in fact) and thereby receive the right error. This leaves us with our likelihood function

of choice:

$$\mathscr{L}(\epsilon,\mu,\mu_{norm},\vec{\mu}_{CR},\vec{\theta}\,) = \prod_{j}^{N_{jets}}\prod_{i}^{N_{bins}} P\Big(N_{i,j} \,|\, \mu_{norm,j}\,\big(\,\mu\,(\epsilon\, S_{SM,i,j}(\vec{\theta}) + (1-\epsilon)\, S_{alt,i,j}(\vec{\theta})) + B_{i,j}(\vec{\theta},\vec{\mu}_{CR})\big)\Big) \times \prod_{k}^{N_{sys}} A(\tilde{\theta}_k|\theta_k) \times \prod_{l}^{N_{CR}} P(N_{CRs,l} \,|\, \mu_{CR,l}\; b_{CR,l}) \tag{6.10}$$

For each jet channel the likelihood receives one μ_{norm} normalisation factor and control region. For all the fit results presented in the next chapters we show also the best fit-values for μ_{norm}, which is expected to be close to 1 and having a small error.

6.4 Systematic Uncertainties

There are three kinds of systematic uncertainties that influence the final result of the likelihood fit, namely theoretical, experimental and MC statistics. The theoretical uncertainties come from the uncertainties on the QCD scale, the parton density functions and MC modelling. Experimental uncertainties are related to the precision and resolution of the detector components. The MC statistic reflects that we have finite computing resources in particular to generate large background samples. These uncertainties effect either the normalisation or shape of the Constructed Variables distribution used to distinguish the different models.

The uncertainties enter the likelihood as nuisance parameters, as in Eq. 6.10, where they are constrained according to the probability density function of their uncertainties. This could be a Gaussian centred at the expected value θ_0 with a width of σ_θ. The uncertainty, for example, the energy resolution is modelled by using 3 template histograms: the nominal and $\pm\sigma$ histograms, where the uncertainty is set to the nominal value and $\pm\sigma$ respectively. The fit is allowed to interpolate/extrapolate between the 3 template histograms to find the best value for the nuisance parameter. This technique is called template morphing[119] and is especially useful when it is difficult to determine a priori the effect of a certain systematic on the discriminating variables.

The main assumption of factorising the nuisance parameters in the likelihood of Eq. 6.10 is that there is no correlation between them. The likelihood fit has the potential to improve the initial knowledge of the systematic uncertainty. The fit could pull the nuisance parameter to a value that would lead to a better data/MC description, or reduce the error with respect to the initial input error.

Nuisance parameters are neglected when their corresponding systematic uncertainty has a negligible impact on the Constructed Variables. For the normalisation the parameters are neglected if an effect of less than 0.1% is observed and no bin in the distribution changes by 5% or more.

6.4.1 Theoretical Uncertainties

Table 6.5 summarises the theoretical uncertainties on the extrapolation factors α explained in section 5.6.1. The WW background is the most dominant background for the analysis and special extrapolation factors from the Top and $Z/\gamma^* \to \tau\tau$ backgrounds for the WW control region are included to get a better estimate of the sample purity. The different components that contribute to the total uncertainty are described below.

- Determining uncertainties of the QCD scale are done by varying the renormalisation and factorisation scales up and down by a factor of 2 and taking the largest difference as the $\pm\sigma$ uncertainty.
- PDF uncertainties are taken from the CT10 PDF error set with difference between the central values NNPDF2.3 and CT10[120].
- For the parton shower (PS) and generator modelling (UE) uncertainties the difference between respectively Herwig versus Pythia and Powheg+Herwig versus aMC@NLO+Herwig were taken.

For the spin-0 samples an additional Higgs transverse momentum reweighing was applied to match the Powheg+Pythia8 p_T^H distribution in order to prevent any differences due to the MadGraph5_aMC@NLO generator versus Powheg. No p_T^H shape uncertainty is considered for the spin-2 samples, because it is negligible compared to effect of the required p_T^H cut for the non-universal coupling samples.

The PDF and scale uncertainties turned out to be negligible for the shape and are therefore only included as normalisation uncertainties. The PS and generator modelling had a significant effect on the shape, so bin-by-bin uncertainties are applied for these.

6.4.2 Experimental Uncertainties

The most important contributions to the experimental uncertainties come from the jet energy scale, jet energy resolution and b-tagging as shown in Table 6.6. Detailed studies on the experimental uncertainties can be found in Ref. [79].

Category	QCD Scale	PDF	Gen	EW	UEPS	$p_{T,Z}$	Total (%)
			WW background				
SR 0-jet	0.9	3.8	6.9	−0.8	−4.1	-	9.0
SR 1-jet	1.2	1.9	3.3	−2.1	−3.2	-	5.5
			Top background				
SR 1-jet	−0.8	−1.4	1.9	-	2.4	-	3.5
WW CR 1-jet	0.6	0.3	−2.4	-	2.0	-	3.2
			$Z/\gamma^* \to \tau\tau$ background				
SR 0-jet	−7.1	1.3	-	-	−6.5	19	21.3
SR 1-jet	6.6	0.66	-	-	−4.2	-	7.9
WW CR 0-jet	−11.4	1.7	-	-	−8.3	16	21.4
WW CR 1-jet	−5.6	2.2	-	-	−4.8	-	7.7

Table 6.5: Theoretical uncertainties in terms of percentages for the extrapolation factor α for the WW, Top and $Z/\gamma^* \to \tau\tau$ backgrounds. The SR label means that the extrapolation is from the control region to the signal region, while the label WW CR means the extrapolation from the control region to the WW control region. The sign indicates if the uncertainty entails an increase or reduction of the background signal yield. Summing all uncertainties in quadrature is displayed in the last column as the "Total". Table is taken from Ref. [112].

The bias and pull of the theoretical and experimental uncertainties, as well as the impact they have on the fit's POI ϵ, will be discussed in detail in the next two chapters.

6.5 Example Fit Results SM

Fig. 6.3 shows the resulting histograms of the Constructed Variables after a fit of the likelihood defined in Eq. 6.10. The best values for the normalisation factors for the different backgrounds are applied, the nuisance parameters are constrained, and ϵ is fixed to 1 making this a SM test with respect to data. In order to quantify the difference between data and MC, Fig. 6.4 shows the pull for each bin from Fig. 6.3. No significant deviations are observed and the χ^2 over the degrees of freedom is displayed in the figure, indicating a good agreement between data and the SM hypothesis.

6.6 Model Testing

The outcome of the fit result by using the constructed likelihood function from the previous section gives in general a good indication if the data prefers a model or not. However, due to the complexity of the constructed likelihood in Eq. 6.10, the fit to data for several

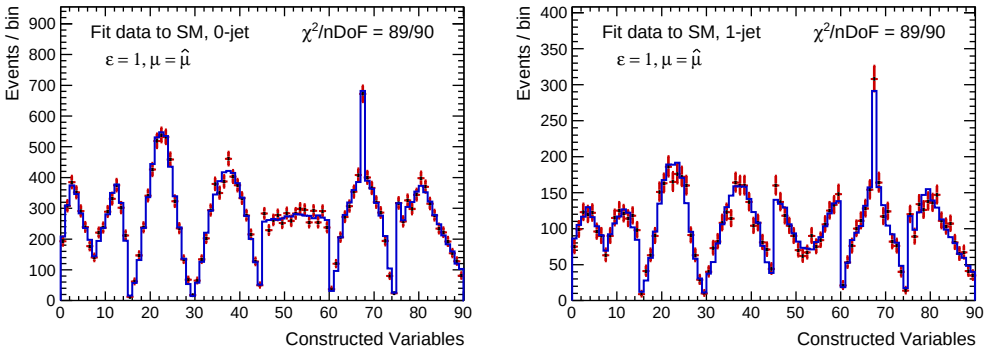

Figure 6.3: The data (red crosses) compared to the SM (blue line), which is scaled to yield the best fit result, for the 0-jet (left) and 1-jet (right). ϵ is fixed to 1 and μ is a used as a free parameter in the fit. Errors on the MC are not shown to prevent overcrowding.

hypotheses is very hard to interpret and therefore it is necessary to perform toy MC studies. We introduce a test statistic, which is a powerful mathematical tool to compare the fit results of different models with each other. For each hypothesis we generate pseudodata and calculate the corresponding test statistic. This procedure will yield a probability density distribution for the test statistic, from which it is possible to calculate the probability of the fit result. However, this method has its limitations when two models are very hard to

Source of uncertainty	Treatment in the analysis and its magnitude
Jet energy scale	$1-7\%$ in total as a function jet η and p_T
Jet energy resolution	$5-20\%$ as a function of jet η and p_T Relative uncertainty on the resolution is $2-40\%$
b-tagging	b-jet identification: $1-8\%$ decomposed in p_T bins Light quark jet misidentification: $9-19\%$ as a function of η and p_T c quark jet misidentification: $6-14\%$ as a function of p_T
Leptons	Reconstruction, identification, isolation, trigger efficiency: below 1% except for the electron identification: $0.2-2.7\%$ depending on η and p_T Momentum scale and resolution: $< 1\%$
Missing transverse momentum	Propagated jet energy and lepton momentum scale uncertainties Resolution ($1.5-3.3$ GeV) and scale variation ($0.3-1.4$ GeV)
Pile-up	The number of pile-up events is varied by 10%
Luminosity	2.8%[121]

Table 6.6: Sources of experimental systematic uncertainties taken from Ref. [112]

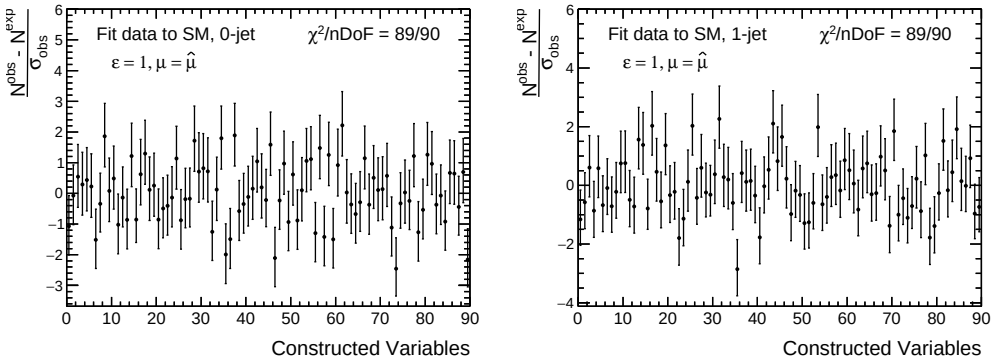

Figure 6.4: Pull distributions of the 0-jet (left) and 1-jet (right) distributions in Fig.6.3.

distinguish from each other. Therefore we will apply the CL_s method to prevent spurious exclusions.

6.6.1 Definition of the Test Statistic

For the definition of the test statistic we use the q observable:

$$\begin{aligned} q &= -2\ln\frac{\mathscr{L}(\epsilon=0,\hat{\mu}_{\epsilon=0},\hat{\theta}_{j,\epsilon=0})}{\mathscr{L}(\epsilon=1,\hat{\mu}_{\epsilon=1},\hat{\theta}_{j,\epsilon=1})} \\ &= -2\Delta\mathrm{LL} \end{aligned} \tag{6.11}$$

It is the logarithm of the likelihood ratio between two models, or difference between the logarithms, each with their own $\hat{\mu}$ and $\hat{\theta}_j$ estimators set to maximise that particular likelihood. The quantity q is known as the test statistic and indicates the preference of the fit for one hypothesis or the other. With the above definition, large positive values of q mean a stronger preference for the $\epsilon = 1$ hypothesis, while for large negative values the data agrees more with the alternative $\epsilon = 0$ hypothesis. q values close to 0, indicate that the data does not have a clear preference for either model, but more for something in between.

Having defined the meaning of the possible values the test statistic q can have, we need to estimate which q values can be expected assuming that nature is described by one of the hypotheses. In order to do that, a technique to generate pseudodata or toy experiments is applied. One toy experiment can be seen as a new data set generated from the discriminating variable of one particular hypothesis. From each bin of the discriminating variable a random pull is done, based on the expected value from the hypothesis for that bin and taking into account the statistical and systematic uncertainties in that bin. The result is a

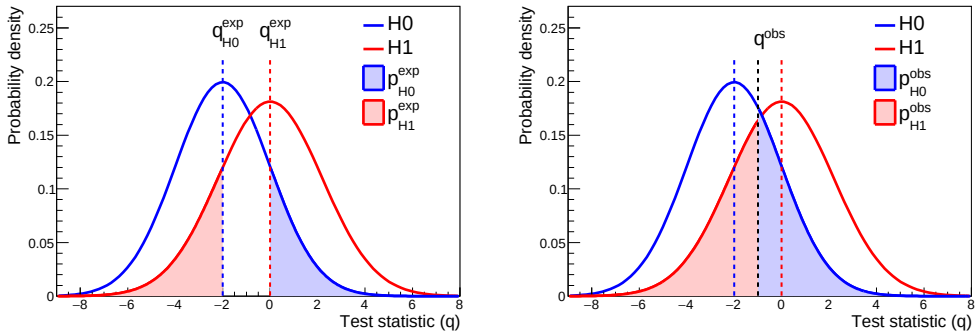

Figure 6.5: Definition of the p values for the used hypotheses. On the left, the expected sensitivity and on the right, the observed p values for a hypothetical measurement.

new generated histogram describing the discriminant variable, but for a virtual data set. Doing this procedure multiple times, is known as generating toys. For each toy experiment the test statistic from Eq. 6.11 is calculated and with enough experiments it results in a distribution for q. Fig.6.5 shows a typical example of what to expect for the q distribution assuming two arbitrary but different hypotheses. The blue distribution assumes the $\epsilon = 0$ hypothesis to be true and yields more negative values for q, while positive values are more compatible with the red distribution indicating the $\epsilon = 1$ hypothesis.

The probability of some q value for a hypothesis assuming the alternative hypothesis is defined as the expected exclusion limit:

$$p_{exp}^{H1} = \int_{-\infty}^{q_{H0}^{exp}} f(q|\epsilon = 1)dq \tag{6.12}$$

and

$$p_{exp}^{H0} = \int_{q_{H1}^{exp}}^{\infty} f(q|\epsilon = 0)dq \tag{6.13}$$

where $f(q)$ is the probability distribution for q, q_{H0}^{exp} the median for the H0 hypothesis and q_{H1}^{exp} the median for the H1 hypothesis. Fig.6.5 displays a possible outcome for the expected limits from Eq.6.13 and 6.12. The expected p values correspond with the coloured areas, and the smaller the area the better the exclusion. When doing the measurement on data, the outcome of the test statistic is called q_{obs}, and the observed exclusion limits can be calculated. In principle that is done by replacing q_{H1}^{exp} and q_{H0}^{exp} in Eq.6.12 and 6.13 by q_{obs}. However, the rule is always to do the integration towards the median or expected value of the tested hypothesis. For example, if the observed test statistic would be higher than q_{exp}^{H1} the integration limits in Eq.6.12 will change to the range from q_{obs} to infinity.

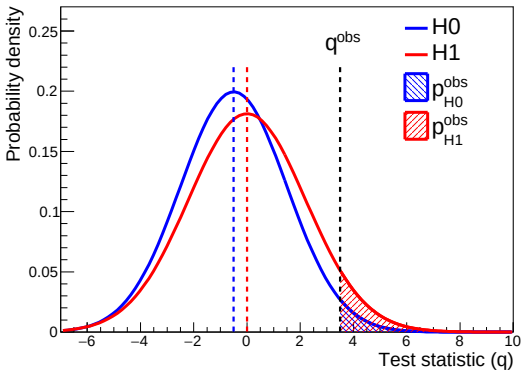

Figure 6.6: A case of spurious exclusion, the H0 hypothesis would be excluded in the conventional sense, however, the observed q lies in a region that is not so likely for the H1 hypothesis either.

In some cases, the discrimination between two models is very difficult, due to the lack of statistics or if the models have weak unique features to separate them from each other. A classic example is when a very weak signal is expected on top of a dominating background. The signal+background hypothesis is almost identical to the background-only hypothesis. This would result in $f(q)$ distributions as in Fig. 6.6. The exclusion limits can still be calculated, but the following problem can occur: measuring less events in data than is expected from the background-only hypothesis would result in higher probabilities to exclude the signal+background hypothesis, while the analysis is in fact not sensitive enough to discriminate between the two. A method to prevent these spurious exclusions is known as "CL_s method"[122], where CL_s is defined as:

$$CL_s = \frac{CL_{H0}}{CL_{H1}} \tag{6.14}$$

where $CL_{H0} = p^{H0}_{exp}$ as in Eq. 6.13 and the denominator is defined as:

$$CL_{H1} = \int_{q_{obs}}^{\infty} f(q|\epsilon = 1)dq \tag{6.15}$$

Note that the integration range for Eq. 6.15 always stays the same, regardless the value of q^{H1}_{exp}. Technically speaking, Eq. 6.14 is not a probability, but a probability ratio. By definition, the denominator is always bigger than the numerator (unless H0 = H1) so the outcome will always be between 0 and 1. The net effect is that the p value for H0 hypothesis is increased, making the exclusion less likely and the result more conservative. In Fig. 6.6 the CL_s value would be the ratio between the coloured areas.

6.7 Summary

We made a selection out of five spin-2, three BSM spin-0 and six SM interference models that will be compared to the SM hypothesis. Table 6.1 and 6.2 display the settings used for the EFT in order to generate these. From the kinematic variables of the charged leptons we defined Constructed Variables, which settings are in Table 6.4.

We introduced to concept of a likelihood function, Eq.6.10, and explained how that can be used to test the SM hypothesis versus an alternative hypothesis. The inclusion of theoretical and detector systematics uncertainties into the likelihood as nuisance parameters, has been briefly discussed. Lastly, we motivated the need for toy MC studies and the definition of the q observable, as in Eq.6.11, that will be used as a test statistic. A distribution for q will put the outcome of the fit into perspective by calculating the expected and observed exclusion limits. For the case of spurious exclusions, we introduced the "CL_s method" and it will be used when presenting the results. In the next chapter we will discuss the results of the analysis applied to the spin-2 models. The chapter thereafter will discuss the results of the BSM spin-0 and SM interference models.

Results Spin-2 Analyses

7

In this chapter we will present the results of the SM hypothesis compared to the spin-2 models defined in Table 6.1 from the previous chapter. First an overview is given of the fit results displaying the normalisation factors, the signal yield $\hat{\mu}$ and the parameter of interest (POI) $\hat{\epsilon}$. We parametrised the Standard Model with $\epsilon = 1$, whereas any alternative hypothesis corresponds to $\epsilon = 0$. Subsequently, we show the results of impact studies that quantify the effect of the nuisance parameters on the final fit result. What follows is the toy MC studies to interpret the fit to data. Several cross-checks of the analysis will be presented as well as a χ^2 compatibility test to quantify the difference of the MC shape distributions and the data. Lastly, we will compare the results obtained in this thesis with the outcome of other analyses, performed within the ATLAS collaboration, that also tested spin-2 Higgs models.

7.1 Model Fit to Data

The data has been fit to the Constructed Variables as defined in section 6.2 for the SM and the selected spin-2 hypotheses. Fig. 7.1 shows the pull for each bin of the Constructed Variables for the 0-jet and 1-jet categories after doing a spin-2 UC ($\epsilon = 0$) fit on the data. The SM fit ($\epsilon = 1$) is indicated by the red dots and put in for comparison. For the fit results on the POI $\hat{\epsilon}$ the 0-jet and 1-jet categories have been combined and all fit results are displayed in Table 7.1. It shows the best fit for $\hat{\epsilon}$, the signal strength μ for various ϵ (conditional or unconditonal fit) and in the last three columns the ΔLL of the different hypotheses.

The $\hat{\mu}$ values are the best fit values for the signal yield and a value of 1 corresponds to the expected SM signal yield. For both the conditional and the unconditional fits, the signal yield is higher than 1, so more signal events give a better fit to the data. The fits to all spin-2 models give a higher signal yield $\hat{\mu}_{\epsilon=0}$ than the fitted SM signal yield $\hat{\mu}_{\epsilon=1}$ when doing the SM fit. The reason why it is higher for the spin-2 models, is due to the cut on $\Delta\phi_{ll}^{lab} < 2.7$ in the selection of events. This cuts mainly in the sensitive region for the spin-2 models and therefore a higher signal yield is needed to compensate for this effect. The spin-2 UC and NUCg models have the largest difference for ΔLL when compared to the

Hypothesis	$\hat{\epsilon}$	$\hat{\mu}_{\hat{\epsilon}}$	$\hat{\mu}_{\epsilon=1}$	$\hat{\mu}_{\epsilon=0}$	$\Delta\text{LL}^{\hat{\epsilon}}_{\epsilon=1}$	$\Delta\text{LL}^{\hat{\epsilon}}_{\epsilon=0}$	$\Delta\text{LL}^{\epsilon=1}_{\epsilon=0}$
2^+, UC	0.24 ± 0.21	1.69 ± 0.09	1.23 ± 0.24	1.71 ± 0.11	2.46	0.41	-2.05
2^+, NUCg125	0.23 ± 0.17	1.64 ± 0.09	1.20 ± 0.21	1.64 ± 0.09	2.69	0.41	-2.28
2^+, NUCg300	0.21 ± 0.18	1.68 ± 0.09	1.23 ± 0.22	1.67 ± 0.09	3.14	0.34	-2.80
2^+, NUCq125	0.49 ± 0.18	1.48 ± 0.09	1.19 ± 0.18	1.52 ± 0.11	0.94	1.42	0.48
2^+, NUCq300	0.44 ± 0.19	1.55 ± 0.09	1.23 ± 0.20	1.57 ± 0.11	1.23	1.22	-0.01

Table 7.1: Outcome of the fit results, including all the theoretical and detector systematic uncertainties, for the SM compared to all the spin-2 hypotheses. $\hat{\epsilon}$ indicates the preference of the data for the SM or the alternative model. $\hat{\mu}$ indicates the signal strength to be used for the best fit. The last three columns show the ΔLL: the first two are the fits with ϵ fixed compared to the unconditional fit and the last one is the SM hypothesis compared with respect to the alternative model.

Hypothesis	$\mu_{\text{norm,0j}}$	$\beta_{WW,\text{0j}}$	$\beta_{Z\tau\tau,\text{0j}}$	$\mu_{\text{norm,1j}}$	$\beta_{WW,\text{1j}}$	$\beta_{Z\tau\tau,\text{1j}}$	$\beta_{Top,1j}$
2^+, UC: $\epsilon = 0$	1.0100 ± 0.0101	1.18 ± 0.01	0.94 ± 0.03	1.0200 ± 0.0109	1.08 ± 0.03	1.05 ± 0.04	1.01 ± 0.01
2^+, NUCg125: $\epsilon = 0$	1.0200 ± 0.0108	1.17 ± 0.01	0.93 ± 0.04	1.0200 ± 0.0106	1.08 ± 0.03	0.97 ± 0.07	1.00 ± 0.02
2^+, NUCg300: $\epsilon = 0$	1.0100 ± 0.0097	1.18 ± 0.01	0.94 ± 0.03	1.0200 ± 0.0103	1.11 ± 0.02	0.98 ± 0.06	1.00 ± 0.01
2^+, NUCq125: $\epsilon = 0$	1.0200 ± 0.0147	1.17 ± 0.01	0.92 ± 0.04	1.0300 ± 0.0120	1.06 ± 0.02	0.96 ± 0.07	1.00 ± 0.02
2^+, NUCq300: $\epsilon = 0$	1.0100 ± 0.0217	1.18 ± 0.01	0.93 ± 0.04	1.0200 ± 0.0135	1.10 ± 0.02	0.98 ± 0.08	0.99 ± 0.02
2^+, UC: $\epsilon = 1$	1.0100 ± 0.0080	1.17 ± 0.03	0.94 ± 0.05	1.0200 ± 0.0113	1.10 ± 0.05	1.08 ± 0.05	1.00 ± 0.04
2^+, NUCg125: $\epsilon = 1$	1.0100 ± 0.0073	1.17 ± 0.01	0.95 ± 0.02	1.0300 ± 0.0125	1.06 ± 0.03	1.07 ± 0.05	1.00 ± 0.01
2^+, NUCg300: $\epsilon = 1$	1.0100 ± 0.0125	1.17 ± 0.03	0.95 ± 0.04	1.0200 ± 0.0116	1.10 ± 0.02	1.08 ± 0.09	1.00 ± 0.01
2^+, NUCq125: $\epsilon = 1$	1.0100 ± 0.0077	1.17 ± 0.01	0.95 ± 0.03	1.0300 ± 0.0114	1.06 ± 0.02	1.07 ± 0.07	1.00 ± 0.01
2^+, NUCq300: $\epsilon = 1$	1.0100 ± 0.0109	1.17 ± 0.02	0.95 ± 0.03	1.0200 ± 0.0117	1.10 ± 0.02	1.08 ± 0.10	1.00 ± 0.01

Table 7.2: The best fit values for the normalisation μ_{norm} and the normalisation factors β for the WW, $Z \to \tau\tau$ and Top control regions after doing the conditional $\epsilon = 1$ (SM) and $\epsilon = 0$ (spin-2) fits including all theoretical and detector systematic uncertainties.

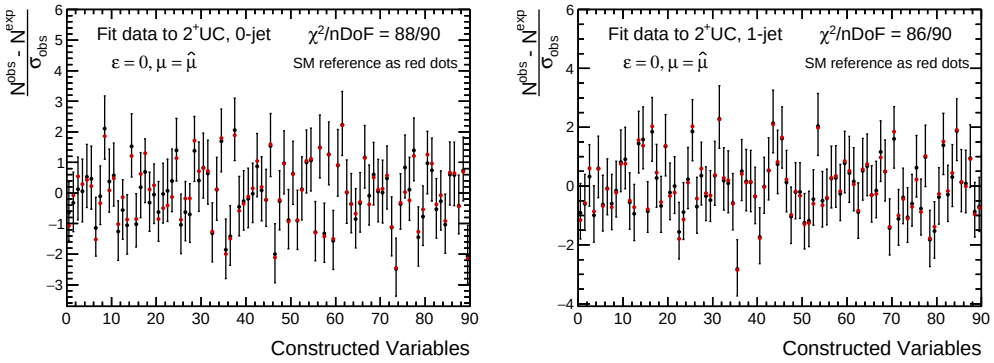

Figure 7.1: Pull for each bin of the Constructed Variables when doing a spin-2 UC ($\epsilon = 0$) fit to the data. On the left, the 0-jet and on the right, the 1-jet categories are presented. The red dots drawn on top are the points from the SM fit ($\epsilon = 1$) from Fig.6.3, but without error bars. As can be seen from the pull figures, there are no large difference between the SM and spin-2 UC hypothesis.

SM hypothesis fit. The best fit $\hat{\epsilon}$ and ΔLL tell us that these spin-2 hypotheses are preferred with respect to the SM hypothesis. Section 7.1.2 will show how significant this preference is. For the spin-2 NUCq models the fit prefers values for $\hat{\epsilon}$ closer to 0.5, which is in between the SM and alternative hypothesis, and thereby not preferring either hypothesis above the other.

Table 7.2 shows the best fit values for the normalisation μ_{norm} and normalisation factors β from the control regions for the signal yield, WW, $Z \to \tau\tau$ and Top backgrounds after doing the fit with all the theoretical and detector systematics. The fits are done for keeping ϵ fixed to 1 and 0 to do the SM fit and spin-2 fit respectively. The normalisation factors are overall very similar for each hypothesis test and the normalisation μ_{norm} is close to 1. This consistency when switching hypotheses ensures the reliability of the normalisation factors.

Table 7.1 and 7.2 show that there were no problems when performing either the conditional or unconditional fits. The SM hypothesis and alternative spin-2 hypotheses show each good fit results. Before we discuss the significance of the spin-2 UC and NUCg models above the SM, we will present the impact of the systematic uncertainties on the fit.

7.1.1 Impact of Systematic Uncertainties

Fig.7.2 shows the pulls and impact of the theoretical and detector systematic uncertainties on the POI $\hat{\epsilon}$ after doing a fit with both jet channels combined for the spin-2 UC model.

The x axis is divided in an upper and a lower x axis, which are normalised to the impact on the POI and the pulls respectively. We will describe the interpretation in the two sections below.

The lower x axis shows the pull of a nuisance parameter, that is, the difference of the best fit value $\hat{\theta}$ compared to the nominal value θ_0 divided by the expected error $\Delta\theta$ for that nuisance parameter. The fit will be biased when the pull will be significantly larger or smaller than 0. The red bar indicates the expected 1 standard deviation for $\hat{\theta}$, while the black is the calculated 1 standard deviation from the fit. When both overlap and the bias is 0, the nuisance parameter is properly modelled. However, when the fitted error is much smaller then the expected error it can indicate two things: 1) the fit in the signal region is better at constraining the nuisance parameter then the auxiliary measurement for that particular parameter; 2) there are correlations between certain nuisance parameters causing the errors to be more constrained. The first case can happen when expected fluctuations due to the nuisance parameter in the signal region are not supported by the data[123]. The likelihood changes more rapidly with an increasing deviation from the nominal value than is expected beforehand. The second case occurs when there are correlations factors between parameters not taken into account in the likelihood expression Eq.6.10 or if the model is not detailed enough. In the last case, more nuisance parameters have to be included to give a more accurate description[124].

The upper axis of Fig. 7.2 shows the change in the POI $\hat{\epsilon}$, when varying one nuisance parameter at a time. This is done in the following way: first the POI is set floating between -5 and 5, and an unconditional fit is performed with all the the nuisance parameters set to float. After this fit, all but one nuisance parameter are set fixed to their best fit value and the POI is set to floating. The fit is redone and the up and down standard deviations for the nuisance parameter that was set to float are extracted. The next step is to fix this one nuisance parameter to $\pm$ 1 standard deviation and redo the fit. By extracting the POI for the two fits and comparing this to the fitted POI from the first unconditional fit, gives the prefit impact of the particular nuisance parameter on the POI. The last step is again to fix this particular nuisance parameter, but this time to $\pm$ the up and down standard deviations extracted from the fit, where only this nuisance parameter and the POI were set free to float. The change of the POI acquired this way is the postfit impact. As is clear from the procedure, the pre and post indicate that the nuisance parameter was varied up and down by the standard deviations extracted from before and after the fit. This procedure is repeated for all nuisance parameters. In the figure the nuisance parameters are ordered with decreasing impact on the POI.

Fig. 7.2 shows that most of the nuisance parameters show the expected behaviour, as the pulls are close to 1. The parameters related to the $Z \to \tau\tau$ modelling seem a little bit over constrained, but this can be attributed to the clear features of the $Z \to \tau\tau$ contribution to the signal region. Slight changes would have large impact on the shapes of the kinematic

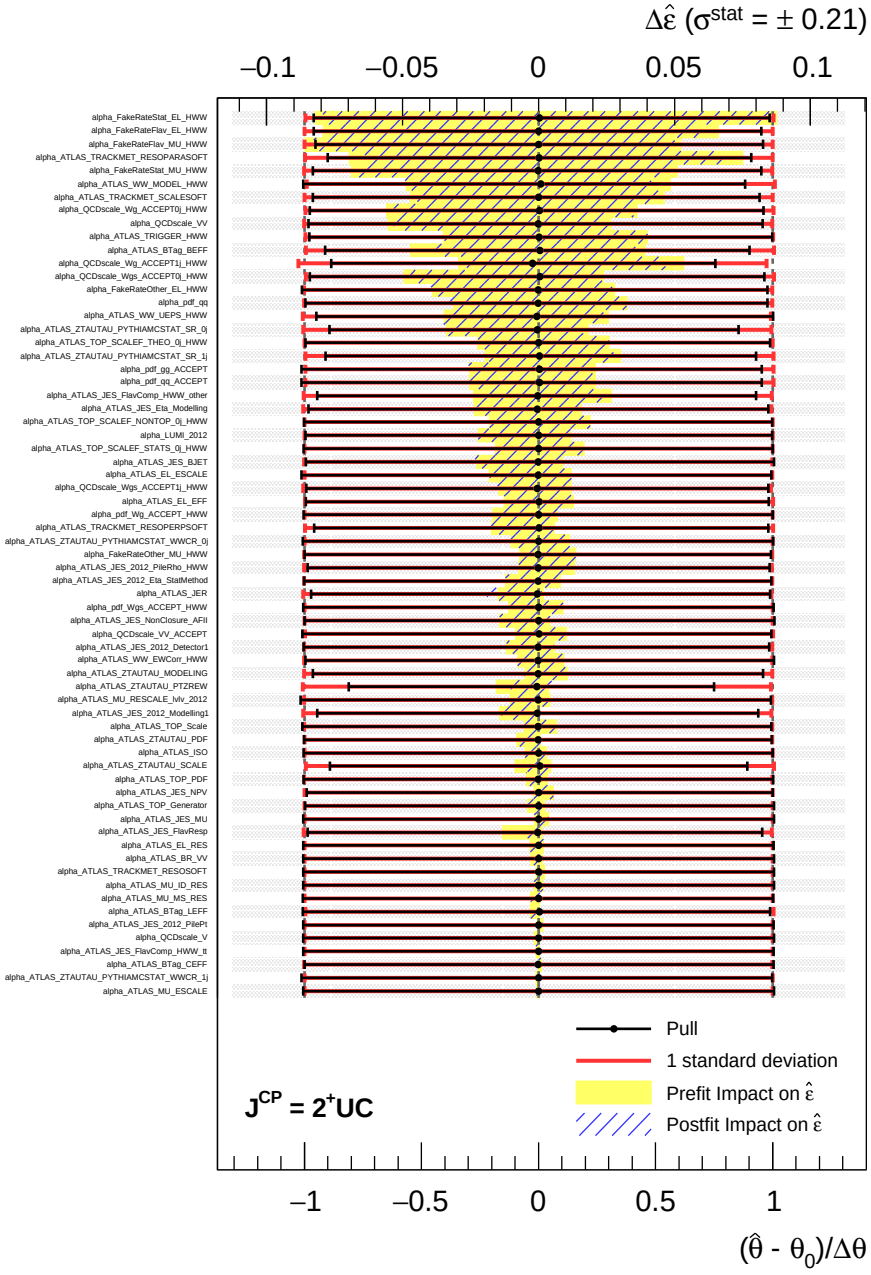

Figure 7.2: Pulls of the main systematic uncertainties (see section 6.4) and their impact on the POI $\hat{\epsilon}$, when doing the unconditional fit of the spin-2 UC model compared to the SM hypothesis. The nuisance parameters are ordered with decreasing impact on the POI. The statistical uncertainty on $\hat{\epsilon}$ is also indicated at the top in the brackets.

variables and thereby constrain the allowed fluctuation of the $Z \to \tau\tau$ background. The largest impact on the POI comes from the fake rate estimation (jets misidentified as leptons) and causes a change of 0.08 on the POI. Nevertheless, this change is small compared to the impact due to the statistical error of 0.21, indicated in the brackets besides $\Delta\hat{\epsilon}$ and taken from Table 7.1. The fit result is therefore dominated by the statistical uncertainty.

The pull and POI impact studies show similar results for the spin-2 NUC models: the nuisance parameters show the expected behaviour and the fit result is dominated by the statistical uncertainty. It is important to note that none of the systematic uncertainties has a large enough impact to bias the fit result in favour of any of the spin-2 hypotheses. As Table 7.1 shows that the spin-2 UC and NUCg models have an $\hat{\epsilon}$ around 0.24, the strongest nuisance parameters have an effect of 0.08 on $\hat{\epsilon}$. To go from $\epsilon = 1$, the SM hypothesis, down to the best fit of 0.24 would entail approximately 9 standard deviations for the strongest nuisance parameter. Therefore the spin-2 UC and NUCg preference of the data can not be attributed to one or more (possibly underestimated) systematic errors.

With the proper modelling of the systematic uncertainties, we can proceed to look at the combined effect of the statistical and systematic uncertainties on the fit results. This is done by performing toy MC experiments and their result follows next.

7.1.2 MC Toy Distributions

In Fig. 7.3 the distributions of the test statistic q of the SM versus all spin-2 hypotheses are shown. For each hypothesis 5000 toy data sets were generated. The red solid line is the SM expectation for the test statistic and the red dashed line is the median of the distribution. The blue solid lines represent the alternative spin-2 hypotheses and the blue dashed lines represent their medians. The expected limits are calculated with respect to these medians, as explained in section 6.6. The fit results to the data shown in Table 7.1 correspond to the black lines. Comparing the SM hypothesis with the spin-2 NUCq models, the fit to data ends up in between the distributions, preferring neither of the hypotheses. The preference of the spin-2 UC and NUCg models is evident, because the data fit is well within the spin-2 distributions, while being in the lower tail of the SM expectation.

Table 7.3 shows the expected and observed exclusions based on the test statistic distributions in Fig. 7.3. The table also shows the observed significance Z_{obs} for the observed p_{obs}. There is no spin-2 model that can be excluded with 95% confidence level or more. The observed exclusion limit of the SM hypothesis for the spin-2 UC and NUCg models is below 2.5% and the highest significance for these exclusion limits is 2.4. In order to state a significant deviation from the SM hypothesis in favour of the alternative hypothesis, this significance has to be at least 3.0. The fit to data therefore shows no significant deviation from the SM expectation.

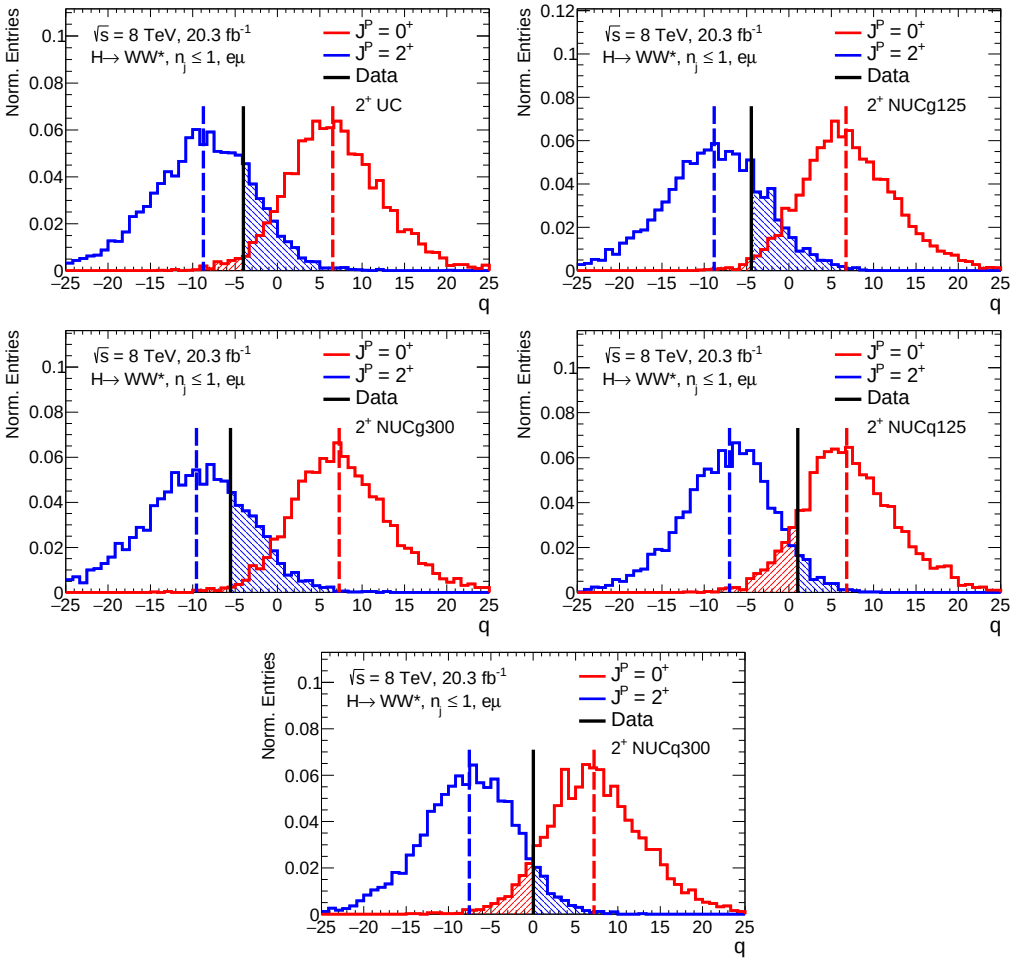

Figure 7.3: Distributions of the test statistic q for the SM hypothesis and all spin-2 models. For each distribution 5000 toys have been generated, assuming either the SM hypothesis or one of the spin-2 models as input. The data line in black corresponds to the fit values in Table 7.1.

Hypothesis	p_{exp}^{SM}	p_{exp}^{alt}	p_{obs}^{SM}	p_{obs}^{alt}	Z_{obs}^{SM}	Z_{obs}^{alt}	$1-\mathrm{CL}_s$
2^+, UC	0.002	0.005	0.021	0.207	2.0	0.8	78.8%
2^+, NUCg125	0.001	0.003	0.011	0.224	2.3	0.8	77.3%
2^+, NUCg300	0.001	0.002	0.008	0.256	2.4	0.7	74.2%
2^+, NUCq125	0.004	0.002	0.123	0.050	1.2	1.6	94.3%
2^+, NUCq300	0.004	0.003	0.082	0.071	1.4	1.5	92.3%

Table 7.3: Expected and observed exclusion limits for the SM and all spin-2 hypotheses. The numbers are based on the test statistic distributions from Fig. 7.3. The last column shows the exclusion limits for the alternative hypothesis based on the CL_s method.

Even though not significant enough, the preference of the data for the spin-2 UC and NUCg models asks for a closer look on the input variables used for the analysis. If all input variables have a preference for the alternative spin-2 models, it is not surprising that the Constructed Variables will also reflect this preference. If that is indeed the case, a future analysis including a larger data set would possibly make the SM deviation significant. However, if the input variables do not show a consistent preference for the SM or spin-2 hypothesis, the question arises if the measured spin-2 preference is due to a statistical fluctuation of the data. In order to cross-check this, we do a χ^2 compatibility test of the MC shapes with respect to the data which is the topic of the next section.

7.2 Data Compatibility Test

The results from the MC toy distributions indicate a preference for the spin-2 UC and NUCg models, which is remarkable because if the result would be significant ($Z_{obs}^{SM} \geq 3.0$) the SM Higgs boson hypothesis would be in serious trouble. Therefore, this section will focus on the data compatibility test of the SM and spin-2 UC hypothesis by means of applying a χ^2 fit to the distribution of the Constructed Variables. It will mainly serve as a cross-check for the goodness of fit to data. We will perform the χ^2 test to the toy MC data as well, so we obtain the expected χ^2 distributions for the SM and spin-2 hypothesis. With these distributions we can calculate the p value of the observed χ^2 for each hypothesis and thereby validate the goodness of fit. Besides that, the values of the χ^2 tests gives us valuable insight which hypothesis results in a better fit to data.

Secondly, we will perform the SM and spin-2 UC compatibility test on the six kinematic variables from Eq. 6.4 for each jet category separately, resulting in two times twelve χ^2 measurements and the same amount of distributions when doing the χ^2 test on the toy MC data.

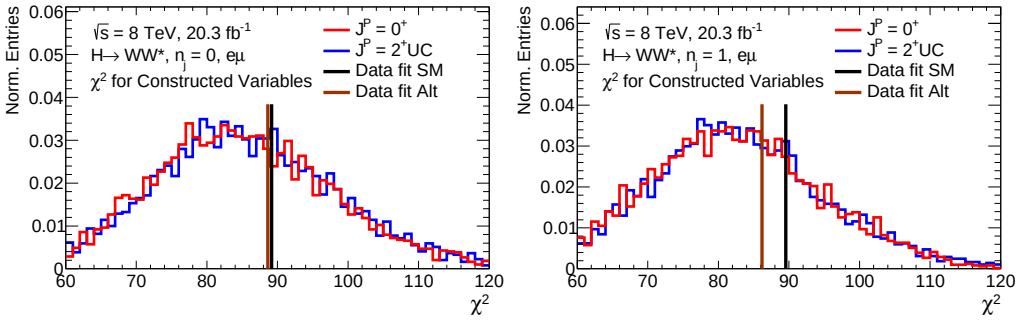

Figure 7.4: Outcome of the χ^2 fit results for the SM and spin-2 UC hypothesis to the toy data, generated from the SM and spin-2 UC hypothesis. The red and blue lines are the χ^2 fit of the toy data to SM and spin-2 UC model respectively. For both the 0-jet (left) and 1-jet (right) categories the χ^2 values are well within the ranges of the distributions.

7.2.1 χ^2 Results of the Constructed Variables

Fig. 7.4 shows the outcome of the χ^2 fit of the SM hypothesis to the toy data set generated from the SM hypothesis (red) and the χ^2 fit of the spin-2 UC hypothesis to the spin-2 UC toy data (blue). The black and brown lines are the observed χ^2 values from the fit to data assuming the SM and spin-2 UC hypothesis respectively. The tests are performed on the 0-jet and 1-jet categories separately. The results are well within the probability range of the distributions. The χ^2 fit for the 0-jet results in similar values for the SM and the spin-2 alternative, but there is a noticeable difference between the two models for the 1-jet fit. The spin-2 model has a lower χ^2 value compared to the SM, indicating a data preference for spin-2. This preference is expressed as the $\Delta\chi^2$ in Table 7.4.

Table 7.4 shows the outcome of the χ^2 fit result, p values and the $\Delta\chi^2$ for the SM and all the spin-2 hypotheses. The p value is defined the following way:

$$p = \int_{\chi^2_{obs}}^{\infty} F(\chi^2)\, d\chi^2 \tag{7.1}$$

where $F(\chi^2)$ is the distribution as in Fig. 7.4 and χ^2_{obs} is obtained after the fit to data. None of the values indicates an incompatibility of the SM hypothesis with the data, because all of its p values are above 25%. The $\Delta\chi^2$ values show that the spin-2 UC model fits better to the data with respect to the SM for the 1-jet category and that both the 0-jet and 1-jet categories give a bit better fit results for the spin-2 NUCg models. For the other cases, the SM and spin-2 hypotheses have similar fit results. None of the $\Delta\chi^2$ values is significant enough to prefer any of the spin-2 models above the SM hypothesis and the other way around.

Hypothesis	χ^2_{SM}		χ^2_{alt}		$\Delta\chi^2$		$p^{SM}_{\chi^2}$		$p^{alt}_{\chi^2}$	
	0j	1j	0j	1j	0j	1j	0j	1j	0j	1j
2^+, UC	89.2	89.6	88.6	86.2	-0.5	-3.4	0.36	0.27	0.38	0.37
2^+, NUCg125	89.1	86.7	87.5	83.9	-1.6	-2.8	0.36	0.33	0.41	0.41
2^+, NUCg300	89.2	89.0	87.4	85.0	-1.8	-4.0	0.37	0.30	0.41	0.41
2^+, NUCq125	89.1	86.7	90.1	86.4	0.9	-0.3	0.36	0.33	0.33	0.34
2^+, NUCq300	89.2	89.0	89.9	87.7	0.7	-1.2	0.37	0.29	0.35	0.33

Table 7.4: The measured χ^2 values for the 0 and 1-jet categories for the Constructed Variables when assuming the SM hypothesis or any of the spin-2 models. $\Delta\chi^2$ is obtained by subtracting the corresponding χ^2 value of the SM from the χ^2 value of the alternative hypothesis. The p values are calculated with Eq. 7.1 and based on the distributions as in Fig. 7.4.

7.2.2 χ^2 Results of the Kinematic Variables

The results of the shape compatibility tests for the six kinematic variables for the SM and spin-2 UC hypothesis are shown in Fig. 7.5 and 7.6 for the 0-jet and 1-jet categories respectively. Table 7.5 shows the observed χ^2, $\Delta\chi^2$ and p values of the six variables for each jet category. We point out the following things:

- 0-jet $\Delta\phi^{cs}_{ll}$ and Σp^{cs}_{ll} have a SM preference with respect to the spin-2 UC hypothesis ($\Delta\chi^2 = 1.6$ and 1.7 respectively).
- 0-jet Δp^{cs}_{ll} and $\Sigma\phi^{cs}_{ll}$ have a slight spin-2 UC preference ($\Delta\chi^2$ = -0.4 and -0.7 respectively).
- The observed χ^2 values for the $\Sigma\phi^{cs}_{ll}$ variable for the 0-jet category are in the tail of the distribution for both the SM and the spin-2 hypothesis.
- 0-jet $\Delta\theta^{cs}_{ll}$ and $\Sigma\theta^{cs}_{ll}$ show no preference for either model.
- 1-jet $\Delta\theta^{cs}_{ll}$ shows a spin-2 UC preference ($\Delta\chi^2 = -2.7$).
- 1-jet Δp^{cs}_{ll}, $\Sigma\phi^{cs}_{ll}$ and Σp^{cs}_{ll} prefer spin-2 UC ($\Delta\chi^2$ = -1.3, -1.3 and -1.0 respectively).
- 1-jet $\Delta\phi^{cs}_{ll}$ and $\Sigma\theta^{cs}_{ll}$ have no preference for either model.

The p values for each distribution indicate that all results for the SM are well within expected limits, with only the 0-jet $\Sigma\phi^{cs}_{ll}$ as exception to be in the tail of the distribution. However, its p value for both the SM and the spin-2 hypothesis is not large enough to indicate a significant deviation.

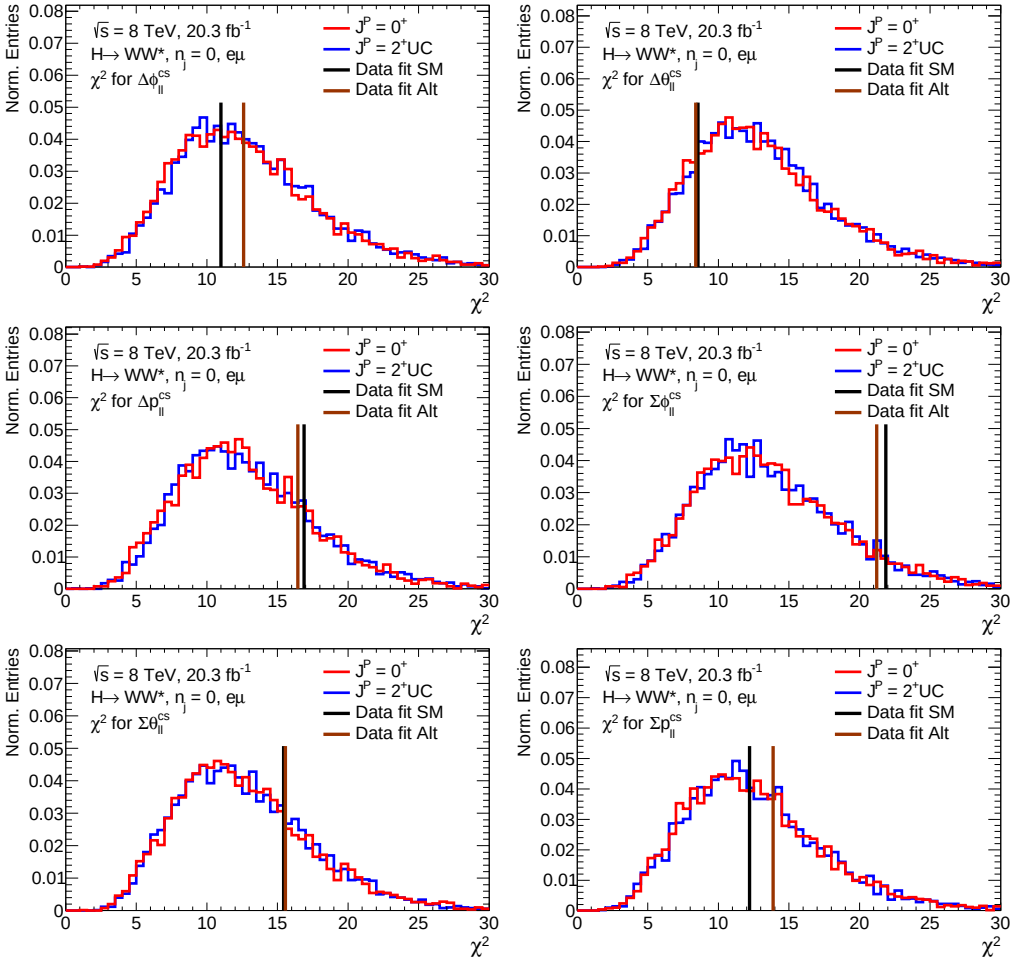

Figure 7.5: 0-jet category of the χ^2 distributions of the 6 kinematic variables used to construct the Constructed Variables. The distributions are obtained after generating 5000 toy samples from the SM (red) and spin-2 UC (blue) distributions and subsequently doing a χ^2 fit of the SM and spin-2 UC hypothesis to the samples. The black and brown lines are the χ^2 fit of the data to the SM and spin-2 UC hypotheses respectively.

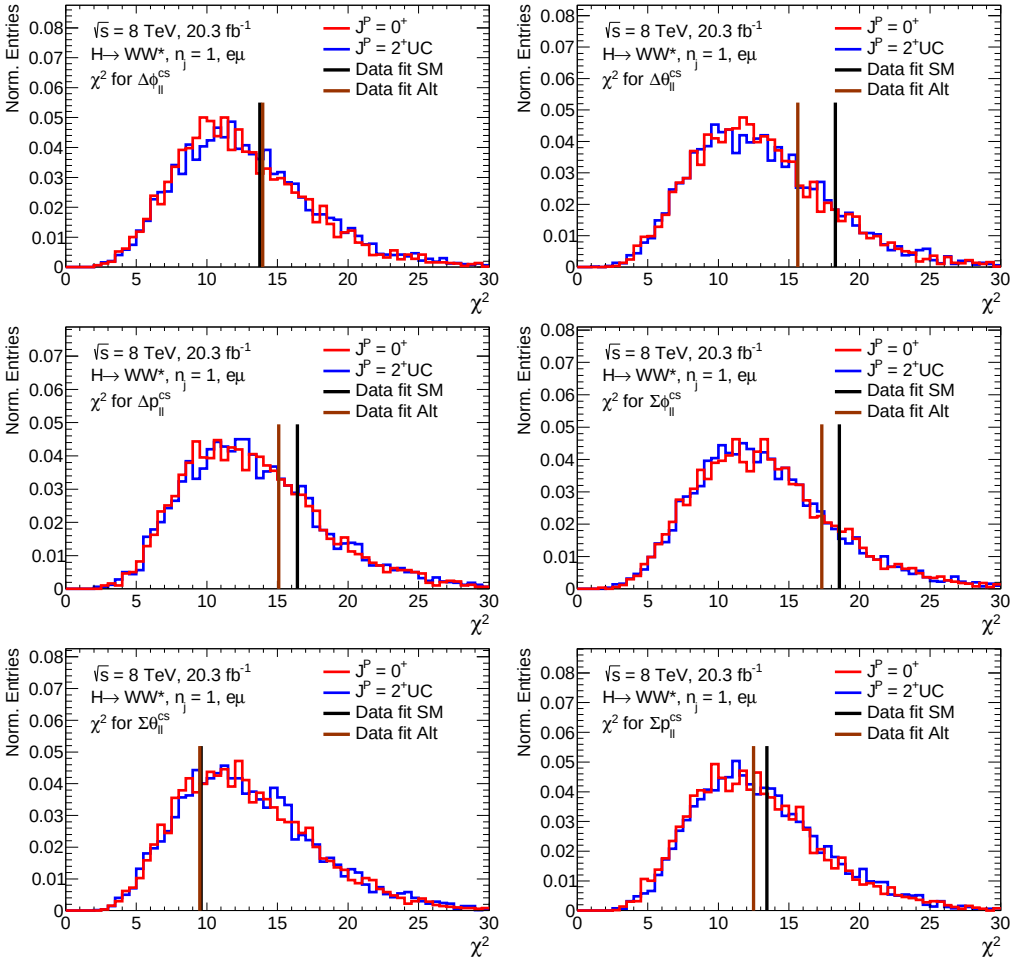

Figure 7.6: 1-jet category of the χ^2 distributions of the 6 kinematic variables used to construct the Constructed Variables. The distributions are obtained after generating 5000 toy samples from the SM (red) and spin-2 UC (blue) distributions and subsequently doing a χ^2 fit of the SM and spin-2 UC hypothesis to the samples. The black and brown lines are the χ^2 fit of the data to the SM and spin-2 UC hypotheses respectively.

Hypothesis	χ^2_{SM}		χ^2_{alt}		$\Delta\chi^2$		$p^{SM}_{\chi^2}$		$p^{alt}_{\chi^2}$	
	0j	1j	0j	1j	0j	1j	0j	1j	0j	1j
2^+, UC, $\Delta\phi^{cs}_{ll}$	11.0	13.7	12.6	14.0	1.6	0.2	0.58	0.35	0.45	0.34
2^+, UC, $\Delta\theta^{cs}_{ll}$	8.6	18.3	8.4	15.6	-0.2	-2.7	0.81	0.14	0.82	0.26
2^+, UC, Δp^{cs}_{ll}	16.9	16.4	16.4	15.1	-0.4	-1.3	0.18	0.23	0.21	0.32
2^+, UC, $\Sigma\phi^{cs}_{ll}$	21.9	18.6	21.2	17.3	-0.7	-1.3	0.07	0.15	0.08	0.20
2^+, UC, $\Sigma\theta^{cs}_{ll}$	15.4	9.6	15.6	9.5	0.1	-0.1	0.25	0.72	0.24	0.73
2^+, UC, Σp^{cs}_{ll}	12.2	13.4	13.9	12.5	1.7	-1.0	0.48	0.39	0.35	0.47

Table 7.5: χ^2, $\Delta\chi^2$ and p values for the distributions in Fig. 7.5 and 7.6.

The preference for the spin-2 UC model with respect to the SM hypothesis taking the Constructed Variables is not reflected consistently in the distributions of all the kinematic variables. The 0-jet $\Delta\phi^{cs}_{ll}$ and Σp^{cs}_{ll} have a spin-0 preference, but the other four variables do not prefer the spin-0 above the spin-2 hypothesis. Most of the 1-jet variables have a little spin-2 preference.

In App. C the toy distributions of the test statistic q for all the spin-2 hypotheses are split up for each jet category. Also the p values and exclusion limits for all spin-2 models are shown there. From these figures and tables it becomes clear that there is a preference for the alternative hypothesis for the 1-jet category when testing the SM versus any of the spin-2 models. Choosing to combine both the 0-jet and 1-jet categories of the six variables results in a spin-2 preference. The underlying distributions for the six kinematic variables for all jet categories are compatible with both the SM spin-0 hypothesis as well as the spin-2 UC hypothesis. A larger data set is necessary to be able to significantly discriminate between the two models. It would be interesting to see if the spin-2 preference trend in the 1-jet events would persist.

7.3 Other Analysis

To put the obtained results for the spin-2 models in a wider perspective, we present the results of two other studies on the Higgs spin and CP in the $H \to WW \to e\nu_e\mu\nu_\mu$ channel performed within the ATLAS collaboration.

The first analysis makes use of kinematic variables in the lab-frame and by optimising a BDT classifier[112]. The variables are $\Delta\phi^{lab}_{ll}$, M_{ll}, M_T and p^{ll}_T are used to train the BDT classifier and the same selection procedure for the events as described in chapter 5 has been applied, except for the cut on M_T for the 0-jet category. Five spin-2 models are tested with the exact same settings as in Table 6.1 and Table 9 in the respective paper shows

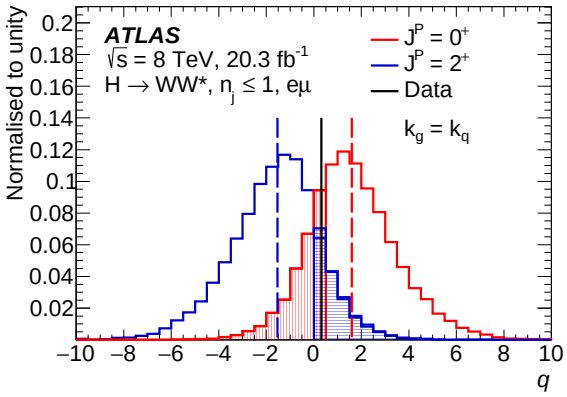

Figure 7.7: Distribution for the test statistic comparing the SM hypothesis with the spin-2 UC model. 5000 toys have been generated using the SM or the spin-2 as input. A BDT classifier based on kinematic variables defined in the lab-frame has been used to optimise the discrimination between the two models and is used in the likelihood fit. The fit to data falls in between the two models and the exclusion limit for spin-2 is set at 84.5% confidence limit. The figure is taken from Ref. [112].

the exclusions to be above 92% confidence level for the spin-2 NUC models. The spin-2 UC model exclusion limit is set at 84.5% confidence level and its test statistic distribution, displayed as Fig. 15 in the paper, has been reproduced here as Fig. 7.7. The data falls in the middle between the expected spin-2 UC and the SM hypothesis. The variables used to train the BDT classifier are mainly related to the correlations in the azimuthal angles ϕ and the momenta of the charged leptons and Fig. 7.5 and 7.6 shows that these lead to mixed preference when testing the SM hypothesis with respect to the spin-2 UC model. Both the BDT analysis and the Constructed Variables analysis lead to similar results when testing the SM hypothesis versus the spin-2 UC model. The expected sensitivity for the BDT studies is also displayed in Table 9 of Ref. [112] and shows that the expected p values for the spin-2 hypotheses are between 3.3% and 0.4%. From Table 7.3 we can see that the expected p values for the spin-2 hypotheses remain below 0.5% by using the Constructed Variables.

A noticeable difference of the BDT analysis compared to the analysis described in this thesis, is the effect of the Higgs transverse momentum in the lab-frame. The p_T^H spectrum for the spin-2 NUC models induces shape changes for the $\Delta\phi_{ll}^{lab}$ and p_T^{ll} distributions on which the BDT classifier is trained, but the p_T^H effects are mitigated for large part due to the boosting to the Higgs rest-frame. Due to this effect, the additional information on the specific p_T^H shape is not propagated to the kinematic variables used in the Constructed Variables. Therefore, the BDT analysis performs better in excluding the spin-2 NUC models than the analysis with the Constructed Variables presented in this thesis.

The second analysis follows the same event selection procedure as described in this thesis, uses the dineutrino reconstruction algorithm as described in chapter 4 and boosts to the Higgs rest-frame[16]. It uses the lab-frame coordinates for its orientation, while in the analysis presented in this chapter we rotated to the CS-frame. The analysis makes use of mainly two variables to test the five spin-2 models which correspond to the ones presented in Table 6.1. The variables are a combination of the lepton and neutrino energies E^*_{sum} and the opening angle of the charged leptons in the $r-z$ plane $\Delta\psi^*_{ll}$, described in section 5.5 of Ref. [16]. The E^*_{sum} variable can be related to the Σp^{cs}_{ll} variable from this analysis and the $\Delta\psi^*_{ll}$ can be mapped one to a linear combination of the $\Delta\phi^{cs}_{ll}$ and $\Delta\theta^{cs}_{ll}$ variables in the CS-frame. As can be seen in Fig. 7.5 and 7.6 combining these variables leads to a mixed preference. Taking this into account it is surprising to see that the analysis described in Ref. [16] excludes all the spin-2 models with more than 96% confidence level. Its expected p values for the spin-2 hypotheses are between 9.1% and 7.3%.

Depending on the choice of the kinematic variables, either a spin-0 or spin-2 preferred result can be obtained. We have seen that for the kinematic variables the 0-jet distributions tend to prefer a spin-0 hypothesis, while the 1-jet distributions are more prone for the alternative spin-2 hypothesis. But overall there is no strong spin-0 or spin-2 preference and the data is compatible with both hypotheses. Ref. [16] is able to exclude all the spin-2 models from Table 6.1. The BDT analysis from Ref. [112] uses for the training a set of variables with mixed spin-0/spin-2 preference, resulting in a lower exclusion limit for the spin-2 UC model. However, the BDT classifier is also trained on the p^H_T, yielding better exclusion limits on the spin-2 NUC models than the Constructed Variables.

7.4 Summary

We have presented the results of the SM compared to the spin-2 models from Table 6.1. A fit to maximise the likelihood resulted remarkably in a preference of the data for the spin-2 UC and NUCg models with $\hat{\epsilon}$ around 0.24 ± 0.2 statistical uncertainty. However, for the NUCq models the fit showed no preference for either the SM nor the alternative hypothesis. The best fit values for the normalisation factors and studying the impact of the nuisance parameters on the fit results, indicated that there were no problems with the outcome of the fit and that the results are dominated by the statistical uncertainty. Toy MC studies have shown the probability of the fit result and none of the spin-2 models can be excluded at a 95% confidence level, neither is there a significant deviation from the SM hypothesis. Also an additional χ^2 compatibility test of the data with the SM and spin-2 UC hypothesis showed that the data is compatible with either model.

The spin-2 results presented in this thesis were compared to two other analyses on Higgs spin/CP within the ATLAS collaboration using the same data set and similar selection

criteria. One analysis trains a BDT classifier on kinematic variables defined in the lab-frame. It obtains similar results compared to the Constructed Variables when testing the spin-2 UC hypothesis, that is, not showing any preference for either the SM or spin-2 UC hypothesis. The BDT also uses the shape of the p_T^H distribution for the spin-2 NUC models and it is therefore more sensitive in excluding these models than the Constructed Variables. The other analysis also makes use of kinematic variables in the Higgs rest-frame. However, the chosen variables for that particular analysis have a mixed spin-0/spin-2 preference for the used data set and it is surprising to see it excludes all spin-2 models at 96% confidence level.

We can conclude that the presented analysis shows that the data is compatible with both the SM and the spin-2 hypotheses. More data in the $H \to WW \to e\nu_e \mu\nu_\mu$ channel is needed in order to confirm spin-0 or spin-2 when using the Constructed Variables. Especially, it is interesting to see if the trend for a spin-2 preference continues in the 1-jet distributions for the new data sets.

Results Spin-0 and CP Mixing Studies

8

In this chapter we present the results of the analysis on the spin-0 models with respect to the SM hypothesis. The fit results and the normalisation factors will be discussed, followed by the studies of the impact of the nuisance parameters on the final result. Three samples with a BSM spin-0 resonance and 6 samples, where the SM interferes with a CP-even or CP-odd spin-0 coupling, were used and their settings are defined in Table 6.2. We present the results of the toy MC studies and set exclusion limits on the tested BSM spin-0 and SM interference models by using the data. Further on, we compare these results to other spin and CP studies performed within the ATLAS collaboration. Lastly, in the context of CP mixing studies, we introduce an analysis that performs a scan of CP-even and CP-odd spin-0 couplings interfering with the SM HWW coupling. For several points along the scan we fit the likelihood and study how it changes.

8.1 Fit Results

For the final spin-0 fit results on the Constructed Variables for the 0-jet and 1-jet categories have been combined and the results on the normalisation factors, signal yield $\hat{\mu}$ and POI $\hat{\epsilon}$ are displayed in Table 8.1 and 8.2.

In Table 8.1 the normalisation factors are displayed for each control region when fixing ϵ to the SM ($\epsilon = 1$) or the alternative spin-0 ($\epsilon = 0$) hypothesis. The background normalisation factors β_{WW}, $\beta_{Z\tau\tau}$ and β_{Top} are consistent for all the different hypotheses. Also the normalisation factor μ_{norm} is very close to its nominal expectation of 1 for all the fits. Therefore, we can conclude that the normalisation factors are handled properly during the fit and do not bias the result in any particular way.

Table 8.2 shows the best fit for the POI $\hat{\epsilon}$, the signal strength $\hat{\mu}$ for various ϵ and in the last three columns the ΔLL of the different hypotheses. We can conclude three things from the respective table. 1) All the results are compatible with the SM hypothesis. 2) All the fits for $\hat{\epsilon}$ prefer the SM hypothesis above the alternative BSM spin-0 models. 3) We can predict that two models will be excluded with respect to the SM hypothesis when doing the toy MC studies, namely the interference models SM $- 0^+h$ and SM $- 0^+\partial$. The values for $\hat{\epsilon}$

Hypothesis	$\mu_{\text{norm,0j}}$	$\beta_{WW,\text{0j}}$	$\beta_{Z\tau\tau,\text{0j}}$	$\mu_{\text{norm,1j}}$	$\beta_{WW,\text{1j}}$	$\beta_{Z\tau\tau,\text{1j}}$	$\beta_{Top,1j}$
0^-: $\epsilon = 0$	1.0000 ± 0.0180	1.17 ± 0.01	0.94 ± 0.03	1.0300 ± 0.0232	1.09 ± 0.07	1.08 ± 0.04	0.99 ± 0.01
0^+h: $\epsilon = 0$	1.0000 ± 0.0118	1.17 ± 0.03	0.94 ± 0.05	1.0300 ± 0.0116	1.11 ± 0.02	1.09 ± 0.03	0.99 ± 0.03
$0^+\partial$: $\epsilon = 0$	1.0000 ± 0.0066	1.17 ± 0.01	0.95 ± 0.03	1.0200 ± 0.0139	1.10 ± 0.02	1.08 ± 0.03	1.00 ± 0.01
SM + 0^-: $\epsilon = 0$	0.9990 ± 0.0103	1.17 ± 0.01	0.94 ± 0.02	1.0200 ± 0.0147	1.10 ± 0.04	1.09 ± 0.03	0.99 ± 0.01
SM − 0^-: $\epsilon = 0$	1.0000 ± 0.0068	1.17 ± 0.01	0.94 ± 0.02	1.0200 ± 0.0145	1.10 ± 0.03	1.08 ± 0.03	1.00 ± 0.01
SM + 0^+h: $\epsilon = 0$	1.0000 ± 0.0105	1.17 ± 0.02	0.94 ± 0.04	1.0200 ± 0.0123	1.11 ± 0.02	1.09 ± 0.03	0.99 ± 0.02
SM − 0^+h: $\epsilon = 0$	1.0300 ± 0.0559	1.18 ± 0.03	0.91 ± 0.04	1.0400 ± 0.0228	1.08 ± 0.03	1.04 ± 0.06	0.99 ± 0.02
SM + $0^+\partial$: $\epsilon = 0$	1.0000 ± 0.0066	1.17 ± 0.01	0.94 ± 0.02	1.0200 ± 0.0163	1.10 ± 0.02	1.09 ± 0.03	1.00 ± 0.01
SM − $0^+\partial$: $\epsilon = 0$	1.0100 ± 0.0361	1.17 ± 0.01	0.93 ± 0.04	1.0300 ± 0.0222	1.06 ± 0.08	1.04 ± 0.07	1.00 ± 0.02
0^-: $\epsilon = 1$	1.0000 ± 0.0063	1.17 ± 0.01	0.94 ± 0.03	1.0200 ± 0.0118	1.10 ± 0.04	1.08 ± 0.03	1.00 ± 0.01
0^+h: $\epsilon = 1$	1.0000 ± 0.0066	1.17 ± 0.02	0.94 ± 0.04	1.0200 ± 0.0123	1.10 ± 0.02	1.09 ± 0.03	0.99 ± 0.01
$0^+\partial$: $\epsilon = 1$	1.0000 ± 0.0066	1.17 ± 0.01	0.94 ± 0.02	1.0200 ± 0.0106	1.10 ± 0.02	1.08 ± 0.03	1.00 ± 0.01
SM + 0^-: $\epsilon = 1$	0.9990 ± 0.0063	1.17 ± 0.01	0.94 ± 0.02	1.0200 ± 0.0106	1.10 ± 0.02	1.09 ± 0.03	0.99 ± 0.01
SM − 0^-: $\epsilon = 1$	1.0000 ± 0.0063	1.17 ± 0.01	0.94 ± 0.02	1.0200 ± 0.0104	1.10 ± 0.02	1.08 ± 0.03	1.00 ± 0.01
SM + 0^+h: $\epsilon = 1$	1.0000 ± 0.0063	1.17 ± 0.01	0.94 ± 0.02	1.0200 ± 0.0118	1.10 ± 0.02	1.09 ± 0.03	0.99 ± 0.01
SM − 0^+h: $\epsilon = 1$	1.0100 ± 0.0506	1.17 ± 0.02	0.95 ± 0.05	1.0200 ± 0.0248	1.11 ± 0.04	1.09 ± 0.07	1.00 ± 0.01
SM + $0^+\partial$: $\epsilon = 1$	1.0000 ± 0.0065	1.17 ± 0.01	0.94 ± 0.02	1.0200 ± 0.0100	1.10 ± 0.02	1.08 ± 0.03	0.99 ± 0.01
SM − $0^+\partial$: $\epsilon = 1$	1.0100 ± 0.0158	1.17 ± 0.01	0.95 ± 0.03	1.0200 ± 0.0176	1.10 ± 0.10	1.08 ± 0.08	1.00 ± 0.03

Table 8.1: The best fit values for the normalisation μ_{norm} and the normalisation factors β for the WW, $Z \to \tau\tau$ and Top control regions after doing the conditional $\epsilon = 1$ (SM) and $\epsilon = 0$ (BSM spin-0 or BSM/SM mixture) fits including all theoretical and detector systematic uncertainties.

Hypothesis	$\hat{\epsilon}$	$\hat{\mu}_{\hat{\epsilon}}$	$\hat{\mu}_{\epsilon=1}$	$\hat{\mu}_{\epsilon=0}$	$\Delta LL^{\hat{\epsilon}}_{\epsilon=1}$	$\Delta LL^{\hat{\epsilon}}_{\epsilon=0}$	$\Delta LL^{\epsilon=1}_{\epsilon=0}$
0^-	1.12 ± 0.74	1.22 ± 0.09	1.23 ± 0.22	1.18 ± 0.18	0.05	1.12	1.07
0^+h	1.87 ± 0.76	1.40 ± 0.41	1.22 ± 0.26	0.96 ± 0.20	0.71	2.23	1.52
$0^+\partial$	3.21 ± 1.94	1.40 ± 0.59	1.23 ± 0.24	1.14 ± 0.23	0.53	0.91	0.38
$SM + 0^-$	2.02 ± 2.21	1.23 ± 0.11	1.23 ± 0.09	1.23 ± 0.09	0.13	0.34	0.21
$SM - 0^-$	1.28 ± 1.82	1.22 ± 0.09	1.22 ± 0.09	1.22 ± 0.09	0.05	0.20	0.15
$SM + 0^+h$	2.20 ± 1.10	1.40 ± 0.46	1.23 ± 0.27	1.05 ± 0.22	0.62	1.55	0.93
$SM - 0^+h$	0.79 ± 0.18	1.36 ± 0.09	1.23 ± 0.22	1.09 ± 0.23	0.27	5.22	4.94
$SM + 0^+\partial$	3.36 ± 2.63	1.29 ± 0.37	1.23 ± 0.23	1.18 ± 0.23	0.33	0.56	0.23
$SM - 0^+\partial$	0.73 ± 0.28	1.37 ± 0.09	1.23 ± 0.19	1.41 ± 0.14	0.25	2.55	2.30

Table 8.2: Outcome of the fit results, including all the theoretical and detector systematic uncertainties, for the SM compared to the alternative spin-0 and SM interference models. $\hat{\epsilon}$ indicates the preference of the data for the SM or the alternative model. $\hat{\mu}$ indicates the signal strength to be used for the best fit. The last three columns show the ΔLL; the first two are the fits with ϵ fixed compared to the unconditional fit and the last one is the SM hypothesis compared with respect to the BSM spin-0 or SM interference model.

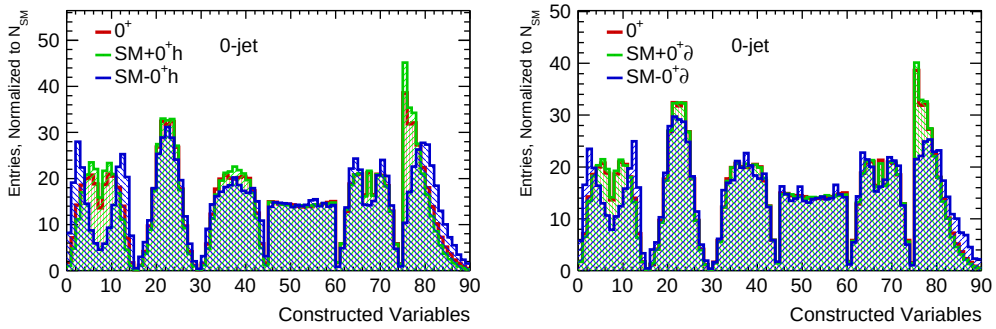

Figure 8.1: The Constructed Variables for the 0-jet category for the SM hypothesis compared to SM interference with positive/negative κ_{HWW} terms (left) and SM interference with positive/negative $\kappa_{H\partial W}$ terms (right). Due to the destructive interference between the SM coupling κ_{SM} and the negative $\kappa_{HWW}/\kappa_{H\partial W}$ terms, some of the kinematic variables get significant shape changes.

are 0.79 ± 0.18 and 0.73 ± 0.28 for each unconditional fit respectively. Firstly, due to the relative small error it shows the good discrimination power between the SM and these two interference models. This is also reflected in the ΔLL values in the last column. Secondly, $\hat{\epsilon}$ is for both fits more than two standard deviations away from $\epsilon = 0$. With the toy MC studies presented later on, we can indeed show that we can exclude these two interference models with more than 95% confidence level. The discrimination power between the SM and the other 7 models is not strong enough to set exclusions. Nevertheless, the values for $\hat{\epsilon}$ and ΔLL prefer more SM-like features.

It is interesting to take a closer look at the good separation power between the SM and models where the SM interferes with negative terms of κ_{HWW} and $\kappa_{H\partial W}$. As noted in section 6.1 and based on Fig. 6.1 and App. A, the negative κ_{HWW} and $\kappa_{H\partial W}$ terms interfere maximally destructive with the κ_{SM} coupling yielding low cross-sections. Another consequence of this destructive coupling is displayed in Fig.8.1, where the Constructed Variables are shown for the SM together with the SM interference models with positive and negative κ_{HWW} and $\kappa_{H\partial W}$ terms. For the negative κ_{HWW} and $\kappa_{H\partial W}$ terms, the $\Delta\phi_{ll}^{cs}$ and Σp_{ll}^{cs} get significant shape changes. Other variables like $\Delta\theta_{ll}^{cs}$ and Δp_{ll}^{cs} also change shape, but in lesser amounts.

8.1.1 Impact of Systematic Uncertainties

The bias and pull of the nuisance parameters as well as their impact on the POI for the 0^- model are shown in Fig.8.2. The definitions of the bias, pull, postfit and prefit are given in section 7.1.1. From the figure there is no indication that any of the nuisance parameters is

biased or over-constrained. It is also evident that the statistical uncertainty on $\hat{\epsilon}$ is much larger, about one order, than the largest impact of the nuisance parameters, making the fit result dominated by the statistical uncertainty.

The impact studies on the other BSM spin-0 models and SM interference models give similar results, so also there the fit results are dominated by the statistical uncertainty. This is also the case for the SM-0^+h and SM$-0^+\partial$ models, where there is the strongest separation power compared to the SM hypothesis. Therefore, the nuisance parameters do not bias the final fit result and behave as expected for all the BSM spin-0 and SM interference models.

8.1.2 MC Toy Distributions

Fig. 8.3 and 8.4 show the distributions of the test statistic of the SM and the three BSM spin-0 and six SM interference models respectively. For each hypothesis 5000 toy data sets were generated. One immediate feature of both figures is that the best fit for the data prefers values for the test statistic that are more SM-like. The distributions for 0^- and 0^+h are still distinguishable from the SM distribution, while the $0^+\partial$ distribution is almost identical due to the low discrimination power between the two models. Also, most of the SM interference models are very much on top of the SM distribution, besides the SM-0^+h and SM$-0^+\partial$ distributions, as was expected from the results of the likelihood fit. The data is very close to the SM expectation and strong exclusion limits can be set on these two particular models.

8.1.3 Exclusion Limits on Spin-0 Models

Table 8.3 displays the expected and observed p values for the SM hypothesis and the spin-0 models based on the distributions in Fig.8.3 and 8.4. The last column shows the confidence level on the exclusion for the alternative model with respect to the SM. The strongest exclusion limit can be set on the SM-0^+h model with 99.9% confidence level, followed by the SM$-0^+\partial$ model with an exclusion at 98.4% confidence level. The other BSM spin-0 models and SM interference models are well below the 95% limit and can not be excluded with the analysis presented in this thesis.

In App.C, the toy distributions of the test statistic q and the exclusion limits for the spin-0 results are split up for each jet category. It is worth to notice that for almost all distributions there is preference for the SM hypothesis, except for the 1-jet distributions where both the SM-0^+h and SM$-0^+\partial$ interference models are tested with respect to the SM. For these cases there is a preference for the alternative model, but the very strong preference for the SM in the 0-jet overrules this result when the 0-jet and 1-jet are combined.

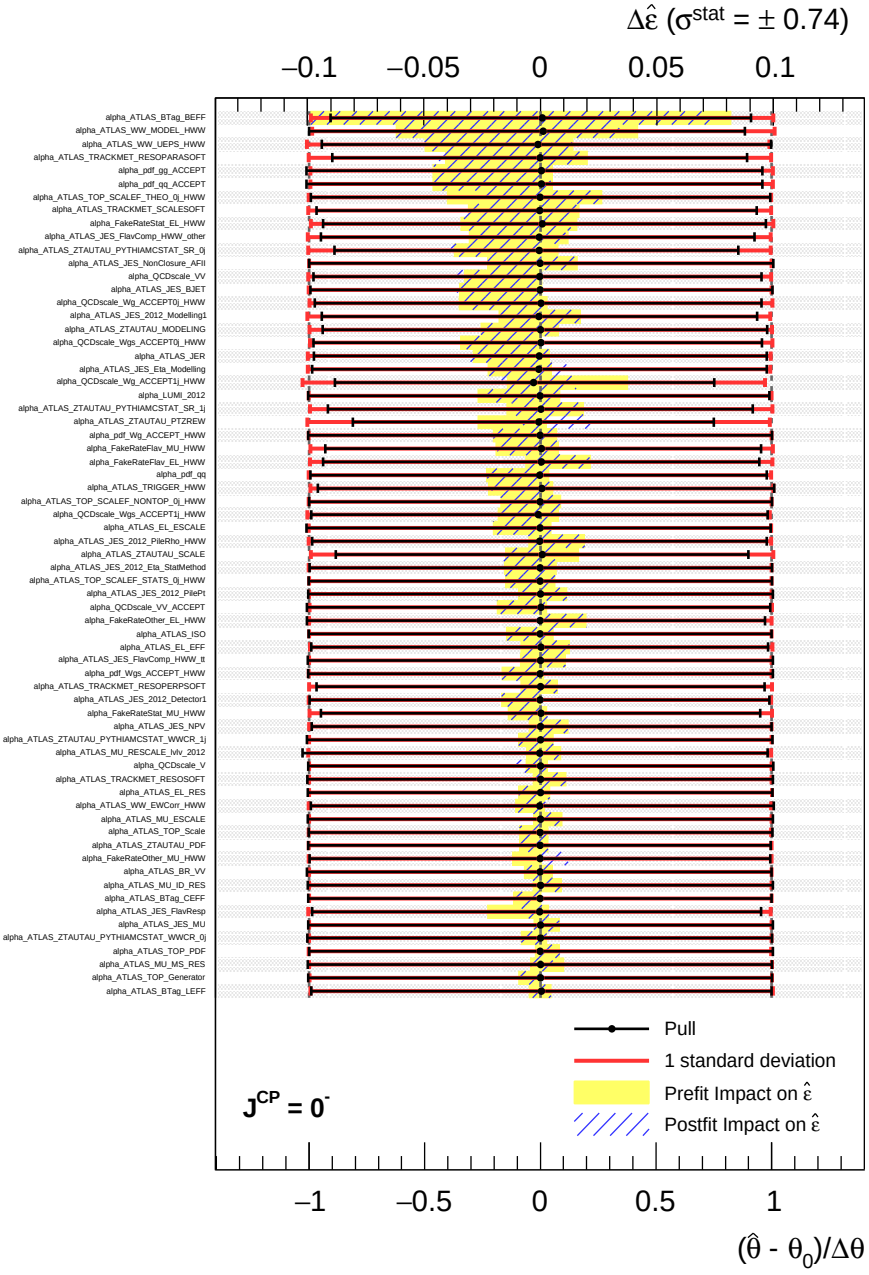

Figure 8.2: Pulls of the main systematic uncertainties and their impact on the POI $\hat{\epsilon}$, when doing the unconditional fit of the 0^- model compared to the SM hypothesis. The nuisance parameters are ordered with decreasing impact on the POI. The statistical uncertainty on $\hat{\epsilon}$ is also indicated at the top in the brackets.

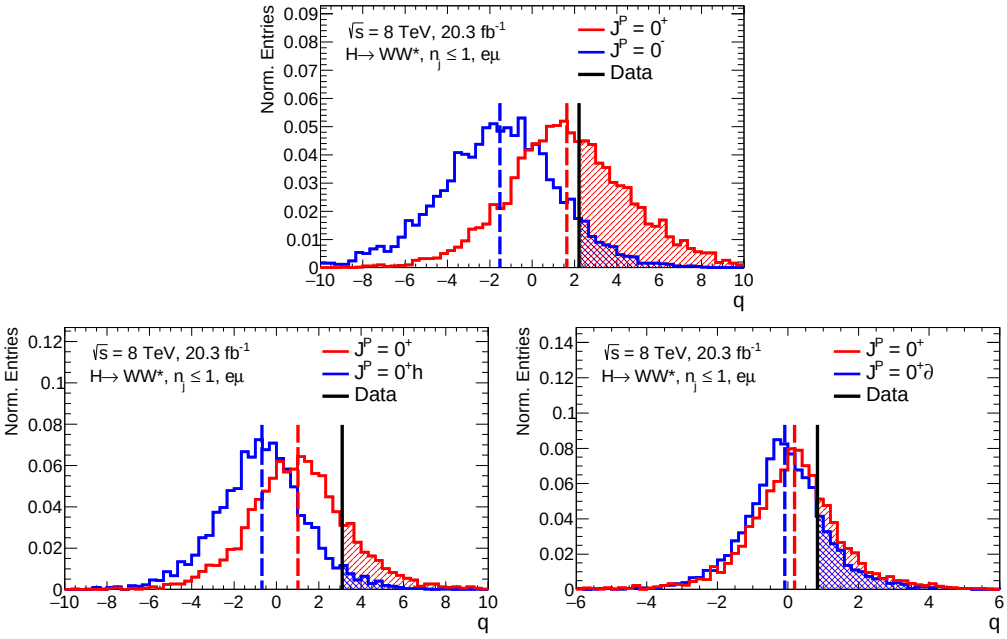

Figure 8.3: Distributions of the test statistic q for the SM hypothesis versus the 0^-, 0^+h and $0^+\partial$ models. For each distribution 5000 toys have been generated, assuming either the SM hypothesis or one of the BSM spin-0 models as input.

Hypothesis	p^{SM}_{exp}	p^{alt}_{exp}	p^{SM}_{obs}	p^{alt}_{obs}	Z^{SM}_{obs}	Z^{alt}_{obs}	$1-\mathrm{CL_s}$
0^-	0.117	0.119	0.417	0.081	0.2	1.4	80.7%
0^+h	0.218	0.186	0.172	0.039	0.9	1.8	77.1%
$0^+\partial$	0.394	0.390	0.275	0.190	0.6	0.9	31.0%
$\mathrm{SM}+0^-$	0.381	0.388	0.384	0.281	0.3	0.6	26.8%
$\mathrm{SM}-0^-$	0.363	0.357	0.458	0.322	0.1	0.5	29.7%
$\mathrm{SM}+0^+h$	0.292	0.283	0.210	0.085	0.8	1.4	59.5%
$\mathrm{SM}-0^+h$	0.002	0.000	0.382	0.001	0.3	3.2	99.9%
$\mathrm{SM}+0^+\partial$	0.427	0.416	0.330	0.254	0.4	0.7	23.1%
$\mathrm{SM}-0^+\partial$	0.007	0.003	0.329	0.011	0.4	2.3	98.4%

Table 8.3: Expected and observed exclusion limits for the SM, the alternative spin-0 and the SM interference models based on the Fig. 8.3 and 8.4. The last column displays the exclusion limits for the alternative hypotheses based on the $\mathrm{CL_s}$ method (See section 6.6.1).

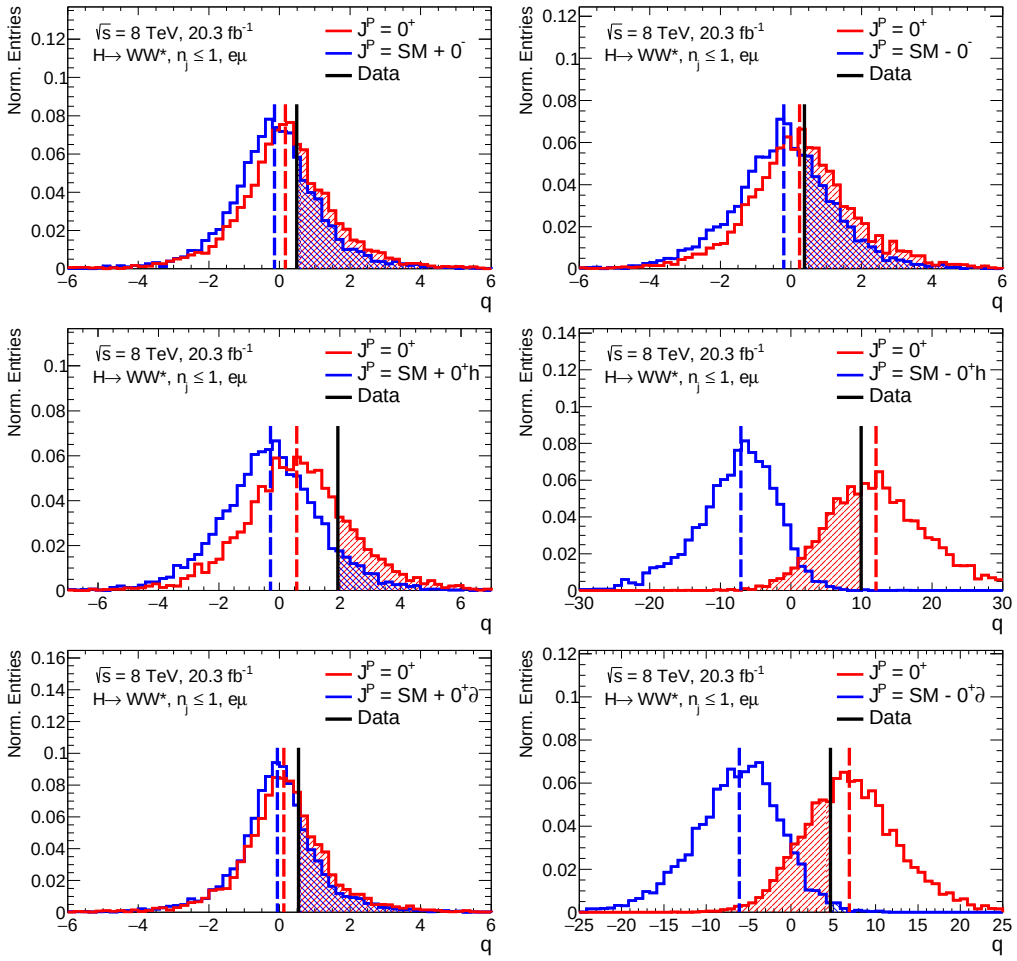

Figure 8.4: Distributions of the test statistic q for the SM hypothesis and the six spin-0 SM interference models. For each distribution 5000 toys have been generated, assuming either the SM hypothesis or one of the SM interference models as input.

8.1.4 Other ATLAS Results

We compare the obtained exclusion limits presented in this thesis with two other analysis studying the spin and CP of the Higgs performed within the ATLAS collaboration. One uses a BDT discriminant of lab-frame kinematic variables, described in Ref. [112] and the other one uses variables defined in the Higgs rest-frame, described in Ref. [16]. Section 7.3 gives a more detailed description of these two analyses. Not all the BSM spin-0 models studied in this thesis are studied in the other two analysis. The study performed in Ref. [16] only sets a limit on the pseudoscalar Higgs with 98.2% confidence level (expected

Scan Over	κ_{SM}	κ_{HWW}	$\kappa_{H\partial W}$	κ_{AWW}	α	$\tan(\alpha)$	Λ
κ_{HWW}/κ_{SM}	1	$[-9;9]$	0	0	0	0	59
$\kappa_{H\partial W}/\kappa_{SM}$	1	0	$[-9;9]$	0	0	0	143
$\tan(\alpha)\cdot\kappa_{AWW}/\kappa_{SM}$	1	0	0	1	$[0;\pi]$	$[-9;9]$	62

Table 8.4: Settings used for the CP mixing studies. Only one BSM spin-0 coupling is allowed to mix with the SM κ_{SM}. The brackets indicate the ranges from which the grid points are chosen for the scan. Note the similarity of the settings with the ones from Table 6.2.

p value of 11.5%) and no SM interference models are studied. The study with the BDT discriminant sets limits on the pseudoscalar Higgs and a BSM spin-0 model (0^+h) at 96.5% and 70.8% confidence level respectively, while their expected p values are 3.2% and 28.7% respectively. The derivative operator model, $0^+\partial$ is not taken into account.

8.2 CP Mixing Studies

This section will describe a study performed on the mixing of CP-even or CP-odd BSM spin-0 coupling interfering with the SM HWW coupling. The used settings are exactly the same as the SM interference models defined in Table 6.2, but for the CP mixing the BSM couplings κ_{HWW}, $\kappa_{H\partial W}$ and the mixing parameter α are allowed to vary. For the CP-even mixing, a scan over positive and negative values of κ_{HWW} and $\kappa_{H\partial W}$ is performed, while interfering with κ_{SM}. For the CP-odd scan the κ_{AWW} and κ_{SM} terms are fixed, but the parameter α is varied from values between 0 and π. For each variable parameter a certain range is chosen and along this range several grid points are selected, for which we do a fit to determine the likelihood. The likelihood will then be compared to the SM likelihood, resulting in a scan of the likelihood over the respective range. For the grid points only the theoretical systematic uncertainties are included. As pointed out in the section 8.1.1, the statistical uncertainty is dominating, therefore, the detector systematic uncertainties can be left out without compromising the results. Only one BSM spin-0 coupling at a time was chosen to interfere with the SM.

The settings for CP mixing studies are displayed in Table 8.4. The BSM spin-0 couplings are normalised with respect to the SM coupling κ_{SM}, even though this one is fixed to 1. The reason for this is to show explicitly that the ratio κ_{BSM}/κ_{SM} is important to quantify the degree of interference between the two terms (given a fixed Λ and α). It gives the freedom to pick arbitrary values for κ_{BSM} and κ_{SM}, but the result will always be the same if the ratio is kept fixed to a certain value.

The sensitivities of the results along the scan are estimated by using the asymptotic approximation, which is simpler but less time consuming than the toy experiments[125]. For each scan point a fit is performed and the likelihood extracted. This is then compared to the likelihood from the SM prediction in terms of the quantity -2ΔLL, which is just the test statistic q as defined in Eq.6.11. The SM prediction has a -2ΔLL = 0, because the numerator and denominator in Eq.6.11 are then the same. The SM also predicts that this will be the minimum value for the test statistic of the scan, because any interference with κ_{BSM} can only increase the test statistic, indicating more discrepancy with the SM expectation. Note that for the previously presented results for spin-2 and BSM spin-0 models there was no such prediction for the minimum of the test statistic a priori. When we do the fit to data, there is no restriction to the minimum of -2ΔLL. For instance, a point along the scan with a negative value for the test statistic means a preference of the data for this particular point above the SM. The values -2ΔLL = 1 and -2ΔLL = 3.84 correspond respectively to the 68% and 95% exclusion limits with respect to the SM hypothesis.

It should be pointed out that the six SM interference models from Table 6.2 represent fixed points along the scans used for the CP mixing studies. The scans can give us information how the sensitivity of the analysis changes when moving around these points. To put it another way, the results of the SM interference models from Table 8.3 can be considered as cross-checks for the corresponding points along the scans.

8.2.1 CP-even Mixing Scans

For the CP-even mixing κ_{HWW} and $\kappa_{H\partial W}$ a range is chosen starting from -9 to 9 and the amount and the places of grid points are chosen such to capture the changes in the likelihood with a high enough resolution. The SM coupling κ_{SM} and cos(α) are set equal to 1 for each grid point, so only at the point where κ_{HWW} and $\kappa_{H\partial W}$ are 0 would yield the SM expectation. The cutoff scale Λ is chosen in accordance with Table 6.2, so a maximal interference with the SM is expected at -1 for κ_{HWW} or $\kappa_{H\partial W}$ as was pointed out in section 6.1 and visible in Fig.8.1. At the border of the range, the BSM couplings are so strong that the interference sample can effectively be considered as a pure κ_{HWW} or $\kappa_{H\partial W}$ sample and similar results for the ΔLL can be expected as in Table 8.2.

Fig. 8.5 and 8.6 show the expected (blue) and observed (black) results of the κ_{HWW}/κ_{SM} and $\kappa_{H\partial W}/\kappa_{SM}$ scans in terms of -2ΔLL. The peak in the distributions of the SM expectation around $\kappa_{HWW}/\kappa_{SM} = -1$ and $\kappa_{H\partial W}/\kappa_{SM} = -1$ are due to the strong shape changes with respect to the SM as discussed before. For more negative or positive values of κ_{HWW}/κ_{SM} and $\kappa_{H\partial W}/\kappa_{SM}$ the expected sensitivities are very low, because there is almost no discrimination power between the SM hypothesis and these scan points. In the observed results

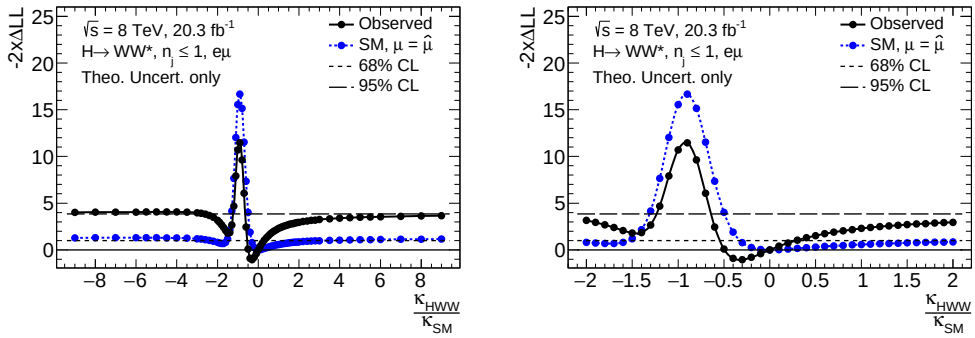

Figure 8.5: Scan over κ_{HWW}/κ_{SM} as defined in Table 8.4. Only the statistical and theoretical uncertainties are included. The result is expressed in terms of -2ΔLL with respect to the SM. The blue line and dots are the SM expectation, while the black line and dots are the observed data. Also the 68% and 95% exclusion levels are shown with respect to the SM. On the right, a close up of the peak structure and the minima.

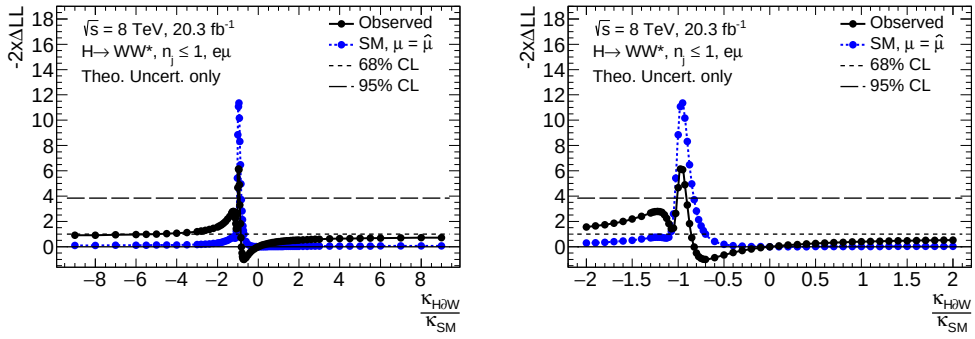

Figure 8.6: Scan over $\kappa_{H\partial W}/\kappa_{SM}$ as defined in Table 8.4. Only the statistical and theoretical uncertainties are included. The result is expressed in terms of -2ΔLL with respect to the SM. The blue line and dots are the SM expectation, while the black line and dots are the observed data. Also the 68% and 95% exclusion levels are shown with respect to the SM. On the right, a close up of the peak structure and the minima.

we see as well large peaks around $\kappa_{HWW}/\kappa_{SM} = -1$ and $\kappa_{H\partial W}/\kappa_{SM} = -1$, but the sensitivity is not as strong as expected. The observed κ_{HWW}/κ_{SM} scan, shows to be more sensitive overall than would be expected and is in general consistent with the expectation.

The 68% and 95% exclusion lines in Fig.8.5 and 8.6 are with respect to the SM. Table 8.5 shows the observed best fit values and which ranges are expected and which are observed to be excluded at 95% confidence limit. The observed scans show that the best fits are at $\kappa_{HWW}/\kappa_{SM} = -0.3^{+0.50}_{-0.20}$ and $\kappa_{H\partial W}/\kappa_{SM} = -0.7^{+\infty}_{-0.15}$. The up and down errors are chosen to be the points, where the black observed line crosses the 68% line. The ∞ sign indicates

that this 68% line is never crossed. This is not so strange, considering the fact that the analysis almost has no sensitivity to discriminate the SM hypothesis from the $0^+\partial$ model as can be seen from the toy distributions in Fig.8.3. Even though the data prefers a different minimum in the κ_{HWW}/κ_{SM} and $\kappa_{H\partial W}/\kappa_{SM}$ scans than the SM predicts, the discrepancy of the SM with respect to these minima are about one standard deviation (-2ΔLL ≈ -1.0). Therefore, the CP-even mixing scans confirm the overall compatibility of the data with the SM hypothesis and the scan points in the close proximity of the SM prediction.

The CP-even scan results for the 0-jet and 1-jet have been done separately as well and the corresponding figures can be found in App.C. It is interesting to point out that the observed scan result for the 0-jet category is very much in line with the SM expectation. The 1-jet on the other hand, shows large dips around $\kappa_{HWW}/\kappa_{SM} = -1.0$ and $\kappa_{H\partial W}/\kappa_{SM} = -1.0$, indicating a preference for these scan points above the SM. Also the 1-jet toy distributions of the test statistic q for the SM-0^+h and SM$-0^+\partial$ (as well in App.C) show a preference for the SM interference model above the SM expectation. The preference disappears when combining the 0-jet and 1-jet categories, but it would be interesting to see if the trend in the 1-jet scan continues in future data sets and becomes more significant.

8.2.2 CP-odd Mixing Scan

For the CP-odd mixing a scan was performed over $\tan(\alpha)\cdot\kappa_{AWW}/\kappa_{SM}$ with $\tan(\alpha)$ to be in the range from -9 to 9. κ_{SM}, κ_{AWW} and Λ are defined in Table 8.4. The amount of grid points are chosen such to get a good resolution of the -2ΔLL shape. The expected (blue) and observed (black) results are shown in Fig. 8.7. The observed scan agrees well with what is expected, but there is a small shift in the observed minimum as can be seen in the zoom-in of the scan on the right of Fig.8.7. The observed minimum is at $\tan(\alpha)\cdot\kappa_{AWW}/\kappa_{SM} = -0.3$, but its value of -2$\Delta$LL is barely different from the SM. The minimum of the SM expectation is shifted to $\tan(\alpha)\cdot\kappa_{AWW}/\kappa_{SM} = 0.25$ and is supposed to be at 0. The fit is having problems to properly discriminate points to which the analysis has almost no sensitivity. Seen the very small impact this has on the value of -2ΔLL it is no reason for concern.

The CP-odd mixing scan is not sensitive enough to set limits at 95% confidence level. The best fit value for the data is at $\tan(\alpha)\cdot\kappa_{AWW}/\kappa_{SM} = -0.3^{+2.70}_{-2.40}$ and is displayed with all the CP-mixing results in Table 8.5. The up and down errors are the points where the black observed line crosses the 68% line. In App.C the $\tan(\alpha)\cdot\kappa_{AWW}/\kappa_{SM}$ scan results are shown for the 0-jet and 1-jet categories separately. The observed data shows, contrary to the expectation, a maximum at the SM expectation of $\tan(\alpha)\cdot\kappa_{AWW}/\kappa_{SM} = 0.0$ for the 1-jet events. From the 1-jet toy distribution of the test statistic q for testing the SM versus the BSM 0^-, we can see that there is a very small 0^- preference. The grid points become

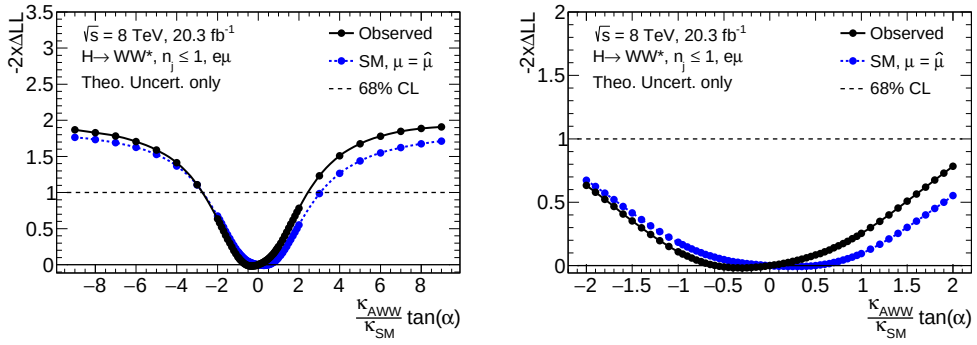

Figure 8.7: Scan over $\tan(\alpha)\cdot\kappa_{AWW}/\kappa_{SM}$ as defined in Table 8.4. Only the statistical and theoretical uncertainties are included. The result is expressed in terms of -2ΔLL with respect to the SM. The blue line and dots are the SM expectation, while the black line and dots are the observed data. Also the 68% exclusion level is shown with respect to the SM. On the right, a close up of the minimum.

Scan Over	Best fit value	95% CL Exclusion regions	
	observed	Expected	Observed
κ_{HWW}/κ_{SM}	$-0.3^{+0.50}_{-0.20}$	$[-1.30\,;-0.50]$	$[-9.00\,;-2.80]$ & $[-1.20\,;-0.70]$
$\kappa_{H\partial W}/\kappa_{SM}$	$-0.7^{+\infty}_{-0.15}$	$[-1.03\,;-0.85]$	$[-1.00\,;-0.93]$
$\tan(\alpha)\cdot\kappa_{AWW}/\kappa_{SM}$	$-0.3^{+2.70}_{-2.40}$	–	–

Table 8.5: The observed best fit values and expected versus observed ranges for the CP-even and CP-odd scans that can be excluded at 95% confidence level with respect to the SM. The ∞ sign indicates that the interference sample can effectively be replaced by a pure BSM CP-even coupling.

gradually more 0^- like when moving away from $\tan(\alpha)\cdot\kappa_{AWW}/\kappa_{SM} = 0.0$ and causing the observed line to go down.

8.3 Summary

In this chapter the results have been presented for the analysis on spin-0 Higgs models. Three samples with a BSM spin-0 resonance and six samples where the SM interferes with a CP-even or CP-odd spin-0 coupling were created and were defined in Table 6.2. The best fit values for the normalisation factors and the impact studies of the nuisance parameters indicate that the results are reliable and are dominated by the statistical uncertainties. The

results for fitting the POI $\hat{\epsilon}$ and signal yields $\hat{\mu}$ are displayed in Table 8.2. It shows that all results are compatible with the SM hypothesis, that the data has an overall preference for the SM and that the $SM-0^+h$ and $SM-0^+\partial$ models can be excluded with respect to the SM hypothesis.

Toy MC distributions have been generated to put the spin-0 fit results into perspective. The toy MC studies confirm the results of the fit and the $SM-0^+h$ and $SM-0^+\partial$ models have observed exclusion limits at 99.9% and 98.4% CL respectively. The other BSM spin-0 and SM interference models can not be excluded at the 95% CL, but there is an observed preference for the SM hypothesis in all cases.

The results of the 0^- and 0^+h models have been compared to two other analysis performed within the ATLAS collaboration. One uses a BDT discriminant[112] and the others kinematic variables defined in the Higgs rest-frame[16]. The former analysis sets limits on the 0^- and 0^+h models at 96.5% and 70.8% CL respectively. The later analysis only studies the 0^- model and sets an exclusion limit at 98.2% CL.

Furthermore, in the context of CP mixing studies samples were created with CP-even or CP-odd BSM HWW couplings interfering with the SM HWW coupling at various strengths. Scans have been performed over κ_{HWW}/κ_{SM} and $\kappa_{H\partial W}/\kappa_{SM}$ to test the CP-even mixing and a scan over $\tan(\alpha)\cdot\kappa_{AWW}/\kappa_{SM}$ tested the CP-odd mixing. Along the scans a likelihood fit was performed and compared to the SM likelihood fit in terms of the test statistic -2ΔLL. The set of grid points was chosen such as to get a good resolution of the -2ΔLL distribution. Exclusions on the CP mixing have been obtained by setting limits at the 95% CL with respect to the SM expectation. For the κ_{HWW}/κ_{SM} scan the fit to data excludes the $[-9.00\,;-2.80]$ and $[-1.20\,;-0.70]$ regions at 95% CL. For the $\kappa_{H\partial W}/\kappa_{SM}$ scan the fit to data excludes the region $[-1.00\,;-0.93]$ at 95% CL. For the CP-even scans the data has the best fit at $\kappa_{HWW}/\kappa_{SM} = -0.3^{+0.50}_{-0.20}$ and $\kappa_{H\partial W}/\kappa_{SM} = -0.7^{+\infty}_{-0.15}$, where the ∞ sign indicates that the SM interference sample can effectively be replaced by a pure $0^+\partial$ sample. The minima are about one standard deviation of the SM expectation, so there is no discrepancy with the SM hypothesis. For the $\tan(\alpha)\cdot\kappa_{AWW}/\kappa_{SM}$ scan there are no regions that can be excluded at the 95% limit. The best fit at $\tan(\alpha)\cdot\kappa_{AWW}/\kappa_{SM} = -0.3^{+2.70}_{-2.40}$ is compatible with the SM hypothesis.

It is interesting to see that there is preference for the SM-0^+h and SM$-0^+\partial$ models above the SM expectation when looking at the 1-jet events. This preference is also reflected in the κ_{HWW}/κ_{SM} and $\kappa_{H\partial W}/\kappa_{SM}$ scans when there is a maximum destructive interference around -1.0. More data from the future runs of the ALTAS detector should point out if this is a significant trend or not.

Conclusion and Outlook

9

In this thesis I have presented the spin and parity measurement in the $H \to WW \to e\nu_e \mu\nu_\mu$ channel in combination with zero or one jet. The goal was to test if the discovered Higgs-like boson is compatible with the SM prediction, which states that it is a parity-even spin-0 particle. For the analysis we used the full 2012 data set of 20.3 fb^{-1}, which was collected with the ATLAS detector from pp collisions at an energy of $\sqrt{s} = 8$ TeV. The analysis was performed by reconstructing and studying the charged leptons from the $H \to WW \to e\nu_e \mu\nu_\mu$ channel in the Higgs rest-frame. The dineutrino system had to be reconstructed first in order to find the Higgs boost vector. The algorithm that reconstructed the dineutrino system is sensitive to the resolution of the missing transverse energy. We introduced a method to improve the transverse momentum of the Higgs boson by combining information from ATLAS's calorimeter and inner detector. The improved resolution in p_T^H resulted in a better performance of the dineutrino reconstruction algorithm.

Hypotheses have been tested where the spin can be different from zero or whether it is compatible with a parity-odd boson. By means of a statistical analysis, we compared the SM prediction with fourteen alternative spin/CP scenarios: five spin-2 bosons, three BSM spin-0 bosons and six SM interference models, where a SM Higgs boson interferes with a BSM spin-0 particle. Three mixing-studies were performed and limits were set on the mixing of a SM Higgs boson with a BSM CP-even or CP-odd spin-0 coupling.

The results of the analysis indicated that the data have a preference for two of the five spin-2 models with a significance of 2.4 σ when comparing to the SM hypothesis. We could trace back the spin-2 preference to the 1-jet events, while for the 0-jet evens the data preferred the SM hypothesis. A data compatibility test showed that the SM is still compatible with the measurement for the 1-jet events. All the spin-2 results are displayed in Table 7.3, Table 7.4 and Table 7.5.

The results for the three BSM spin-0 and the six SM interference models enabled us to exclude two SM interference models with more than 95% confidence level. In these models a SM Higgs boson destructively interferes with a higher dimensional spin-0 coupling or a spin-0 derivative operator. However, we observed that the 1-jet events showed a slight preference for the excluded SM interference models. Only when combining the 0-jet events, resulted in the exclusion of these models. The analysis was not sensitive enough to exclude the three BSM spin-0 models and the other four SM interference models, but the

data shows a preference for the SM hypothesis. All the BSM spin-0 and SM interference results can be found in Table 8.3.

The BSM CP-even and CP-odd mixing studies showed that the SM hypothesis is compatible with the measurement from data. When mixing with a higher dimensional operator or a derivative operator, we were able to exclude certain regions for the mixing parameter with more than 95% CL. For the CP-odd mixing, we were not able to exclude regions. The results of all mixing studies can be found in Table 8.5.

Other ATLAS spin and parity analyses performed on the $H \to WW \to e\nu_e \mu\nu_\mu$ channel and using the 2012 data set of 20.3 fb^{-1}, are able to put higher exclusion levels on the spin-2 and spin-0 models and even exclude some of these models at the 95% CL[16, 112]. However, only one of them is able to exclude the spin-2 model with universal coupling.

The combination[102] of $H \to WW \to e\nu_e \mu\nu_\mu$ channel with the $H \to \gamma\gamma$ and the $H \to ZZ \to 4l$ channels results in exclusions at 99.9% CL for five spin-2 models and the two BSM spin-0 models, with a pseudoscalar spin-0 coupling and a higher dimensional spin-0 coupling. The BSM spin-0 derivative operator has not been tested for the combination. Also the CMS collaboration confirms the compatibility with the SM prediction when combining several Higgs decay channels for the spin and parity measurement[126–128].

As of 2015, the LHC is collecting data for Run-II. Even though the combination of several Higgs decay channels excludes all the tested spin-2 models, it is important for analyses on the Higgs spin and parity to monitor the 1-jet events of the $H \to WW \to e\nu_e \mu\nu_\mu$ channel. It would be very interesting to see if the data preference for spin-2 and SM interference models as observed in this thesis would persist in the 1-jet events. A data set similar in size as the one obtained in 2012 and a similar analysis as presented in this thesis would be enough to give a definite answer. Seeing the excellent performance of the LHC at the moment of this writing, we should be able to answer that question at the end of 2016.

EFT Cross-section Studies

A

Appendix A

In this appendix we show the results of the cross-section studies with the aMC@NLO generator. The process was the following:

$$pp \to X_0 \to W^+W^- \to e^+ \nu_e \mu^- \bar{\nu}_\mu \tag{A.1}$$

where the X_0WW coupling is determined by the κ from the effective field theory Lagrangian defined in Eq. 1.17 from chapter 1. In order to explain Fig. A.1 and A.2 we will slightly redefine Eq. 1.17:

$$\begin{aligned}\mathscr{L}_0^W = \Big\{ & c_\alpha \kappa_{SM}\, g_{HWW}\, W_\mu^+ W^{-\mu} \\ & - \frac{1}{2}\left[c_\alpha \frac{\kappa_{HWW}}{\Lambda_1} W_{\mu\nu}^+ W^{-\mu\nu} + s_\alpha \frac{\kappa_{AWW}}{\Lambda_2} W_{\mu\nu}^+ \tilde{W}^{-\mu\nu} \right] \\ & - c_\alpha \frac{\kappa_{H\partial W}}{\Lambda_3} \left(W_\nu^+ \partial_\mu W^{-\mu\nu} + h.c. \right) \Big\} X_0. \end{aligned} \tag{A.2}$$

where $\Lambda_1 = 59$ GeV, $\Lambda_2 = 62$ GeV and $\Lambda_3 = 143$ GeV. The three Λ do not represent three cutoff scales, but convenient choices for which we can expect maximum interference from the κ_{HWW}, $\kappa_{H\partial W}$ and κ_{AWW} terms when setting them to -1.0. These settings correspond to the Λ values in Table 6.2.

In Fig.A.1 and A.2 it visible that certain settings of the κ_{BSM} in combination with κ_{SM} lead to large positive or destructive interferences. For the cross-section studies we led single or multiple κ_{BSM} terms interfere with κ_{SM}, while for the analysis presented in the main text we only allowed for one κ_{BSM} term to interfere with the SM coupling.

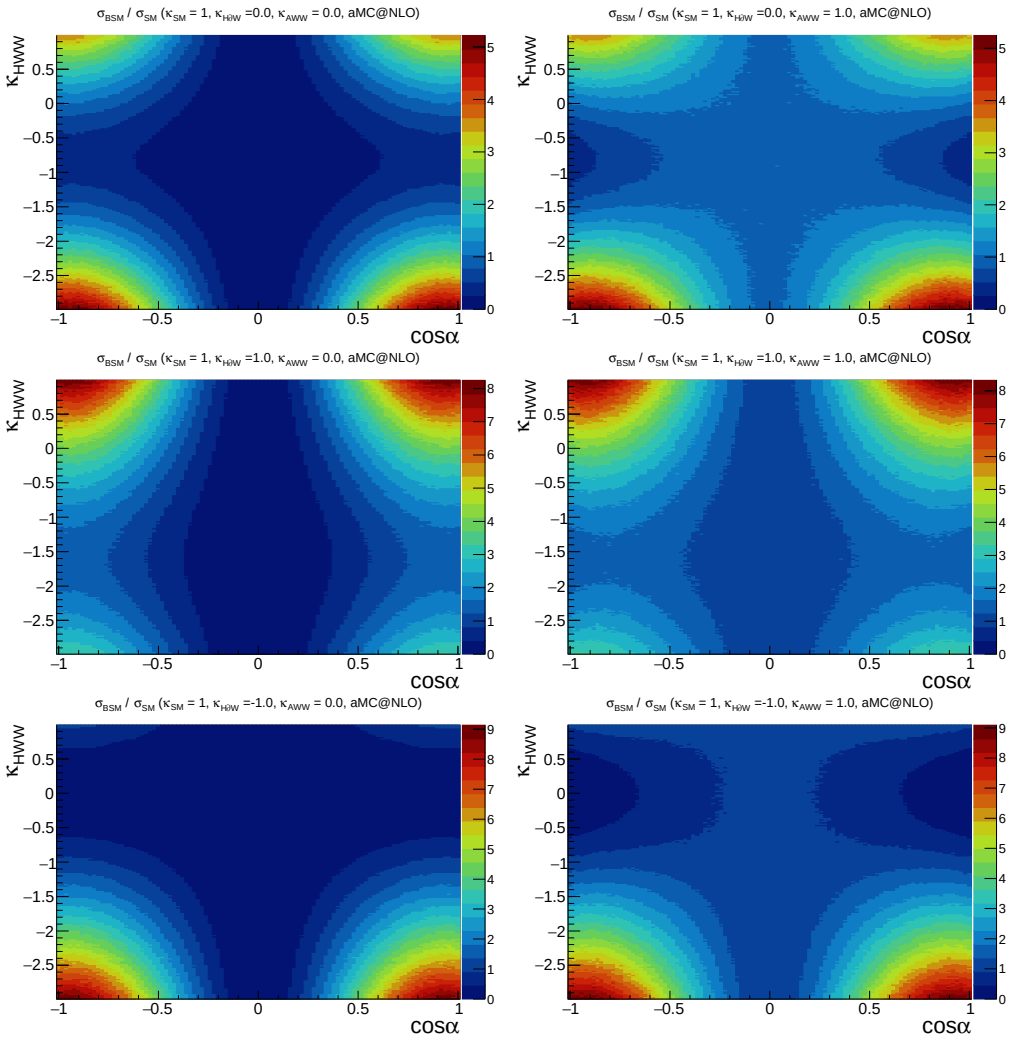

Figure A.1: Cross-section scans of κ_{SM} interfering with κ_{HWW} as a function of κ_{HWW} versus cos(α). $\kappa_{H\partial W}$ and κ_{AWW} can be either set to -1, 0 or 1, causing extra interference effects. The plot without $\kappa_{H\partial W}$ and κ_{AWW} interference (top, left), shows the destructive interference at κ_{HWW} = -1 and also shows that the cross-section then recovers and quickly rises for the more negative values of κ_{HWW}. Settings are in accordance with Eq.A.2

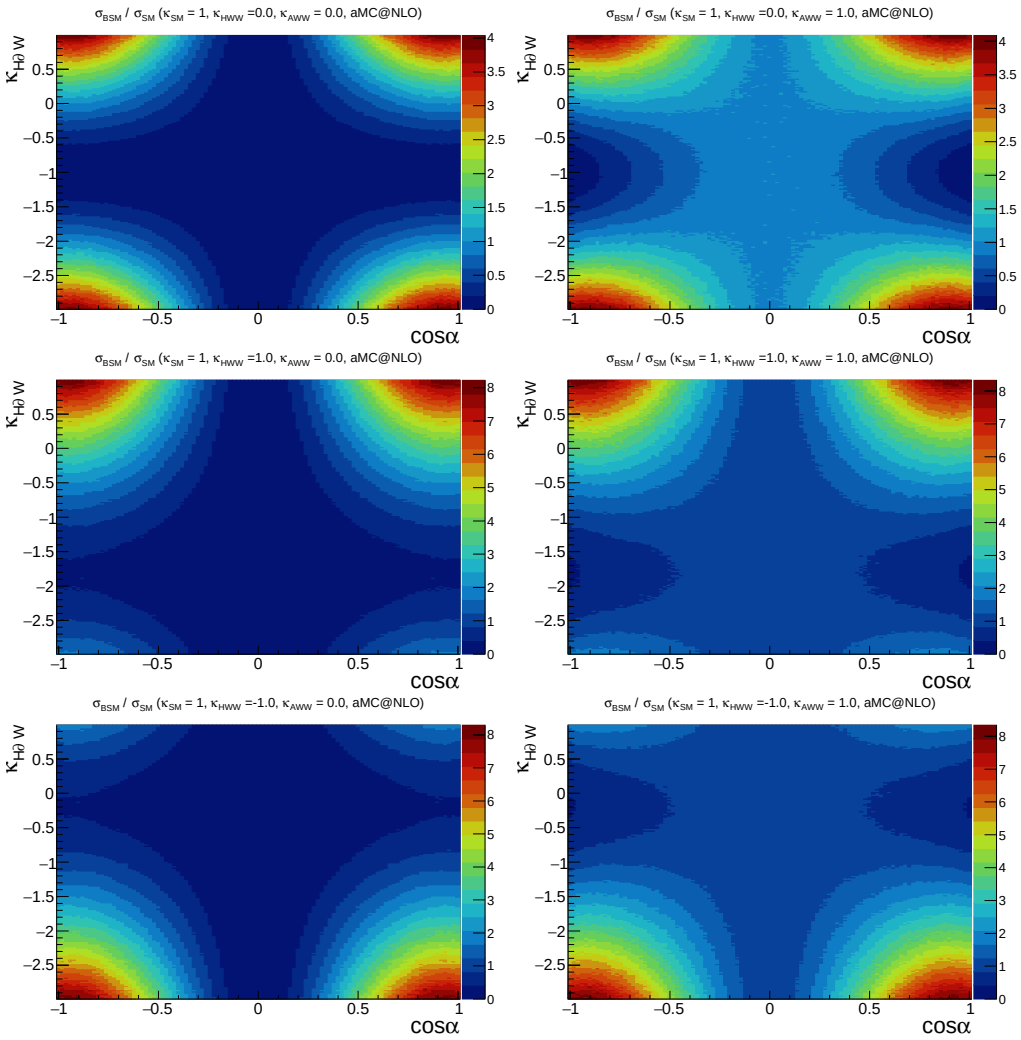

Figure A.2: Cross-section scans of κ_{SM} interfering with $\kappa_{H\partial W}$ as a function of $\kappa_{H\partial W}$ versus cos(α). κ_{HWW} and κ_{AWW} can be either set to -1, 0 or 1, causing extra interference effects. The plot without κ_{HWW} and κ_{AWW} interference (top, left), shows the destructive interference at $\kappa_{H\partial W}$ = -1 and also shows that the cross-section then recovers and quickly rises for the more negative values of $\kappa_{H\partial W}$. Settings are in accordance with Eq.A.2

Remapped Distributions

B

Appendix B

Fig. B.1 and B.2 show the distributions of the remapped variables from Table 6.4 in the signal region for the 0-jet and 1-jet categories. The variables $\Delta\phi_{ll}^{cs}$ and $\Sigma\phi_{ll}^{cs}$ did not have to be remapped and are therefore not shown here (see Fig.5.5 and 5.6).

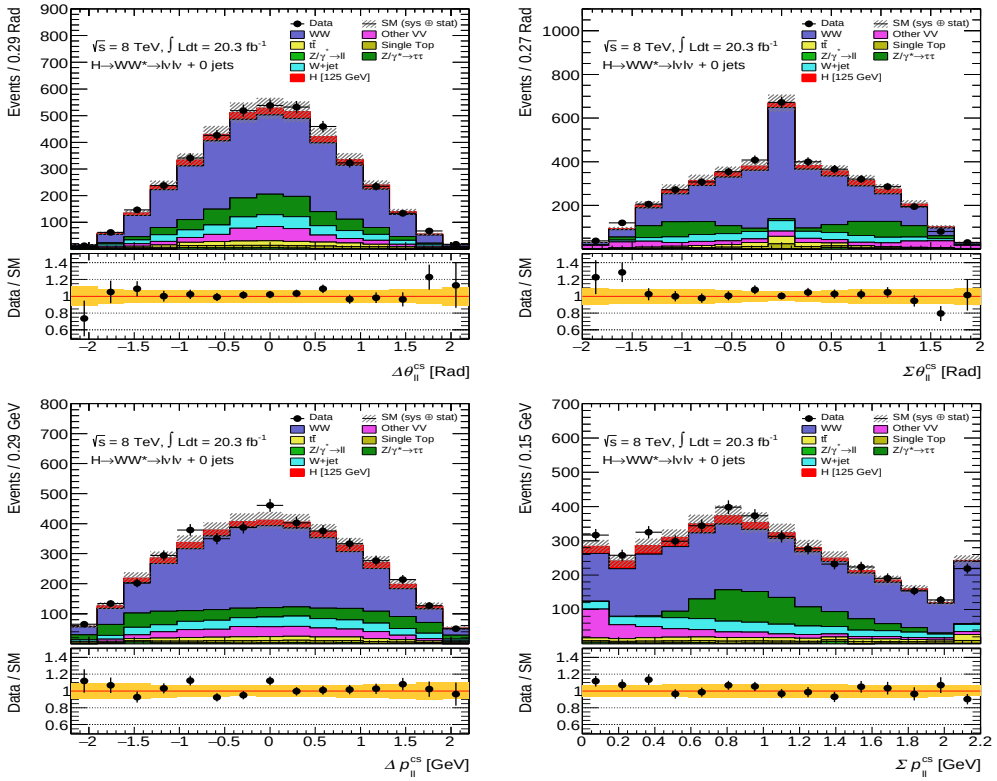

Figure B.1: Remapped $\Delta\theta_{ll}^{cs}$, $\Sigma\theta_{ll}^{cs}$, Δp_{ll}^{cs} and Σp_{ll}^{cs} distributions for the Signal Region 0-jet category. Preselection cuts and 0-jet final selection cuts have been applied.

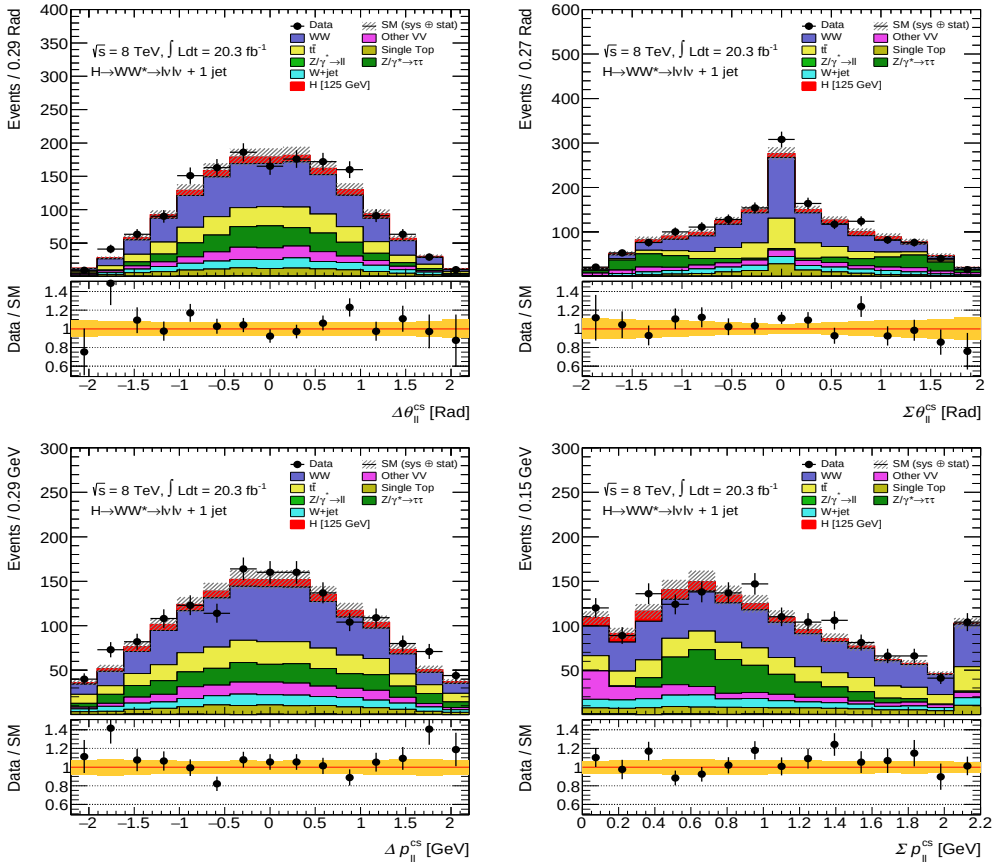

Figure B.2: Remapped $\Delta\theta_{ll}^{cs}$, $\Sigma\theta_{ll}^{cs}$, Δp_{ll}^{cs} and Σp_{ll}^{cs} distributions for the Signal Region 1-jet category. Preselection cuts and 1-jet final selection cuts have been applied.

Results per Jet Category

C

Appendix C

In this appendix we split up the results of the toy MC studies of all spin-2 and spin-0 hypotheses into the 0-jet and 1-jet categories. First we show the distributions of the test statistic q, followed by tables with the p values and CL_s exclusion levels. At the end, we show the CP-even and CP-odd mixing scans split up into their 0-jet and 1-jet categories.

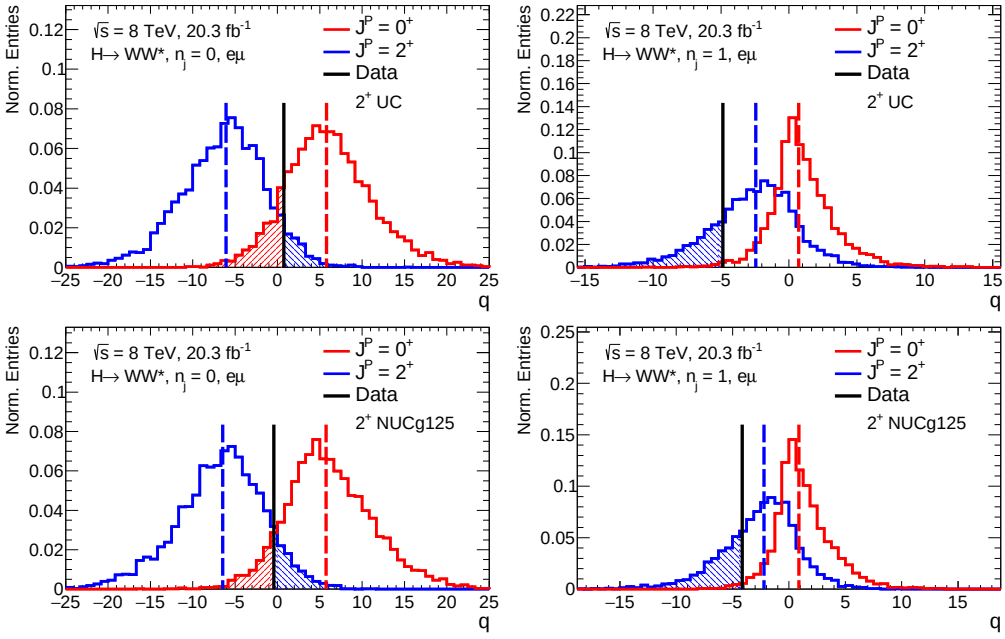

Figure C.1: Toy distributions for the SM versus the spin-2 UC (top) and spin-2 NUCg (bottom) models. For the 0-jet (left) distributions the data prefers neither the SM nor the spin-2 alternative. For the 1-jet (right) distributions the data has strong spin-2 preference.

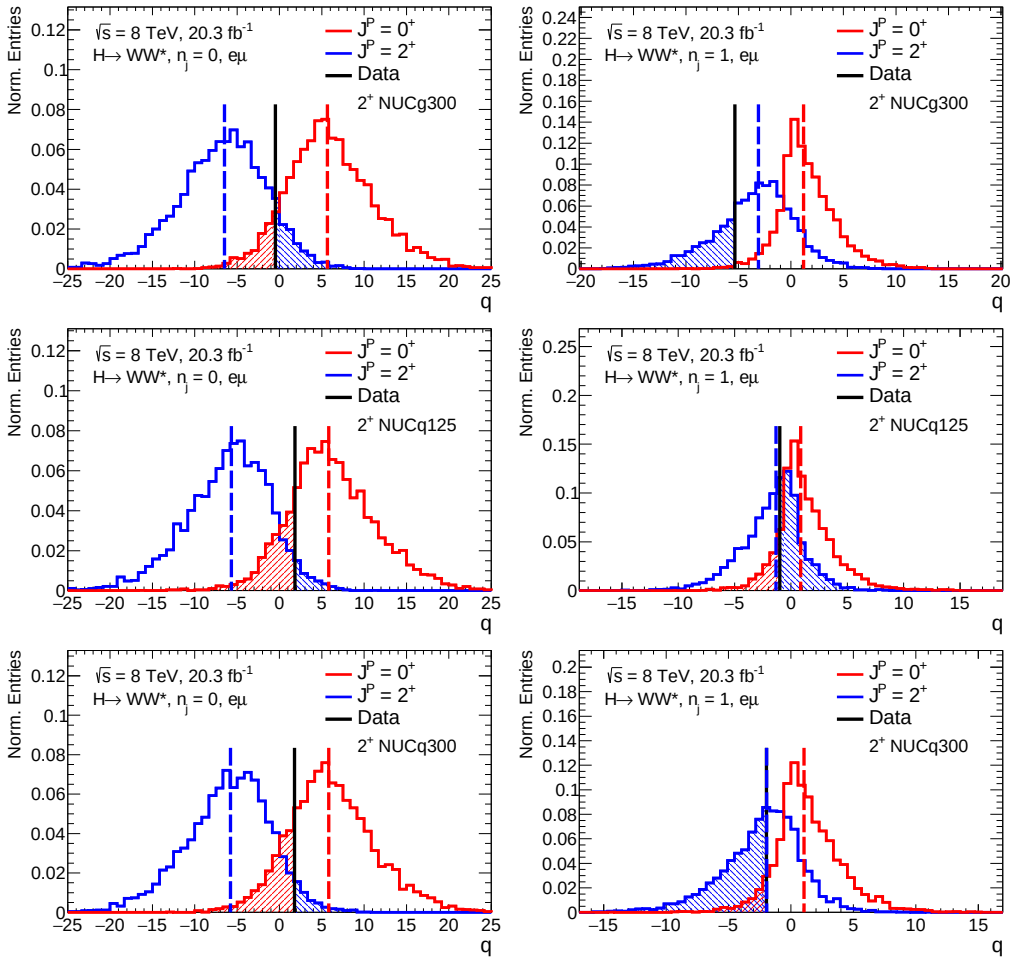

Figure C.2: Toy distributions for the SM versus the spin-2 NUCg (top) and spin-2 NUCq (middle and bottom) models. For the 0-jet (left) distributions the data prefers neither the SM nor the spin-2 alternative for the spin-2 NUCg model. For the spin-2 NUCq models the 0-jet distributions show a slight preference for the SM hypothesis. For the 1-jet (right) distributions the data has strong preference for the spin-2 NUCg model. The 1-jet distributions for the NUCq models show small preference for the alternative above the SM hypothesis.

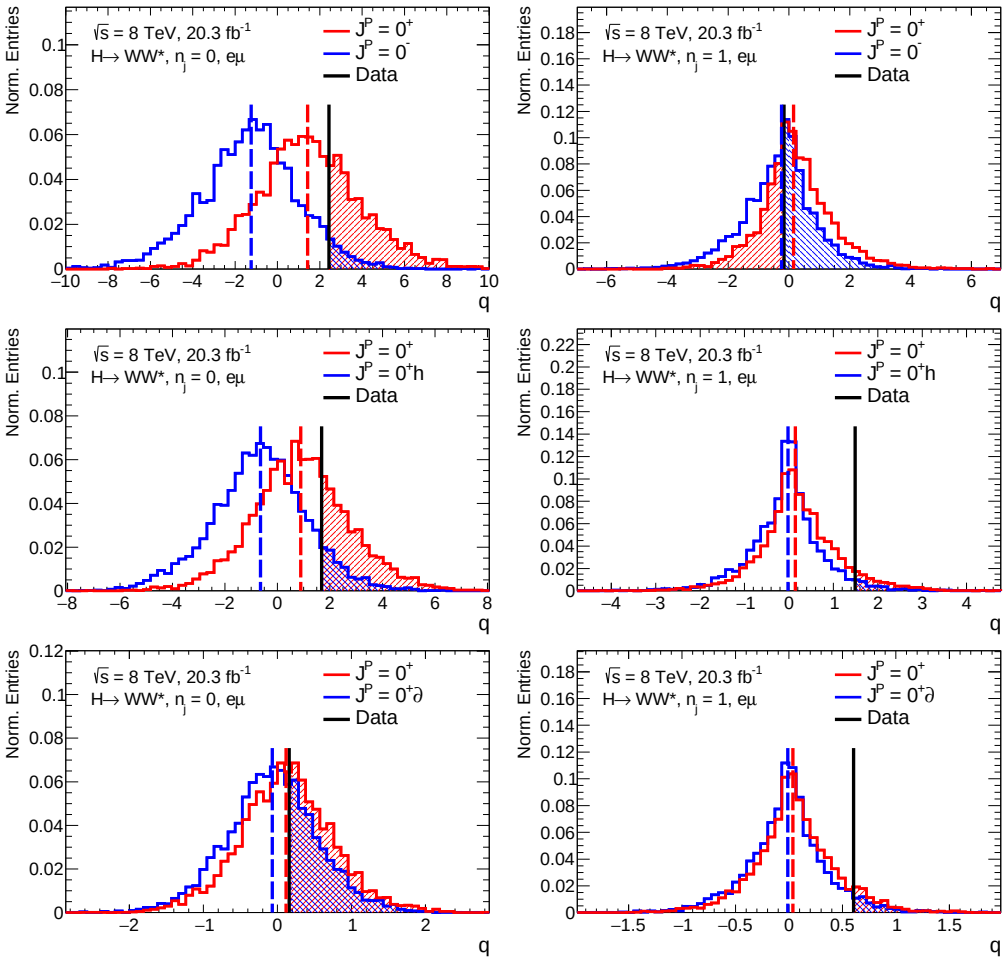

Figure C.3: Toy distributions for the SM versus the pure BSM 0^- (top), 0^+h (middle) and $0^+\partial$ (bottom) hypotheses. The 0-jet (left) distributions show a preference for the SM hypothesis. For the 1-jet (right) distributions the SM is very difficult to distinguish from the alternative spin-0 hypothesis. However, the data in the 1-jet 0^+h and $0^+\partial$ prefers more SM-like features.

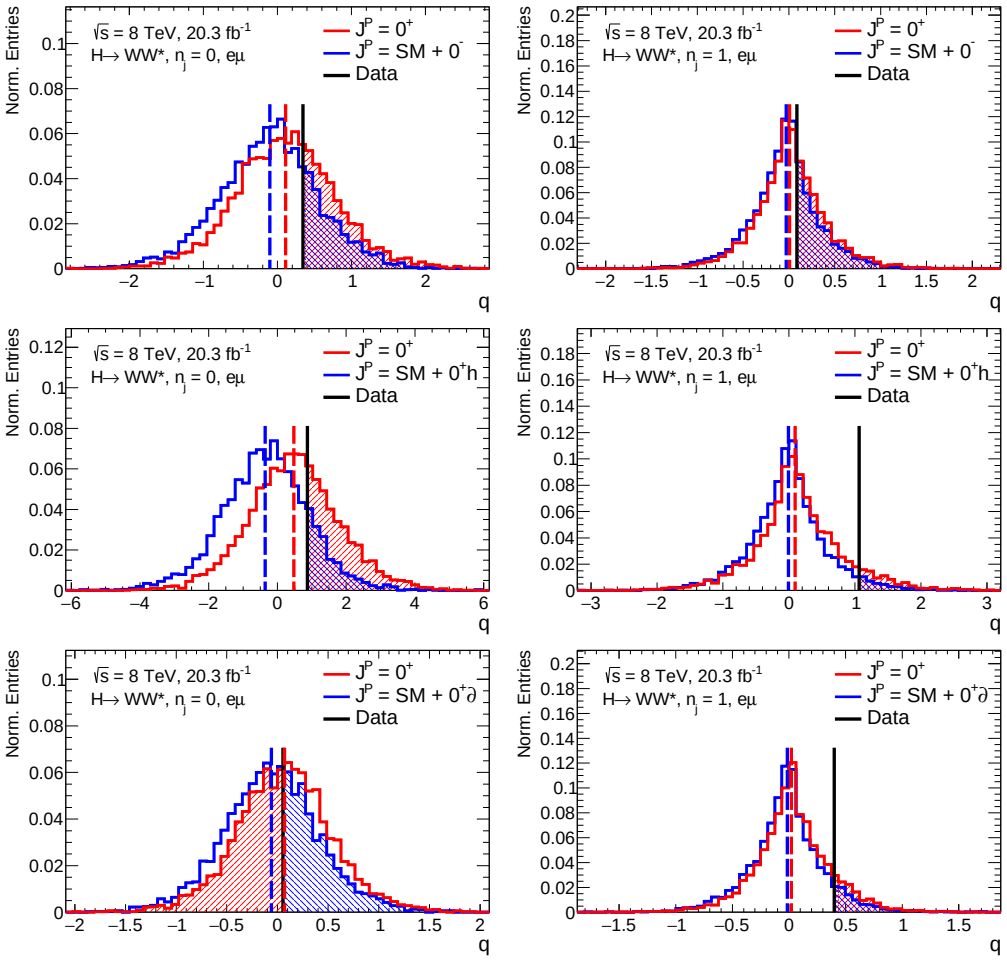

Figure C.4: Toy distributions for the SM versus the SM interfering with positive signs of κ values for 0^- (top), 0^+h (middle) and $0^+\partial$ (bottom). Both for the 0-jet (left) and 1-jet (right) distributions the SM is very difficult to distinguish from the alternative hypotheses. The data prefers for both jet categories more SM-like features.

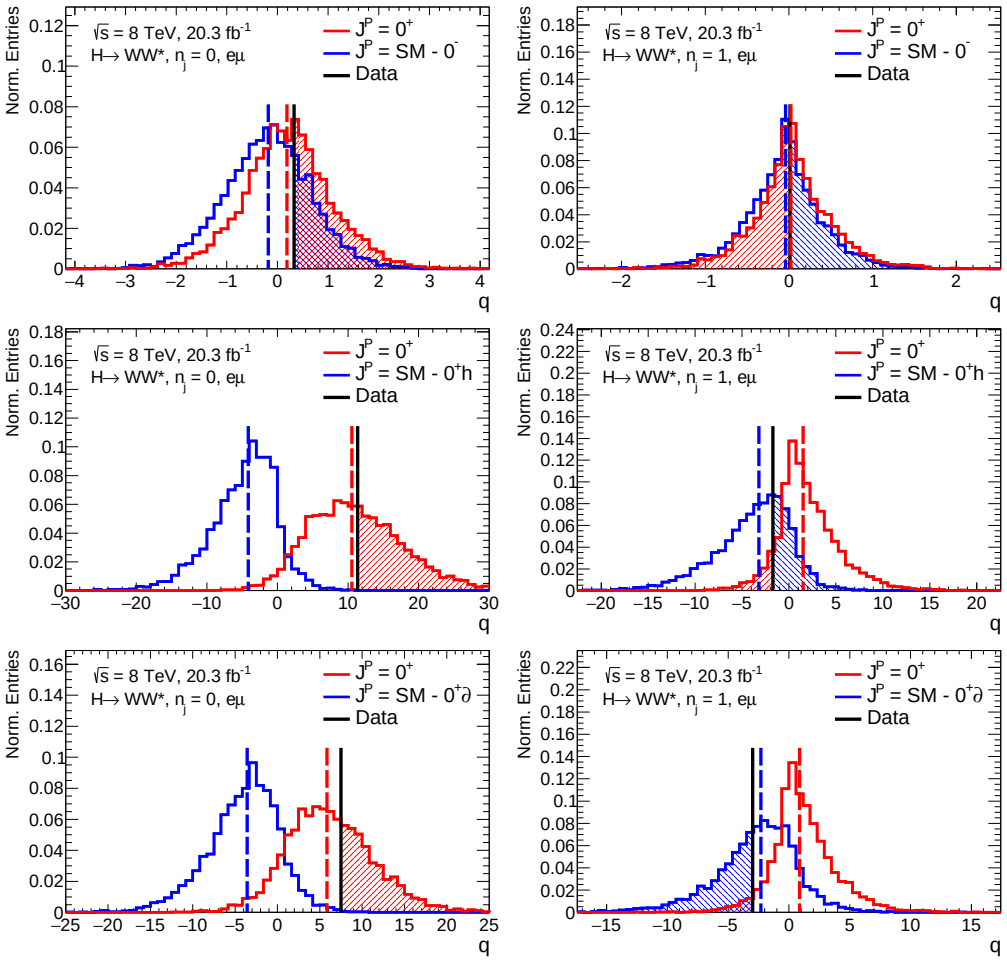

Figure C.5: Toy distributions for the SM versus the SM interfering with negative signs of κ values for 0^- (top), 0^+h (middle) and $0^+\partial$ (bottom). Both for the 0-jet (left) and 1-jet (right) distributions the SM is very difficult to distinguish from SM-0^- hypothesis. However, the discrimination power for the SM-0^+h and SM-$0^+\partial$ hypothesis is very strong. It is interesting to see that here for the 0-jet distributions there is a very strong preference for the SM hypothesis, while for the 1-jet distributions there is a preference for the alternative hypotheses.

Hypothesis	p_{exp}^{SM}	p_{exp}^{alt}	p_{obs}^{SM}	p_{obs}^{alt}	Z_{obs}^{SM}	Z_{obs}^{alt}	$1-\mathrm{CL}_s$
2^+, UC	0.006	0.004	0.134	0.062	1.1	1.5	92.8%
2^+, NUCg125	0.004	0.005	0.082	0.094	1.4	1.3	89.7%
2^+, NUCg300	0.004	0.004	0.087	0.101	1.4	1.3	89.0%
2^+, NUCq125	0.009	0.004	0.182	0.040	0.9	1.8	95.1%
2^+, NUCq300	0.008	0.006	0.184	0.044	0.9	1.7	94.6%

Table C.1: Expected and observed exclusion limits for the 0-jet distributions from Fig.C.1 and C.2. The last column shows the exclusion limit for the alternative hypothesis based on the CL_s method.

Hypothesis	p_{exp}^{SM}	p_{exp}^{alt}	p_{obs}^{SM}	p_{obs}^{alt}	Z_{obs}^{SM}	Z_{obs}^{alt}	$1-\mathrm{CL}_s$
2^+, UC	0.050	0.118	0.009	0.229	2.4	0.7	76.9%
2^+, NUCg125	0.056	0.119	0.014	0.280	2.2	0.6	71.6%
2^+, NUCg300	0.032	0.082	0.008	0.273	2.4	0.6	72.5%
2^+, NUCq125	0.105	0.130	0.135	0.437	1.1	0.2	49.5%
2^+, NUCq300	0.071	0.113	0.070	0.498	1.5	0.0	46.5%

Table C.2: Expected and observed exclusion limits for the 1-jet distributions from Fig.C.1 and C.2. The last column shows the exclusion limit for the alternative hypothesis based on the CL_s method.

Hypothesis	p_{exp}^{SM}	p_{exp}^{alt}	p_{obs}^{SM}	p_{obs}^{alt}	Z_{obs}^{SM}	Z_{obs}^{alt}	$1-\mathrm{CL_s}$
0^-	0.124	0.110	0.333	0.047	0.4	1.7	85.8%
0^+h	0.190	0.176	0.321	0.087	0.5	1.4	73.0%
$0^+\partial$	0.375	0.374	0.475	0.349	0.1	0.4	26.5%
$\mathrm{SM}+0^-$	0.375	0.359	0.360	0.233	0.4	0.7	35.2%
$\mathrm{SM}-0^-$	0.317	0.323	0.432	0.265	0.2	0.6	38.7%
$\mathrm{SM}+0^+h$	0.254	0.244	0.371	0.156	0.3	1.0	57.9%
$\mathrm{SM}-0^+h$	0.004	0.000	0.455	< 0.01	0.1	3.5	$> 99.9\%$
$\mathrm{SM}+0^+\partial$	0.394	0.387	0.484	0.400	0.0	0.3	22.4%
$\mathrm{SM}-0^+\partial$	0.021	0.007	0.376	0.002	0.3	2.9	99.5%

Table C.3: Expected and observed exclusion limits for the 0-jet distributions from Fig. C.3,C.4 and C.5. The last column shows the exclusion limit for the alternative hypothesis based on the $\mathrm{CL_s}$ method.

Hypothesis	p_{exp}^{SM}	p_{exp}^{alt}	p_{obs}^{SM}	p_{obs}^{alt}	Z_{obs}^{SM}	Z_{obs}^{alt}	$1-\mathrm{CL_s}$
0^-	0.310	0.308	0.340	0.467	0.4	0.1	29.2%
0^+h	0.381	0.352	0.079	0.033	1.4	1.8	58.3%
$0^+\partial$	0.418	0.412	0.080	0.050	1.4	1.6	38.2%
$\mathrm{SM}+0^-$	0.435	0.435	0.390	0.322	0.3	0.5	17.6%
$\mathrm{SM}-0^-$	0.408	0.405	0.486	0.417	0.0	0.2	18.9%
$\mathrm{SM}+0^+h$	0.402	0.385	0.087	0.041	1.4	1.7	52.2%
$\mathrm{SM}-0^+h$	0.036	0.056	0.085	0.329	1.4	0.4	64.1%
$\mathrm{SM}+0^+\partial$	0.426	0.414	0.125	0.084	1.1	1.4	32.6%
$\mathrm{SM}-0^+\partial$	0.064	0.107	0.042	0.409	1.7	0.2	57.3%

Table C.4: Expected and observed exclusion limits for the 1-jet distributions from Fig. C.3,C.4 and C.5. The last column shows the exclusion limit for the alternative hypothesis based on the $\mathrm{CL_s}$ method.

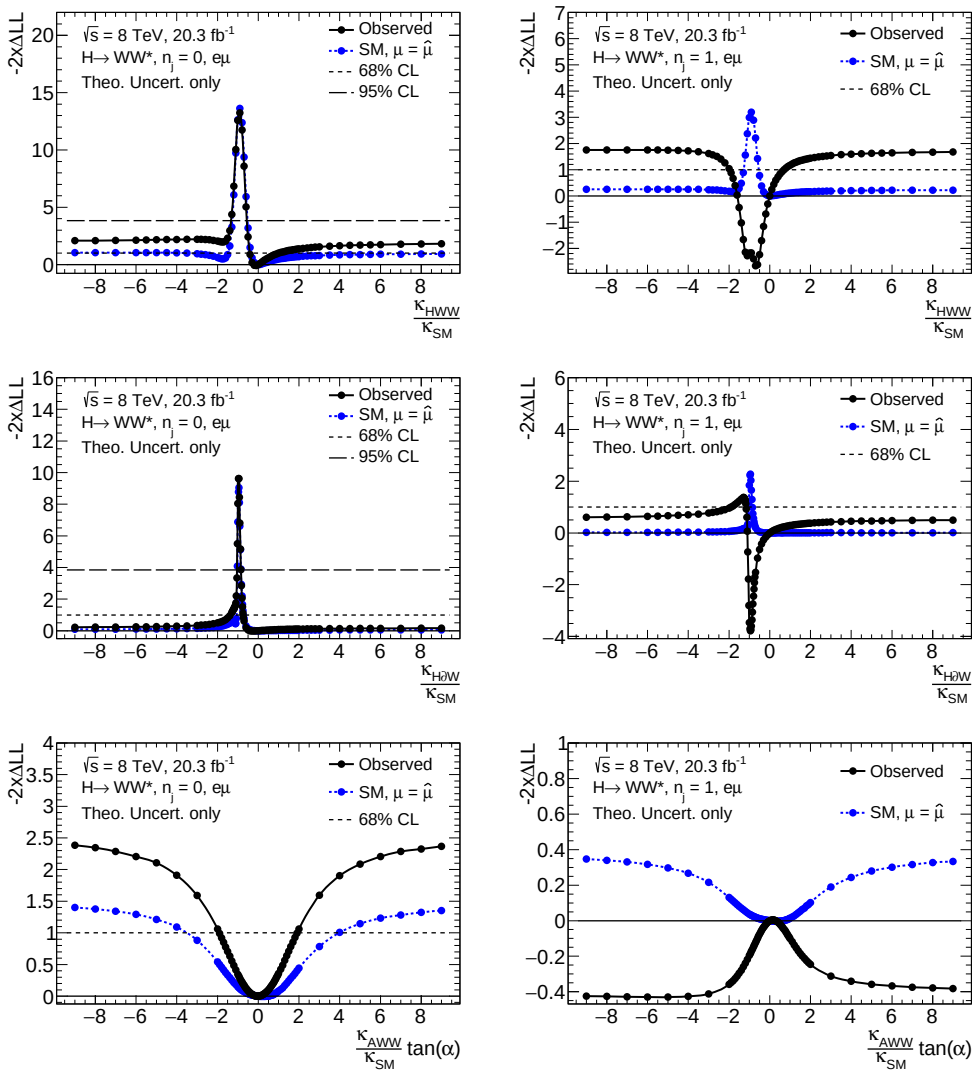

FIGURE C.6: Scans over κ_{HWW}/κ_{SM} (top), $\kappa_{H\partial W}/\kappa_{SM}$ (middle) and $\tan(\alpha)\cdot\kappa_{AWW}/\kappa_{SM}$ (bottom) split up in the 0-jet (left) and 1-jet (right) categories. Only the statistical and theoretical uncertainties are included. The SM expectation is indicated by the blue line and dots, while the black line and dots are the observed data. Notice the difference between the observed 0-jet compared to the observed 1-jet lines. The 68% and 95% exclusion levels are with respect the SM expectation.

Bibliography

B

[1] S. L. Glashow, *Partial Symmetries of Weak Interactions*, Nucl. Phys. **22** (1961) pp. 579–588.

[2] G. 't Hooft and M. J. G. Veltman, *Regularization and Renormalization of Gauge Fields*, Nucl. Phys. **B44** (1972) pp. 189–213.

[3] A. Salam, *Weak and Electromagnetic Interactions*, Conf. Proc. **C680519** (1968) pp. 367–377.

[4] S. Weinberg, *A Model of Leptons*, Phys. Rev. Lett. **19** (1967) pp. 1264–1266.

[5] I. J. R. Aitchison and A. J. G. Hey, *Gauge theories in particle physics: A practical introduction. Vol. 1: From relativistic quantum mechanics to QED*, 2003, URL: http://www-spires.fnal.gov/spires/find/books/www?cl=QC793.3.F5A34::2012.

[6] I. J. R. Aitchison and A. J. G. Hey, *Gauge theories in particle physics: A practical introduction. Vol. 2: Non-Abelian gauge theories: QCD and the electroweak theory*, 2004, URL: http://www-spires.fnal.gov/spires/find/books/www?cl=QC793.3.F5A34::2012:V2.

[7] D. Griffiths, *Introduction to Elementary Particles, second revised edition*, Wiley-VCH, 2008.

[8] C. Quigg, *Gauge Theories of the Strong, Weak, and Electromagnetic Interactions*, USA: Princeton University Press, 2013, URL: http://chrisquigg.com/gauge-theories/.

[9] The Particle Data Group Collaboration, *Review of Particle Physics (RPP)*, Phys. Rev. **D86** (2012) p. 010001.

[10] P. W. Higgs, *Broken symmetries, massless particles and gauge fields*, Phys. Lett. **12** (1964) pp. 132–133.

[11] P. W. Higgs, *Broken Symmetries and the Masses of Gauge Bosons*, Phys. Rev. Lett. **13** (1964) pp. 508–509.

[12] F. Englert and R. Brout, *Broken Symmetry and the Mass of Gauge Vector Mesons*, Phys. Rev. Lett. **13** (1964) pp. 321–323.

[13] G. S. Guralnik, C. R. Hagen, and T. W. B. Kibble, *Global Conservation Laws and Massless Particles*, Phys. Rev. Lett. **13** (1964) pp. 585–587.

[14] P. W. Higgs, *Spontaneous Symmetry Breakdown without Massless Bosons*, Phys. Rev. **145** (1966) pp. 1156–1163.

[15] T. W. B. Kibble, *Symmetry breaking in nonAbelian gauge theories*, Phys. Rev. **155** (1967) pp. 1554–1561.

[16] R. Z. Aben, "Spinning the Higgs - Spin and parity measurement of the discovered Higgs-like boson in the $H \to WW \to l\nu l\nu$ decay mode", PhD thesis: University of Amsterdam, 2015.

[17] H. M. Georgi, S. L. Glashow, M. E. Machacek, and D. V. Nanopoulos, *Higgs Bosons from Two Gluon Annihilation in Proton Proton Collisions*, Phys. Rev. Lett. **40** (1978) p. 692.

[18] R. N. Cahn and S. Dawson, *Production of Very Massive Higgs Bosons*, Phys. Lett. **B136** (1984) p. 196, [Erratum: Phys. Lett. B138, 464 (1984)].

[19] S. L. Glashow, D. V. Nanopoulos, and A. Yildiz, *Associated Production of Higgs Bosons and Z Particles*, Phys. Rev. **D18** (1978) pp. 1724–1727.

[20] Z. Kunszt, *Associated Production of Heavy Higgs Boson with Top Quarks*, Nucl. Phys. **B247** (1984) p. 339.

[21] LHC Higgs Cross Section Working Group, *Cross Sections*, URL: https://twiki.cern.ch/twiki/bin/view/LHCPhysics/CrossSections.

[22] The ATLAS Collaboration, *Observation of a new particle in the search for the Standard Model Higgs boson with the ATLAS detector at the LHC*, Phys. Lett. **B716** (2012) pp. 1–29, arXiv: 1207.7214 [hep-ex].

[23] The CMS Collaboration, *Observation of a new boson at a mass of 125 GeV with the CMS experiment at the LHC* (2012), eprint: 1207.7235, URL: http://arxiv.org/abs/1207.7235.

[24] The ATLAS Collaboration, *Measurements of the Higgs boson production and decay rates and coupling strengths using pp collision data at $\sqrt{s} = 7$ and 8 TeV in the ATLAS experiment*, Eur. Phys. J. **C76**.1 (2016) p. 6, arXiv: 1507.04548 [hep-ex].

[25] *Quantum Diaries*, URL: http://www.quantumdiaries.org/2011/11/14/what-exactly-is-cp-violation/.

[26] N. Cabibbo, *Unitary Symmetry and Leptonic Decays*, Phys. Rev. Lett. **10** (1963) pp. 531–533, [,648(1963)].

[27] M. Kobayashi and T. Maskawa, *CP Violation in the Renormalizable Theory of Weak Interaction*, Prog. Theor. Phys. **49** (1973) pp. 652–657.

[28] G. C. Branco, P. M. Ferreira, L. Lavoura, M. N. Rebelo, M. Sher, and J. P. Silva, *Theory and phenomenology of two-Higgs-doublet models* (2011), eprint: 1106.0034, URL: http://arxiv.org/abs/1106.0034.

[29] J. F. Gunion and H. E. Haber, *The CP conserving two Higgs doublet model: The Approach to the decoupling limit*, Phys. Rev. **D67** (2003) p. 075019, arXiv: hep-ph/0207010 [hep-ph].

[30] P. Artoisenet et al., *A framework for Higgs characterisation*, JHEP **11** (2013) p. 043, arXiv: 1306.6464 [hep-ph].

[31] J. Alwall, M. Herquet, F. Maltoni, O. Mattelaer, and T. Stelzer, *MadGraph 5 : Going Beyond*, JHEP **06** (2011) p. 128, arXiv: 1106.0522 [hep-ph].

[32] N. Karastathis, "Determination of spin and parity of the Higgs boson in the $WW^* \to e\nu\mu\nu$ decay channel with the ATLAS detector", PhD thesis: University of Twente, 2016.

[33] A. Alloul, B. Fuks, and V. Sanz, *Phenomenology of the Higgs Effective Lagrangian via FeynRules* (2013), eprint: 1310.5150, URL: http://arxiv.org/abs/1310.5150.

[34] L. Randall and R. Sundrum, *A Large mass hierarchy from a small extra dimension*, Phys. Rev. Lett. **83** (1999) pp. 3370–3373, arXiv: hep-ph/9905221 [hep-ph].

[35] O. S. Bruning, P. Collier, P. Lebrun, S. Myers, R. Ostojic, J. Poole, and P. Proudlock, *LHC Design Report Vol.1: The LHC Main Ring* (2004).

[36] O. Buning, P. Collier, P. Lebrun, S. Myers, R. Ostojic, J. Poole, and P. Proudlock, *LHC Design Report. 2. The LHC infrastructure and general services* (2004).

[37] M. Benedikt, P. Collier, V. Mertens, J. Poole, and K. Schindl, *LHC Design Report. 3. The LHC injector chain* (2004).

[38] L. Evans and P. Bryant, *LHC Machine*, JINST **3** (2008) S08001.

[39] F. Marcastel, *CERN's Accelerator Complex. La chaıne des accélérateurs du CERN (2016), General Photo*, URL: https://cds.cern.ch/record/1621583.

[40] The ATLAS Collaboration, *ATLAS: Detector and physics performance technical design report. Volume 1*, CERN-LHCC-99-14, ATLAS-TDR-14 (1999).

[41] The ATLAS Collaboration, *ATLAS: Detector and physics performance technical design report. Volume 2*, CERN-LHCC-99-15, ATLAS-TDR-15 (1999).

[42] The ATLAS Collaboration, *The ATLAS Experiment at the CERN Large Hadron Collider*, JINST **3** (2008) S08003.

[43] The CMS Collaboration, *The CMS experiment at the CERN LHC*, JINST **3** (2008) S08004.

[44] The LHCb Collaboration, *The LHCb Detector at the LHC*, JINST **3** (2008) S08005.

[45] The ALICE Collaboration, *The ALICE experiment at the CERN LHC*, JINST **3** (2008) S08002.

[46] The ATLAS Collaboration, URL: https://twiki.cern.ch/twiki/bin/view/AtlasPublic/LuminosityPublicResults.

[47] *Approved plots for the performance of the ATLAS detector October 2012*, URL: https://twiki.cern.ch/twiki/bin/view/AtlasPublic/ApprovedPlotsATLASDetector.

[48] C. Bernius, *Performances of the ATLAS High Level Trigger in the 2012 and 2012 runs, Presented at the CHEF Conference in April 2013 in Paris, France*, URL: https://indico.in2p3.fr/event/7691/session/11/contribution/78/material/slides/0.pdf.

[49] The ATLAS Collaboration, *Trigger Operation Public Results* (2015), URL: https://twiki.cern.ch/twiki/bin/view/AtlasPublic/TriggerOperationPublicResults.

[50] S. Agostinelli et al., *GEANT4: A Simulation toolkit*, Nucl. Instrum. Meth. **A506** (2003) pp. 250–303.

[51] The ATLAS Collaboration, *The ATLAS Simulation Infrastructure*, Eur. Phys. J. **C70** (2010) pp. 823–874, arXiv: 1005.4568 [physics.ins-det].

[52] The ATLAS Collaboration, *The ATLAS calorimeter simulation FastCaloSim*, J. Phys. Conf. Ser. **331** (2011) p. 032053.

[53] J. Mahlstedt, "Search for excited leptons with the ATLAS detector", PhD thesis: University of Amsterdam, 2016.

[54] G. Besjes, "Pushing Susy's Boundaries, Searches and prospects for strongly-produced supersymmetry at the LHC with the ATLAS detector", PhD thesis: Radboud Universiteit Nijmegen, 2015.

[55] T. Cornelissen, M. Elsing, S. Fleischmann, W. Liebig, and E. Moyse, *Concepts, Design and Implementation of the ATLAS New Tracking (NEWT)*, ATL-SOFT-PUB-2007-007 (2007), ed. by A. Salzburger.

[56] The ATLAS Collaboration, *Charged-particle distributions in pp interactions at $\sqrt{s} = 8$ TeV measured with the ATLAS detector at the LHC* (2016), arXiv: 1603.02439 [hep-ex].

[57] R. E. Kalman, *A New Approach to Linear Filtering and Prediction Problems*, Trans. ASME J. Basic Eng. **D**.82 (1960) pp. 35–45.

[58] The ATLAS Collaboration, *Performance of primary vertex reconstruction in proton-proton collisions at $\sqrt{s}$ =7 TeV in the ATLAS experiment*, ATLAS-CONF-2010-069 (2010).

[59] The ATLAS Collaboration, *Vertex Reconstruction Plots* (2012), URL: http://atlas.web.cern.ch/Atlas/GROUPS/PHYSICS/IDTRACKING/PublicPlots/ATL-COM-PHYS-2012-474/.

[60] The ATLAS Collaboration, *Electron reconstruction and identification efficiency measurements with the ATLAS detector using the 2011 LHC proton-proton collision data*, Eur. Phys. J. **C74**.7 (2014) p. 2941, arXiv: 1404.2240 [hep-ex].

[61] The ATLAS Collaboration, *Improved electron reconstruction in ATLAS using the Gaussian Sum Filter-based model for bremsstrahlung*, ATLAS-CONF-2012-047 (2012).

[62] The ATLAS Collaboration, *Electron efficiency measurements with the ATLAS detector using the 2012 LHC proton-proton collision data*, ATLAS-CONF-2014-032 (2014).

[63] The ATLAS Collaboration, *Electron efficiency measurements with the ATLAS detector using the 2012 LHC proton-proton collision data*, ATLAS-CONF-2014-032 (2014).

[64] The ATLAS Collaboration, *Muon Reconstruction Performance*, ATLAS-CONF-2010-064 (2010).

[65] The ATLAS Collaboration, *Measurement of the muon reconstruction performance of the ATLAS detector using 2011 and 2012 LHC proton–proton collision data*, Eur. Phys. J. **C74**.11 (2014) p. 3130, arXiv: 1407.3935 [hep-ex].

[66] S. Hassani, L. Chevalier, E. Lancon, J. F. Laporte, R. Nicolaidou, and A. Ouraou, *A muon identification and combined reconstruction procedure for the ATLAS detector at the LHC using the (MUONBOY, STACO, MuTag) reconstruction packages*, Nucl. Instrum. Meth. **A572** (2007) pp. 77–79.

[67] T. Lagouri et al., *A Muon Identification and Combined Reconstruction Procedure for the ATLAS Detector at the LHC at CERN*, IEEE Trans. Nucl. Sci. **51** (2004) pp. 3030–3033.

[68] The ATLAS Collaboration, *Monte Carlo Calibration and Combination of In-situ Measurements of Jet Energy Scale, Jet Energy Resolution and Jet Mass in ATLAS*, ATLAS-CONF-2015-037 (2015).

[69] W. Lampl, S. Laplace, D. Lelas, P. Loch, H. Ma, S. Menke, S. Rajagopalan, D. Rousseau, S. Snyder, and G. Unal, *Calorimeter clustering algorithms: Description and performance*, ATL-LARG-PUB-2008-002 (2008).

[70] M. Cacciari, G. P. Salam, and G. Soyez, *FastJet User Manual*, Eur. Phys. J. **C72** (2012) p. 1896, arXiv: 1111.6097 [hep-ph].

[71] M. Cacciari, G. P. Salam, and G. Soyez, *The Anti-k(t) jet clustering algorithm*, JHEP **04** (2008) p. 063, arXiv: 0802.1189 [hep-ph].

[72] The ATLAS Collaboration, *Jet energy measurement and its systematic uncertainty in proton-proton collisions at $\sqrt{s} = 7$ TeV with the ATLAS detector*, Eur. Phys. J. **C75** (2015) p. 17, arXiv: 1406.0076 [hep-ex].

[73] The ATLAS Collaboration, *Update of the $H \to WW^{(*)} \to e\nu\mu\nu$ Analysis with 13 fb^{-1} of $\sqrt{s} = 8$ TeV Data Collected with the ATLAS Detector*, ATLAS-CONF-2012-158 (2012).

[74] The ATLAS Collaboration, *Calibration of the performance of b-tagging for c and light-flavour jets in the 2012 ATLAS data*, ATLAS-CONF-2014-046 (2014).

[75] The ATLAS Collaboration, *Commissioning of the ATLAS high-performance b-tagging algorithms in the 7 TeV collision data*, ATLAS-CONF-2011-102 (2011).

[76] The ATLAS Collaboration, *Measurement of the b-tag Efficiency in a Sample of Jets Containing Muons with 5 fb^1 of Data from the ATLAS Detector*, ATLAS-CONF-2012-043 (2012).

[77] The ATLAS Collaboration, *Performance of Missing Transverse Momentum Reconstruction in ATLAS studied in Proton-Proton Collisions recorded in 2012 at 8 TeV*, ATLAS-CONF-2013-082 (2013).

[78] The ATLAS Collaboration, *Performance of Missing Transverse Momentum Reconstruction in ATLAS studied in Proton-Proton Collisions recorded in 2012 at 8 TeV*, ATLAS-CONF-2013-082 (2013).

[79] The ATLAS Collaboration, *Observation and measurement of Higgs boson decays to WW^* with the ATLAS detector*, Phys. Rev. **D92**.1 (2015) p. 012006, arXiv: 1412.2641 [hep-ex].

[80] The ATLAS Collaboration, *Performance of the ATLAS muon trigger in pp collisions at $\sqrt{s} = 8$ TeV*, Eur. Phys. J. **C75** (2015) p. 120, arXiv: 1408.3179 [hep-ex].

[81] M. Gosselink, "Radiating Top Quarks", PhD thesis: University of Amsterdam, 2010.

[82] T. Gleisberg, S. Hoeche, F. Krauss, M. Schonherr, S. Schumann, F. Siegert, and J. Winter, *Event generation with SHERPA 1.1*, JHEP **02** (2009) p. 007, arXiv: 0811.4622 [hep-ph].

[83] J. D. Bjorken and E. A. Paschos, *Inelastic Electron Proton and gamma Proton Scattering, and the Structure of the Nucleon*, Phys. Rev. **185** (1969) pp. 1975–1982.

[84] The ZEUS and H1 Collaborations, *Combined Measurement and QCD Analysis of the Inclusive e+- p Scattering Cross Sections at HERA*, JHEP **01** (2010) p. 109, arXiv: 0911.0884 [hep-ex].

[85] A. D. Martin, W. J. Stirling, R. S. Thorne, and G. Watt, *Parton distributions for the LHC*, Eur. Phys. J. **C63** (2009) pp. 189–285, arXiv: 0901.0002 [hep-ph].

[86] H.-L. Lai, M. Guzzi, J. Huston, Z. Li, P. M. Nadolsky, J. Pumplin, and C.-P. Yuan, *New parton distributions for collider physics*, Phys. Rev. **D82** (2010) p. 074024, arXiv: 1007.2241 [hep-ph].

[87] T. Sjostrand, S. Mrenna, and P. Z. Skands, *PYTHIA 6.4 Physics and Manual*, JHEP **05** (2006) p. 026, arXiv: hep-ph/0603175 [hep-ph].

[88] T. Sjostrand, S. Mrenna, and P. Z. Skands, *A Brief Introduction to PYTHIA 8.1*, Comput. Phys. Commun. **178** (2008) pp. 852–867, arXiv: 0710.3820 [hep-ph].

[89] G. Corcella, I. G. Knowles, G. Marchesini, S. Moretti, K. Odagiri, P. Richardson, M. H. Seymour, and B. R. Webber, *HERWIG 6: An Event generator for hadron emission reactions with interfering gluons (including supersymmetric processes)*, JHEP **01** (2001) p. 010, arXiv: hep-ph/0011363 [hep-ph].

[90] J. M. Butterworth, J. R. Forshaw, and M. H. Seymour, *Multiparton interactions in photoproduction at HERA*, Z. Phys. **C72** (1996) pp. 637–646, arXiv: hep-ph/9601371 [hep-ph].

[91] M. L. Mangano, M. Moretti, F. Piccinini, R. Pittau, and A. D. Polosa, *ALPGEN, a generator for hard multiparton processes in hadronic collisions*, JHEP **07** (2003) p. 001, arXiv: hep-ph/0206293 [hep-ph].

[92] S. Frixione and B. R. Webber, *Matching NLO QCD computations and parton shower simulations*, JHEP **06** (2002) p. 029, arXiv: hep-ph/0204244 [hep-ph].

[93] P. Nason, *A New method for combining NLO QCD with shower Monte Carlo algorithms*, JHEP **11** (2004) p. 040, arXiv: hep-ph/0409146 [hep-ph].

[94] J. Alwall et al., *Comparative study of various algorithms for the merging of parton showers and matrix elements in hadronic collisions*, Eur. Phys. J. **C53** (2008) pp. 473–500, arXiv: 0706.2569 [hep-ph].

[95] J. Alwall, R. Frederix, S. Frixione, V. Hirschi, F. Maltoni, O. Mattelaer, H.-S. Shao, T. Stelzer, P. Torrielli, and M. Zaro, *The automated computation of tree-level and next-to-leading order differential cross sections, and their matching to parton shower simulations* (2014), eprint: 1405.0301, URL: http://arxiv.org/abs/1405.0301.

[96] A. J. Barr, B. Gripaios, and C. G. Lester, *Measuring the Higgs boson mass in dileptonic W-boson decays at hadron colliders*, JHEP **07** (2009) p. 072, arXiv: 0902.4864 [hep-ph].

[97] N. Cabibbo and A. Maksymowicz, *Angular Correlations in Ke-4 Decays and Determination of Low-Energy pi-pi Phase Shifts*, Phys. Rev. **137** (1965) B438–B443, [Erratum: Phys. Rev. 168, 1926 (1968)].

[98] K. Gottfried and J. D. Jackson, *On the Connection between production mechanism and decay of resonances at high-energies*, Nuovo Cim. **33** (1964) pp. 309–330.

[99] J. C. Collins and D. E. Soper, *Angular Distribution of Dileptons in High-Energy Hadron Collisions*, Phys. Rev. **D16** (1977) p. 2219.

[100] S. D. Drell and T.-M. Yan, *Massive Lepton Pair Production in Hadron-Hadron Collisions at High-Energies*, Phys. Rev. Lett. **25** (1970) pp. 316–320, [Erratum: Phys. Rev. Lett. 25, 902 (1970)].

[101] E. Mirkes, *Angular decay distribution of leptons from W bosons at NLO in hadronic collisions*, Nucl. Phys. **B387** (1992) pp. 3–85.

[102] The ATLAS Collaboration, *Study of the spin and parity of the Higgs boson in diboson decays with the ATLAS detector*, Eur. Phys. J. **C75**.10 (2015) p. 476, arXiv: 1506.05669 [hep-ex].

[103] F. Maltoni, K. Mawatari, and M. Zaro, *Higgs characterisation via vector-boson fusion and associated production: NLO and parton-shower effects*, Eur. Phys. J. **C74**.1 (2014) p. 2710, arXiv: 1311.1829 [hep-ph].

[104] B. P. Kersevan and E. Richter-Was, *The Monte Carlo event generator AcerMC versions 2.0 to 3.8 with interfaces to PYTHIA 6.4, HERWIG 6.5 and ARIADNE 4.1*, Comput. Phys. Commun. **184** (2013) pp. 919–985, arXiv: hep-ph/0405247 [hep-ph].

[105] N. Kauer, *Interference effects for $H \to WW/ZZ \to \ell\bar{\nu}_\ell\bar{\ell}\nu_\ell$ searches in gluon fusion at the LHC*, JHEP **12** (2013) p. 082, arXiv: 1310.7011 [hep-ph].

[106] P. M. Nadolsky, H.-L. Lai, Q.-H. Cao, J. Huston, J. Pumplin, D. Stump, W.-K. Tung, and C.-P. Yuan, *Implications of CTEQ global analysis for collider observables*, Phys. Rev. **D78** (2008) p. 013004, arXiv: 0802.0007 [hep-ph].

[107] A. Sherstnev and R. S. Thorne, *Parton Distributions for LO Generators*, Eur. Phys. J. **C55** (2008) pp. 553–575, arXiv: 0711.2473 [hep-ph].

[108] The ATLAS Collaboration, *The simulation principle and performance of the ATLAS fast calorimeter simulation FastCaloSim*, ATL-PHYS-PUB-2010-013 (2010).

[109] J. M. Campbell, R. K. Ellis, and C. Williams, *Vector boson pair production at the LHC*, JHEP **07** (2011) p. 018, arXiv: 1105.0020 [hep-ph].

[110] M. Czakon and A. Mitov, *Top++: A Program for the Calculation of the Top-Pair Cross-Section at Hadron Colliders*, Comput. Phys. Commun. **185** (2014) p. 2930, arXiv: 1112.5675 [hep-ph].

[111] S. Catani, L. Cieri, G. Ferrera, D. de Florian, and M. Grazzini, *Vector boson production at hadron colliders: a fully exclusive QCD calculation at NNLO*, Phys. Rev. Lett. **103** (2009) p. 082001, arXiv: 0903.2120 [hep-ph].

[112] The ATLAS Collaboration, *Determination of spin and parity of the Higgs boson in the $WW^* \to e\nu\mu\nu$ decay channel with the ATLAS detector*, Eur. Phys. J. **C75**.5 (2015) p. 231, arXiv: 1503.03643 [hep-ex].

[113] D. de Florian, G. Ferrera, M. Grazzini, and D. Tommasini, *Transverse-momentum resummation: Higgs boson production at the Tevatron and the LHC*, JHEP **11** (2011) p. 064, arXiv: 1109.2109 [hep-ph].

[114] M. Grazzini and H. Sargsyan, *Heavy-quark mass effects in Higgs boson production at the LHC*, JHEP **09** (2013) p. 129, arXiv: 1306.4581 [hep-ph].

[115] The ATLAS Collaboration, *Pile-up subtraction and suppression for jets in ATLAS*, ATLAS-CONF-2013-083 (2013).

[116] The ATLAS Collaboration, *Performance of Missing Transverse Momentum Reconstruction in Proton-Proton Collisions at 7 TeV with ATLAS*, Eur. Phys. J. **C72** (2012) p. 1844.

[117] S. Asai et al., *Prospects for the search for a standard model Higgs boson in ATLAS using vector boson fusion*, Eur. Phys. J. **C32S2** (2004) pp. 19–54, arXiv: hep-ph/0402254 [hep-ph].

[118] A. J. Armbuster, "Discovery of a Higgs Boson with the ATLAS Detector", PhD thesis: University of Michigan, 2010.

[119] The ROOT Collaboration, *HistFactory: A tool for creating statistical models for use with RooFit and RooStats* (2012).

[120] R. D. Ball et al., *Parton distributions with LHC data*, Nucl. Phys. **B867** (2013) pp. 244–289, arXiv: 1207.1303 [hep-ph].

[121] The ATLAS Collaboration, *Improved luminosity determination in pp collisions at sqrt(s) = 7 TeV using the ATLAS detector at the LHC*, Eur. Phys. J. **C73**.8 (2013) p. 2518, arXiv: 1302.4393 [hep-ex].

[122] A. L. Read, "Modified frequentist analysis of search results (The CL(s) method)", *Workshop on confidence limits, CERN, Geneva, Switzerland, 17-18 Jan 2000: Proceedings*, 2000, URL: http://weblib.cern.ch/abstract?CERN-OPEN-2000-205.

[123] V. Dao, "Over the Top: from $t\bar{t}$ measurements to the search for te associated production of the Higgs boson and a top quark pair with the ATLAS detector", PhD thesis: Radboud Universiteit Nijmegen, 2014.

[124] W. Verkerke, *Statistical Analysis, lecture notes for the course Topical Lectures at Nikhef*, Nikhhef, 2013.

[125] G. Cowan, K. Cranmer, E. Gross, and O. Vitells, *Asymptotic formulae for likelihood-based tests of new physics*, Eur. Phys. J. **C71** (2011) p. 1554, [Erratum: Eur. Phys. J. C73, 2501 (2013)], arXiv: 1007.1727 [physics.data-an].

[126] The CMS Collaboration, *Study of the Mass and Spin-Parity of the Higgs Boson Candidate Via Its Decays to Z Boson Pairs*, Phys. Rev. Lett. **110**.8 (2013) p. 081803, arXiv: 1212.6639 [hep-ex].

[127] The CMS Collaboration, *Measurement of Higgs boson production and properties in the WW decay channel with leptonic final states*, JHEP **01** (2014) p. 096, arXiv: 1312.1129 [hep-ex].

[128] The CMS Collaboration, *Observation of the diphoton decay of the Higgs boson and measurement of its properties*, Eur. Phys. J. **C74**.10 (2014) p. 3076, arXiv: 1407.0558 [hep-ex].

Summary

S

As of today, we know that our Universe is composed of elementary particles, like quarks, gluons and electrons. Elementary means that these particles are not composed of even smaller particles. The quarks and gluons form the protons and neutrons of an atomic nucleus and the electrons orbit around it. We know of 17 elementary particles that can be described by the so-called Standard Model, SM for short, which is a mathematical model and it can make very precise predictions on how these particles interact with each other. Up till now, a great amount of SM predictions were experimentally confirmed, but there are clues that not everything can be explained by the SM. From observations of distant galaxies we know that all particles from the SM can only describe about 4% of the total mass in the Universe. The other 96% is referred to as dark matter and dark energy and in order to describe these, we need mathematical models that go beyond the SM. We indicate these type of models with New Physics (NP), which predict the existence of more elementary particles besides those from the SM. Science has the responsibility to keep testing the SM through new experiments. A significant deviation from the SM prediction during a measurement could be a sign of the presence of NP particles. It is also possible to observe something that is outside the scope of the SM.

In this thesis, I'm on the lookout for deviations in the SM by looking at the spin and parity[1] of the Higgs boson. Spin is something like the rotation-momentum of a particle and parity compares a particle with its mirror image. The SM predicts the Higgs boson to be a spin-0 parity-even particle, in other words, it has no rotation-momentum and it is identical to its mirror image. Figure S.1 gives an example of the parity operation, a.k.a reflection, applied on a particle with spin and a Higgs boson. The orientation of the spin is indicated with the red and blue arrows for the particle with spin. After reflection, de spin orientation is turned around and therefore we call this type of particle parity-odd. To give another example: if you have a birth mark on your left cheek, your mirror image has the same birth mark, but on the right cheek. The Higgs boson stays identical under reflection so it is parity-even.

There are various NP models that predict the Higgs boson to have a spin different from zero or it can be parity-odd. There are as well NP models that predict more than one Higgs boson and these new bosons can be parity-even or odd. These extra Higgs bosons could

[1] Actually I'm looking at the CP operation, which is a combination of the C operation that changes a particle's charge and a parity operation P. The Higgs boson does not have an electric charge so only its parity quantity remains.

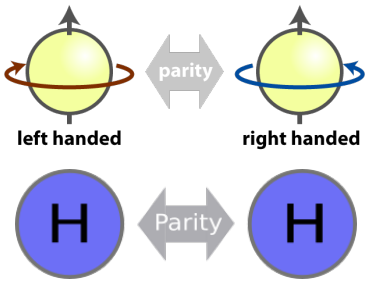

Figure S.1: A parity operation executed on a left-handed particle with spin (top,[25]) and on the Higgs boson (bottom). The orientation of the spin changes sign and the left-handed particle becomes right-handed. Because of this, it is called parity-odd. The Higgs boson stays identical under this mirror operation and is therefore called parity-even.

influence the measurement when we want to test spin and parity. I tested a total of 14 different scenarios, where either the spin or parity is different from that of the SM Higgs, and are described in chapters 1 and 6. The main purpose is to check whether the SM prediction can withstand the test or if any of the 14 models can give a better description and opens up the possibility to NP.

In order to produce a Higgs boson, a lot of particles have to collide head-on at very high energies. The Large Hadron Collider (LHC) at CERN accelerated protons to an energy of 4 TeV (4,000,000,000,000 electron volt) and collided these head-on at four different locations. One of these locations houses the ATLAS detector. It is the largest LHC detector and in 2012 it recorded the collisions at a total energy of 8 TeV. Even with the large amount of proton-proton collisions (about 20 million every second), the production of a Higgs boson is very rare (about 1 in every 200 milliard collisions). On the 4th of July 2012, about a thousand-billion collisions were analysed by the ATLAS and CMS experiments to finally announce the existence of a new particle with a mass of about 125 GeV (milliard electron volt). To check whether this new particle is indeed the Higgs boson of the SM, various tests have to be performed, like the measurement of its production cross-section, its exact mass, its coupling to other particles and finally, its spin and parity properties.

After its production, a Higgs boson lives very shortly. It almost immediately decays to lighter SM particles. During the decay, the spin and parity of the Higgs are passed on to its decay products. For the analysis in this thesis, I studied the $H \to WW \to e\,\nu_e\,\mu\,\nu_\mu$ decay channel, where the Higgs boson decays via two W bosons to finally an electron (e), a muon (μ) and two neutrinos (ν). This decay channel is schematically drawn on the left in figure S.2. It is challenging to measure the spin and parity in this channel, but in chapters 3 and 4 I explain that spin and parity are preferably measured in a configuration where the Higgs is at rest. The spin and parity can then be measured by looking at the angles and the energies of the decay particles. One of these angles is the opening angle between

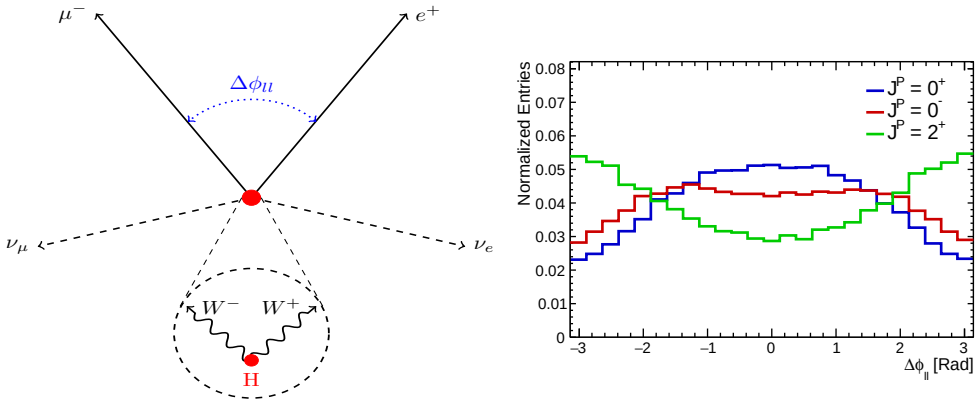

Figure S.2: Left, a schematic overview showing Higgs decay to two electrically charged W bosons, which subsequently decay to a positron (e^+), a muon (μ^-) and two neutrinos (ν_e and ν_μ). The opening angle, indicated with $\Delta\phi_{ll}$, is between the positron and the muon. Right, there are three distributions for $\Delta\phi_{ll}$, one for a SM Higgs (0^+), a parity-odd Higgs (0^-) and a spin-2 boson (2^+).

the electron and the muon, indicated with $\Delta\phi_{ll}$. The prediction for a SM Higgs boson is a distribution for $\Delta\phi_{ll}$ that has a maximum around zero. For a different spin, this maximum is found at higher values, something I explain in chapter 1. Figure S.2 shows on the right which $\Delta\phi_{ll}$ distributions are expected for a SM Higgs (blue), a parity-odd Higgs (red) and a spin-2 boson (green). In total, I created six different variables such as $\Delta\phi_{ll}$, each of them sensitive to the spin and/or parity of the Higgs boson. The description can be found in chapter 4.

In order to make distributions such as $\Delta\phi_{ll}$ in figure S.2, a lot of statistics is needed. For the spin and parity measurement, I used the complete ATLAS data set of 2012 with a centre-of-mass energy of 8 TeV. To select the collisions where a Higgs boson is produced, is a complicated matter. However, in chapter 2, I explain that the ATLAS detector is well-qualified to do just that. In chapter 5, I discuss in detail what the selection procedure is to obtain as many collisions, where a Higgs is produced, as possible. In the end, a data set remains with about 300 signal collision events, which belong to the $H \to WW \to e\nu_e\mu\nu_\mu$ decay channel, and about 5000 background collision events. It is of utmost importance to understand these background events in order to have a successful measurement on the spin and parity.

In chapter 6, I explain how the six spin and parity sensitive variables, introduced in chapter 4, can help to distinguish several models from each other. That will be done with a statistical method that takes into account the expected signal as well as the expected background. It enables us to assign signal events to the Higgs boson from the SM or to, for example, a spin-2 boson form a NP model. The predictions will then be compared

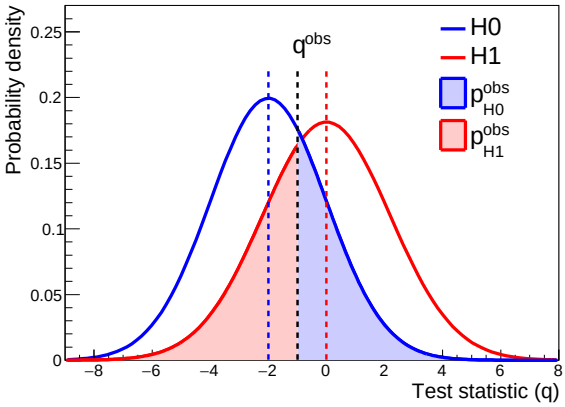

Figure S.3: A statistical method to compare two models, indicated as H1 in red and H0 in blue. The test statistic q gives the amount of preference for the H0 model with respect to the H1 model. The black dashed line gives a possible measurement from experiment and is indicated as q^{obs}. The red and the blue areas indicate the probability, given a certain q^{obs}, that respectively H0 or H1 is more likely.

with the measurement from the experiment. Figure S.3 gives an example. The blue and red lines each represent a separate model and on the x axis the likelihood of the models is indicated by the variable q. More to the right (positive q) means the red model (H1) is more likely, while more to the the left (negative q) prefers the blue model (H0). The dashed black line represents a hypothetical measurement (q^{obs}), so a possible value for q that can be obtained during a measurement. The red and blue dashed lines give the most probable value for q according to the red and blue model respectively. The red and blue coloured areas indicate the probabilities for each model. The bigger the area, the more likelier the respective model describes the measurement. However, if the observed q is too far from the model expectations (red and blue dashed lines), then both models give a bad description of the measurement. In the figure, the black dashed line is an example where the measurement falls right in between and neither prefers the red nor the blue model.

Figure S.4 shows the results from the 2012 ATLAS data for the test statistic for 2 of my 14 spin and parity scenarios. On the left, the SM (red) versus a spin-2 model (blue) and it looks like the measurement (black) prefers the spin-2 model. This is remarkable, because this measurement could confirm a spin-2 particle and thereby announce the end of the SM. In chapter 7, I focus more deeply on this result and introduce a thorough statistical analysis. The data is split up into collisions without any jets[2] (0-jet) and collisions with

[2]jets are sprays of particles originating from quarks or gluons that remain after the collision. Quarks and gluons have the tendency to emit other gluons or quark-antiquark pairs and thereby eventually create a spray of particles. The $H \to WW \to e\nu_e \mu\nu_\mu$ decay channel can have such a quark or gluon remnant, originating from the the gluons needed to make the Higgs boson.

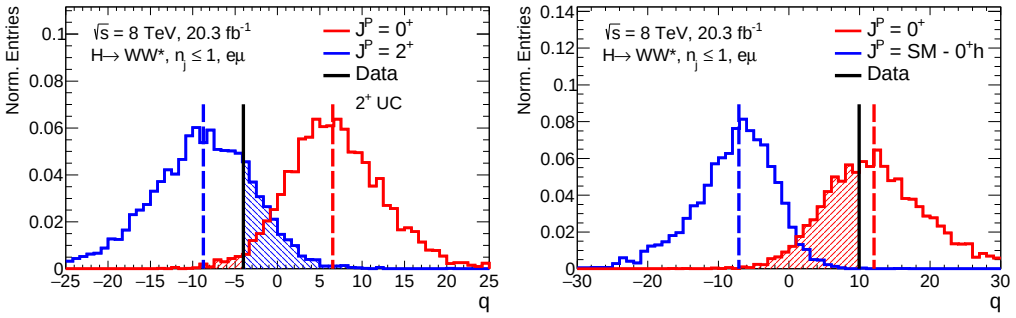

Figure S.4: Two results of the test statistic just as in figure S.3. On the left, the SM Higgs is compared to a model with a spin-2 particle. It looks like the data (black line) prefers the spin-2 model. On the right, the SM Higgs is compared to NP model with multiple Higgs bosons. In this case it is clear that the data prefers the SM prediction.

exactly one jet (1-jet). In the end, it turned out that the events without any jets are in good agreement with the SM prediction, but the events with exactly one jet prefer mostly the spin-2 model. However, the results are, statistically speaking, not significant enough and more data is necessary to confirm if the observed boson is either a spin-0 or a spin-2 particle.

The right figure of S.4 shows the SM (red) versus a NP model (blue) which predicts multiple Higgs bosons. It is clear that the data (black) prefers the SM prediction above the NP model. In chapter 8, I present this result together with the results of the other NP models where the Higgs is parity-odd or which have multiple Higgs bosons. For most of the cases, the SM is preferred above the NP models or the analysis is not able to discriminate sufficiently between them.

From the 14 tested NP models, only two are so unlikely compared to the measurement that they can be excluded at 95% confidence level. The NP model tested in the right figure of S.4 is one of these excluded models. For the other 12 NP models, more data is needed to make a similar statement. All results can be found in tables 7.3 and 8.3 of chapters 7 and 8.

Finally, in chapter 8, I present a couple of other studies in which I let the SM Higgs boson mix with a NP spin-0 particle[3]. It is similar to mixing two types of paint having each a different colour. If the SM Higgs is represented by blue paint and the NP spin-0 particle indicated with green paint, then during a measurement I try to see if the data paint is 100% blue or if it has traces of green in it. The more green, the more of the NP spin-0 particle is present in the mixture. For the (colour)measurement, I make use again of the

[3]Actually, I let the SM HWW coupling interfere with a non-SM spin-0 coupling by making use of an effective field theory, but to explain that goes beyond the scope of this summary and for a detailed explanation I refer the interested reader to section 1.4.

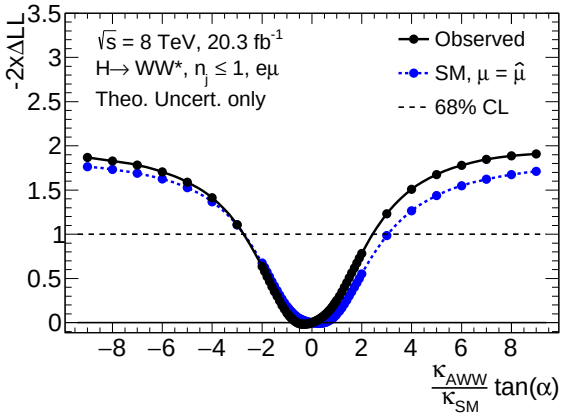

Figure S.5: Result of a study where the SM Higgs is mixed with a NP parity-odd Higgs boson. In the middle, at zero, there is no mixing, so a 100% SM Higgs. The more away from the middle, the more parity-odd Higgs is added to the mixture. The blue dots and dashed line give the prediction for the SM, while the black dots and line represent the measurement. On the *y* axis, the discrepancy of the measurement with respect to the mixing variable. It is clear that around zero, there is the least discrepancy with the data, so a preference for 100% SM Higgs without any mixing.

six spin and parity sensitive variables introduced in chapter 6. Figure S.5 shows the results of one of the mixing studies, in this particular case the mixing of a SM Higgs boson with a NP parity-odd Higgs boson. On the *x* axis, the SM prediction is at zero (100% blue, 0% green) and the further away you go, the more the contribution of the parity-odd Higgs (blue : green, → 95% : 5%, 90% : 10%, etc.) until only parity-odd Higgs remains. On the *y* axis of the same figure, the amount of discrepancy of the data with respect to mixing variable is displayed. The more discrepancy, the more unlikely the particular mixture. In the figures it can be seen that the 2012 ATLAS data (black dots and line) are a little bit shifted with respect the the SM expectation (blue dots and dashed line), but the difference between the two is minimal and not significant. Therefore, the SM prediction is in good agreement with the data for this mixing study.

In total, I conducted three mixing studies, where the SM Higgs boson was mixed with a NP spin-0 particle. For two of these three studies, the data prefers a light mixture, but it turns out that a pure SM Higgs sample, so no mixing, is still in good agreement with the data. In these same two studies, I was able to exclude certain mixtures at more than 95% confidence level. However, these mixing studies are not sensitive enough to exclude more mixtures at the same level. More data is needed to do just that. All results of the three mixing studies are presented in table 8.5 at the end of chapter 8.

Since the beginning of 2015, the LHC is colliding protons as scheduled and the ATLAS detector is collecting more data. The new data supplement the data collected in 2012 and enable us to measure the Higgs spin and parity with an even higher precision and thereby put tighter constraints on NP models. My analysis was able to exclude certain NP models, but I also observed tensions with the 2012 measurement with respect to the SM prediction for Higgs production with one additional jet. A similar analysis as the one I presented would be able to definitely confirm or reject this result with the newly collected data from the ATLAS detector. Maybe the discovered boson mixes with other Higgs bosons, just as in my mixing studies. I'm curious to find out.

Samenvatting

S

Voor zover wij weten is ons Heelal opgebouwd uit elementaire deeltjes, zoals quarks, gluonen en elektronen. Met elementair bedoelen we dat ze de kleinste deeltjes zijn en niet zijn opgebouwd uit nog kleinere deeltjes. De quarks en gluonen vormen de protonen en neutronen in een atoomkern en daaromheen bevinden zich de elektronen. Er zijn in totaal 17 elementaire deeltjes bekend en die worden beschreven door het zogenaamde Standaard Model, kortweg SM, wat een wiskundig model is en zeer precieze voorspellingen kan maken over deze deeltjes en hun interacties. Tot nu toe zijn er een groot aantal voorspellingen van het SM uitgekomen, maar er zijn aanwijzingen in ons Heelal te vinden dat het SM niet alles kan verklaren. We weten uit observaties aan sterrenstelsels dat alle deeltjes uit het SM maar slechts 4% beschrijven van het totale Heelal. De overige 96% wordt aangegeven met termen als donkere materie en donkere energie en om die te kunnen beschrijven zijn er wiskundige modellen nodig die verder gaan dan het SM. Deze modellen worden ook wel aangeduid met Nieuwe Natuurkunde (NN) en voorspellen ook extra elementaire deeltjes naast de deeltjes van het SM. Het is de taak van de wetenschap om het SM te blijven toetsen door middel van nieuwe experimenten. Een significante afwijking van de SM voorspelling bij een experimentele meting kan een teken zijn van de aanwezigheid van NN deeltjes. Ook kan er iets geobserveerd worden dat buiten het SM valt.

In dit proefschrift ben ik op zoek gegaan naar afwijkingen van het SM door te kijken naar de spin en pariteit[1] van het Higgs deeltje, ook wel Higgs boson genoemd. Spin is zoiets als het draai-moment van een deeltje en met pariteit vergelijkt men een deeltje met zijn spiegelbeeld. Het SM voorspelt dat de Higgs spin-0 en even-pariteit heeft, wat wil zeggen dat het geen draai-moment heeft en dat zijn spiegelbeeld identiek is aan zichzelf. Figuur S.1 geeft een voorbeeld van een pariteit-operatie, oftewel spiegeling, op een deeltje met spin en een Higgs deeltje. Voor het spin-deeltje is de spin-oriëntatie aangegeven met de rode en blauwe pijlen. Na een spiegeling verandert de spin van het deeltje van oriëntatie en daarmee heeft het spin-deeltje een oneven-pariteit. Om een ander voorbeeld te geven van oneven-pariteit: als je een moedervlek op je linkerwang hebt dan heeft jouw spiegelbeeld

[1] In feite kijk ik naar de CP-operatie, wat een combinatie is van de C-operatie die de elektrische lading van teken laat veranderen en een pariteit-operatie P. Het Higgs deeltje heeft geen elektrische lading dus blijft allen pariteit over.

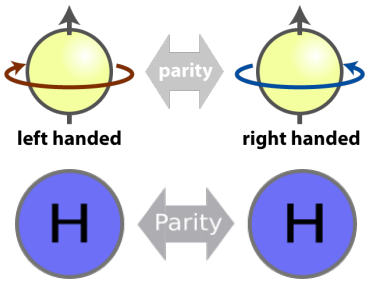

Figuur S.1: Een pariteit-operatie uitgevoerd op een linkshandig deeltje met spin (boven,[25]) en het Higgs deeltje volgens het SM (onder). De spin-oriëntatie keert om en het spin-deeltje wordt rechtshandig. Het heeft daarmee een oneven-pariteit. Het Higgs deeltje blijft identiek onder spiegeling dus heeft daarmee een even-pariteit.

een moedervlek op de rechterwang. Het Higgs deeltje blijft identiek na de spiegeling en heeft dus een even-pariteit.

Er zijn verscheidene NN modellen die voorspellen dat het Higgs deeltje een andere spin dan 0 kan hebben of bijvoorbeeld oneven-pariteit. Er zijn ook NN modellen waarbij er meer dan één Higgs deeltje wordt voorspeld en die nieuwe Higgs deeltjes kunnen zowel even- als oneven-pariteit hebben. De extra Higgs deeltjes kunnen invloed uitoefenen op de meting als er gekeken wordt naar spin en pariteit. Ik heb in totaal 14 verschillende spin en pariteit-scenarios getest, die worden beschreven in de hoofdstukken 1 en 6. Het doel is om te kijken of de SM voorspelling stand houdt of één van de 14 modellen een betere beschrijving kan geven en daarmee de deur opent naar NN.

Om een Higgs deeltje te kunnen maken, moeten we heel veel deeltjes op elkaar botsen bij zeer hoge energiën. De Large Hadron Collider (LHC) van CERN versnelde in 2012 protonen naar een energie van 4 TeV (4.000.000.000.000 electron-volt) en botste die vervolgens op elkaar op 4 verschillende plekken. Op één van die plekken staat de ATLAS detector. Dit is het grootste experiment van de LHC waar in het jaar 2012 botsingen bij een energie van 8 TeV plaatsvonden. Ondanks de grote hoeveelheid proton-proton botsingen (ongeveer 20 miljoen per seconde), was het produceren van een Higgs deeltje vrij zeldzaam (ongeveer 1 per 200 miljard botsingen). Er moesten ongeveer een quadriljoen (1 met 15 nullen) botsingen door het ATLAS en CMS experiment worden geanalyseerd om op 4 Juli 2012 het bestaan van een nieuw deeltje met een massa van ongeveer 125 GeV (miljard electron-volt) te bevestigen. Om na te gaan of dit daadwerkelijk het Higgs deeltje van het SM is of een ander exotisch NN deeltje, moeten er verscheidene dingen gemeten worden zoals, de werkzame-productie-doorsnede, de precieze massa, de koppelingen aan andere deeltjes en tenslotte ook de spin en pariteit.

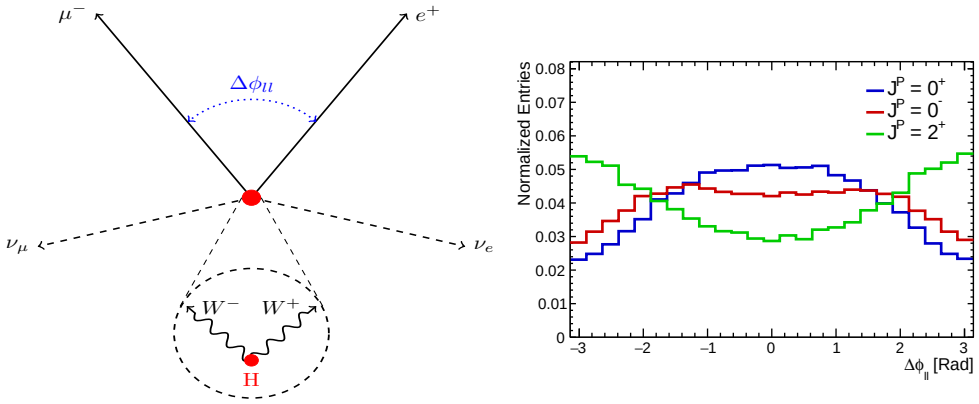

Figuur S.2: Links, een schematische weergave hoe Higgs vervalt naar twee elektrisch geladen W deeltjes, die op hun buurt vervallen naar een positron (e^+), een muon (μ^-) en twee neutrinos (ν_e en ν_μ). De openingshoek aangegeven met $\Delta\phi_{ll}$ is tussen het positron en het muon. Rechts, zijn de drie distributies voor $\Delta\phi_{ll}$ voor een SM Higgs (0^+), een spin-0 oneven-pariteit Higgs (0^-) en een spin-2 deeltje (2^+).

Nadat het Higgs deeltje geproduceerd is, leeft het maar zeer kort. Het vervalt vrijwel direct in lichtere SM deeltjes. Tijdens dat verval wordt de informatie van de spin en pariteit overgedragen op de vervaldeeltjes. Ik heb voor mijn proefschrift het $H \to WW \to e\nu_e\mu\nu_\mu$ vervalkanaal bestudeerd, waarbij een Higgs deeltje via twee W deeltjes vervalt naar een electron (e), een muon (μ) en twee neutrinos (ν). Dit vervalkanaal is schematisch weergegeven in de linkerfiguur van figuur S.2. Het is een lastig vervalkanaal om de spin en pariteit te meten, maar in hoofdstukken 3 en 4 leg ik uit dat de spin en pariteit het beste gemeten kan worden door terug te gaan naar een configuratie waarbij de Higgs stilstaat. De Higgs spin en pariteit is dan te meten via de hoeken en energiën van de vervaldeeltjes. Eén van die hoeken is de openingshoek tussen het electron en het muon, aangegeven met $\Delta\phi_{ll}$. Voor een spin-0 Higgs uit het SM is de voorspelling dat de distributie voor $\Delta\phi_{ll}$ een maximum bij nul heeft. Voor een andere spin hypothese ligt dat maximum bij hogere waardes, iets wat ik uitleg in hoofdstuk 1. Figuur S.2 geeft in het rechter plaatje aan welke waarden je voor $\Delta\phi_{ll}$ krijgt voor een Standaard Model Higgs (blauw), een oneven-pariteit Higgs (rood) en een spin-2 deeltje (groen). Ik heb in totaal 6 verschillende variabelen gemaakt zoals $\Delta\phi_{ll}$, die elk gevoelig zijn voor de spin en/of pariteit van het Higgs deeltje. De beschrijving daarvan is te vinden in hoofdstuk 4.

Om distributies zoals die van $\Delta\phi_{ll}$ in figuur S.2 te kunnen maken is het nodig om veel statistiek te hebben. Voor de spin en pariteit-metingen heb ik gebruik gemaakt van de complete 2012 data set van ATLAS bij een massa-middelpunts-energie van 8 TeV. Om juist die botsingen te selecteren waar een Higgs deeltje wordt geproduceerd, is een complexe zaak. Echter, in hoofdstuk 2 vertel ik dat de ATLAS detector uitermate geschikt is voor deze taak. In hoofdstuk 5 bespreek ik in detail de selectie procedure om zoveel mogelijk

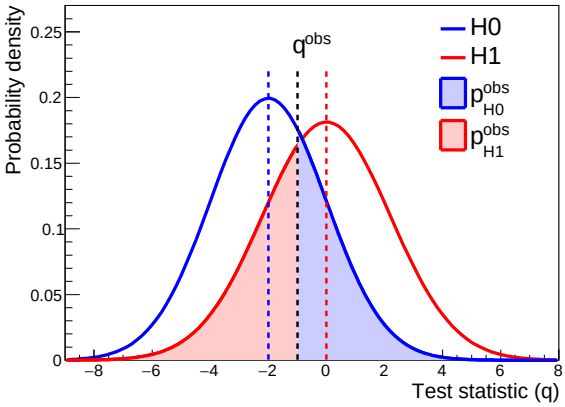

Figuur S.3: Een statistische methode om twee modellen, aangegeven als H1 in het rood en H0 in het blauw, met elkaar te vergelijken. De test-statistiek q geeft de mate van voorkeur aan voor H0 ten opzichte van H1. De zwarte stippellijn geeft een mogelijke experimentele meting aan, aangeduid met q^{obs}. Het rode en blauwe gebied geven aan hoe groot de kans is, gegeven uitkomst q^{obs}, dat H0 respectievelijk H1 het meest waarschijnlijk is.

botsingen te selecteren waarbij mogelijk een Higgs deeltje is geproduceerd. Uiteindelijk blijft er een data set over met 300 signaalbotsingen, welke afkomstig zijn van het $H \to WW \to e\nu_e \mu\nu_\mu$ vervalkanaal, en ongeveer 5000 achtergrondbotsingen. Het is daarom zaak om ook deze achtergrondbotsingen goed in kaart te brengen om de spin en pariteit-meting tot een succes te maken.

In hoofdstuk 6 leg ik uit hoe je via zes spin en pariteit-variabelen, welke zijn uitgelegd in hoofdstuk 4, het beste modellen met elkaar kunt vergelijken. Dat wordt gedaan met behulp van een statistische analyse die rekening houdt met zowel het verwachte signaal als de achtergrond. Het stelt ons in staat om de signaalbotsingen toe te kennen aan een Higgs deeltje uit het SM of bijvoorbeeld een NN model met een spin-2 deeltje. De voorspellingen worden vervolgens vergeleken met de experimentele data. Figuur S.3 geeft daar een voorbeeld van. De blauwe en rode lijnen geven elk een model aan en op de x-as geeft de variabele q aan welk model waarschijnlijker is. Meer naar rechts (positieve q) betekent dat het rode model (H1) waarschijnlijker is, terwijl dat geldt voor het blauwe model (H0) voor meer naar links (negatieve q). De zwarte stippellijn geeft een hypothetische meting (q^{obs}) aan, dus een mogelijke waarde voor q tijdens een experimentele meting. De rode en blauwe stippellijnen geven de meest waarschijnlijke waarde voor q volgens het rode respectievelijk blauwe model. De in blauw en rood gekleurde gebieden geven de waarschijnlijkheid weer hoe juist respectievelijk het blauwe en rode model is. Een groter gekleurd gebied betekent een grotere kans dat het model van de desbetreffende kleur de juiste is voor een bepaalde meting. Echter, als de observatie zich te ver van de verwachte

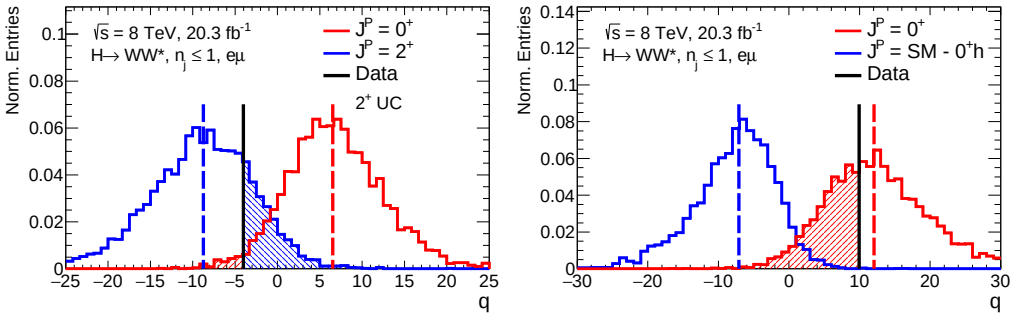

Figuur S.4: Twee uitkomsten voor statistische vergelijkingen zoals in figuur S.3. Links wordt het SM Higgs vergeleken met een spin-2 deeltje model. Het ziet ernaar uit dat het spin-2 model wordt geprefereerd door de data (zwarte lijn). Rechts het SM Higgs vergeleken met een NN model met meerdere Higgs deeltjes. Hier is duidelijk dat de data het SM prefereert.

q-waarden bevind (rode en blauwe stippellijnen) dan beschrijven beide modellen de data slecht. In de figuur is in het zwart een voorbeeld-meting te zien waarbij de meting precies in het midden valt en noch het rode model noch het blauwe model prefereert.

Figuur S.4 geeft de resultaten voor de 2012 ATLAS data voor de statistische analyse van 2 van mijn 14 spin en pariteit-scenarios. Links is de test van het SM (rood) versus een spin-2 (blauw) deeltje model en het lijkt erop dat de gegevens (zwart) het spin-2 model prefereert boven het SM. Dit is bijzonder, want deze meting zou wel eens de bevestiging van een spin-2 deeltje kunnen zijn en daarmee het einde inluiden van het SM. In hoofdstuk 7 ga ik dieper in op dit resultaat en doe een grondige statistische analyse. De data werd opgesplitst in botsingen zonder jets[2] (0-jet) en botsingen met exact één jet (1-jet). Uiteindelijk bleek dat de botsingen zonder jets goed overeenkwamen met de SM voorspelling, maar dat vooral de botsingen met precies één jet een spin-2 deeltje prefereren. Echter, het resultaat is statistisch gezien (nog) niet significant genoeg. Er zijn dus meer meetgegevens nodig om definitief vast te stellen of het geobserveerde boson een spin-0 of een spin-2 deeltje is.

In de rechterfiguur van figuur S.4 wordt het SM (rood) vergeleken met een NN model met meerdere Higgs deeltjes (blauw). Het is duidelijk dat de meting (zwart) het SM sterk prefereert boven het NN model. Dit resultaat presenteer ik in hoofdstuk 8 samen met de resultaten van de andere NN modellen met oneven-pariteit Higgs of meerdere Higgs deeltjes. De uitkomst is in de meeste gevallen dat het SM geprefereerd wordt of dat de analyse niet gevoelig genoeg is om het SM van het NN model te onderscheiden.

[2]jets zijn sproeiers van deeltjes die afkomstig zijn van quarks of gluonen die overblijven na de botsing. Quarks en gluonen hebben de neiging om andere gluonen en quark-antiquark paartjes uit te stralen en creëeren daarmee uiteindelijk een deeltjessproeier. Voor het $H \to WW \to e\nu_e \mu\nu_\mu$ verval-kanaal kan een quark/gluon overblijven als restant van de gluonen die nodig waren om een Higgs deeltje te maken.

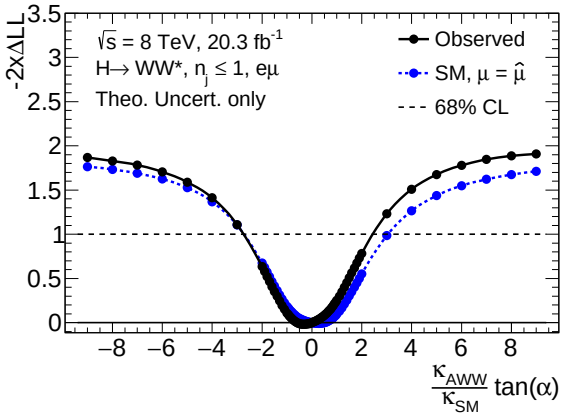

Figuur S.5: Uitkomst van een studie waarbij het SM Higgs wordt gemixt met een NN oneven-pariteit Higgs. In het midden bij 0, is er geen mixing, dus 100% SM Higgs. Hoe meer er naar buiten wordt gegaan, des te meer oneven-pariteit Higgs er wordt toegevoegd aan de samenstelling. De blauwe bollen en stippellijn geven de verwachting weer voor het SM, terwijl de zwarte bollen en lijn de gemeten data voorstellen. Op de y-as staat de discrepantie van data ten opzichte van de mixing-variabele. Er is duidelijk de minste discrepantie vlakbij 0, dus zo goed als 100% SM Higgs zonder mix.

Van de 14 geteste NN modellen zijn er twee waarvan de meting aangeeft dat ze zo onwaarschijnlijk zijn dat ze kunnen worden uitgesloten met een 95% zekerheidsniveau. Het NN model in de rechterfiguur van figuur S.4 is er daar één van. Voor de overige 12 NN modellen is meer data nodig voor een soortgelijke uitspraak. Alle resultaten zijn terug te vinden in tabellen 7.3 en 8.3 in hoofdstukken 7 en 8.

Als laatste, in hoofdstuk 8 presenteer ik nog een paar extra studies, waarbij ik het SM Higgs deeltje laat mixen met een ander NN spin-0 deeltje[3]. Dit is te vergelijken met het mixen van twee verschillende kleuren verf. Als het SM de blauwe verf zou zijn en het NN spin-0 deeltje de groene verf voorstelt, dan doe ik een meting aan de kleur van de verf om te kijken of de kleur 100% blauw is of tinten groen heeft. Hoe meer groen, des te meer het NN spin-0 deeltje aanwezig is in de samenstelling. Bij de (kleur)meting maak ik weer gebruik van de eerder genoemde 6 spin en pariteit-variabelen. Figuur S.5 geeft het resultaat van één van die mixing-studies weer, in dit geval het mixen van het SM Higgs deeltje met een ander NN oneven-pariteit Higgs deeltje. Op de x-as bij 0 is de SM voorspelling (100% blauw, 0% groen) en hoe verder je daarvandaan gaat hoe meer de oneven-pariteit Higgs gaat bijdragen (blauw : groen → 95% : 5%, 90% : 10%, etc.) tot uiteindelijk er alleen het oneven-pariteit Higgs deeltje overblijft. Op de y-as van diezelfde figuur wordt de

[3] In feite laat ik de SM HWW koppeling interfereren met een niet-SM spin-0 koppeling door gebruik te maken van een effectieve veldentheorie, maar de uitleg hiervan is te ingewikkeld voor deze samenvatting en ik verwijs naar sectie 1.4 voor de geïntereseerde lezer.

mate van discrepantie met de data weergegeven. Hoe groter de discrepantie, des te onwaarschijnlijker is de betreffende waarde voor de mixing-variabele. In de figuur is te zien dat de meetresultaten aan de 2012 ATLAS data (zwarte bollen en lijn) een klein beetje verschoven zijn ten opzichte van de SM verwachting (blauwe bollen en stippellijn). Het meetresultaat ligt iets onder de SM verwachting (bij 0 in het midden), maar dit verschil is miniem en niet significant. Het SM geeft daarmee een prima voorspelling voor deze mixing-resultaten.

Ik heb in totaal drie mixing-studies gedaan waarbij de SM Higgs werd gemixt met een ander NN spin-0 deeltje. Bij twee van de drie studies geeft de data een voorkeur voor een lichte mixing, maar het blijkt dat een pure SM Higgs, dus geen mixing, nog steeds overeenkomt met de data. Bij diezelfde twee studies kon ik bepaalde mixing-verhoudingen met meer dan 95% zekerheidsniveau uitsluiten. Echter, de mixing-studies zijn niet gevoelig genoeg om meerdere regio's uit te sluiten bij dit zekerheidspercentage. Daar is meer data voor nodig. Alle resultaten voor de drie mixing-studies staan vermeld in tabel 8.5 aan het eind van hoofdstuk 8.

Sinds begin 2015 vinden er weer, zoals gepland, proton-proton botsingen plaats bij de LHC en verzamelt ATLAS nog meer data. De hiermee behaalde resultaten vormen een aanvulling op de data uit 2012 en stellen ons in staat de Higgs spin en pariteit nog preciezer te meten en dus nog scherpere limieten te zetten op NN modellen. Met mijn analyse kon ik bepaalde NN modellen uitsluiten, maar ik zag ook spanningen tussen de metingen aan de 2012 data en de SM voorspelling bij de botsingen waar Higgs werd gemaakt in combinatie met één jet. Een soortgelijke analyse als de mijne kan dit resultaat, met de nieuwe gegevens die ATLAS verzamelt, de komende jaren definitief bevestigen of ontkrachten. Misschien mixt het Higgs deeltje met meerdere Higgs deeltjes, zoals in mijn mixing-studies. Ik ben benieuwd.

“Because we do most things relying only on our own sagacity we become self-interested, turn our backs on reason, and things do not turn out well. As seen by other people this is sordid, weak, narrow, and inefficient. When one is not capable of true intelligence, it is good to consult with someone of good sense. An advisor will fulfil the Way when he makes a decision by selfless and frank intelligence because he is not personally involved. This way of doing things will certainly be seen by others as being strongly rooted. It is, for example, like a large tree with many roots. One man’s intelligence is like a tree that has been simply stuck in the ground.”

Yamamoto Tsunetomo - Hagakure, The Book of The Samurai

Acknowledgements

It's done! Four-and-a-half years have passed and I can finally smell victory in the form of freshly printed thesis copies. To get to this point, so many things have happened that it's impossible to write it all down on these few pages. These last few years, I've met a whole lot of interesting and cool people, who left an everlasting impression on me. All the good times, but also all the hardships shaped me into the person I'm today. I would like to thank all the persons involved for making it happen! Let me pick out a couple of people I'm indebted to in particular.

Allereerst wil ik mijn dank betuigen aan mijn promotor, Stan Bentvelsen, en mijn copromotor, Peter Kluit. Stan, bedankt dat je mijn interesse voor Higgs fysica heb aangewakkerd en me altijd heb gesteund in de tijden dat de analyse niet zo mee zat. De keren dat ik voor een dichte deur stond, die vergeef ik je en ik vind dat je, ondanks je vaardigheden om te plannen, het uitstekend doet als directeur en een goed voorbeeld stelt aan anderen. Peter, ik moet toegeven dat ik niet zo goed wist waar ik aan begon toen ik met je samen begon te werken aan het ATLAS muon systeem en we later samen een analyse probeerden op te zetten. Het duurde even voordat we op elkaar waren ingesteld, maar ik heb ontzettend veel van je geleerd en mijn dank is daarvoor groot. Ik stel het ook zeer op prijs dat je ook tijdens mijn wat mindere periodes me er toch steeds van overtuigde om netjes en secuur te werk te gaan. Ik wens je veel succes bij de activiteiten met de ILC en wie weet komen we elkaar nog wel eens tegen in Japan! Ook wil ik Paul de Jong, Paul Kooijman, Bert Schellekens, Eric Laenen, Gerhard Raven en Valerio Dao bedanken voor het lezen van het manuscript en om deel uit te maken van mijn verdedigingscommissie.

For the people at Nikhef, I really felt like being a part of a family when I joined the ATLAS group for my master thesis. It was not a difficult choice for me to apply for a PhD position there when I was done with the project. I want to thank Marcel and Ivo for supervising me back then and helping me get started at the beginning of the PhD. To all my former office mates, Aagje, Nika, Rosemarie, Marco and Birgit, I would like to thank you for the nice time and tolerating my sometimes erratic behaviour. I would also like to thank the whole LHCb group for the nice times while invading the ATLAS Friday afternoon drinks and going out together. Thank you, Lydia, Vince, Pierfrancesco, Tim, Matteo, Remco, Dominik, Marc, Wouter, Ivan, Joern, Stefan, Antonio, Priscilla, Geert-Jan, Rogier, Pier-Olivier, Hartger, Robin, Nicole, Ido, John, Egge, Jeroen, Roel, Serena, Daan, Faab, Veerle, Pieter, Rose, Sipho, Alis, Naghme, Carlos, Joris, Rolf, Panos, Lodewijk, Brent and the list goes on ... sorry if I can't remember all of you.

For the people at CERN, I would like to thank Pamela, Tatjana and Nikos to let me join the HWW properties group even though I didn't really care too much about the BDT studies.

I would also like to thank my “grumpy” office mate, Valerio, from who I learned a ton of things and listened to my whining about how annoying other people are. Thanks a lot for giving me so many constructive comments, basically on everything written down in the thesis!

To my non-physicist friends in Geneva, Sanne, Boryana, Joao, Doro, Maria, Christina, it was great to hang out with you guys! If it was paragliding, skydiving, walking on an active volcano, it doesn’t matter! Thanks to you my time in Geneva was not as dull as is common to the Swiss. Also to the people on “The Boat”, Felix, Martin, Abdo, Douwe-Sjoerd and Thijs, it was a pleasure to share a place on the water and have crazy parties together! I hope you guys are doing great with whatever you’re up to at the moment and in the future.

I would like to thank in particular Ingrid, Siim, Akshay and Suvayu for not only the awesome time we spent together during coffee breaks, drinks, trips and many other activities, but also for supporting me while I felt the world was just one pile of shit. My time at Nikhef and CERN would definitely have been much much lamer if you were not around. Yes, I can act a little bit like a retard and say what I think without caring too much about the feelings of others, but I’m really glad that I could just be myself around you guys without having to keep up appearances or anything phony like that. You are the best friends I could ever wish for so let’s keep in touch and keep doing cool stuff in the future!

Ik wil ook graag mijn familie bedanken voor hun steun en luisterend oor als ik weer iets te vertellen had over “Het CERN” en het Higgs deeltje. Ik vond het erg fijn om gewoon mezelf te kunnen zijn als ik bij jullie was voor een verjaardag, een wintersportvakantie, een familieweekend, een brusjesdag, een borrel of om gewoon aan te schuiven bij het avondeten en wat bij te kletsen. Ik hoop dat jullie nu ongeveer een idee hebben wat ik de afgelopen 5 jaar heb zitten uitspoken! Opa en Oma, ik ben erg blij dat jullie dit werk nog kunnen meemaken, want jullie hebben de basis gelegd bij die stille, 10-jarige jongen die zo geïnteresseerd was in geologie en later bijna alles wilde weten en leren wat er te leren viel!

Ik wil mijn broer Robin en collega Lydia heel erg bedanken om de verantwoordelijk op zich te nemen om mijn paranimfen te zijn. Ik ben blij om jullie aan mijn zijde te hebben tijdens de verdediging en ik hoop dat jullie niet al te veel dingen achter mijn rug om hoeven te regelen ;) Merel, hartstikke bedankt voor het ontwerpen van de mooie cover voor mijn proefschrift! Het zou er een stuk minder cool uit hebben gezien als ik het allemaal zelf had moeten doen!

Finally, the last thing I want to say: Keep Spinning Eddy!